Instrument Development for Nanomaterial Risk Assessment

Brossell, Dirk

DOI
10.4233/uuid:fe1ecd53-b939-4efc-b6e9-34ec098efde2

Publication date
2016

Document Version
Final published version

Citation (APA)
Brossell, D. (2016). *Instrument Development for Nanomaterial Risk Assessment*. [Dissertation (TU Delft), Delft University of Technology]. https://doi.org/10.4233/uuid:fe1ecd53-b939-4efc-b6e9-34ec098efde2

Instrument Development for Nanomaterial Risk Assessment

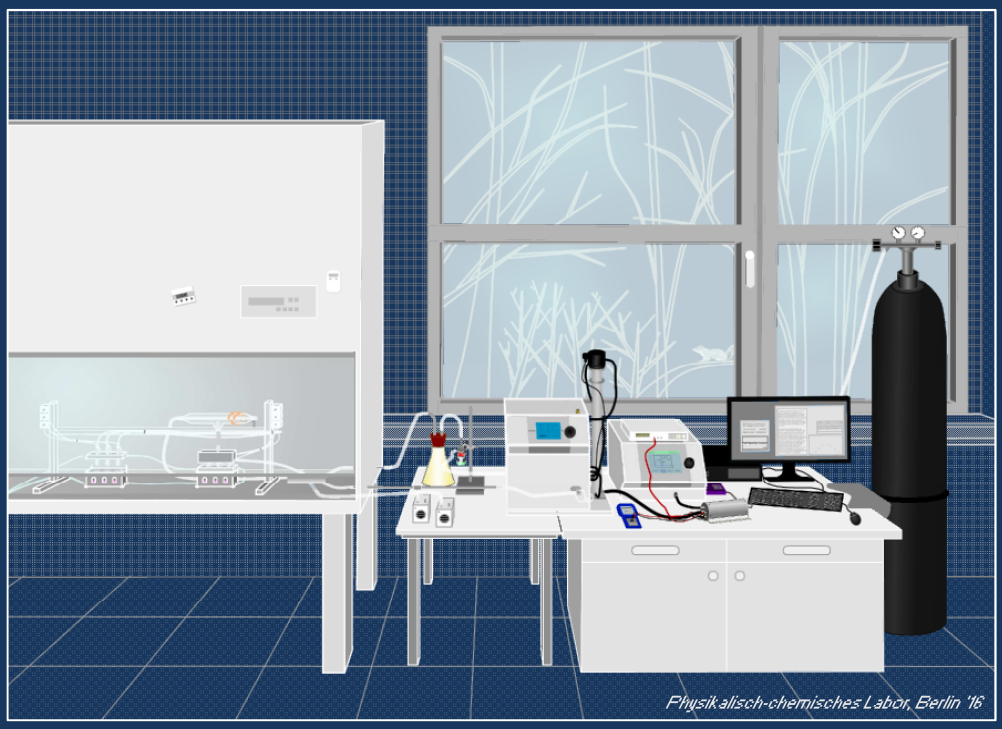

Dirk Broßell

Instrument Development for Nanomaterial Risk Assessment

Proefschrift

ter verkrijging van de graad van doctor
aan de Technische Universiteit Delft,
op gezag van de Rector Magnificus prof. ir. K.C.A.M. Luyben;
voorzitter van het College voor Promoties,
in het openbaar te verdedigen op
donderdag 20 oktober om 10:00 uur

door

Dirk BROßELL
Diplom-Phyiker, Freie Universität Berlin, Germany
geboren te Papenburg, Germany

This dissertation has been approved by the
promotor: Prof. dr. A. Schmidt-Ott

Composition of the doctoral committee:

Rector Magnificus	chairman
Prof. dr. A. Schmidt-Ott	Delft University of Technology

Independent members:

Prof. dr. H. Fissan	University of Duisburg-Essen, Germany
Prof. dr. ir. J.R. van Ommen	Delft University of Technology
Prof. dr. G. Biskos	University of the Aegean, Greece
Prof. dr. T. Gebel	Federal Institute for Occupational Safety and Health., Germany
Dr. C. Asbach	Institute for Energy and Environmental Technology e.V., Germany
Dr. O. Schmid	Helmholtz Zentrum München, Germany
Prof. dr. F.M. Mulder	Delft University of Technology, reserve member

This work has received funding from the European Union Seventh Framework Programme (FP7/2007-2013) under grant agreements n° 211464-2 and n° 310584.

Stellingen behorende bij het proefschrift

Instrument Development for Nanomaterial Risk Assessment

Dirk Broßell, Technische Universiteit Delft

1. Zeer gevoelige in vitro modellen die Cyto-TP gebruiken, kunnen betrouwbaar voorspellen of verdere toxiciteitsproevennodig zijn en de noodzaak van dierproeven verminderen.

2. Door het scheiden van enkele vezels van een vezel-bevattendestof, maakt de nano-PMC het mogelijk elke vezel te tellen, eeninstrumentale gat in de Expositionsschatting.

3. Een geoptimaliseerde aerodynamische lens in de inlaat die deeltjes dwingt dicht bij het radiale centrum van de classificator in te treden, zal de scheming van de nano-PMC verbeteren.

4. De constructie van een modulair instrument met uitwisselbarecomponenten is de juiste manier om met onverwachte complicaties om te gaan.

5. Zolang serum-supplementen die nodig zijn voor celkweek uit het bloed van runder foetussen gekweekt worden, zijn in vitro tests niet echt bevorderlijk voor het welzijn van dieren.

6. De opmerking van Voltaire dat "gezond verstand niet zo wijdverbreid is" moet het leidend principe voor bedrijfsveiligheidsfunctionarissen zijn.

7. Een regulerende "nano"-definitie is nodig, zodat fabrikanten hun innovatieve materiaal kunnen markeren als „non-nano“.

8. Een voorwaarde om het predikaat "wetenschapper" te verdienen, is in staat te zijn niet dat ene storende feit dat de meest gekoesterde hypothese ernstig bedreigt te negeren.

9. Pogingen van de administratie afdelingen om de bureaucratie te vereenvoudigen door het invoeren van inteligente software resulteert vaak in meer complexiteit.

10. Een objectieve Nederlands-Duitse vergelijking van het fietstalent en de systemen voor fietswegen verklaart de noodzaak om in Duitsland een helm te dragen.

Deze stellingen worden opponeerbaar en verdedigbaar geacht en zijn als zodanig goedgekeurd door de promoter, Prof. dr. A. Schmidt-Ott.

Propositions belonging to the thesis

Instrument Development for Nanomaterial Risk Assessment

Dirk Broßell, Delft University of Technology

1. Highly sensitive *in vitro* models applying the Cyto-TP can reliably predict if further toxicity testing is required and can reduce the need for animal experiments.

2. By separating single fibres from a fibre-containing dust, the nano-PMC enables single fibre counting, an instrumental gap in exposure assessment.

3. An optimized aerodynamic lens in the inlet that forces particles to enter the classifier near its radial centre would increase the resolution of the nano-PMC.

4. Constructing a modular instrument with interchangeable components is the proper way to manage unforeseen complications.

5. As long as serum-supplements that are needed for cell cultivation are harvested from the blood of bovine foetuses, *in vitro* tests are not really beneficial for animal welfare.

6. An observation by Voltaire that "common sense is not so common" should be the guiding principle for occupational safety officers.

7. A regulatory "nano"-definition is desired so that manufacturers can confidently label their innovative materials as "non-nano".

8. One prerequisite for deserving to be called a scientist is the ability not to ignore that one annoying fact seriously challenging the cherished hypothesis.

9. Endeavours of administration departments to simplify bureaucracy by implementing clever software often results in more complexity.

10. An objective Dutch-German comparison of cycling talent and the bikeway systems explains the necessity to wear bicycle helmets in Germany.

These propositions are considered opposable and defendable and as such have been approved by the supervisor, Prof. Dr. Andreas Schmidt-Ott.

Acknowledgements

I consider myself quite fortunate to be able to work an interesting and fulfilling job in a governmental research institute, the Federal Institute for Occupational Safety and Health (BAuA), and at the same time use my research to strive for a doctor's title at Delft University of Technology. Therefore, I'd like to take the opportunity to thank certain people that helped me in various ways during my time as a PhD student.

First of all, I want to thank Andreas, my promoter. You always gave me helpful advice when I needed it and at the same time gave me much freedom over my research. In my understanding, the academic title of "Doctor" acknowledges one's ability to establish a scientific hypothesis and then commit to its proof or disproof. One mayor quality a scientist should therefore have is the courage to take chances because the result of one's commitment is often uncertain. Andreas, you took your chances with me. Most of my research was conducted in Berlin and I could not be in your direct care. Nonetheless, you put trust into me as a person and into my dedication for my research. Not only for that will I forever be grateful.

Of all my great colleagues at the BAuA, I want to thank Sabine Plitzko the most. You not only have helped me getting accustomed to our mutual workplace, but also trusted me, a fresh and inexperienced graduate, to manage our first international research project which also served the purpose to initiate our continuing international collaborations. I also want to thank Gunter Linsel, not only a fellow physicist but also an expert in cell physiology who collaborated with me in developing the Cyto-TP. Silke, thank you for patiently teaching me the necessary skills in cell biology and helping me to validate the Cyto-TP. Nico, thank you for giving me a helping hand whenever I needed one and for being a good friend. I consider myself to be very lucky to have so many great colleagues in my group and work environment, who I had great scientific and personal talks with, helped me in various ways during my research, accompanied me on business trips and even vacations and took me along to after-work dinners and Christmas market visits. Therefore, I want to thank my current and former colleagues of my workgroup at BAuA, Barbara, Dani, Carmen, Elisabeth, Jana, Dominic, Gabi, Volker, Asmus, John, Gabi and Erhardt for making my daily labour a lot more enjoyable. Finally, I want to thank Peter Kujath, Rolf Packroff and Rüdiger Pipke for the continuous support of my work. Without the financial backup by BAuA, my developmental work would not have been possible and a complex instrument like the nano-PMC would have never seen the light of day.

At TU Delft, I met many great people at the Faculty of Applied Science. George, I want to thank you for being a great collaborator in developing and testing the nano-PMC and your effort in helping me to write the paper. Tobias and Marco, you have been great accomplices as fellow PhD students, helped me when I arrived at Delft and showed me how to literally climb walls. I will also fondly remember how we accomplished multicultural exchange in South Korea, when playing football with bhuddist monks at the Golgulsa temple or drinking with locals at the beach in Busan.

The research and development regarding the Cyto-TP was conducted under the umbrella of the European Union, first in the Nanodevice project and subsequently in the NANoREG project. I had the opportunity to get to know many European scientists who are leading experts in the field of aerosol science. I want to highlight the fruitful collaboration with Christof Asbach from the Institute for Energy and Environmental Technology e.V., who not only had the initial idea behind the Cyto-TP but also helped me developing the prototype and write my first paper. Christof, you have also been a great table-mate at various conference dinners and someone who I could share my passion about football with.

I also want to thank Otmar Schmid, a member of my doctoral committee for providing comments and suggestions that helped to raise the scientific level of my thesis.

Zum Schluss möchte ich meiner Familie danken, die mir immer eine Unterstützung während dieser nicht immer einfachen Zeit war. Mein Vater und meine Mutter waren nicht nur während meines Studiums, sondern auch während meiner Zeit als Doktorand immer eine emotionale Stütze und unser Haus in Papenburg ein willkommenes Rückzugsgebiet. Mama und Papa, zusammen mit meinen Großeltern habt ihr meine Interessen an der Naturwissenschaft schon im Kindesalter entdeckt und dieses aktiv gefördert. Letztendlich möchte ich mich dafür entschuldigen, dass ich jetzt erst meine akademische Ausbildung abgeschlossen habe. Es war ein langer Weg, den zu gehen ihr mir alle geholfen habt.

Dirk

Contents

Chapter 1: General Introduction

Technological sustainability is strongly connected to the precautionary principle that has been part of the environmental and health policy of the European Union. It is the practice to identify and reduce risks before they can emerge. A requirement is the ability to correctly predict the risk. For relatively new technologies like nanotechnology, prediction tools are often missing and must be developed. The current inability to comprehensibly address the fear that nanotechnology might be harmful to humans and the environment has lowered the public confidence in nanotechnology. Risk prediction tools are limited partly due to instrumental gaps that hamper the ability to examine nanomaterials for features that can be associated with their risk. In the following sections, these gaps are identified, providing the rationale for new instruments, developed over the course of this thesis, namely the nano-PMC and the Cyto-TP.

The nano-PMC is a classifier for particle mass. In short, the nano-PMC can help to better characterize the potential of human exposure. The other device, the Cyto-TP, is an exposure module for an in vitro toxicity test for aerosols comprising nanomaterials. The Cyto-TP might be suitable to allow the correlation of results obtained in vitro with health effect observed in vivo and can therefore help to drastically reduce the need to conduct animal studies. Since exposure and toxicity are both important aspects of risk assessment, both instruments can play a significant role in promoting sustainable nanotechnology by enabling better and more frequent testing, for example in the concept of safety-by-design, that was developed as a direct consequence of the precautionary principle to promote sustainability of nanotechnology.

1.1. Rising concerns about nanotechnology

Ever since Richard Feynman proposed in 1959 in his famous lecture "There is Plenty of Room at the Bottom" that scientists and engineers should think small, nanotechnology has rapidly gained momentum and is now a fast growing source of innovations. By 2013, more than 70.000 workers in Germany alone are employed in ca. 110 enterprises that develop nanotechnology products, generating revenue of around 1.7 billion € [1]. Simultaneously, concerns about possible negative impacts on human health and the environment by nanotechnology have been expressed, established by fear that the very properties that make nanomaterials so useful might also render them more harmful. In fact, influential non-government organizations like the German Bund für Umwelt und Naturschutz Deutschland (BUND) have already established tools like „nanowatch.de", a register to inform (or warn) consumers about products containing nanomaterials [2]. The underlying general assumption is that the risk associated with nanotechnology is insufficiently characterized so that nanomaterials need to be put under suspicion. Consequently, there is a public call for sustainable nanotechnology where the notion of safety plays a significant role in its development process. New developments should pose no risk to human health or the environment while retaining their functionality. Sustainability should be achieved with strategic risk research that accompanies innovation research. Otherwise, a loss of public confidence in nanotechnology will ultimately result in a loss of interest for investors and engineers in what, under different circumstances, would be a promising field of research and development [3].

Basically, two questions are asked when the risk posed by nanomaterials has to be assessed: Is there a chance that humans and the environment are exposed uncontrollably to the nanomaterial, and does the nanomaterial feature a new quality of toxicity? Both questions cannot be answered separately. For example, exposure must be expressed in a metric that can be related to health effects. Potential health effects first have to be identified. In turn, a toxicity test probing for a dose-dependent health effect must first specify the dose metric so that the exposure conditions can be chosen appropriately. Based on current knowledge about fine dust particles, for inhalation exposure assessment and inhalation toxicology, appropriate exposure dose metrics should be based on mass. This notion has been established after evaluating numerous studies on the health effects caused by fine dust particles [4]. Also, modes of action of lung-deposited particles are mediated by particle properties with their quantity scaling with deposited particle mass. It is reasonable to assume that the abovementioned notion also holds for particulate nanomaterials. However, there is an ongoing scientific debate whether mass alone can describe the dose appro-

priately [5, 6]. Other metrics like number, volume and surface area have been suggested to describe the dose more adequately [7, 8].

When being expressed in deposited mass, the dose in the lung after inhalation depends on factors like breathing rate, inhaled volume and deposition efficiency of particles in the pulmonary tract and also on the particle mass concentration in the breathing zone of the exposed subject. It is therefore useful to measure the particle mass concentration. However, methods traditionally used to determine the mass concentration of fine dust are not suitable for nanoparticles. These methods are usually gravimetrical, i.e. based on measureing the mass increase by particle deposition by weighing the collected samples [9]. However, the lower mass detection limit of even the most sensitive of scales, for example quartz crystal microbalances [10], is simply not reached in appropriate particle collection times as nanoparticles exhibit masses that are many orders of magnitude smaller compared to their micro-particle counterparts. This leaves an instrumental gap for the accurate determination of the nanoparticle mass concentration in both exposure assessments and inhalation toxicity studies.

Apart from accurately assessing the exposure in terms of mass, the assessment of the toxicity of nanoparticles is a particular challenge, simply due to the great number of nanomaterials that basically have to be tested individually. Chemicals are traditionally regulatory tested according to animal models to determine their potential to be hazardous to humans. *In vivo* studies are expensive and time-consuming and also ethically questionable. Alternatives for animal studies have therefore been put under consideration, but so far, only a handful of tests that look for specific toxic endpoints have been approved, like the Ames-test that predicts the mutagenic potential of chemicals after assessing its genotoxicity on bacteria [11]. However, no such *in vitro* test exists to predict the inhalation toxicity of particulate matter, due to the lack of predictive value of results obtained in *in vitro* tests that have been developed so far, because these models are inappropriate towards inhalation exposure [12]. Correlations of determined toxicities and observed health effects therefore usually fail. Taking the example of the Ames-test which releases the chemical into the culture substrate of the bacteria, the exposure mode would require a suspension of the particulate matter in liquid. However, phase transitions can evidently change the chemistry of particles [13]. Similarly, cells are traditionally exposed to particles by suspending granular materials in the culture media, also causing changes of the particles' chemistry [14]. Toxicity results obtained with such tests can be misleading. As a consequence, it can be considered as more appropriate to deposit particles onto the biological system from their natural airborne state when probing for inhalation toxicity *in vitro*. This

recommendation defines another instrumental gap, the ability to controllably deposit nanoparticles as aerosols on cellular (or bacterial) cultures.

In the following sections, both identified instrumental gaps are further described. The scope of this thesis was to reduce these instrumental gaps with targeted device development. Two instruments, the nano-PMC and the Cyto-TP, were developed over the course of this thesis. The nano-PMC can measure the mass of individual particles, addressing the first instrumental gap. The Cyto-TP is an exposure system for toxicity studies that can deposit nanoparticles from the gas-phase onto living cells, developed to achieve what traditional *in vitro* methods cannot, namely to provide an appropriate *in vitro* inhalation model for inhalation toxicity studies.

Mass measurement is an essential step towards determining the exposure of humans to nanoparticles, and toxicity defines the hazard associated with them. Thus filling the abovementioned gaps are logical necessities in risk assessment according to the principle of "Risk = Hazard × Exposure".

1.2. Instrumental gaps in nanomaterial exposure assessment

Human exposure to nanotechnology most probably happens with nanomaterials situated as airborne dust particles – nanoparticles – in the breathing zone. Inhaled nanoparticles can reach deep into the lung and contaminate pulmonary tissue which is sensitive to toxic stimuli. To be able to detect and characterize airborne nanoparticles is challenging but a necessity for nanomaterial exposure assessment. Commonly employed instruments have limitations which become particularly visible when the data describing the exposure needs to be expressed in regulatory relevant metrics, namely aerodynamic size and particle mass concentration. The specific reason for this problem can be reduced to the difficulty to accurately measure the mass of nanoparticles, calling for new methods that are much more sensitive than conventional gravimetric analyses. Particle mass spectrometers, so-called particle mass classifier (PMC), can directly measure the mass of individual microparticles but are not suited for very small nanoparticles. A PMC which can be applied to classify the mass of nanoparticles might therefore reduce the instrumental gap that prevents nanomaterial exposure assessment to be comprehensive. The nano-PMC, as part of this thesis, was developed with this specific goal in mind.

1.2.1. Challenges in detecting and characterizing airborne nanoparticles

To identify and quantify the exposure to inhalable nanoparticles, instruments must be able to detect and characterize aerosols that contain nanoparticles. Larger particles are usually detected optically, i.e. by measuring the back-scattered light after illumination of the particle with laser light. Nanoparticles are so small that the intensity of the scattered light would be far too weak to be detected by common optical sensors, considered that the laser wavelength is in the visible light spectrum. This problem can be solved by artificially enlarging nanoparticles in instruments such as Condensation Particle Counters (CPCs) [15, 16]. Prior to optical detection, the CPC makes use of a chamber filled with a gas of polar molecules, e.g. isopropyl alcohol, where the nanoparticles act as condensation seeds for droplets that grow to dimensions of several microns. Other methods control the charge distribution of an aerosol so that the signal of an electrometer, where particles are deposited, can be interpreted in terms of number [17]. Particle characterization happens by analysing the behaviour of nanoparticles under controlled conditions of the carrier gas that influence their aerodynamics. Classifiers act like property-filters, only allowing nanoparticles within a narrow range of property values to be detected. The Differential Mobility Analyser (DMA) classifies charged particles on the basis of their electrical mobility, a property that scales with the velocity of a particle being moved by an electrical force against the Drag force (see section 2.2.2 for a detailed description). Particle size can then be expressed as the diameter of a sphere with the equivalent electrical mobility – the electrical mobility diameter. A system of a DMA with CPC downstream, a so-called Scanning Mobility Particle Sizer (SMPS), can determine the number distribution of electrical mobilities of the aerosol that is translated to a particle electrical mobility diameter distribution. The SMPS is currently the method-of-choice for the size-characterization of nanoparticle-laden aerosols.

In practice, the measured number distribution of electrical mobility diameters is often simply called particle size distribution. This label is misleading for particles that are non-spherical since the mobility diameter is, strictly speaking, a parameter that depends on extrinsic particle properties like shape and the conditions of the measurement, like the alignment of the particle with the flow streamlines. Particles occur in arbitrary shapes and very rarely as perfect spheres or other symmetric forms, especially in uncontrolled environments like urban and occupational sites. In fact, the more a particle shape diverts from being spherical the more the mobility equivalent diameter deviates from equivalent diameters that are based on inherent particle properties, like the diameter of a sphere with equivalent volume. This issue becomes very relevant when trying to characterize the hu-

man exposure to nanoparticles in terms of health-related properties. Particle deposition efficiencies in the respiratory tract are determined by another equivalent diameter, the aerodynamic diameter, the diameter of a sphere and density of $\rho_0 = 1\ \mathrm{g/cm^3}$ with equivalent sedimentation velocity in air. Figure 1.1 (a) shows the human respiratory tract as it is divided into three regions, the nasopharyngeal (green), tracheobronchial (red) and alveolar region (blue). This is, of course, a simplified depiction as, for example, only the main bronchial branches are shown whereas the secondary and tertiary branches reach far deeper into the blue area. Particles have deposition efficiencies in each region that vary with particle aerodynamic diameter. The smaller their aerodynamic size, the more probable it is for them to reach deeper into the lung. Figure 1.1 (b) shows deposition efficiencies curves as a function of the aerodynamic diameter for each region as well as the total deposition efficiency. The curves were plotted according to the Human Respiratory Tract Model for Radiological Protection [18]. This model is an internationally established convention. It demonstrates that particles in the aerodynamic size range of 10-300 nm, i.e. nanoparticles, deposit dominantly in the alveolar region[1].

By employing an impactor, a device that deposits particles in several stages for selected ranges of the aerodynamic diameter, different aerodynamic size fractions of the aerosol are quantifiable. In combination with gravitational determination of deposited mass, the aerodynamic size mass distribution can be measured. The median aerodynamic diameter of this distribution is called mass median aerodynamic diameter (MMAD), useful for the estimation, which region of the pulmonary tract experiences deposition of the largest mass fraction of the aerosol. Aerosols with a mean MMAD smaller than the limit value of 100 nm are called ultra-fine dusts, whereas aerosols with larger MMAD fall into the category of fine dust. For the sake of completeness, it is to be mentioned that fine dust (or PM – particulate matter) itself is divided into PM-2.5 and PM-10 dust, accounting for the fact that the particles smaller than 2.5 μm deposit more probably in the alveolar and tracheobronchial area (lower respiratory tract) whereas larger particles deposit mostly in the

[1] The ICRP-model assumes inertial deposition of particles. However, the dominant deposition mechanism in the lung for nanoparticles smaller than ~0.1 μm is diffusion and not inertia. Instead, the mobility diameter might be a more appropriate metric for nanoparticles (see section 2.1.1 for definition of mobility).

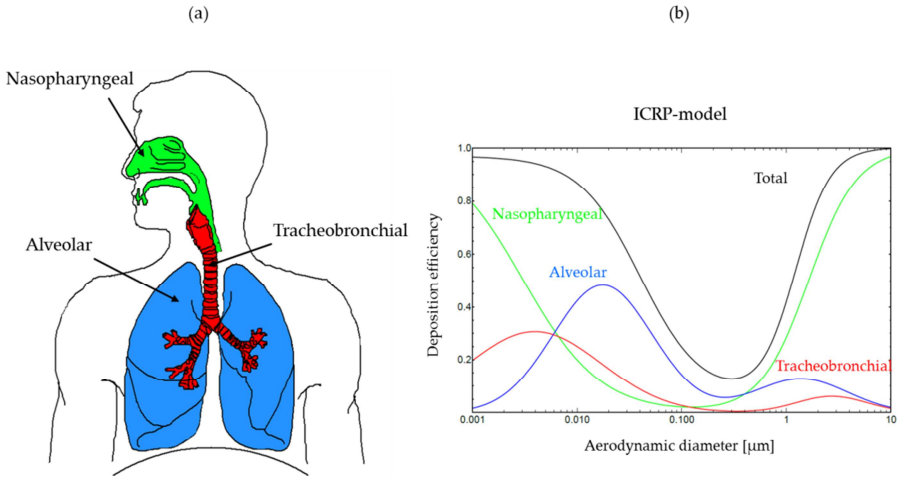

Figure 1.1. (a) Simplified depiction of the human respiratory tract with its three region: nasopharyngeal (mouth, nasal region, throat), tracheobronchial (windpipe, bronchia) and alveolar (air sacs). (b) Deposition efficiencies for particles with aerodynamic diameters of 1 nm – 10 μm in the three regions of the respiratory tract and total deposition efficiency, as numerically calculated with the ICRP-model (ICRP – International Commission of Radiological Protection).

nasopharyngeal region (upper respiratory tract), as it is visible in Figure 1.1 (b) [19][2]. Note that for dust exposure occurring at occupational sites, like in Germany, a different convention can exist, where dust fractions are divided by an aerodynamic diameter of 4 μm. Particles smaller are allocated to the respirable dust fraction whereas larger particles to the inhalable fraction [20].

The impactor method has extensively been used to characterize the exposure to fine dusts. However, most nanoparticles fall into the category of ultra-fine dust. As described earlier, gravitational determination of the particle concentration of nanoparticles in terms of mass is inadequate. Common practice is therefore the measurement of the particle number concentration and characterization of the aerosol on the basis of the electrical mobility

[2] The referenced standard by the US Environmental Protection Agency on the categorization of particulate matter is the final rule that became effective in 2012. It is also being applied in the European Union (Directive 2008/50/EC).

diameter, using a SMPS. Conveniently, conversion of the mobility diameter d_m to the aerodynamic diameter d_{ae} is feasible, when the so-called apparent density ρ_{ap} of the particle is known, the density of the mobility-equivalent sphere having equal mass, given by [17]:

$$d_{ae} = d_m \left(\frac{1}{\chi} \frac{\rho_{\mathrm{ap}}}{\rho_0}\right)^{1/2} \left(\frac{C_C(d_m)}{C_C(d_{ae})}\right)^{1/2}, \qquad [1.1]$$

where χ is the dynamic shape factor that corrects for the particle's non-sphericity and $C_C(d_m)$ and $C_C(d_{ae})$ are the respective Cunningham slip correction factors for d_m and d_{ae} (introduced in section 2.1.1). It is therefore fundamentally possible to characterize the exposure to nanoparticles with commonly used instrumentation and express the results in a health-related metric. Both apparent density and dynamic shape factor of particles can be derived when their mass and mobility is known. Measuring the particle mass is thereby very useful for exposure assessment.

Particle mass is also an essential property for the determination of the inhaled mass dose, which based on current knowledge, relates best to observed health effects. The next section in this chapter will elaborate on this. This notion has direct consequences for exposure assessment, reflected in the metric choice of regulative exposure limit values, e.g. occupational exposure limits (OELs). Such values are usually given as mass concentrations $\left(\mathrm{mg/m^3}\right)$ in the near-field air. When conducting exposure assessment at urban or occupational sites, only measuring the number concentration is therefore not sufficient. Particle characterization is required to compare the determined exposure with the relevant exposure limit. Again, when employing a SMPS-system for this task, the measured particle electrical mobility number distribution $n(d_m)$ can only be converted to particle mass number distribution $n(M)$ when the apparent density is known:

$$n(M) = n\left({d_m}^3 \frac{\pi}{6} \rho_{ap}\right). \qquad [1.2]$$

The particle mass concentration can then be derived by the integral of the particle mass number distribution.

For a polydisperse aerosol, common in almost all workplaces or urban sites, such an analysis can become very complex or simply impossible. Manufacturers of SMPS-systems and similar instruments instead usually assume a generalized apparent density. Their evaluation software often offers the possibility for this conversion, because it is very useful for

exposure assessment. This practice can lead to an error of judgement of the exposure by unaware personnel conducting the assessment. It is therefore more useful to measure the particle mass distribution directly.

1.2.2. Particle mass classification

A new type of particle mass spectrometer was introduced in 1996 by Ehara *et al.* (1996) [21], called the Aerosol Particle Mass Analyser (APM). This device was the first in a series of instruments that now form the group of Particle Mass Classifiers (PMC). The working principle of these instruments makes use of a rotating cylindrical capacitor that allows balancing of an outbound, particle-mass-dependent, centrifugal force and inbound, charge-dependent, electrical force acting on a particle. Under certain conditions, i.e. the strength of the electrical and centrifugal potentials, only particles within a specific band of mass-to-charge ratios can pass through the classifier. When the charge of the particles is known, the particle mass of the penetrating particles can be derived. PMC's can measure the particle mass by changing one potential, most often the electrical, and counting the penetrating particles downstream. The resulting response spectrum exhibits a number peak at which the mass-to-charge ratio of the particles is optimal for the penetration of the classifier. The dominantly classified particle mass can be derived for the respective operating conditions of the PMC. The lowest detectable mass limit is capped by the maximum centrifugal force that can be exerted on the particle. If the centrifugal force is too small, particles with a wide band of masses can traverse the classifier, so that the mass determination becomes inaccurate. Manufacturers of the current generation of PMC's state that these instruments are able to measure nanoparticle masses down to ca. half an attogram (ag) corresponding to spherical particles with a diameter of ca. 10 nm and standard density [22, 23]. But realistically, classification of small masses is only feasible for monodisperse aerosols. The relative window of particle mass-to-charge ratios allowing particles to traverse is too large, resulting in a large error when classifying polydisperse aerosols. The current generation of PMC's are thereby mostly employed to characterize aerosols with particle sizes in the range of 100-500 nm [24, 25].

This leaves an instrumental gap for PMC's, namely the ability to classify particle masses of aerosols made of nanoparticles or ultra-fine dust, respectively. In addition, such a PMC's could be employed in series with the SMPS-system to determine the apparent density of particles as well as obtain shape information. Employing such a PMC could help not only to accurately determine both the aerodynamic size distribution of an aerosol but also to measure the mass fractions for a comprehensible exposure assessment.

Figure 1.2: CAD-model of the nano-PMC. Depicted are the aluminium frame enclosing the classifier, inlet, outlet, electrical connections and water conduit for temperature control.

This work introduces the nano-PMC, developed with the specific goal in mind to be able to classify masses of nanoparticles. The new instrument is shown in Figure 1.2 as a CAD-model. The nano-PMC can accurately measure particles as light as 20 zg (zeptograms, 20×10^{-21} g), corresponding to a particle with a diameter of 3 nm and standard density.

1.3. Instrumental gaps in nanomaterial toxicity testing

Inhalation of nanoparticles and subsequent contamination of the respiratory tract can result in the interaction of the nanomaterial with pulmonary tissue. Extensive reviews have been written regarding their hazard potential by a number of authors [26-29]. The following sections describe how some lung diseases are associated with inhalative exposure to nanoparticles. Note that by the time this thesis was written, no general consensus has been reached in both the scientific and regulatory community, whether nanomaterials should a priori be viewed as more hazardous than larger particles of the same chemical composition. It must be mentioned, that the framework of nanotoxicology is far too complex and multifarious to be comprehensively described within the scope of this thesis. Thereby, emphasis is put on the description of known toxicity mechanisms and how they can be used to group nanomaterials for the purpose of hazard assessment.

Toxicity tests both research the hazard of nanomaterials and are developed and refined to reliably predict health effects as part of hazard assessment [30, 31]. Because *in vivo* studies are considered to be too expensive and ethically questionable, there is a need for alternative tests [32]. Conventional *in vitro* tests are unsuitable for this task because their conditions of particle exposure can evidently change the toxic effects of nanomaterials [13, 33, 34]. Advancements of *in vitro* models have therefore focussed on providing exposure modes that mimic the mechanisms of particle contamination in the lung, i.e. deposition from the gas-phase. Naturally, this exposure mode calls for the cells not to be submerged in culture medium like in conventional *in vitro* tests. Prominent candidates are cell cultures hosted at the air-liquid interface that allows for the cells to be left exposed to gas. For nanoparticles, deposition via gravity or diffusion on cells is a very slow process which is why so-called air-liquid interface samplers additionally precipitate nanoparticles with the help of an external force, for example via electrical precipitation [35]. The Cyto-TP, which was developed as part of this thesis uses thermophoresis as the nanoparticle deposition mechanism. Its development aims to reduce the instrumental gap by providing an exposure module for *in vitro* tests that are adequate for inhalation toxicity studies.

1.3.1. Dust-induced lung diseases

Health effects of inhaled particles are not a concern that has arisen only recently with the appearence of nanotechnology but are well-known for dust particles [36]. The most noted particle-mediated lung diseases are named after the substances they are historically associated with: asbestosis and silicosis.

Amphibole (needle-like) asbestos particles have a fibre-like shape and high rigidity. Such morphology impedes the normal immune reaction called lung clearance, which is the removal of particles from the pulmonary tissue via intake by macrophages and subsequent expectoration. Macrophages are unable to fully internalize long and rigid fibres (an example is shown in Figure 1.3 (B)) (Image taken from Matthew S.P. Boyles (2014) [37]). Subsequently, an apoptotic reaction called frustrated phagocytosis can be induced, in which they release a battery of toxic agents into their environment [38]. This action has the basic purpose to destroy microbial pathogens that the macrophage failed to remove, but can also be damaging to healthy cells and tissue. Chronic exposure to amphibole asbestos can lead to a convulsive proliferation of conjunctive lung tissue, called fibrosis [39]. The biopersistent fibres can also migrate into the lung stroma and ultimately to the pleura. Exposure to asbestos is one of the common causes for pleural mesothelioma, a type of cancer [40].

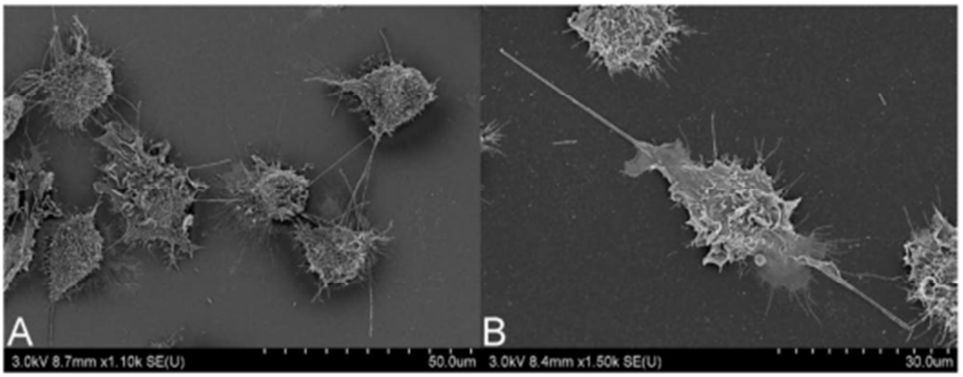

Figure 1.3. Scanning electron microscopy image of J774.A1 cells undergoing frustrated phagocytosis, induced by (A) multi-walled carbon nanotubes and (B) long fibre amosite asbestos.

Silica particles, on the other hand, don't induce lung toxicity because of their morphology but due to their active surface chemistry [41]. In this case, macrophage-supported lung clearance can be impeded due to the production of reactive oxygen species (ROS) by the silica particles that have been internalized [42]. In case ROS-levels are too high for the macrophages to handle, frustrated phagocytosis can be induced. The long-term effect of chronic silica particle exposure can also include fibrosis.

Asbestosis and silicosis both denote lung diseases. Both are due to certain physicochemical properties of the particles, morphological or chemical. Together, according to a report of the German government in 2013, they are the cause of about 20% of all recognized occupational diseases in Germany [43].

It is reasonable to suspect a similar impact on human health from inhaled nanoparticles since they are usually engineered to possess morphological or chemical properties being optimal for their desired purpose [27]. In fact, silica nanoparticles were found to be more toxic compared to larger silica particles, with the exposure dose being expressed as inhaled mass or mass concentration being present in the breathing zone [44]. This result is not surprising since the surface area to mass ratio increases with decreasing particle size and the toxicity of silica particles strongly depends on active surface area. Increased toxicity is not limited to silica nanoparticles. Animals in *in vivo* studies showed consistent pulmonary and also extrapulmonary inflammatory responses after inhaling diverse types of nanoparticles which seemed to be greater than those induced by larger particles of equal

composition at equivalent mass concentration doses [45, 46]. Similarly, these findings can also be explained with the fact that the surface area to mass ratio of nanoparticles is naturally larger. Schmid and Stoeger (2016) [7] recently published a retrospective analysis of nine *in vivo* studies investigating acute pulmonary toxicity of five different types of nanomaterials, ranging from insoluble materials like polystyrene to transition metals like copper. They found that when the dose metric was surface area, the variance in the acute pulmonary toxicity between the different nanomaterials could be explained best.

Similarly, evidence has been gathered suggesting that equivalent morphological features of nanoparticles, when compared to larger particles, can also lead to the same toxicity mechanism. As an example, Figure 1.3 shows images taken with a scanning electron microscope (SEM) of phagocytized multi-walled carbon nanotubes (MWCNT) (A) and amosite asbestos fibres (B) [37]. The similarity in the morphology between both particulate materials is obvious. Both consist of seemingly regid fibres, long enough to puncture macrophages that attempt to internalize the particle, causing apoptosis. Since both materials exhibit a similar toxicity mechanism once deposited in the lung, it is most probable that both materials have the same negative impacts on human health [47]. Sargent *et al.* (2012) [48] showed that single-walled carbon nanotubes (SWCNT) that were internalized by human airway epithelial cells can cause uneven allocation of chromosomes during cell mitosis in case they disrupt the mitotic spindle apparatus. As a consequence, genetic information is unevenly distributed between the two sister cells which is an early event in the development of tumor cells. This genotoxic mechanism is already known to occur for asbestos fibres [49].

1.3.2. Toxicity mechanisms as the basis for nanomaterial grouping

Based on this current knowledge, the Advisory Board of the German Society of Toxicology introduced criteria for the categorization of potentially lung toxic nanoparticles for the purpose of hazard assessment [50], which are as follows:

- Nanomaterials that mediate toxic action chemically which can happen via ion release or chemically reactive groups on their surface. Toxicity may be increased compared to the 'bulk' material by a more efficient cell uptake of chemicals in particulate form and changed toxicokinetics. The latter describes the fate of the material in the body, e.g. its probability to be translocated via blood stream into extrapulmonary organs.

- Nanomaterials consisting of or embedding fibrous and rigid particles with high biodurability. Similar to asbestos fibres, nanomaterials like carbon nanotubes (CNT) can induce carcinogenesis in the lung and mesothelium, if the so-called WHO fibre definition applies (length > 5 μm, diameter < 3 μm, aspect ratio > 3:1).

- Nanomaterials that are granular, biodurable and do not exhibit chemically mediated toxicity, so-called granular, biopersistent particles (GBP). Their toxicity is caused by a common mode of action associated with the impairment of a macrophage-supported immune reaction, lung clearance, if such particles accumulate in the respiratory tract. Impairment is associated with the volume a macrophage can internalize. Nanoparticles might exhibit increased toxicity at equivalent mass dose since they usually occur in an agglomerated state featuring apparent densities that can be smaller compared to those of agglomerates of larger particles.

A similar approach to nanomaterial grouping based on their intrinsic physic-chemical properties has been given by Arts *et al.* (2015) [51], who proposed a decision tree aiming to group nanomaterials in four groups, soluble nanomaterials, biopersistent high-aspect ratio nanomaterials (HARN), passive and active nanomaterials. Passive nanomaterials are basically GBP whereas active nanomaterials are non-soluble but chemical active (e.g due to surface reactivity).

What all categories have in common is that the identified toxicity mechanisms are also observable for larger particles and are described by particle toxicology [29]. So far, lung toxicity mechanisms unique to nanoparticles have not been observed *in vivo* [50, 52]. Some toxicologists argue that based on current knowledge, nanomaterials pose no specific risk [53]. However, despite of this, the general public is still concerned about negative impacts of nanomaterials to exposed humans and environments, as the initial example of the "nanowatch.de"-tool showed. Just because no nano-specific toxic effects were identified yet, it doesn't mean that there aren't any. *In vivo* toxicity studies might be too sparse, resulting in a relative uncertainty about nanomaterial-specific toxicity.

Braakhuis *et al.* (2016) [54] recently critically stated that grouping solely on the basis of inherent properties of the nanomaterial is not sufficient. This is argued by the example of the use of silver nanoparticles in deodorant sprays. After silver nanoparticles have been added to the other compounds of the deodorant, they can agglomerate and release silver

ions via dissolution. In this case, their life-cycle might change the inhaled dose and the form of the resulting aerosol altered after the atomization of the deodorant. After inhalation, the *in situ* characteristics of the aerosol can be different to its characteristics before inhalation due to the aerosols biokinetics that include size-dependent particle deposition rates in the pulmonary tract, protein corona formation on the deposited particles or additional dissolution, amongst others. The authors therefore conclude that future approaches should not only take the intrinsic physico-chemical nanomaterial properties into account, but also their life-cycle before human exposure as well as their biokinetics that might lead to altered *in situ* characteristics. However, in particular the latter aspect needs more experimental data as it is currently unclear how biokinetics, in situ characteristics and the change of dose cohere.

1.3.3. Advancements towards in vitro models as alternatives for animal studies

In vitro alternatives for animal studies are highly in demand, to allow for much faster, cheaper and ethical toxicity testing [32, 55]. The most common concept behind any development of an animal study alternative follows the "three R's", reduction, refinement and replacement [56], i.e. to reduce the number of animals needed to obtain statistically relevant study results, to refine the study design so that animals experience a minimal amount of pain and distress and to replace 'higher' life forms (mammals) with more simple organisms. Approaches aim to deliver either a 'relative' alternative or 'absolute' alternative to animal studies, the former meaning that animals are used but not exposed to any harmful stimulant and the latter the complete abandonment of the use of animals. Relative alternatives therefore focus more on the reduction of the number of animals and refinement of the study design. For absolute alternatives, it can be argued that the aspects of reduction and refinement are irrelevant in light of the complete replacement of animals.

Most approaches to develop alternatives for animal studies for the study and test of nanomaterial toxicity aim for their complete replacement by providing *in vitro* testing protocols that reliably predict specific health effects based on identified toxic effects on cell cultures. Hence, their validation requires sufficient data on human health effects after exposure to nanomaterial. But epidemiological studies on humans that were potentially exposed to nanomaterials are sparse and usually have limited significance, as Liou *et al.* (2015) [57] concluded in their recent meta-study. Alternatively, results from *in vitro* tests can be put into relation with health effects observed in animal studies. The success rate of animal models for the prediction of human health effects is relatively high, e.g. 71% for

pharmaceutical products according to Olson *et al.* (2000) [58]. It is therefore reasonable to assume that *in vitro* models that reliably correlate toxicity data on cells with health effects observed in animal studies after exposure to nanomaterials are also predictive towards health effects that occur in humans after exposure to nanomaterials.

It has only recently come into practice to both expose animals and cells to nanomaterials to investigate how exactly the biological response of the cellular system is related to the health effects observed in the animals. Landsiedel *et al.* (2014) [59] concluded in their review that to date, *in vitro* cell culture assays were not successful in providing dose-response relationships that correlate well with dose-dependent *in vivo* effects. Still, some studies report that such a correlation might be possible. Hong *et al.* (2013) [60] exposed both pulmonary macrophages and mice to zinc oxide nanoparticles. For the *in vitro* test, the nanoparticles were suspended in the culture medium and cell exposure happened via sedimentation. The mice were exposed via injection of a nanoparticle suspension into the peritoneum as well as gastrointestinal tract. The *in vitro* test showed a dose-depended toxicity of the zinc oxide nanoparticles. For the *in vivo* study, the authors remained careful in their conclusions by only reporting "an obvious dose-dependent trend" towards lesser vitality of the mice (e.g. decrease of body and organ weight). Kim *et al.* (2014) [61] exposed mice by dispersing a specific mass dose of suspended nanomaterials via oropharyngeal aspiration. In this practice, mice are narcotized and positioned vertically. While pulling the tongue to supress the swallowing reflex, a suspension of nanoparticles is dispersed into the throat. The suspension can now run down towards the lung and wet its surface. Simultaneously, lung tissue slices *(ex vivo)* and alveolar macrophages *(in vitro)* were exposed to the nanomaterials that were suspended in the culture media. Pro-inflammatory responses were observed in all three biological systems with similar dose-response relationships. A similar approach was chosen by Mirowsky *et al.* (2015) [62] who exposed human pulmonary endothelial cells and mice to suspensions of collected ubiquitous particulate matter. Analogous to the abovementioned study, the mice exposed via oropharyngeal aspiration. This study was specifically analysing the differences in toxicity between rural and urban PM. Their findings showed a toxic effect on both models, visible in the ROS response of the cells and inflammatory response of the mice.

Such studies are certainly a step in the right direction. However, one certain aspect of this particular study design is questionable: Both animals and cells were exposed to suspended nanoparticles and not aerosols. In other words, the exposure mode was not representative to the actual mode of exposure which is inhalation of airborne nanoparticles. For once, oropharyngeally aspirated nanoparticles most probably deposit differently in the

lung compared to aerosols, in different ratios in different areas. Second of all, once suspended, nanoparticles are known to change in number, size and morphology [13]. It can be assumed that their toxicity is also affected.

A nanoparticle inhalation study design to investigate the correlation of *in vitro* with *in vivo* results must therefore focus on exposure to aerosols. *In vivo* inhalation studies are usually carried out by exposing a number of animals to an aerosol in their breathing zone, with homogenous and timely stable dose rate. Following the argumentation from before, an *in vitro* test that probes for inhalation toxicity is only adequate with the cells exposed to the same aerosol. An *in vitro* 'inhalation' study design that deposits nanoparticles from the gas-phase on living cells was made feasible with the introduction of air-liquid interfaces (ALIs) [63]. In the ALI-technique, cells function as a barrier (interface) between the nutrient solution (liquid) and the exposure atmosphere (air). Cell carpets are grown as monocultures of pneumocytes (epithelial cells) or multicultures of pneumocytes and monocytes (macrophages) on semipermeable membranes see Figure 4.4). The nutrient solution is fed through holes in the membrane. On the opposide side, the cell cultures can be left exposed to air. This model resembles the anatomy of pulmonary alveolus, with the membrane representing the basal membrane that hosts local cell types which are exposed to inhaled air and the nutrient solution representing blood.

ALI-exposure of cells to particles are viewed as most promising to be able to correlate *in vitro* to *in vivo* results and ultimately providing validated protocols as alternatives for animal toxicity studies [64]. So-called ALI-samplers combine the ALI-technique with particle deposition supported by particle precipitation, since diffusion alone would be too slow for the deposition mechanism. State-of-the-art ALI-Samplers use either droplet formation with subsequent sedimentation by cloud settling [65] or electrophoresis for deposition [35].

In this work, an ALI-sampler is introduced that allows for the deposition of nanoparticles from the gas-phase on living cells with the help of thermophoresis, called the Cyto-TP (TP: Thermal Precipitator). Different models were developed over the course of this thesis. Thermal precipitation as the fundamental nanoparticle deposition mechanism was chosen because of four major features.

- Gentle deposition of particles with a diffusion based mechanism. Apart from a lesser cellular stress level, this exposure mode is therefore assumed

to be more representative since diffusion is the dominating depositing mechanism in the alveolar region.

- Thermophoresis does not require manipulation of particle properties. Particles can be deposited while retaining their natural physicochemical properties.

- Thermophoresis becomes weaker for larger particles, i.e. it is most suited for the deposition of nanoparticles.

- Nanoparticle deposition via thermophoresis is size-independent. A size-fractioned dose density profile on the cell culture is therefore improbable.

Another important aspect of *in vitro* / *in vivo* correlations is the choice of the dose metric. Without equivalence or convertibility of dose metrics, results obtained with both *in vitro* and *in vivo* toxicity studies simply can't be compared. In *in vivo* inhalation studies, the lung-deposited total particle dose is determined by the dose rate and exposure time. The dose rate can be estimated by the measured particle concentration in the breathing zone, the deposition efficiency of the particles in the lung and the usually known breathing parameters of the test animal, i.e. breathing rate and inhaled volume per breath. For the deposition efficiency, complex models like multiple-path-particle-deposition (MPPD) exist which numerically calculates deposition efficiencies in individual regions of the lung based on the particle and lung characteristics [66]. Since deposition efficiencies and breathing parameters can be assumed to be constant during the exposure, the dose rate can be controlled by generating a specific particle concentration in the exposure atmosphere. For *in vitro* studies, a similar approach can be chosen. The Cyto-TP is constructed in such way, that the exposure dose rate can be extrapolated with the help of the particle deposition efficiency on the cells when monitoring the particle concentration in the exposure atmosphere.

The Cyto-TP might be a solution to provide an *in vitro* exposure module that mimics the situation in the lung as close as possible. Cells are hosted in a similar cellular configuration as in the lung alveoli and particles are deposited in a similar manner and retain their physicochemical identity. A future comparative study correlating results obtained with the Cyto-TP and observed in *in vivo* inhalation studies might yield more comprehensible data.

1.4. Sustainability of nanotechnology by safety-by-design

Safety-by-design is a label describing development of new materials, with not only the optimization for their purpose but also aspects of safety in mind, by reducing their risk for humans and the environment. The risk of chemical substances is associated with their interaction with biological systems, toxicity, and their availability for these biological systems, exposure. Mitigation of one or both traits can lead to a great reduction of the risk. Engineered nanomaterials in particular offer the opportunity to design and optimize critical material properties for their desired purpose. Similarly, these properties might be optimized towards a mitigation of the associated risk.

A historic example for a successful redesign of a hazardous material is the development of surrogate materials for man-made vitreous fibres (MMVFs), engineered amorphous silicate fibres (e.g. fiberglass) that found a wide range of applications but showed carcinogenicity in *in vivo* tests [67]. In Germany, handling MMVFs requires similar technical guidelines as handling asbestos [68]. By changing the chemical composition of the vitreous fibres, their biopersistence could be mitigated. They were eventually reintroduced as "highly biosoluble fibres", a new product. Lower and eventually no carcinogenicity was found in *in vivo* studies [69, 70], rendering them "safe". The development of harmless MMVFs was conducted after the initial product was found hazardous. This practice is called forensic engineering.

Different to forensic engineering, safety-by-design is already applied during the development process. The main condition for its feasibility is that material properties can be modefied. Nanotechnology provides this opportunity since material properties can be engineered on a molecular scale. In fact, safety-by-design has already been applied in the development of some commercial nanomaterials, e.g. carbon nanotubes (CNT). As mentioned in the last section, rigid and fibrous CNTs are carcinogenic due to the same mechanism as biopersistent vitreous or asbestos fibres [71, 72]. However, a redesign procedure similar to MMVFs, change of chemical composition, could also result in a loss of properties essential for their application, e.g. their high tensile strength. Instead of mitigating biopersistence, some manufacturers focussed on minimizing the probability that humans are exposed by making the material less dusty. In addition, even if dust was released from the nanomaterial, the dust particles would not exhibit fibre-like morphology and thereby not show fibre-specific toxicity. The result was a CNT-material that only released large spherical dust particles, bundles of a great number of CNTs. Figure 1.4 shows two images of sampled CNT aerosols, captured by scanning electron microscopy. In (a), the particles

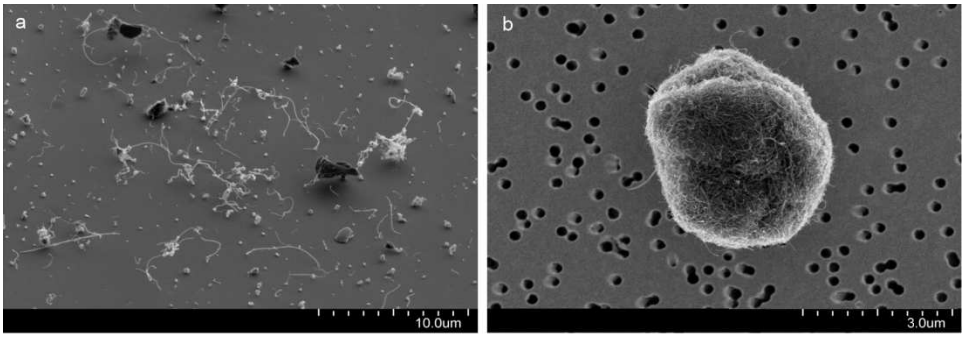

Figure 1.4: SEM-images of MWCNT particles from sampled air. (a) Fibrous and rigid nanotubes with asbestos-like toxicity. (b) Bundle-like aggregates of nanotubes without pulmonary toxicity associated with fibers.

consist of single and rigid nanotubes whereas in (b), all particles were found to be large, bundle-like aggregates. Where CNTs with morphologies similar to the ones depicted in (a) have shown the typical toxicity known from fibres like asbestos [47], CNT-bundles show health effects similar to GBP [73, 74]. The propensity to release dust particles, dustiness, of the CNT powder used in (b) was also far lower than in (a).

Several essential advantages over the usual practice of forensic engineering present themselves in case the developer of materials follows the safety-by-design concept. In Europe, a new chemical must undergo regulatory chemical testing, specified by REACH[3], after its yearly production volume exceeded a certain limit value, currently one ton. The extensive costs for the tests must be paid for by the manufacturer. If a material shows high risk potential, it can be grouped as a hazardous material which can be devastating for its marketability. Safety-by-design increases the chance that a nanomaterial is regarded as harmless. Consequently, the risk for manufacturers and distributors that the nanomaterial fails at the market is reduced greatly. These factors can be crucial especially for small and medium companies with limited resources.

Approaches to safety-by-design employ material testing as a pre-regulatory procedure. Following certain development steps, nanomaterial developers assess the risk potential of their innovations and plan the next development phase based on the results. Similar to

[3] The **R**egistration, **E**valuation, **A**uthorisation and Restriction of **Ch**emicals by the EU

regulatory testing, pre-regulatory tests also comprise examination of exposure and toxicity, but with far less extensive protocols. Instead of exposing animals to the nanomaterial, toxicity is tested *in vitro.* Similarly, the dustiness of the nanomaterial can be tested and the morphology of the dust particles analysed. However, at the time this thesis is written, the safety-by-design strategy is not established yet.

The NanoSafety-Cluster, a European umbrella project joining several EU-funded projects that engage in research and development towards safety-by-design identified several technological and knowledge gaps that have to be closed in order to implement safety-by-design [75]. Major building blocks were proposed, that will help to close these gaps. Those building blocks are amongst others:

- "Establishing advanced and realistic *in vitro* models for nanomaterial toxicity testing"

- "Utilizing material characterization techniques, and identifying association of material characteristics or bio-identity with hazardous effects of engineered nanomaterials with living organisms"

The Cyto-TP can be regarded as an advanced and realistic *in vitro* model for nanomaterial toxicity testing. Section 6.3.1 provides a full evaluation of the potential application of the Cyto-TP in a proposed safety-by-design strategy, in light of the high requirements that such a toxicity test has to fulfil. Considering the discussion in the previous section and concluding that *in vitro* models currently cannot predict health effects, it can only reasonably be proposed for the Cyto-TP to find (pre)-regulatory application as part of a toxicity study design with the purpose to attest that a nanomaterial has a low hazard potential and not that it is toxic. Only toxicity tests with high negative predictive value can provide a solid base for this prediction. The Cyto-TP is a promising candidate to provide the right conditions for such a test.

Based on known toxic modes-of-actions of conventional particles, solubility and ROS-production in aqueous media, aspect ratio and apparent density serve as the material properties that define the material's bio-identity. Bio-identity in this context means the compilation of values for material properties that evidently mediate biological responses of a biological system. For nanoparticles, other critical properties might exist but are currently not clearly identified. In conjunction with methods testing for the other identified characteristics, the nano-PMC could be part of a testing strategy to identify the bio-

identity of nanoparticles. The nano-PMC, employed downstream a DMA, can measure the apparent density of all types of airborne granular biopersistent nanoparticles. This experimental setup can be part of a dustiness test within a safety-by-design strategy, which is described in detail in section 6.3.3.

1.5. Conclusions and scope of this thesis

Fear of harmful nanotechnology slows down an otherwise accelerating source of innovation. But fears can be eased by shedding light on its causes. Risk research could thereby ultimately lead to sustainable nanotechnology, i.e. nanotechnology that on the one hand provides revolutionary applications and on the other its risk for humans and the environment is reduced or well-managed. To reach this goal, one emphasis lies on the development of instruments that can help to answer both scientific and regulatory challenges. This work introduces two devices developed with this intention, the Cyto-TP and nano-PMC.

The Cyto-TP was developed and validated with the specific goal in mind to provide an instrument that might serve as the exposure module of an *in vitro* toxicity test that can be useful for a variety of applications. Since it comes as close as currently possible in emulating both the anatomy of the biological system and the exposure mode, results obtained with this toxicity test might be easier to correlate with health effects observed *in vivo* compared to results obtained from submerged testing. For toxic effects that scale with the mass dose, the nano-PMC can be used to convert the particle number concentration that is usually monitored to a particle mass concentration. Equivalent dose metrics are one condition for the comparability of toxicity results obtained with complementary methodology. The Cyto-TP could also potentially be employed in a toxicity test for nanomaterials in development to promote safety-by-design.

Apart from toxicity testing, the assessment of the human exposure to aerosols containing nanoparticles also requires sophisticated instrumentation, since the current generation of aerosol monitors and classifiers are not able to yield results that can be easily interpreted for nanoparticles. The nano-PMC, as part of a dedicated experimental setup, can directly and accurately measure the particle mass distribution of an aerosol, a metric more useful in the quantification of exposure, since exposure limit values are usually mass-based. In conjunction with a DMA, the nano-PMC can be used to obtain the apparent density of an aerosol that is useful in the conversion particle number concentration to mass concentra-

tion. Apparent density is also a nanomaterial property that is a health-relevant particle property for GBP.

The second chapter first introduces the so-called apparent properties, useful to allocate properties of mobility-equivalent spheres to non-spherical particles which would otherwise be difficult to describe. However, apparent properties must be interpreted accordingly. Very important for this thesis is the description of the interpretation of the apparent density of particles, agglomerates in particular, in health-related terms. Following this, the general concept of describing instruments with their systems function is introduced. The systems function is the mathematical description of the instrument's manipulation of an input signal that results in an output signal. For classifiers like the nano-PMC, the systems function is called transfer function that fully describes the classification performance of the device. Chapter 2 characterizes the transfer functions of the nano-PMC as well as the DMA that were both used individually and in combination to predict the response of the system to an inbound aerosol mobility/mass distribution. The comparison of the predicted to the measured response serves as the validation test for the working principle of the DMA-nano-PMC system that was extensively used in chapter 3. Lastly, thermal precipitation of particles is described; the deposition mechanism in the Cyto-TP. Thermophoresis is the result of a disturbance of the molecular velocity distribution in a gas due to the presence of a temperature gradient. In presence of a particle, imbalanced transfers of momentum of gas molecules colliding with the particle surface results in particle motion against the temperature gradient.

The third chapter is comprised of the article describing the rationale, development, construction and application of the nano-PMC that was published as a peer-reviewed paper in *Aerosol Science & Technology* [76].

Chapter four is comprised of the article describing the rationale, development, construction and experiments providing a proof-of-concept for the Cyto-TP that was published as a peer-reviewed paper in the *Journal of Aerosol Science* [77].

The fifth chapter provides details for the development and construction of the second prototype of the Cyto-TP. In addition, the concept of implementing the Cyto-TP technology into a commercial ALI-Sampler was elaborated and used experimentally first to determine the deposition efficiency of nanoparticles and second as part of a toxicity study with barium sulphate nanoparticles with low toxicity. The nano-PMC was used in the latter study to further characterize the barium sulphate aerosol to enable conversion of dose

metrics, here from number density (deposited number per cm^2 of cell monolayer) to mass density (deposited mass per cm^2).

Chapter six describes a potential future application of both instruments in a testing strategy that is applied in the development phase of a nanomaterial to compile the so-called bio-identity and bio-availability which can be used to predict whether the nanomaterial has the potential to be harmful to humans. Employed in a safety-by-design concept, this pre-regulatory testing might be the key to ultimately develop nanomaterials that are both optimal for their application and safe.

Chapter 2: Theoretical descriptions

The content describing the instruments developed for this work, the nano-PMC and Cyto-TP, was published in respective papers. The papers give full descriptions of the theories that describe the functions of both instruments. Of course, some basic concepts are not explicitly described but either referenced or assumed to be fundamental. This chapter therefore give a more detailed description of important concepts.

Section 2.1 introduces the concept of apparent particle properties that are attributed to virtual spheres having an equivalent mobility. Apparent size, volume and density are often used to describe asymmetrical particles that cannot be described geometrically. An aerosol is often classified based on mobility in practice. However, the derived apparent properties must be interpreted appropriately. Accordingly, apparent particle properties can be related to health effects.

Particle classifiers can be described by their system function, called transfer function. By convolving the input, unclassified, property distribution with the transfer function, the output, classified, property distribution can be predicted. In practice, predicted output signals are compared to measured classifier responses by using a well-defined property distribution as the unclassified signal. That way, the performance of the instrument can be compared with the model and its functionality validated. This validation procedure is particularly used in chapter 3 to characterize the DMA-nano-PMC system 3. In section 2.2, the transfer function of both the DMA and nano-PMC are derived so that the classification performance can be predicted for each individual instrument and for the combination of both.

Section 2.3 provides a description of the theoretical framework of thermophoresis, the underlying mechanism for depositing nanoparticles in the Cyto-TP prototypes (chapter 4 and 5). This model is used to describe the dosimetric properties of the Cyto-TP (chapter 4) and particularly its successors (chapter 5).

2.1. Apparent particle properties

A particular challenge in the context of characterizing nanoparticles is that physical properties that are peculiar to the nanoparticle - like volume, mass or surface area - are often difficult to be measured directly (i.e. by online measurements). Instead, particle properties are usually determined by classifiers that basically act like property filters, only allowing particles within a specified range of property-values to pass. The 'right' classifier settings for a specific property range are found by modelling the particle dynamics within the classifier, which can depend not only on the particle properties, but also on conditions of the carrier gas. Therefore, the accuracy of the classification depends on the validity of the underlying model. In case the classified property is a dependent parameter, i.e. a parameter that can change when it is measured differently, every value that is derived from it must be interpreted as valid only in the context of the measurement conditions.

The most used aerosol classifiers often act like filters for particle mobility. This property is particularly useful since it determines the particle's path of motion apart from the external force that causes the motion. Classifiers like the DMA, introduced later in this chapter, exert a well-defined force on an aerosol with finitely distributed mobilities, so that only particle's within a certain range of mobilities can be detected at a specified location. Particles that traverse the classifier can therefore be described by the mobility equivalent diameter. However, this diameter cannot be interpreted by geometrical means, since it scales with particle morphology as well as gas properties. Consequently, geometric properties of a mobility equivalent sphere are called *apparent*.

2.1.1. Mobility of a particles in gases

A particle that moves in a gas experiences at least two forces: The force that exerts the motion and the resistance force induced by gas molecules colliding with the surface of the moving particles, called drag force. Isaac Newton thought of an object traveling through air. He assumed that the change of momentum of the object induced by gas resistance is proportional to the volume rate of the air that needs to be pushed aside, given by the projected area of the object in the direction of movement times its velocity [17]. The drag force F_D is then given by:

$$F_D = K\rho_g \frac{\pi}{4} d^2 v^2, \qquad [2.1]$$

where $\boldsymbol{v}$ is the velocity of the object relative to the gas, d is the diameter of the object when it is assumed to be a sphere, ρ_g is the gas density and K is a constant of proportionality, which Newton assumed to be independent of velocity. This assumption is true for spheres with a Reynolds-number Re larger than 1000, given by:

$$Re = \frac{\rho_g v d}{\eta}, \qquad [2.2]$$

where η is the gas viscosity. The Reynolds number can be interpreted as the ratio of the inertial to the viscous forces induced by the gas on the moving object. Newton's equation for the drag force is therefore valid when viscous forces can be neglected compared to the inertial effects. Particles, however, usually move slowly and have small particle sizes, resulting in small Reynolds numbers. Eq. 2.1 is hence not valid for nanoparticles.

Stokes solved the Navier-Stokes equations that generally describe fluid motion, by assuming that the inertial forces can be neglected compared to the viscous forces and the fluid is incompressible. For a rigid sphere with $Re \ll 1000$, the drag force is given by

$$F_D = \frac{3\pi\eta v d}{C_c}. \qquad [2.3]$$

The parameter C_c is the Cunningham-Slip factor that corrects the Drag force for the "slip" of gas molecules by the nanoparticle surface, i.e. the fact that the relative velocity of gas molecules at the particle surface is not zero. This correction factor is given by:

$$C_c = 1 + \frac{\lambda}{d_p}\left(a + be^{-c\frac{\lambda}{d_p}}\right) \qquad [2.4]$$

with $a = 2.34$, $b = 1.05$ and $c = 0.39$ for solid particles [78]. It is size-dependent and becomes influential for particles with $Re < 1$ (or roughly smaller than 1 μm). The velocity of a particle is therefore given by

$$\mathrm{v} = \frac{\mathrm{C_c}}{3\pi\eta\mathrm{d_p}}\mathrm{F_D} = \mathrm{BF_D} \qquad [2.5]$$

For a spherical particle with given diameter and constant gas properties, the factor B is a constant and called (mechanical) mobility. It can be interpreted as the relative ease to produce steady motion of the particle. For example, when gravitational force F_G pulls an airborne particle towards the ground, the settling velocity is given by $v_G = BF_G$. If an electrical force pulls on a charged particle, its relative ease to be moved is called electrical mobility, given by:

$$Z = qB \qquad [2.6]$$

where q is the charge of the particle.

Mobility is important for particle characterization since it is commonly used to describe properties of particles based on the geometric parameters applicable to spheres, like their diameter. However, particles have are usually non-spherical. Instead, one describes a property of a virtual sphere that exhibits a mobility that is equivalent to the original particle.

Consequently, it is appropriate to refer to properties of mobility equivalent spheres as 'apparent properties'.

2.1.2. Apparent size

Figure 2.1 shows a non-spherical particle moving with velocity v through a gas against the drag force, in dependency from its mobility. A mobility equivalent sphere can be described by the diameter d_m, given by:

$$d_m = \frac{C_c}{3\pi\eta B} \qquad [2.7]$$

This diameter is called mobility equivalent diameter. It is not the real diameter of the particle but a virtual diameter of the mobility equivalent sphere. The mobility equivalent diameter thereby describes the apparent size of particles.

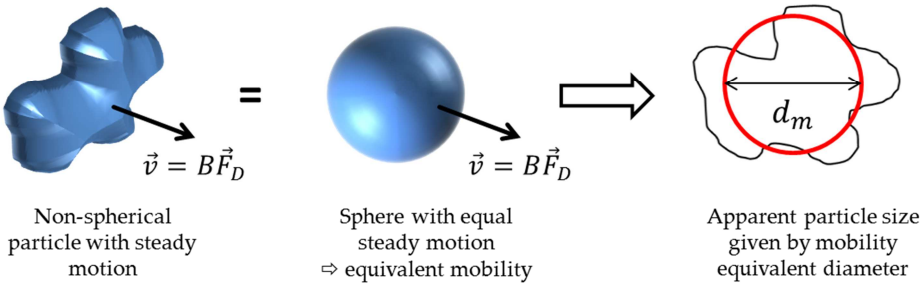

Figure 2.1. A non-spherical particle moving with steady motion with velocity v defined by its mobility times the Drag force. A virtual sphere can be defined as one that moves with equal velocity, i.e. the sphere exhibits equivalent mobility. The diameter of this sphere is the mobility equivalent diameter, describing the apparent size of the non-spherical particle.

2.1.3. Apparent volume

The volume V of a spherical particle is given by:

$$V = \frac{\pi}{6} d^3, \qquad [2.8]$$

When the mobility diameter is known, the volume of the mobility equivalent sphere is given by:

$$V_{ap} = \frac{\pi}{6} d_m^3 \qquad [2.9]$$

This volume must is called the apparent volume.

It is important to note that there is a different definition given by the British Standards Institute that describes the apparent volume of a particle with the help of the particle surface area, excluding the surface area of the internal voids [79]. This apparent volume therefore envelopes the external body of the particle. This definition has a direct consequence for agglomerates. Figure 2.2 shows a cross-section of an agglomerate that shows voids that are interior to the structure and voids that are exterior, called surface pores. The

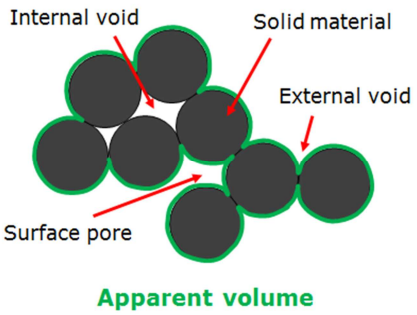

Figure 2.2: Apparent volume as defined by the BSI, including internal voids and the space occupied by solid material, but excluding surface pores and external voids.

enveloping volume is larger than the 'real' volume of the agglomerate, the space occupied by solid material, because it also includes the particle-void spaces.

This external surface area can be expressed by the surface of a sphere with an equivalent external surface area A of the particle. The apparent volume V_{ap} based on particle surface area is given by:

$$V_{ap} = \frac{\pi}{6} d_A^3, \qquad [2.10]$$

where d_A is the diameter of a sphere with equivalent external surface area as the particle. Ku and Maynard (2005) [80] showed that for particles with a wide range of morphologies the mobility equivalent diameter is of similar value compared to the diameter of a sphere with equivalent projected area, which is equal to the diameter of equivalent external surface area. In this case, the abovementioned definitions are equivalent to each other. Li *et al.* (2014) [81] more recently showed that for particles with convex surfaces considered in the free-molecular regime, i.e. where particle motion is determined by single particle-molecule interactions, the diameter of a sphere with an equivalent averaged projection area (averaged for all orientations of the particle) is equal to its mobility diameter.

Based on current knowledge it can therefore be generally assumed that the apparent volume defined by particle mobility is equivalent to the volume of an envelope tightly fitting to the external surface area of the particle.

2.1.4. Apparent density

The density of a body with apparent volume V_{ap} and mass M is called apparent density:

$$\rho_{ap} = \frac{6M}{\pi d_m^3} \quad [2.11]$$

For aggregates like shown in Figure 2.2, the apparent density is a useful quantity. It is the density of an aggregate when considering that not every volume unit has mass but can be void. It is the average material density of the body:

$$\rho_{ap} = \frac{1}{N}\sum_{i=1}^{N} \rho_i, \quad [2.12]$$

where ρ_i is the density of the partial volume V_i.

An aerosol usually comprises particles within a range of densities. The density of particles having a specific mobility is called effective density. The apparent density can therefore be considered as the average effective density or, in case of an aerosol with a dominant mobility, as the dominant effective density. In practice, however, truly monodisperse aerosols don't exist, so using the term apparent density even for a mobility-classified aerosol seems more appropriate and is used throughout this thesis.

2.1.5. Health-relevance of apparent particle properties

As already mentioned in the introduction, which region of the lung is contaminated dominantly when particle are inhaled, can be expressed through the aerodynamic diameter of the particles. With the help Eq. 1.1, the apparent size can be converted into aerodynamic size, with the apparent density as a scaling factor.

The apparent volume of a particle can be interpreted as the volume of an envelope tightly fitting the external surface area. Assuming that the particle surface area is invariant for different gaseous or liquid media surrounding the particle, the apparent volume is therefore equal to the so-called displacement volume, i.e. the volume element that is displaced due to the presence of the particle in the medium. There are indications that the toxicity of GBP particles scales with lung-deposited displacement volume [82]. The toxicity mechanism can be described as the impairment of the lung clearance mechanism due to the

volumetric 'overload' of alveolar macrophages that are otherwise responsible for removing any contaminant from the alveolus. To put it simply, when macrophages internalize more than 6% of their own volume [8], they release factors to signal for help. Based on the knowledge of the total macrophage volume in the alveolus, this volume overload level can be estimated.

The accumulated volume of particles over the exposure time t, deposited in the alveolar region of the lung V_{CV} is estimated by:

$$V_{CV}(t) = \beta(t)\, C_V Q_{br} \phi_A\, t, \qquad [2.13]$$

where C_V is the particle volume concentration in the breathing zone of the exposed subject, Q_{br} its volumetric breathing rate and ϕ_A the deposition efficiency in the alveolar region of the respiratory tract. The factor $\beta(t)$ is the rate of particle removal from the lung by the non-impaired lung clearance mechanism. Assuming that the threshold ratio of accumulated particle volume and total macrophage volume $n \times V_{AV}$ is 0.06 (for rats), where n is the total number of macrophages ($\sim 7 \times 10^{10}$ for rats) and $V_{AV} \sim 1$ µl the volume of an alveolar macrophage, one can calculate the volume concentration C_V that is needed to reach the threshold after time t:

$$C_V(t) = \frac{0.06 \times nV_{AV}}{tQ_{br}} \frac{1}{\beta(t)\phi_A}, \qquad [2.14]$$

Since the particle displacement volume equals its apparent volume, the volume concentration can therefore be converted into mass concentration C_M using the apparent density:

$$C_M(t) = C_V(t)\rho_{ap} = \rho_{ap} \frac{0.06 \times nV_{AV}}{tQ_{br}} \frac{1}{\beta(t)\phi_A} \qquad [2.15]$$

This mass concentration is also called no observed (adverse) effect level (NO(A)EL), since it is the level concentration below which no health effect of GBP is predicted to occur. Predicted NO(A)ELs reported for rats show a good agreement with experimental values, determined in rat *in vivo* studies [8, 83].

The toxicity of granular, poorly-soluble particles, the largest group for nanoparticles, therefore seems to scale with the apparent density of the aerosol particles.

Such NO(A)ELs for animals are converted into human equivalence concentrations (see e.g. [84]). These are the current basis for the definition of derived-no-effect-exposure limit values (DNELs) [85, 86].

Note that the notion introduced by Morrow (1988) [82] that volume is the only dose metric that is predictive for NO(A)ELs has been subject of controversy, surface area being also considered [87].

2.2. Characterization of the DMA-nano-PMC system

In chapter 3, in all experiments shown, the nano-PMC was used in combination with a Differential Mobility Analyzer (DMA). It is therefore appropriate to fully characterize the DMA-nano-PMC system. This is accomplished by first characterizing both instruments individually by describing their transfer function and then predict the response of the system, i.e. the output signal after the input signal (a particle mass distribution) has passed both instruments.

In the next sections, first the general concept of system transfer functions is described and illustrated on the basis of particle size classification. The DMA is then described based on the theory of Stolzenburg and McMurry (2008) [88] as well as Mamakos *et al.* (2007) [89], yielding the DMA's electrical mobility transfer function. The operating principle of the nano-PMC is described and subsequently its particle mass transfer function derived after evaluating the trajectories of the particles in the flow channel of the instrument. The response and response spectrum of the DMA-nano-PMC system is predicted.

2.2.1. Instrumental transfer function

In systems theory, a system is generally defined as a procedure at which a signal is transformed or transmitted. The system can be represented by a mathematical operation that transforms the input signal to an output signal, the transfer function [90]. More commonly used to describe how an electrical input signal is processed by e.g. a low-pass filter to comprehend its output signal, it also useful to characterize instruments, classifiers in particular. With the instrumental transfer function known, the instruments response can be predicted when the input is fully characterized. Particle classifiers that act as particle property filters for an aerosol where the particle property is finitely distributed are usually characterized by the transfer function that is specific for the operating conditions of the classifier. One can therefore predict the classification performance, i.e. the classified prop-

erty distribution, when the unclassified property distribution is known. In practice, the output signal of a classifier can be predicted when a calibration aerosol is classified and compared to the measured output signal to validate the functionality of the classifier.

In general, a transfer function of a causal, continuous, time-invariant system is defined as the linear mapping of the on-sided Laplace transformation $\mathcal{L}$ of the input signal $x(t)$ and output signal $y(t)$, where t is a real variable:

$$\Omega(s) = \frac{Y(s)}{X(s)} = \frac{\mathcal{L}\big(y(t)\big)}{\mathcal{L}\big(x(t)\big)} = \frac{\int_0^\infty y(t)\, e^{-st} dt}{\int_0^\infty x(t)\, e^{-st} dt}. \qquad [2.16]$$

Taking a particle size classifier as an example, an input particle size distribution $n_{in}(d_p) = dn_{in}/d\log d_p$ of an aerosol with total number size distribution $N(\epsilon)$ in the volume-element ϵ, expressed as

$$\frac{dn_{in}}{d\log d_p}(d_p) = \int_0^\infty N(\epsilon)\, e^{-\epsilon \log d_p} d\epsilon \qquad [2.17]$$

is transformed to the output particle size distribution $n_{out}(d_p) = dn_{out}/d\log d_p$, given by

$$n_{out}(d_p) = n_{in}(d_p) \cdot \Omega(d_p). \qquad [2.18]$$

In this case, the transfer function can be interpreted as the ratio of the particle flux at the classifier inlet to the particle flux at the classifier outlet[4].

The right hand side of Eq. 2.18 is a product of two functions, a convolution, given by:

$$n_{out}(d_p) = \int_{-\infty}^{\infty} n_{in}(d_p - d)\Omega(d)\, dd. \qquad [2.19]$$

In most cases, the signal in the region of $(-\infty, 0]$ is zero, so that the convolution can be conducted in the region of $[0, \infty)$.

[4] The integral on the right hand side of Eq. 2.17 can be interpreted as the number flux of particles with size d_p over the volume element ϵ.

The output signal Y of instruments is usually referred to as the response of the instrument and the output signal spectrum $Y(s)$ as the response spectrum.

The transfer function of the nano-PMC is theoretically obtained by evaluating the particle equations of motion in its classifying channel to determine their trajectories and subsequently calculate the particle flux at the exit of the classifier (the particle flux at the entrance is known). Similarly, the transfer function of the DMA, which can be analytically expressed, is used to characterize its mobility classification.

2.2.2. Differential Electrical Mobility Classifier

The Differential Electrical Mobility Classifier, commonly known as the Differential Mobility Analyzer (DMA), acts like an electrical mobility filter for an aerosol. Under certain operating conditions of the DMA, only particles within a finite window of electrical mobilities can pass the filter. By systematically changing the filter setting, the aerosol can be classified to determine its electrical mobility distribution.

Figure 2.3 shows a cross-sectional drawing of the cylindrical Vienna-type DMA that was used over the course of the experiments presented in this work [91, 92]. Its central element is a cylindrical capacitor, i.e. two telescoped metallic cylindrical electrodes with a constant annular spacing between each other. A potential difference is applied between the inner and outer cylinder. Particles with a predefined charge enter the capacitor via an annular inlet. A clean sheath air flow adds to the sample flow to generate a laminar flow in the spacing between the cylinders. The particles move along the channel and are drawn towards the cylinder walls due to the Coulomb-force acting on them. Considering that all particles carry the same charge q, the Coulomb-force becomes equal for all particles and only different mobilities lead to different trajectories. When the trajectory of a particle leads to the classified aerosol outlet port, the particle leaves the DMA via the classified aerosol outlet. Other particles are either deposited on the cylinder walls or are transported out of the instrument with the excess air flow. By changing the voltage of the capacitor, the classified electrical mobility window is shifted. The window of classified electrical mobilities is defined by the transfer function $\Omega_{DMA}(Z)$ of the DMA. In practice, all operating conditions but the potential difference is fixed so that the transfer function is only a function of the capacitor voltage.

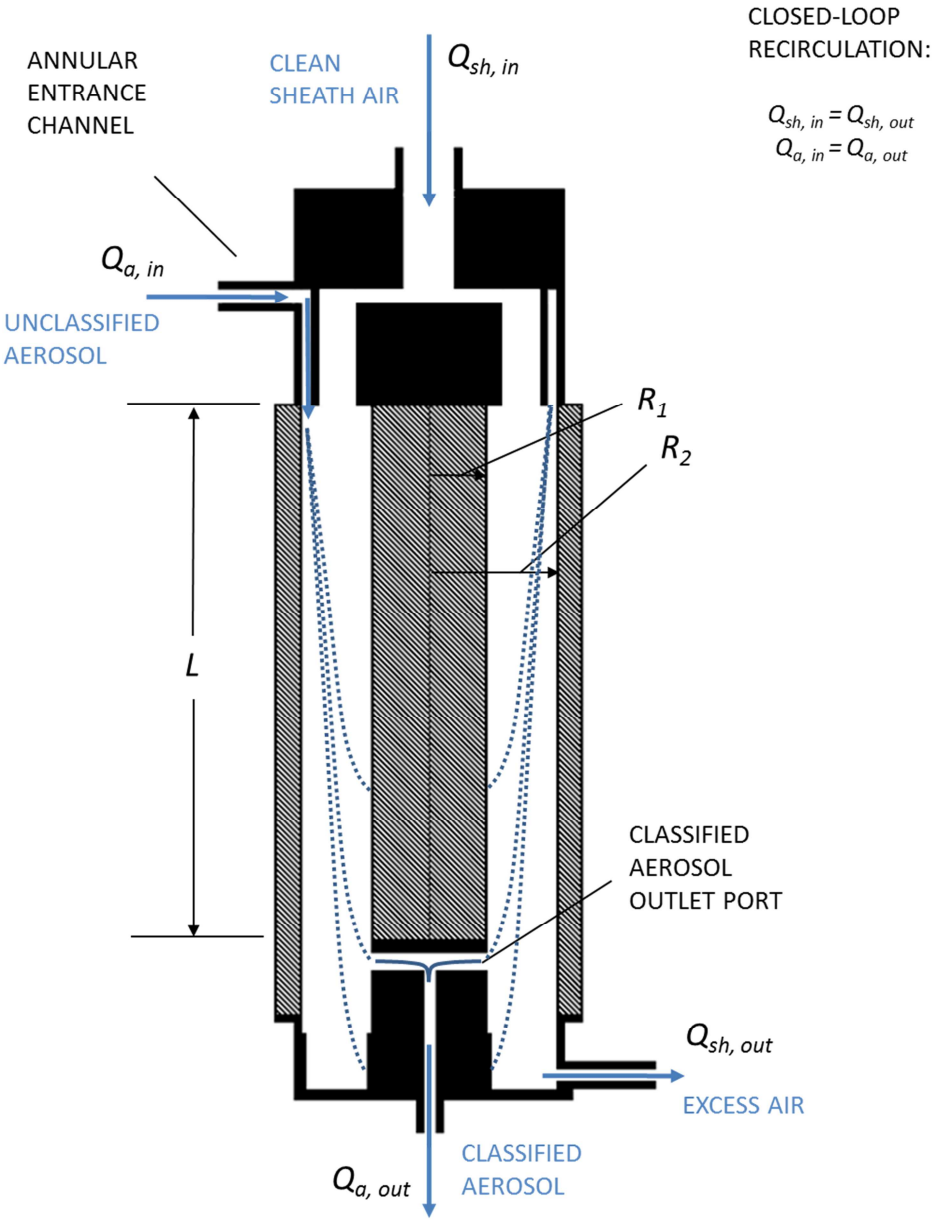

Figure 2.3: Working principle of the cylindrical Vienna-type Differential Mobility Analyzer (DMA). A detailed description is given in the text.

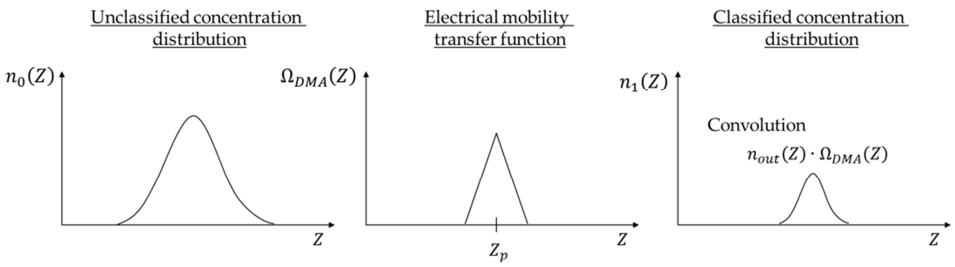

Figure 2.4: Classification of an electrical mobility distribution by the transfer function of the DMA..

The DMA can be used with a so-called closed-loop recirculation system, were the clean sheath flow rate $Q_{sh,in}$ is equal to the excess flow rate rate $Q_{sh,out}$ and the sample flow rate of the unclassified aerosol flow rate $Q_{a,in}$ is equal to the classified aerosol flow rate $Q_{a,out}$. Note that since the classified aerosol outlet port is situated at the inner cylinder, only negative particles are classified when the electrical potential is applied from the inner electrode towards the outer.

Figure 2.4 illustrates the classification principle of the DMA and is based on the depiction in Stratmann *et al.* (1997) [93]. The classified concentration electrical mobility distribution $n_{out}(Z)$ of the classified aerosol leaving the DMA can be determined from the convolution of the unclassified concentration electrical mobility distribution $n_{in}(Z)$ with the transfer function $\Omega(Z)$ of the DMA:

$$n_{\mathrm{out}}(Z) = n_{\mathrm{in}}(Z) \cdot \Omega(Z) \qquad [2.20]$$

The transfer function is triangularly shaped when diffusion has no influence on the particle trajectories and the DMA is operated with a closed-loop recirculation system $Q_{sh,in} = Q_{sh,out} = Q_{sh}$ and $Q_{a,in} = Q_{a,out} = Q_a$. The maximum of the transfer function at $Z = Z_p$ is called centroid electrical mobility. Diffusion causes particles to deviate from their deterministic paths in the flow channel leading to enhanced losses. As a consequence, the transfer function broadens, is reduced in height and adopts a Gaussian shape. Stolzenburg and McMurry (2008) [88] determined the diffusive transfer function of the cylindrical DMA employing a closed-loop recirculation system. The analytical description given here is based on Mamakos (2007) [89].

The diffusive transfer function is given by:

$$\Omega_{DMA}(\tilde{Z}_p) = \frac{\sigma}{\sqrt{2\pi\beta}}\left(\varepsilon\left(\frac{\tilde{Z}_p-(1+\beta)}{\sqrt{2\sigma}}\right)+\varepsilon\left(\frac{\tilde{Z}_p-(1-\beta)}{\sqrt{2\sigma}}\right)-2\varepsilon\left(\frac{\tilde{Z}_p-1}{\sqrt{2\sigma}}\right)\right), \quad [2.21]$$

with

$$\varepsilon(\mathrm{x}) = \mathrm{x}\,\mathrm{erf}(\mathrm{x}) + \frac{\mathrm{e}^{-x^2}}{\sqrt{\pi}}. \quad [2.22]$$

where erf(x) is the error function accounting for the probability of a particle being lost due to diffusion, β is the ratio of the sample flow rate Q_a and the sheath flow rate Q_{sh}. The variable $\tilde{Z}_p$ is the dimensionless electromobility defined by

$$\tilde{Z}_p = \frac{Z}{Z_p}. \quad [2.23]$$

The centroid electrical mobility of the transfer function Z_p is given by:

$$Z_p = \frac{Q_{sh}}{2\pi}\frac{\ln(R_2/R_1)}{L\,U}. \quad [2.24]$$

R_1, R_2 and L are the outer radius of the inner cylinder, inner radius of the outer cylinder and the cylinder length of the DMA, respectively. The standard deviation σ of the transfer function is given by:

$$\sigma = \sqrt{G\,\frac{2\pi LD}{Q_{sh}}} \quad [2.25]$$

where D is the diffusion coefficient. The parameter G is the so-called DMA-geometry factor and dimensionless. Its value depends on the geometry of the DMA and the flow conditions in the classifying region:

$$G = \frac{4(1+\beta)^2}{1-\gamma}\left[I_\gamma(\gamma) + \left(\frac{1}{2(1+\beta)\kappa}\right)^2\right], \quad [2.26]$$

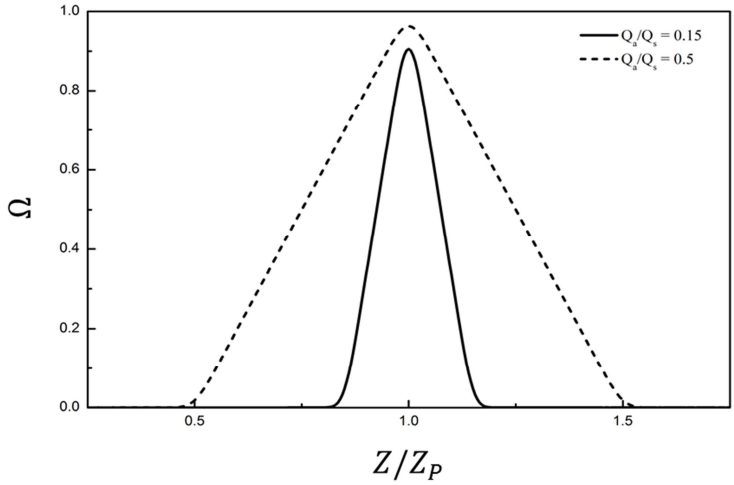

Figure 2.5: Electrical mobility transfer functions of the DMA used for the nano-PMC measurements for two different Q_a-Q_{sh}-ratios.

where $\kappa = L\,R_2(R_2 - R_1^2)^{-1}$ and $\gamma = (R_1/R_2)^2$. The value of I_γ depends on the laminar velocity profile between the inner and outer cylinder, given by

$$I_\gamma(\gamma) = \frac{\left[\frac{(1-\gamma^2)(1-\gamma)^2}{4} + \frac{5(1-\gamma^3)(1-\gamma)\ln(\gamma)}{18} + (1-\gamma^4)\ln(\gamma)^2\right]}{\left[(1-\gamma)\left(-\frac{(1+\gamma)\ln(\gamma)-(1-x)}{2}\right)^2\right]}. \qquad [2.27]$$

Figure 2.5 shows two examples of the transfer function as a function of $\tilde{Z}_p$. These were calculated using Eq. 2.21. The thick line shows a typical Gaussian transfer function that was calculated for a sample flow rate to sheath flow rate ratio (Q_a-Q_{sh}-ratio) of 1.5/10. The larger this ratio is the broader the transfer function becomes, as shown with the dashed curve that was calculated for a Q_a-Q_{sh}-ratio of 0.5.

The transfer function described by Eq. 2.21 is valid for singly charged particles. Even though in most experiments a neutralizer is used to set the aerosol charge distribution to a bipolar Boltzmann-distribution (particles should then carry none, one positive or negative elementary charge), particles still have a small probability to carry more charges, depending on the charging efficiency of the neutralizer. For the response of the DMA-CPC system, i.e. a CPC that counts particles that pass the DMA to obtain the electrical mobility

concentration distribution (SMPS), a correction must then be applied, called multiple-charge correction [94].

2.2.3. Operating principle and transfer function of the nano-PMC

In chapter 3, the theory of the particle mass classification with the nano-PMC is only described briefly. The next section gives a detailed description of the operating principle. Based on the nano-PMC theory, particle trajectories in the classifying region are determined which are subsequently used to obtain the transfer function of the nano-PMC.

2.2.3.1. Equations of motion in a PMC

The particle mass classifier (PMC), first described by Ehara (1996) [21] as the aerosol particle mass analyser (APM), is basically a rotating cylindrical capacitor, i.e. two telescoped concentric cylinders with equidistant spacing $|r_2 - r_1|$ between the inner wall of the outer cylinder at radius r_2 and the outer wall of the inner cylinder at radius r_1. This setup is shown and described in figure 2.6. The width and length L of this rotationally symmetric gap are the characteristic dimensions of the classifier flow channel. The radius for the center of the gap is r_c.

Rotation of the particle carrier gas, induced by the movement of the cylinders, cause the particles in the rotating cylinder gap to be drawn away from the center of rotation due the centrifugal force F_{Cn}:

$$F_{Cn} = M(2\pi\omega)^2 r, \qquad [2.28]$$

where M is the particle mass, ω (rpm) is the rotational speed and r is the distance from the center of rotation. If the particle is charged and an electric field is established by a potential difference between the two cylindrical electrodes, a counteracting electrostatic force F_{Cb} acts on the particles, given by:

$$F_{Cb} = -\frac{neU}{r\,ln\left(\frac{r_2}{r_1}\right)}. \qquad [2.29]$$

Here U (V) is the potential difference between the two electrodes, n is the number of elementary charges and e the elementary charge ($e = 1.602 \times 10^{-19}$ C). As the particle moves relative to the carrier gas, it experiences a drag force in opposite direction to the motion described by Stoke's law:

$$F_{Dr} = \frac{3\pi\eta d_p v}{C_c(d_p)}. \quad [2.30]$$

Here v and d_p are the velocity and diameter of the particle, respectively, and η the dynamic viscosity of the gas. C_c is the Cunningham Slip correction factor given by:

$$C_C = 1 + \frac{\lambda}{d_p}\left(A + Be^{-C\frac{d_p}{\lambda}}\right), \quad [2.31]$$

where λ is the mean free path of the gas ($\lambda \approx 65$ nm at ambient pressure) and $A = 1.142, B = 0.558, C = 0.999$ are empirical constants [78].

Following a simple Newtonian approach, the equation of motion in the direction perpendicular to the flow in the cylinder gap can be expressed as:

$$c\frac{\partial r(t)}{\partial t} = ar(t) - \frac{b}{r(t)}. \quad [2.32]$$

The terms a, b and c in Eq. 2.32 represent respectively the centrifugal force, the Coulomb force and the drag force, given by:

$$a = M(2\pi\omega)^2, \quad [2.33]$$

$$b = neU\left(ln\left(\frac{r_2}{r_1}\right)\right)^{-1}, \quad [2.34]$$

$$c = 3\pi\eta d_p {C_c}^{-1}. \quad [2.35]$$

The particles follow the gas flow which has a Poiseuille profile in the cylinder gap given by [95]:

$$v_x(r) = \frac{3}{2}\tilde{v}\left(1 - 4\left(\frac{r - r_c}{r_2 - r_1}\right)^2\right), \quad [2.36]$$

where $\tilde{v} = Q/A$ is the mean flow velocity, with Q and A being the aerosol volumetric flow rate and the cross-sectional area of the cylinder gap, respectively.

The equation of motion for the particles in flow direction is therefore:

$$x(t) = v_x\big(r(t)\big)t\,. \qquad [2.37]$$

Particles with a certain mass-to-charge ratio that enter flow channel of the classifier at the radial center r_c do not divert from their original path along the flow streamlines. At the radial position r_c the electrostatic and centrifugal forces are balanced for such particles thus preventing motion perpendicular to the flow, resulting in the Stoke drag force becoming zero. In this case, the particle mass can be determined by equating Eqs. 2.29 and 2.30 yielding:

$$M = \frac{neU}{(2\pi\omega)^2 r_c^2}\left(\ln\left(\frac{r_2}{r_1}\right)\right)^{-1}. \qquad [2.38]$$

However, if particles for which equilibrium of forces is established at the radial center of the classifier enter the flow channel at radial positions smaller than r_c, they drift towards the inner wall due to the electrostatic force being greater than the centrifugal force. Similarly, if those particles enter at radial positions larger than r_c, they move towards the outer wall since the centrifugal force dominates. Thereby, even if all particles have equivalent mass-to-charge ratio, particles are lost since they enter the flow channel radially distributed over the cylinder gap. Moreover, particles still might be able to traverse the classifier if they don't experience force equilibrium at radial position r_c. For particles with equal charge but smaller or larger particle mass, other radial positions might exist, where equilibrium of forces is established. However, the probability of such particles exiting the classifier is lower. Under realistic aerosol conditions, i.e. where the particle mass is finitely distributed, the particle mass at which particles traverse the classifier most probably is called ´dominant particle mass´. The mode of the particle mass distribution downstream the nano-PMC is equivalent to the dominant particle mass.

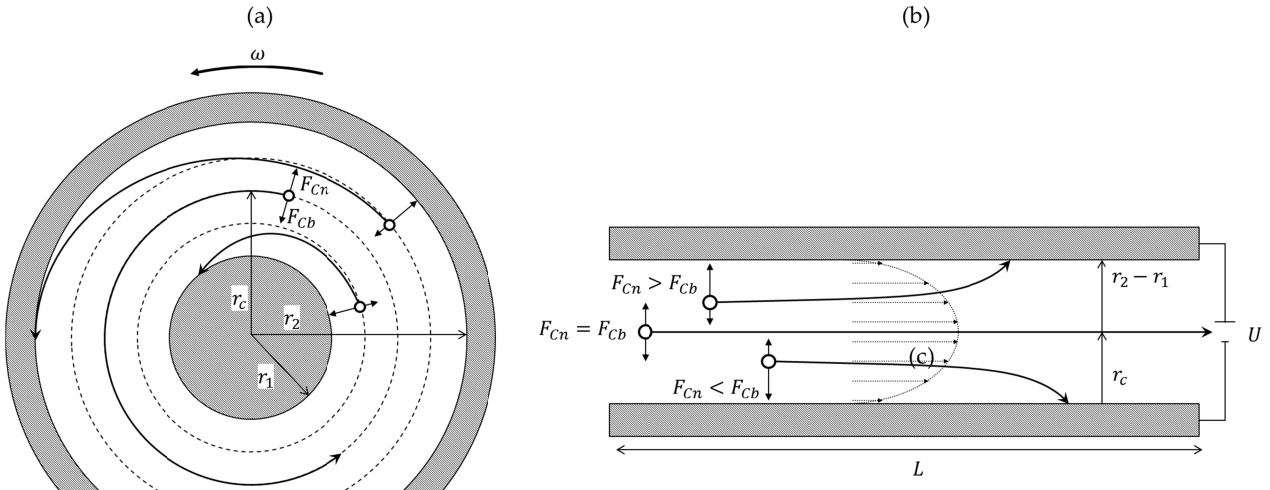

Figure 2.6. Working principle of a PMC illustrated in two side-views of the flow channel. (a) shows the the cylindrical capacitor with radii r_1 and r_2, with the cylinder axis facing towards the viewer. (b) shows the gap between the two cylinders with length L along the rotational axis. The dashed lines show the flow streamlines, in (a) equi-flow velocity lines and in (b) the Poiseuille flow profile between two plates. The thick black arrows demonstrate which trajectories particles follow with centrifugal and electrical force acting on them, F_{Cn} and F_{Cb} respectively. Only at the radial center of the gap, both forces can be balanced resulting in penetration of a particle which gets deposited otherwise.

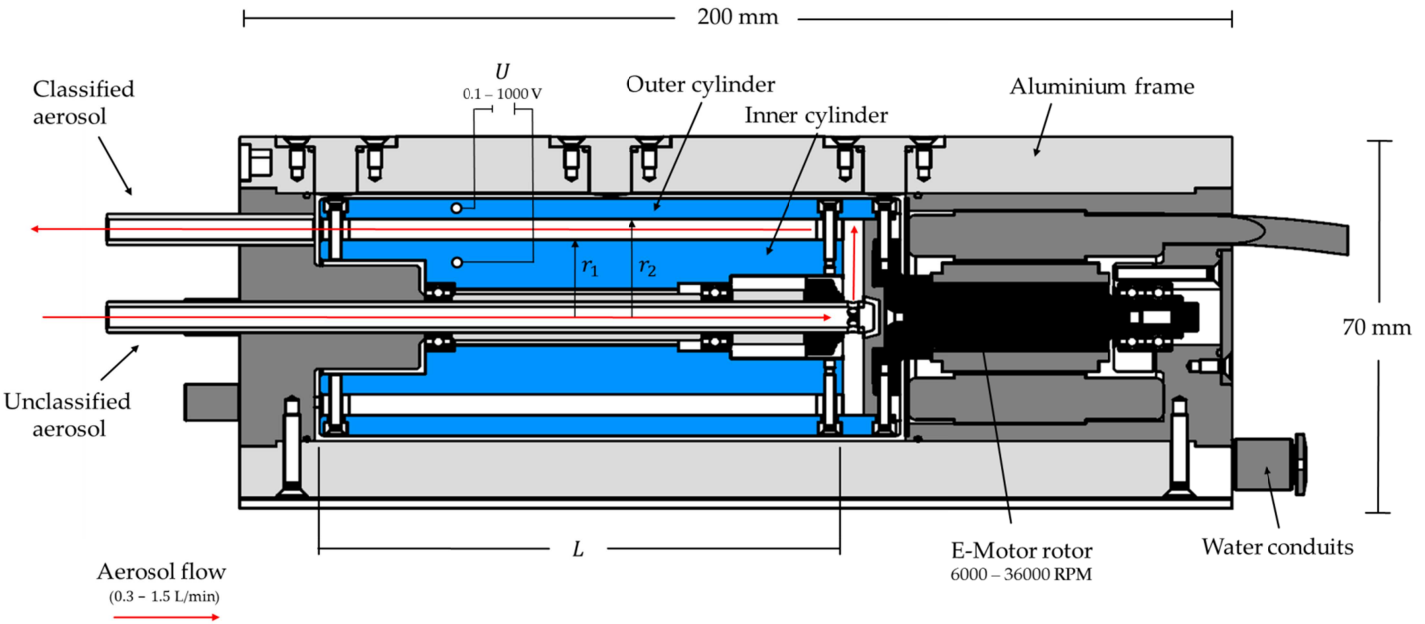

Figure 2.7. Exact Schematic drawing of a cross-sectional cut near the radial center of the nano-PMC. The classifier is coloured blue, whereas the static parts grey, dark grey for insulating parts, light grey for conductive parts.

TABLE 2.1:
Geometric and operating parameters of the nano-PMC

Symbol	Meaning	Value / Value range
Geometry of the flow channel		
r_1	Outer radius of inner cylinder	15 mm
r_2	Inner radius of outer cylinder	19 mm
r_c	Radial position of cylinder gap center	17 mm
L	Length of cylinders /classifier flow channel	100 mm
Operational parameters		
ω	Rotational speed	6000 rpm – 36000 rpm
U	Voltage	0.1 V – 1000 V
Q	Flow rate	0.3 L/min – 1.5 L/min

In addition, all particles undergo Brownian motion as they move along the cylinder gap, which makes them deviate from their deterministic paths. This deviation δ can be estimated by:

$$\delta = \sqrt{2Dt}\, B(t) \qquad [2.39]$$

where D (m²/s) is the diffusion coefficient of the particles, t is time and $B(t)$ is a random variable from a Gaussian distribution with zero mean and standard deviation equal to unity. The random number $\pm B(t + dt)$ effectively scales and directs the diffusive component of the particle path after time interval $t + dt$. The equations of motion in radial (Eq. 2.32) and axial (Eq. 2.37) directions are modified to include particle diffusivity as follows:

$$x(t + dt) = x(t) + \sqrt{2Ddt}\, B(t), \qquad [2.40]$$
$$r(t + dt) = r(t) + \sqrt{2Ddt}\, B(t). \qquad [2.41]$$

This approach was introduced to describe diffusion broadening in the DMA [89, 96]

2.2.3.2. Transfer function of the nano-PMC

Figure 2.7 shows an exact schematic drawing of a cross-sectional cut of the nano-PMC. Table 2.1 summarizes all relevant geometric and operational parameters of the nano-PMC, used for the calculation of particle trajectories in the flow channel of the classifier. Please refer to section 3.1 for a detailed description of the nano-PMC design and section 3.2.2 for

the operational diagram of the nano-PMC. The following calculations of particle trajectories are conducted based on this geometry.

Particle trajectories are calculated by solving the equations of motion (Eq. 2.32 and Eq. 2.37) to yield the current positions of a particle as a function of time. This system of differential equations is coupled, since first the position of the particle radial position must be known to determine its velocity in flow direction defining the position in axial direction. Solving the differential equation Eq. 2.32 is difficult due to stiffness in the system. The system is therefore numerically solved by a Mathematica computer code that is described in Appendix A.

In the nano-PMC, particles enter and exit the classifier flow channel through a 2 mm wide entrance slit, both located radially at the center of the cylinder gap. Figure 2.8 shows examples of particle trajectories for 50−nm particles with standard density (i.e., 1 g/cm^3) in the classifying region of the nano-PMC. The trajectories are influenced by diffusion, as demonstrated in Figure 2.8 (d) that shows a magnification of the trajectory of a particle. When $U = 0\ V$, all particles are deposited on the wall of the outer cylinder as a result of the centrifugal forces they experience. At a voltage of $U = 125\ V$, the majority of the particles migrate successfully through the classifier without depositing on the walls. The particles that enter far away from r_c, however, deposit on the inner or the outer cylinder since the centrifugal and electrostatic forces are not absolutely balanced. When $U = 75\ V$, all particles are deposited on the inner cylinder because the electrostatic force becomes stronger than the centrifugal force.

As mentioned in section 2.3.1, the transfer function is given by the ratio of the particle flux at the entrance and at the exit of the classifying region. Since the nano-PMC's flow channel is angularly symmetric, it is appropriate to define the inlet and outlet particle flux as the number concentration over the cross-section of the entrance and exit gap respectively, so that the input/output number signal is given by:

$$n_{in/out} = \int_{r_1}^{r_2} N_{in/out}(r)\, e^{-r}\, dr\ . \qquad [2.42]$$

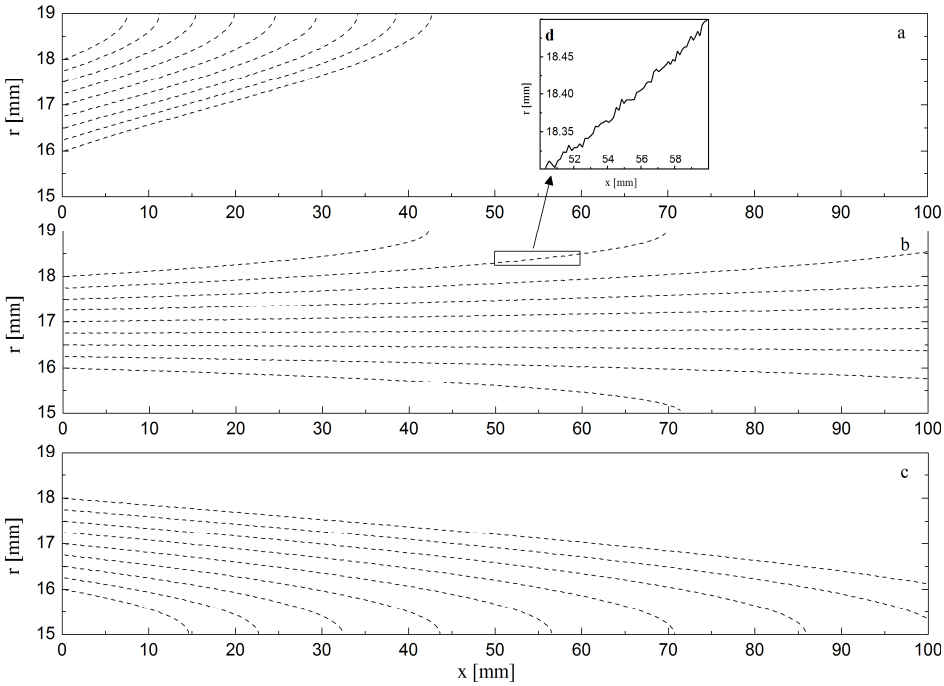

Figure 2.8. Predicted trajectories in the classifying region of the nano-PMC of spherical particles with $d_p = 50$ nm and density $\rho = 1$ g/cm^3 within the cylinder gap that enter at different radial positions. See Table 2.1 for the geometric parameters of the flow channel. For the calculations we assumed that the nano-PMC is operated at $\omega = 20 \times 10^3$ rpm, $Q = 1.5$ L/min and $U = 0$ V (a), $U = 125$ V (b), $U = 175$ V (c). (d) shows a magnification of the boxed area of (b).

Assuming that the number of particles N is spatially invariant, the input and output number signal is simply the number of particles in the entrance and exit of the classifying region, respectively. The input number of particles is simply the number of particle whose trajectories were calculated with the model whereas the output number of particles can be determined by counting all particles whose trajectories reach the exit gap and not collide with the cylinder walls. The ratio of the output number and input number of particles with equal mass at given operational conditions of the nano-PMC is called transferred fraction. The particle mass transfer function Ω_{PMC} is then the transfer fraction as a function of particle mass M:

$$\Omega_{PMC}(M) = \frac{n_{out}(M)}{n_{in}}, \qquad [2.43]$$

when the input number of particles is invariant. Each set of operating conditions of the nano-PMC therefore exhibits a specific particle mass transfer function.

The shape of the particle mass transfer function of the nano-PMC is discussed in chapter 3.5. It can best be fitted with a lognormal peak function.

By evaluating the transfer function, classification performance and resolution of the classifier can be discussed which have consequences for the operational bounds, i.e. the particle mass range, the nano-PMC can be classify under constraints about resolution.

2.2.3.3. Response spectrum of a DMA-nano-PMC system

A system of a DMA and the nano-PMC, as described in chapter 3, is characterized by two transfer functions, the DMA transfer function Ω_{DMA} and nano-PMC transfer function Ω_{PMC}. The output signal of the system, the response, is therefore given by the convolution of the input signal, which is the unclassified mass distribution $n_{in}(M) = dn_{in}/dM$, with both the DMA particle mass transfer function and the particles mass transfer function of the nano-PMC:

$$n_{out}(M) = n_{in}(M) \cdot \Omega_{DMA}(M) \cdot \Omega_{PMC}(M)\,. \qquad [2.44]$$

The DMA particle mobility transfer function must therefore be converted into a particle mass transfer function, by assuming an equal apparent density for the spherical particles with electromobility diameter d_m, classified by the DMA:

$$\Omega_{DMA}(M) = \frac{4}{3}\rho_{ap}\ \Omega_{DMA}\left(\mathrm{d}_m{}^3\right) = \frac{4}{3}\rho_{ap}\ \Omega_{DMA}\left(\left[\frac{neC_c}{3\pi\eta Z}\right]^3\right) \qquad [2.45]$$

The response spectrum is the systems response as a function of usually the potential difference U of the nano-PMC:

$$n_{out}(U, M) = n_{out}(M) \cdot \Omega_{DMA}(M) \cdot \Omega_{PMC}(U, M) \qquad [2.46]$$

In chapter 3, the response spectra of the DMA-nano-PMC system for particles with known masses are measured. The measurements are compared with predictions than were obtained by applying the model described here.

Appendix A shows the Mathematica script to predict the response of the DMA-nano-PMC system based on this description.

2.3. Dosimetry of the Cyto-TP

The Cyto-TP, where TP is an abbreviation of thermal precipitator, comprises two parallel metallic plates with different temperatures to create a temperature gradient in the gas in between those plates. This leads to the effect of thermophoresis, the motion of a particle in gas in negative direction of the gradient – in case of the thermal precipitator the cold plate. This section gives the theoretical description of thermophoresis.

2.3.1. Thermophoresis of spherical particles

When the particle can be considered in the free-molecular regime $\left(\mathrm{Kn}=\lambda/d_p \gg 1\right)$, the thermophoretic motion results from individual collisions of gas molecules with the particle surface causing an uneven transfer of momentum from the gas molecules to the particle. Collisions occur due to Brownian motion of gas molecules and the particle. In a simplified model that is illustrated in Figure 2.9 (a), the surface of the particle pointing towards the warm source receives a higher transfer of momentum $\overrightarrow{p_1}$ compared to the colder side $\overrightarrow{p_2}$, resulting in a total momentum in direction of the cold source. The thermophoretic motion is therefore a function of the rate of momentum that is being transferred to the particle which depends on the velocity profile of the surrounding gas molecules [97]. This profile is described by the Chapman-Enskog distribution $f(\vec{u})$ which corrects the molecular velocity distribution of a gas, given by the Maxwell-Boltzmann distribution, when its thermodynamic equilibrium is disturbed [98].

Waldmann (1959) [99] derived the molecular velocity distribution surrounding a spherical particle by integrating the momentum exchange from collisions between the gas molecules and the particle surface over the surface of the sphere. Using the impulse theorem, he calculated the force on the sphere induced by the momentum transfer from gas molecules colliding with the particle surface. This procedure is shown in Figure 2.9 (b). This is the thermophoretic force, given by

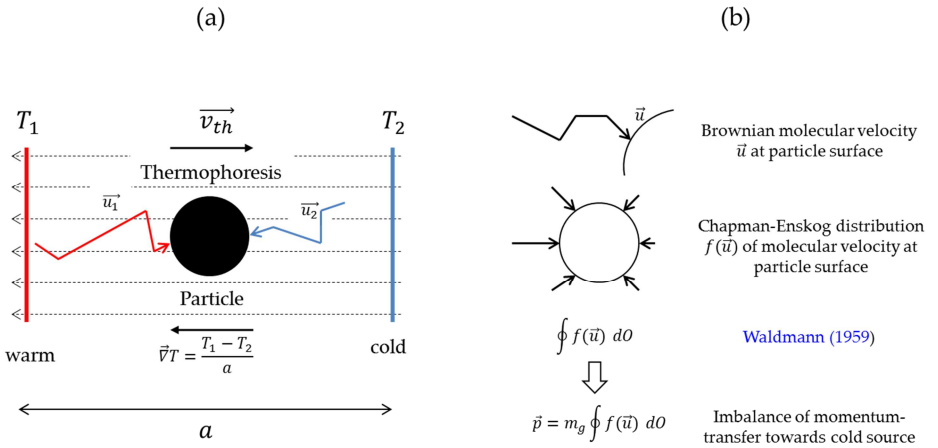

Figure 2.9: Thermophoretic model for spherical particles considered in the free-molecular regime (Kn ≫ 1). (a) illustrates the (uniform) temperature gradient as dashed arrows, quantifiable by the difference between the equi-temperature lines T_1 (warm) and T_2 (cold) over the distance a between the lines. The particle moves with thermophoretic velocity v_{th}. (b) demonstrates the Waldmann-model for the cause for thermophoresis. Gas molecules move with Brownian molecular velocity $\boldsymbol{u}$ and eventually collide with the particle surface. The molecular velocity is distributed, described with the Chapman-Enskog distribution $f(u)$. Waldmann integrated the molecular velocity distribution over the particle surface and applied the impulse theorem, resulting in a particle momentum directed towards the cold source due to the imbalance of momentum transfers when gas molecules collide with the particle surface.

$$F_{th,x} = -\varsigma \left(\frac{\pi d_p^2}{4\, u} \right) \kappa \frac{\partial T}{\partial x}. \qquad [2.47]$$

where κ is the the thermal conductivity of the gas. The thermophoretic parameter ς was estimated by Waldmann to be around 0.679.

For engineering purposes (as in this work), this approximated solution is sufficient [100, 101].

Waldmann (1959) [99] also gave a simplified expression for the resulting thermophoretic velocity v_{th} of the particle, by equating the thermophoretic force with the Stoke Drag force:

$$v_{th,x} = -\mathrm{K}\frac{\eta}{\rho_g T}\frac{\partial T}{\partial x}, \qquad [2.48]$$

where ρ_g is the gas mass density, T the ambient temperature and K the thermophoretic coefficient that in the free molecular regime can be estimated by:

$$\mathrm{K} = \frac{6}{8 + \pi\beta_d}, \qquad [2.49]$$

where β_d is the fraction of gas molecules that is reflected diffusely and the remaining fraction specularly. Waldmann derived a value of $\mathrm{K} = 0.55$.

More recently a numerical approach to calculate the thermophoretic coefficient was provided, using Monte Carlo Simulations to describe Brownian motion of the gas molecules and particles [100, 102]. The thermophoretic coefficient was found to be depending on gas properties, e.g. whether the gas is assumed to be a single-species continuum gas or multi-species, but of similar value.

For larger particles that cannot be considered in the free-molecule regime any more, a continuum model for the particle-gas interaction is more appropriate. In this case, a temperature jump between the particle and the surrounding gas causes a thermal stress slip of a thin layer of gas surrounding the particle, called Knudsen layer, in direction of the temperature gradient [103]. A thermo-osmotic effect causes the thermophoretic force. Brock (1962) [104] gave an expression for the thermophoretic coefficient, derived including frictional slip of gas molecules along the particle surface in addition to their thermal slip as well as assuming a temperature jump between particle surface and gas:

$$K = \frac{2C_s\left(k_g + k_p C_t \mathrm{Kn}\right)}{\left(1 + 2C_m \mathrm{Kn}\right)\left(2k_g + k_p + 2k_p C_t \mathrm{Kn}\right)}, \qquad [2.50]$$

where C_t and C_m are dimensionless coefficients that account for the temperature jump and frictional slip respectively. Talbot *et al.* (1980) [105] derived values for the coefficients C_s, C_t and C_m based on experimental data on the thermophoretic velocity that are 1.17, 2.18 and 1.14, respectively.

Note that in the continuum-regime case, thermophoresis is dependent on particle size. Generally, the larger the particle is, the smaller becomes its thermophoretic motion. However, up to about 300 nm particle diameter, the difference of the thermophoretic velocities derived using both models is neglectable and the Waldmann-equation (Eq. 2.48) is considered as sufficient.

Similar to the electrophoresis of a particle in an electrical potential, it is useful to define the thermophoretic velocity on the basis of the particle mobility in the temperature potential (gradient), called thermophoretic mobility Ψ:

$$\begin{aligned} \mathrm{v}_{th} &= \Psi \nabla \mathrm{T}, \\ \text{where } \Psi &= -\mathrm{K}\frac{\eta}{\rho_g T}. \end{aligned} \qquad [2.51]$$

2.3.2. Thermophoresis of particles with non-spherical shapes

For non-spherical particles, the thermophoretic mobility can be derived by the average of mobility components. For example, an axis-symmetrical oblate spheroid with radii a and b has two thermophoretic mobility components for its longitudinal and transversal symmetry axes, Ψ_L and Ψ_T respectively, given by [103]:

$$\begin{aligned} \Psi_L &= \frac{C_S \eta}{\rho_g T} \nabla_L T \left(1 + \frac{\alpha}{\beta}\tilde{k}\right)^{-1} \\ \Psi_T &= \frac{C_S \eta}{\rho_g T} \nabla_T T \left(1 + \frac{\beta}{\alpha + 1}\tilde{k}\right)^{-1} \end{aligned} \qquad [2.52]$$

where $\nabla_L T$ and $\nabla_T T$ are the longitudinal and translational components of the temperature gradient respectively,

$$\begin{aligned} \alpha &= \left(\left(\frac{a}{b}\right)^2 - 1\right)\left(\frac{a}{b}\coth\left(\frac{a}{b}\right)^{-1} - 1\right) \\ \beta &= \frac{a}{b}\left(\frac{a}{b} - \left(\left(\frac{a}{b}\right)^2 - 1\right)\coth\left(\frac{a}{b}\right)^{-1}\right) \end{aligned} \qquad [2.53]$$

and $\tilde{k}$ the ratio of the thermal conductivity of the particle and of the gas. Keh and Ou (2004) [103] analysed the limiting cases $a/b \to 0$ (a disk-shaped particle) and $a/b \to 0$ (a needle-like particle). In both cases the average thermophoretic mobility was significantly

greater when the dominant radius was aligned with the temperature gradient, i.e. the edge of the disc and the needle oriented parallel to the gradient.

A fractal aggregate, where its individual primary particles would be considered to be in the free-molecular regime ($d_P < \lambda$), has a similar thermophoretic mobility as one isolated primary particle. Again, the thermophoretic mobility is the average of the mobilities respective to each primary particle:

$$\Psi = \frac{1}{N_{pp}} \sum_{i=1}^{N_{pp}} \Psi_{pp}, \qquad [2.54]$$

where N_{pp} is the number of primary particles. Mackowski showed that fractal aggregates, randomly generated via diffusion-limited cluster aggregation, exhibited thermophoretic mobilities 1 to 1.1 greater the mobility of its primary particles, depending on the number of primary particles [106].

2.3.3. Equations of motion in a thermal precipitator

Figure 2.10 shows the working principle of a plate thermal precipitator. A particle moving into its flow channel will deposit on the cold plate at a location given by the particle's trajectory, which can be determined by solving the particle's equations of motion. In Cartesian coordinates, simple ballistic equations of motion are assumed. The particle is moved in x-direction by the flow of the carrier gas, which has a Poiseuille flow profile over the distance h between the two plates (Eq. 2.36). In y-direction, the particle trajectory is determined by the thermophoretic motion and the gravitational settling velocity v_g. The equations of motion are given by:

$$\mathrm{x(t)} = v_x\, t = \frac{3}{2}\tilde{v}\left(1 - 4\left(\frac{y(t)}{h}\right)^2\right) t \qquad [2.55]$$

$$\mathrm{y(t)} = \boldsymbol{v_y}\, t = \left(\boldsymbol{v_g} + \Psi\nabla\mathrm{T}\right) t \qquad [2.56]$$

$$\mathbf{z(t)} = \boldsymbol{v_z}\, t = 0 \qquad [2.57]$$

with

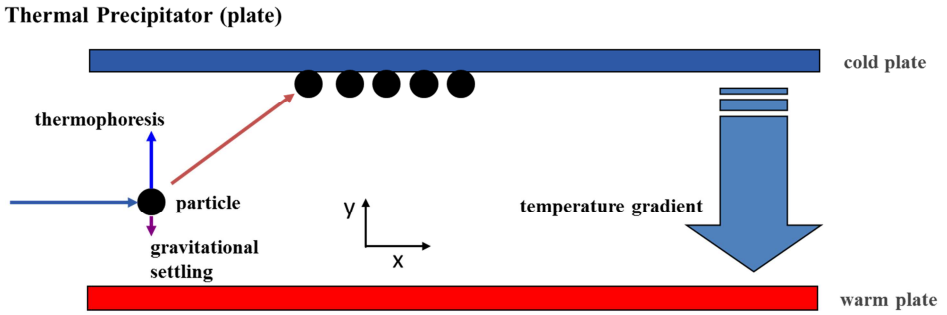

Figure 2.10. Working principle of a plate thermal precipitator. Two parallel plates form a duct flow channel for particles. A temperature different between the colder, top, plate and warm, bottom, plate creates a temperature gradient in the particle-gas. Particle will move towards the cold plate due to thermophoresis acting against the smaller gravitation and eventually deposit.

$$v_g = \frac{d_p^2 \rho_g g}{18\eta}. \qquad [2.58]$$

This system of differential equations is coupled and can be solved numerically.

A Mathematica script to determine the particle trajectories with subsequent analysis is given in Appendix B.

2.3.4. Deposition efficiency and dose rate

The deposition efficiency ϕ is given by the ratio of the deposited dose and the administered dose. Its value can either be theoretically predicted with the script shown in Appendix B and applied for the first and second prototype of the Cyto-TP (chapter 4.2 and 5.1) or experimentally, as shown in chapter 5.2 for the third prototype.

The number dose rate R_N is given by the product of the particle number concentration N, the deposition efficiency ϕ and the flow rate Q:

Number dose rate $$R_N = N\ [1/\mathrm{cm}^3] \times \phi \times Q\ [\mathrm{ml/min}] \qquad [2.59]$$

Surface area, volume and mass are dose metrics that are useful to correlate toxic effects by particles to particle properties. However, those particle properties are usually finitely distributed and must be measured with adequate particle characterization. In case the number based particle size distribution $dN/d\log(d_p)$ is known, it can be converted to particle surface area distribution $SA(d_p)$ and volume distribution $V(d_p)$ or, with known particle density, the mass distribution $M(d_p) = V(d_p) \times \rho_p(d_p)$. The dose rates are then given by:

Surface area dose rate
$$R_{SA} = \phi \times Q \times \int \left[\frac{dN}{d\log(d_p)}(d_p) \times SA(d_p) \right] \mathrm{d}d_p \qquad [2.60]$$

Volume dose rate
$$R_V = \phi \times Q \times \int \left[\frac{dN}{d\log(d_p)}(d_p) \times V(d_p) \right] \mathrm{d}d_p \qquad [2.61]$$

Mass dose rate
$$R_M = \phi \times Q \times \int \left[\frac{dN}{d\log(d_p)}(d_p) \times M(d_p) \right] \mathrm{d}d_p \qquad [2.62]$$

Note, that the surface and volume only requires measurement of the particle size. For the mass dose rate, the particle density must be known. In case, the mobility size is known, the apparent density (that is usually dependent on mobility) must additionally be measured, e.g. with the nano-PMC.

Chapter 3: The nanoparticle mass classifier (nano-PMC)

Abstract

Existing aerosol particle mass classifiers (PMCs) can classify particles having masses down to ca. half an ag (i.e., 10^{-18} g), which corresponds to a diameter of ca. 10 nm for spherical particles with standard density (1 g/cm^3). Here, we describe an improved design of such a classifier, namely the nano-PMC, which can classify particles with masses down to 20 zeptograms (10^{-21} g). The response of the classifier was characterized with spherical polystyrene-latex (PSL) and ammonium sulphate particles, produced by atomization and mobility classification. Measured responses were compared with predictions by a numerical trajectory-based model that considers particle diffusivity. Measurements and predictions of the mean mass of the particles penetrating the classifier agreed within experimental uncertainty (< 6%). Differences in the spectrum width could be attributed to recirculation flows occurring in the classification channel.

To demonstrate the capabilities of the nano-PMC, we used it in a tandem configuration with a Differential Mobility Analyser (DMA) to determine (1) the size-dependent shape factor of cubic sodium chloride particles having diameters from 15 to 120 nm, and (2) the apparent density and mass-mobility coefficient of coalesced and aggregated silver particles generated by spark ablation. Measurements of the shape factor of the cubic sodium chloride particles show good agreement with previous observations. Coalesced silver particles exhibited an apparent density that was lower compared to that of bulk silver, suggesting a slightly non-spherical particle shape. The mass-mobility scaling exponent of the aggregated silver particles determined by the measurements was 2.3 ± 0.1.

This chapter has been published as:
D. Broßell, M. Valenti, S. Bezantakos, A. Schmidt-Ott and G. Biskos (2015):
The nanoparticle mass classifier (nano-PMC): Development, characterisation and application for determining the mass, apparent density and shape of particles with masses down to the zeptogram range,
Aerosol Science and Technology, Volume 49, Issue 7, 2015.

3.1. Introduction

Aerosol classifiers are readily employed for particle characterization in the environment and in view of their numerous technological applications [107, 108]. The most widely used instruments for classifying aerosol particles in the sub-micron size range are based on particle electrical mobility; a property that depends on their size and morphology, but is independent of mass or density. Conversion of particle number size distributions measured by electrical mobility spectrometers to mass-based size distributions therefore requires information on the mass, density and morphology (or apparent density) of the particles.

A number of new methods that can directly determine particle mass, including time-of-flight mass spectrometers and nanoscale cantilevers [109], have been introduced in recent years. Another promising instrument, introduced by Ehara (1996) [21], is the aerosol particle mass analyser (APM), which is now commercially available (Kanomax Model APM-3600). In this instrument, particles enter a rotating cylindrical capacitor, within which they experience a mass-dependent centrifugal force and reach a constant angular velocity. An electrostatic force in the opposite direction is induced by applying an appropriate potential difference between the inner and outer cylinder of the capacitor. By changing this potential difference, centrifugal forces acting on particles of different masses can be balanced by the electrostatic forces. When the two forces are balanced, particles penetrate through the classifier.

Previous advancements on particle mass classifiers (PMC) have mainly focused on the improvement of their sensitivity and resolution. First proposals used either a slightly faster rotation of the inner cylinder to establish a Couette flow profile in the capacitor gap or the division of flow channel into segments with mirrored curvature. The first design was adopted by Olfert and Collings (2005) [23] and Olfert *et al.* (2006) [110], resulting in the commercially available PMC known as the centrifugal particle mass analyser (Cambustion CPMA). More recently, Tajima *et al.* (2013) [111] developed a miniaturized version of the classical APM design, reffered to as the "compact APM".

The maximum rotational speed of PMCs developed so far is 14×10^3 rpm, which makes the centrifugal forces on very small particles insufficient to deflect them from their convective paths. As a result, application of existing systems is limited to particles having masses of the order of half an ag (i.e., 10^{-18} g), which corresponds to particles with a diameter of ca. 10 nm and density of 1 g/cm^3 [24, 25, 112, 113]. In principle, however, PMCs

designed to reach higher rotational speeds are capable of classifying standard-density particles having diameters down to a few nanometers.

Here, we describe the design and characterize the performance of a PMC, namely the nano-PMC, capable of classifying nanoparticles with masses down to 20 zg, corresponding to spherical particles with a diameter of 3.4 nm and density of 1 g/cm³. The resolution, measureable particle mass range and operational constraints of the new classifier were determined theoretically. The instrument was characterised using spherical Polystyrene-Latex (PSL) and ammonium sulphate nanoparticles generated by atomization and classified with a differential mobility analyser (DMA). Measured responses of the system were compared with predictions using a trajectory-based model that considers particle diffusivity. The tandem DMA-nano-PMC system can also be used to determine the dynamic shape factor of cubic sodium chloride particles, having sizes from 15 to 120 nm, generated by atomization. Furthermore, the system was successfully used to measure apparent densities and shapes of coalesced and aggregated silver particles, having mobility diameters from 5 to 50 nm, produced by a spark ablation.

3.2. Design and operating principle of the nano-PMC

Figure 3.1 shows a simplified layout of the nano-PMC. A number of changes to the original design proposed by Ehara (1996) [21] have been made in order to classify particles having masses down to the zg-range, the most important of which being the much higher rotational speeds it can achieve. In brief, the aerosols sampled by the nano-PMC flow through a 100-mm long channel formed between the inner and outer cylinder, i.e., the classifying region. The aerosol particles traveling along that channel experience a centrifugal force F_{Cn}, which pulls the particles towards the outer cylinder. A counteracting electrostatic force F_{Cb} is exerted on the particles by an electric field established between the two concentric cylinders. As a result, particles within a narrow range of mass-to-charge ratios can traverse the capacitor gap without colliding with and sticking to the walls.

The rotor of the electric motor is attached directly on the cylinders, which rotate around a static central tube. By avoiding using a rotor belt, the number of involved mechanical components of the nano-PMC is minimal, thereby helping to achieve much higher maximum rotational speeds. The motor is directly implemented into the nano-PMC assembly, which contributes to the miniaturization of the instrument. An electromotor (Celeroton, model DC41/25/2) which in principle can accelerate to 80×10^3 rpm within one minute is

used in the prototype introduced in this work. The converter controlling the motor can accurately set rotational speeds at 6×10^3 rpm and higher.

The outer radius of the inner cylinder r_1 and the inner radius of the outer cylinder r_2 of the classification region are respectively 15 and 19 mm. The two cylinders are centrally aligned with two segmented rings (having six 2-mm wide slits) made of polyether ether ketone (PEEK) at their two ends, allowing for a 4-mm gap between them (note that the original APM design by Ehara (1996) [21], had a gap of 1 mm between the cylinders). Use of these rings also resulted in an increased mechanical stability by making the two cylinders rotate as one connected body instead of two. The inner cylinder is mounted on two bearings, which in turn are mounted on the static central tube. The bearings use ceramic spheres to electrically insulate the capacitor from the grounded central tube. The spacing between the inner cylinder and the central tube is sealed with a Teflon sealing lip to ensure that the aerosol flows only through the annular space between the two cylinders.

Due to perpendicular motion of the gas to the rotational axis when exiting the central tube, a pumping effect causing a pressure drop between the inlet and the outlet is created when operating the nano-PMC without flow control. In all experiments described below, the flow rate Q (L/min) through the classifier was fixed to 1.5 L/min by the pump of the particle counter used downstream (cf. Fig. 4 further below), causing a negligible pressure build-up inside of the nano-PMC.

The whole system is encapsulated in an aluminium frame with dimensions 200 mm × 70 mm × 70 mm. At high rotational frequencies, the temperature of the metallic parts inside the nano-PMC can increase over time due to friction. To compensate for this heating effect, the metallic frame has a water cooling system with its inlet and outlet at the motor side. Water cooling was necessary to ensure that temperature is uniform along the aerosol flow channel. During the operation of the nano-PMC, no heating effect on the aerosol flow was observed.

The assembly as well as the individual building parts of the nano-PMC were analysed for resonance frequencies, which could potentially occur at high rotational speeds, using finite element calculations implemented in a CAD software [114].The first resonance of the rotor (i.e., for the combination of the rotor of electric motor and the capacitor) was predicted to occur at 49×10^3 rpm. Due to mass imbalances in the rotating cylinders, vibrations that can lower the lifetime of the bearings as well as increase the risk of damaging the motor also occurred at higher rotational speeds. These mass imbalances were can-

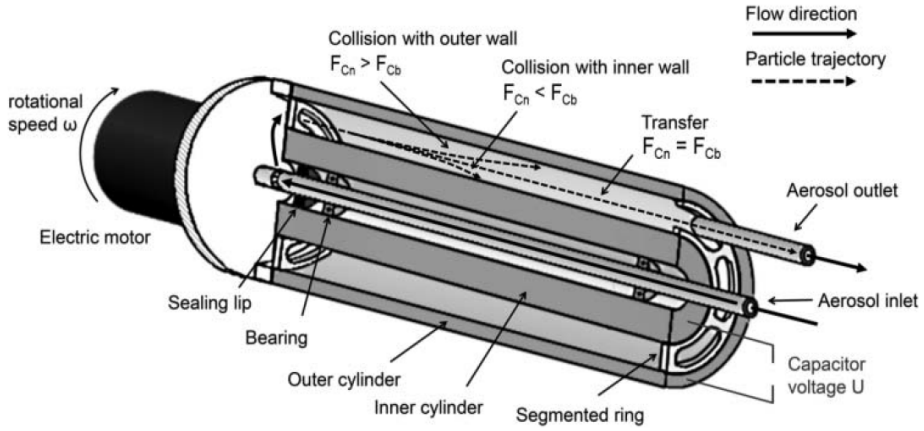

Figure 3.1. Schematic layout of the nano-PMC. The aerosol enters the classifier through the central (static) tube and the classification region through a series of concentrically situated holes. The outer cylinder is connected to the electric motor having rotational speed ω. Particles within a certain mass-to-charge ratio entering the gap through a PEEK segmented ring experience centrifugal and electrostatic forces (F_{Cn} and F_{Cb}, respectively). Particle trajectories are indicated by the dashed lines. The particles can collide with the walls, either on the outer (when $F_{Cn} > F_{Cb}$) or on the inner (when $F_{Cn} < F_{Cb}$) cylinder. If the two forces are balanced (i.e., when $F_{Cn} = F_{Cb}$), the particles exit the cylinder gap. Particles having a specific mass-to-charge ratio exit the classifier through another segmented ring and the outlet tube.

celled out by placing and rearranging screws, whose masses were determined within mg-range accuracy, on the outer cylinder until the vibration amplitude was minimal. For safety reasons, however, the maximum rotational speed of the nano-PMC was set to 36×10^3 rpm which is a factor of 2.5 higher compared to that used in both APM versions and the CPMA.

Four graphite brushes contacted the capacitor (two on the inner and two on the outer cylinder) in order to establish an electrical connection to the power supply, the ground, and the potential meters. The lowest potential difference applied between the two cylinders was 0.1 V, which is just above the amplitude of the noise due to the fluctuations of the contact resistance between the pins and the cylinders induced by mechanical vibrations. The highest potential used in our measurements was 1 kV although the upper limit before reaching the electric breakdown of air was 16 kV.

3.3. Theory

A numerical model was used to calculate the trajectories of particles inside the classifying region and predict the associated transfer function of specific operating conditions. This model was used to describe the response of the nano-PMC.

3.3.1. Classification principle

The nano-PMC uses the same operating principle and a similar geometry as the APM models described by Ehara (1996) [21], Tajima (2011) [22] and Tajima (2013) [111]. The equations of particle motion within the classification region of the nano-PMC can be derived by equating the drag force with the sum of the centrifugal and electrostatic forces acting on the particle, yielding:

$$\frac{M}{\tau}\frac{dr(t)}{dt} = M(2\pi\omega)^2\, r(t) - \frac{keU}{r(t)\, ln\left(\frac{r_2}{r_1}\right)}, \qquad [3.1]$$

$$\frac{M}{\tau}\left[\frac{dr(t)}{dt} - v(r(t))\right] = 0\,, \qquad [3.2]$$

where M (kg) is the mass of the particles, k the number of elementary charges e ($e = 1.602 \times 10^{-19}$C) they carry, τ (s) the relaxation time, ω (rpm) the rotational speed of the nano-PMC, U (V) the potential difference applied between the two concentric electrodes of the classification region and r (m) the radial distance. The axial flow velocity $v(r(t))$ in the gap between the two cylindrical electrodes is described by a parabolic Poiseuille flow profile [95], with a mean value equal to the ratio of the flow rate Q over the cross-sectional area of the classifying region. These equations of motion determine the trajectories of particles in the classifying region.

Particles undergo Brownian motion, which makes them deviate from their deterministic paths along the classification region. Diffusion is described in the model with a stochastic algorithm, analogous to that used for the original APM design [115, 116].

Particles with a certain mass-to-charge ratio do not divert from their original path along the flow streamlines. For these particles, the electrostatic and centrifugal forces are balanced at the force equilibrium radius r_c = 17 mm (i.e., the radial center of the classifying

region), thereby preventing radial migration. In this case, the Stokes drag force is also zero and the particle mass can be determined by equating the centrifugal and electrostatic force, yielding:

$$M_C = \frac{neU}{(2\pi\omega)^2 r_c^2}\left(\ln\left(\frac{r_2}{r_1}\right)\right)^{-1}. \quad [3.3]$$

3.3.2. Response of the nano-PMC

The response of the classifier, expressed as the particle number concentration N (cm^{-3}) at its outlet when charged aerosol particles are passed through, is given by the convolution of the mass distribution of the aerosol at its inlet $n(M) = dN/dM$ with the transfer function of the classifier $\Omega_{nano-PMC}(M)$ [22]:

$$N = \int_0^\infty [n(M)\Omega_{\mathrm{nano-PMC}}(M)]dM. \quad [3.4]$$

The measured response is determined for a set of operating conditions to obtain the response spectrum $N(U, \omega, Q)$.

In all our experiments we employed a DMA upstream the nano-PMC to select particles having electrical mobilities Z within a very narrow range. The specified mobility distribution $n_1(Z) = dZ/dN$ downstream the DMA is given as the product of the mobility distribution of the particles upstream the DMA, $n_0(Z)$ (measured with a Scanning Mobility Particle Sizer), with the transfer function $\Omega_{DMA}(Z)$ of the DMA [93]:

$$n_1(Z) = n_0(Z)\Omega_{\mathrm{DMA}}(Z) \quad [3.5]$$

Assuming that all particles within the narrow mobility band have the same density, the specified mobility distribution can then be converted into the mass distribution $n(M)$ upstream the nano-PMC. For all our calculations we used the DMA transfer function for diffusing particles, using the analytical model provided by Mamakos (2007) [89] and Stolzenburg and McMurry (2008) [88]. Particles were assumed to carry one elementary charge ($k = 1$).

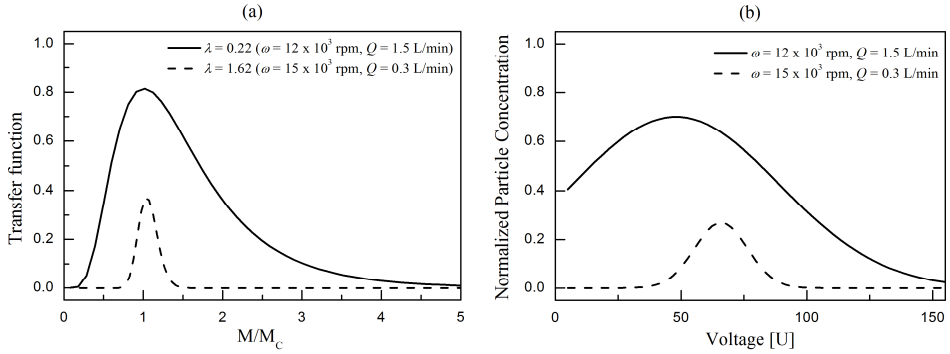

Figure 3.2: Predicted transfer functions of the nano-PMC for different operating conditions and therefore performance parameters $\boldsymbol{\lambda_C}$ (a), and associated response spectra for 50-nm spherical particles of standard density (b).

At given operating conditions U, ω, Q, the trajectories of the particles with mass M that traverse the classifying region can be determined by numerically solving Eqs. 1 and 2. By evaluating the simulated trajectories, $\Omega_{nano-PMC}(M)$ can then be calculated as the ratio of the flux of particles with mass M exiting the classifying region to the particle flux that enters [23]. This ratio peaks for particles with $M = M_C$ that penetrate the classifier with the highest probability when traveling at centreline of the classifying region (i.e., at the radial position r_C). Particles in radial positions other than $r_C$experience force imbalance and therefore travel towards the classifier walls. This effectively lowers the maximum amplitude P of the transfer function, which can be estimated by [22, 111]:

$$P(\lambda_C) = \exp(-\lambda_C). \qquad [3.6]$$

Here λ_C is the classification performance parameter, given by [21]:

$$\lambda_C = \frac{2\,\tau_C\,\omega^2\,L}{\tilde{v}}, \qquad [3.7]$$

TABLE 3.1:
Operational limits for the rotational speed and respective measured mass assuming good classification.

0.3 L/min	ω (rpm)	M_C (ag)
A_1	6.0	30.05×10^{1}
B_1	7.5	3.92×10^{3}
C_1	33.0	1.90×10^{-2}
D_1	36.0	12.50×10^{-1}
1.5 L/min		
A_2	7.5	4.10×10^{3}
B_2	32.0	20.62×10^{1}
C_2	36.0	13.30×10^{-1}
D_2	36.0	11.26×10^{1}

where, L is the length of the classifying region and $\tau_C = M_C C_C / 3\pi\eta d$ is the relaxation time of a particle with diameter d and mass M_C, C_C is the Cunningham correction factor [78], η the dynamic viscosity of the gas and $\tilde{v}$ is the mean flow velocity over the gap. The transfer function of the nano-PMC has a finite width, due to the band of particle masses that traverse the nano-PMC, expressed as the ratio of the peak location M_C to the full base width of the transfer function. This ratio, which is an expression of the classifier resolution, can be estimated by:

$$R(\lambda_C) = \frac{r_c}{4\big((r_2 - r_1)/2\big)} \tanh\left(\frac{\lambda_C}{2}\right), \qquad [3.8]$$

Figure 3.2 (a) shows transfer functions of the nano-PMC, calculated for particles entering and eventually exiting the classifier at $r_c - 1\ \text{mm} \leq r \leq r_c + 1\ \text{mm}$, for different values of λ_C (corresponding to different nano-PMC settings). The shape of the nano-PMC transfer functions is more asymmetric compared to that of the Kanomax APM-3600 due to the larger classifier gap. Figure 3.2 (b) shows predicted response spectra $N(U)$ of the DMA-nano-PMC system, normalized by the total number of particles entering the classifying region N_0, assuming that 50-nm particles with standard density are sampled by the system. As expected, the spectrum calculated for 15×10^3 rpm exhibits a peak at larger voltages than that at 12×10^3 rpm because a stronger electrostatic force is required to balance the forces on the particles. The spectrum with larger λ_C is also reduced in amplitude and width, as a result of the shorter and narrower associated transfer functions.

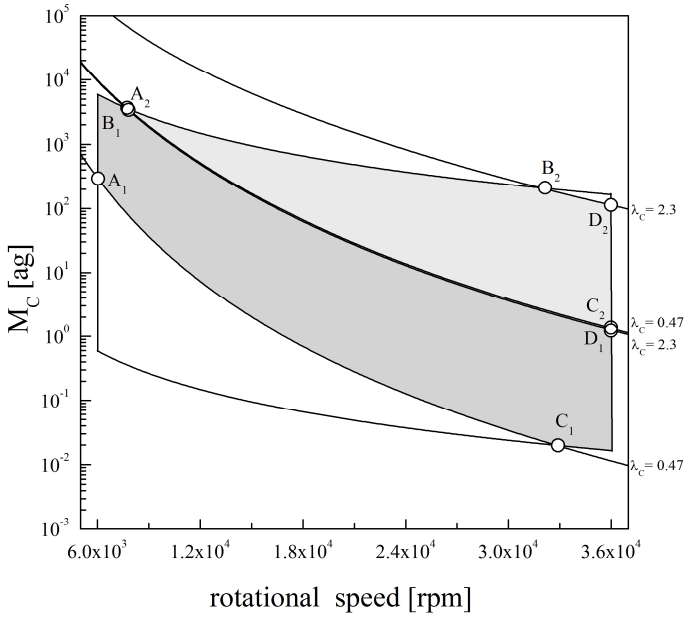

Figure 3.3. Illustration of the operational window in the ω-M_C space (dashed distorted parallelogram) and the masses of the classified particles as a function of rotational speed. The classification performance parameter $\boldsymbol{\lambda_C}$ is held constant at either 0.47 or 2.30 (thick lines). The shaded areas represent regions of the operational window where the nano-PMC exhibits adequate resolution ($R > 0.5$) and penetration ($P > 0.1$) at 0.3 L/min (dark grey) and 1.5 L/min (light grey). Particle masses corresponding to the operational boundaries are marked as points A_1 to D_1 and A_2 to D_2 for 0.3 L/min and 1.5 L/min, respectively, and summarized in Table 3.1.

Considering that the model assumes laminar flow in the classification region, flow disturbances can potentially cause deviations of the real from the predicted response of the system. Lin *et al.* (2014) [117] have already shown that flow recirculation can exist in the Kanomax APM-3600, resulting in reduction of the amplitude and increase of the width of the transfer function due to enhanced diffusional losses [118]. This effect becomes more significant for higher rotational speeds and smaller particles. It can therefore be assumed to significantly affect the performance of the nano-PMC.

Penetration through the nano-PMC is also affected by diffusional deposition on walls of the inlet and outlet channels. These losses, which are not negligible for very small particles, are included in our model (cf. Appendix 3.A for details).

3.3.3. Operational diagram of the nano-PMC

By setting limit values for R and P in Eqs. 6 and 8 one can determine the lower and upper bounds of λ_C, specifying the resolvable mass-range of the nano-PMC. Tajima et al. (2011) proposed that the resolution R of the Kanomax APM-3600 should be 0.5 or greater, while the peak penetration P should be at least 0.1. We chose the same bounds for comparison. Applying Eqs. 6 and 8 yields that λ_C can vary from 0.47 to 2.30.

Figure 3.3 shows the operational diagram of the nano-PMC, similar to those introduced by Tajima (2011) [22] and Tajima (2013) [111]. The dashed distorted parallelogram represents the operational window of the nano-PMC in the ω-M_C space. More specifically, the left and right faces of the dashed parallelogram represent the highest (36×10^3 rpm) and lowest (6×10^3 rpm) rotational speeds, whereas its top and bottom faces represent the operational boundaries of classified particle masses as a function of rotational speed for the lowest (0.1 V) and highest (1000 V) potential difference between the two electrodes. The shaded areas are the regions within the operational boundaries $0.47 < \lambda_C < 2.30$ for Q = 0.3 L/min (dark grey) and Q = 1.5 L/min (light grey). The points A_1 to D_1 and A_2 to D_2 mark the particle masses measured at the operational constraints. Their values are summarized in Table 3.1 and yield the resolvable mass-range. A flow rate of Q = 0.3 L/min offers a much wider range of resolvable masses. Table 3.2 summarizes the operational constraints and resolvable particle-mass range of the nano-PMC for the two different volumetric flow rates studied, in comparison with those of the commercially available Kanomax APM-3600 (cf. Ehara (1996) [21] and Tajima (2011) [22]), the Compact APM [111] and the Cambustion CPMA [23]. Due to the higher rotational speed that can be achieved by the nano-PMC, the instrument exhibits a lower detectable mass limit that is one order of magnitude smaller compared to those of the other devices at a flow rate of 0.3 L/min and one order of magnitude larger at 1.5 L/min. The nano-PMC has a much smaller upper detectable mass range (i.e., in the ag range), limiting its application to particles with diameters smaller than ca. 200 nm and density of 1 g/cm³.

TABLE 3.2
Operational limits of the APM-3600, Compact APM, CPMA and nano-PMC.

Device name	Q (L/min)	ω range (10^3 rpm)	U range (V)	M_C limit (ag)	
				lower	upper
APM-3600	0.3	0.05 – 9.5	0.3 – 2000	0.48	5.9×10^7
Compact APM	0.3	0.5 – 14	0.3 – 2000	0.91	1.2×10^7
CPMA	0.3	0.5 – 12	0.1 – 1000	0.2	1.1×10^7
nano-PMC	0.3	6 – 36	0.1 – 1000	0.02	4×10^3
nano-PMC	1.5	6 – 36	0.1 – 1000	2	4×10^3

3.4. Materials and Methods

Two sets of experiments were conducted. The goal of the first set was to characterize the performance of the nano-PMC using spherical polystyrene-latex (PSL) and ammonium sulphate particles. In the second set of experiments we used the nano-PMC in a tandem configuration with a DMA to determine the dynamic shape factor of cubic sodium chloride particles and the mass-mobility scaling exponent of coalesced and aggregated silver particles. Details of the experimental apparatus are provided in the paragraphs that follow.

3.4.1. Particle generation by atomization

An atomizer (TSI Model 3076) was used to generate particles from aqueous solutions. In all cases, the atomizer was operated by applying a pressure of 2 bar at the nozzle. The resulting droplets were passed through a diffusion dryer system to evaporate the water, decreasing the relative humidity of the aerosol below 15%. To further reduce the water vapour concentration of the aerosol (below 10% RH) ensuring that all particles were solid, the resulting aerosol was mixed with dry air.

Atomization was initially used to disperse PSL spheres and to produces ammonium sulphate or sodium chloride particles from aqueous suspensions. The PSL particles (Polysciences Fluoresbrite YG Microspheres 0.05 μm) were chosen because of their monodispersity, ideal spherical shape and near standard material density (1.05 g/cm^3). In all experiments with PSL spheres we diluted a suspension of 200 μl of the solution provided by the manufacturer in 200 ml Millipore H_2O. The solutions for producing the inorganic salt particles were prepared by dissolving 1 g ammonium sulphate (Fluka-09979) or 2 g sodium chloride (Fluka-71381) in 200 ml Millipore H_2O. These salts were chosen because of

the different particle shapes they yield: sodium chloride particles have a cubic shape, whereas ammonium sulphate particles are spherical.

3.4.2. Particles generated by spark ablation

Silver nanoparticles were generated using a spark dis- charge generator [119, 120]. The generator consists of a high-voltage power supply used to charge a capacitor bank in parallel to a spark gap between two electrodes. For this study we used silver electrodes and pure N_2 (99.9% purity) as the carrier gas. A plasma arc is formed between the two electrodes when the breakdown voltage of the carrier gas is reached. As a result of the high temperature of the spark, silver is evaporated from the tips of the electrodes. The resulting silver vapours then form high-purity primary particles having diameters up to 10 nm that subsequently coagulate to produce polydisperse fractal-like aggregates. In this study, the spark discharge generator was operated with a flow rate of 3 L/min, breakdown voltage of 1.1 kV and spark frequency of 370 Hz. In an additional experiment, the aggregates were coalesced at 850 °C to form nearly spherical particles.

3.4.3. Experimental setup

The experimental setup is shown in Figure 3.4. The generated particles, produced by either an atomizer or a spark discharge generator, were passed through a ^{85}Kr particle neutralizer to set the charge of the particles to an equilibrium Boltzmann distribution. A custom-made DMA, employing a closed-loop recirculation system for the sheath flow and operated at constant voltage, was applied to select particles within a narrow range of electrical mobilities. The particles were then passed through the nano-PMC before being counted by a condensation particle counter (CPC, TSI Model 3775).

To determine the number concentration N_0 we used $U = 0$ and $\omega = 0$ before starting the measurements. The flow rate though the nano-PMC was maintained constant by the pump of the CPC. Initial runs using $Q = 0.3$ L/min and high rotational speeds caused the CPC to fail because the pumping effect of the nano-PMC was too strong for the CPC-pump to compensate, especially at the higher rotational speeds.

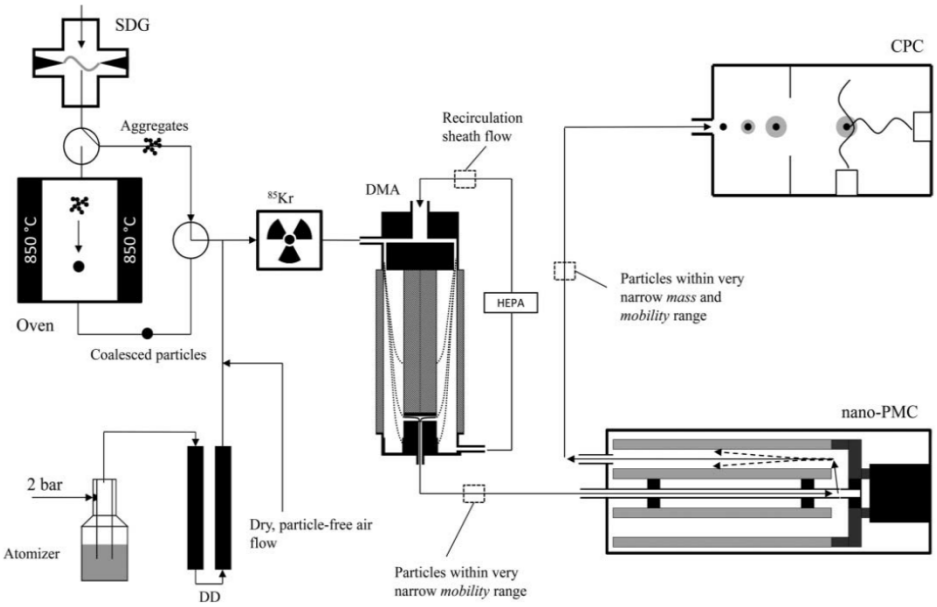

Figure 3.4. Schematic diagram of the experimental setup. Key: SDG: Spark Discharge Generator, DD: Diffusion Dryer, ^{85}Kr: Krypton neutralizer, DMA: Differential Mobility Analyser, CPC: Condensation Particle Counter. Particles are generated with either an atomizer (TSI model 3076) or a spark discharge generator. The aerosol produced by the atomizer is first dried by a diffusion dryer and mixed with dry, particle-free air flow. The particles produced by the SDG are either coalesced by passing them through an oven maintained at 850 °C, or left aggregated. Particles produced by either the atomizer or the SDG are then set to Boltzmann charge distribution by a ^{85}Kr-neutralizer. The polydisperse aerosol is size selected based on their electrical mobility using a DMA employing a recirculation system for the sheath flow. The particles having mobilities within a very narrow range then enter the nano-PMC and the surviving particles within a narrow range of mass are measured with the CPC.

The measured particle number concentrations at the outlet of the nano-PMC were averaged over 15 measurements (one measurement per second) for one respective data point. To obtain the response spectrum, the potential difference was stepwise increased from 0 V up to a maximum value at which the particle concentration was zero again, or the reverse (i.e. from the highest value to 0 V). This procedure was repeated up to 3 times to obtain an averaged response curve.

Particle electrical mobility diameter distributions were determined with a scanning mobility particle sizer (SMPS).

3.4.4. Apparent density, dynamic shape factor and mass-mobility scaling exponent

The tandem DMA-nano-PMC system can be used to measure the mass of particles of a selected mobility. This information can be further used to obtain particle morphology information, which for solid/compact particles can be expressed by a shape factor and for aggregates by a so-called mass-mobility scaling exponent, as described below.

The electrical mobility of aerosol particles depends on their size and shape. For spherical particles, the electrical mobility equivalent diameter d_m is equal to the volume equivalent diameter d_{ve}. In this case, the density of the particles ρ_p can be calculated after measuring their mass with the nano-PMC:

$$\rho_p = \frac{6M}{\pi d_{ve}^3}. \qquad [3.9]$$

For non-spherical particles d_m is different from d_{ve}. Therefore, when using the DMA-nano-PMC system to measure the mass of particles of known d_m, Eq. 3.9 can be used to determine an apparent density as follows:

$$\rho_{ap} = \frac{6M}{\pi d_m^3}. \qquad [3.10]$$

Note that since the DMA transfer function has a finite width, d_m represents the mean mobility diameter of the particles classified by the DMA. An alternative term for the apparent density is the effective density, which is often used as a general term for aggregates [121-123].

Conversion of the electrical mobility equivalent diameter d_m to a volume equivalent diameter d_{ve} can be achieved by knowing the dynamic shape correction factor χ of the particles, according to [124]:

$$\chi = \frac{d_m C_c(d_{ve})}{d_{ve} C_c(d_m)}. \qquad [3.11]$$

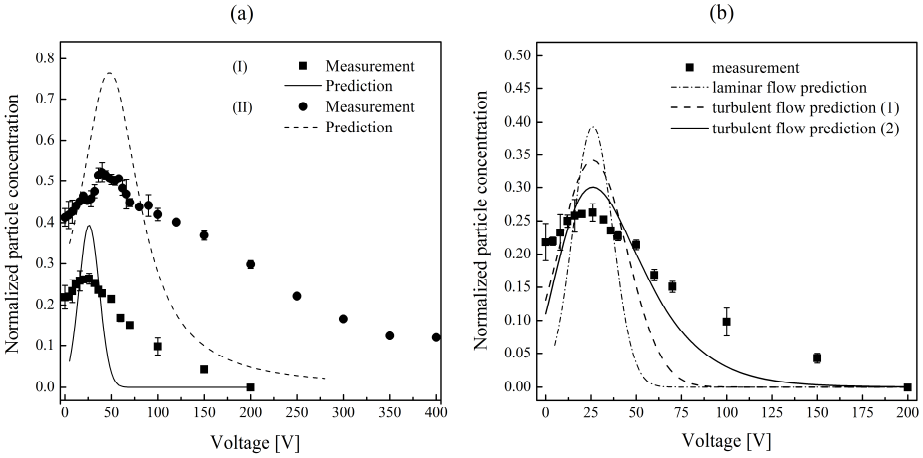

Figure 3.5: Measured response spectra of the nano-PMC operated at (I) $\omega = 9 \times 10^3$ rpm and $Q = 0.3$ L/min and (II) $\omega = 12 \times 10^3$ rpm and $Q = 1.5$ L/min as well as predictions at the same conditions assuming laminar flow (a). Measured response spectrum with the nano-PMC operated at $\omega = 9 \times 10^3$ rpm and $Q = 0.3$ L/min as well as predicted response spectrum were calculated assuming either laminar or turbulent flow with turbulence strength of (1) $v_{rms} = 0.02\ \tilde{v}$ and (2) $v_{rms} = 0.1\ \tilde{v}$ of an uniform flow profile. In all cases the measured response spectra were obtained by passing 50-nm PSL particles through the classifier (b).

Using the tandem DMA-nano-PMC system, d_m can be determined by the settings of the DMA (i.e., flow rate and potential difference between the two electrodes) and d_{ve} from the settings of the nano-PMC (i.e., flow rate, rotational speed and potential difference between the two cylinders), if the composition and therefore the material density of the particles is known. Both diameters can then be input to Eq. 3.11 to determine the shape factor of the particles.

The particle mass and apparent density of aggregated particles has an exponential dependency on the mobility diameter:

$$\mathrm{M} \sim d_m^{\mathrm{D}}\,, \qquad [3.12]$$

$$\rho_{ap} \sim d_m^{\mathrm{D}-3}\,. \qquad [3.13]$$

TABLE 3.3:
Peak voltage, dominant mass, apparent density of the PSL and ammonium sulphate particles, measured with the tandem DMA-nano-PMC system.

	Peak voltage U_C (V)	Particle mass M_C (ag)	Apparent density ρ_{ap} (g/cm³)
PSL 50-nm			
(I)	26 ± 2	68.86 ± 5.21	1.02 ± 0.08
(II)	48 ± 4	71.21 ± 3.11	1.06 ± 0.05
Ammonium sulphate 40-nm			
	45 ± 5	66.82 ± 7.40	1.89 ± 0.21

Here D is the mass-mobility scaling exponent [125, 126], which for aggregates formed via diffusion-limited cluster aggregation (DLCA) in the transition regime is ca. 2.2 ± 0.1 according to Sorensen (2011) [127].

3.5. Results and discussion

In this section we first present the measurements using PSL spheres and ammonium sulphate particles to characterize the nano-PMC, and then compare them with the predictions using the particle-trajectory-based model described above. We then discuss the DMA-nano-PMC measurements and show how they can be used to determine the size-dependent dynamic shape factor of cubic sodium chloride particles as well as the shape and mass-mobility coefficient of coalesced and aggregated silver particles. We also estimated the mass-mobility scaling exponent of the aggregates.

3.5.1. Mass and density measurement of spherical particles

Figure 3.5 (a) compares the normalized response spectra of the nano-PMC (operated at (I) 9×10^3 rpm and 0.3 L/min or at (II) 12×10^3 rpm and 1.5 L/min) using PSL spheres, with predictions. In both cases, the DMA was operated with an aerosol to sheath flow ratio of 0.5 and a potential difference of 544 V to yield particles with a mean electrical mobility diameter of 50.5 nm. The mass distribution of the PSL spheres used in the calculations was determined by assuming that the density of the particles is 1.05 g/cm³. The particle density derived from the measurements (cf. Table 3) is in good agreement with that reported by the manufacturer (i.e., 1.05 g/cm³).

TABLE 3.4:
Dominant mass, apparent density and dynamic shape factor of the NaCl particles measured with the tandem DMA-nano-PMC system.

Diameter d_m (nm)	Rotational speed ω (rpm)	Particle mass M_C (ag)	Apparent Density ρ_{ap}(g/cm³)	Dynamic shape factor χ
14.9 ± 0.3	32 × 10³	2.88 ± 0.32	1.66 ± 0.13	1.18 ± 0.10
25.5 ± 0.4	32 × 10³	15.57 ± 0.94	1.81 ± 0.05	1.13 ± 0.03
60.4 ± 1.2	6 × 10³	237.60 ± 2.40	1.97 ± 0.11	1.03 ± 0.03
80.6 ± 0.6	6 × 10³	475.19 ± 5.94	1.76 ± 0.22	1.13 ± 0.01
119.7 ± 0.4	6 × 10³	1781.97 ± 19.70	2.00 ± 0.12	1.05 ± 0.01

The particle size distribution of the atomized ammonium sulphate particles had a mean electrical mobility diameter of 37 nm and a geometric standard deviation of 1.89. In these measurements, the DMA was operated with an aerosol to sheath flow ratio of 0.15 and a potential difference of 1232 V between the two electrodes, yielding an aerosol with mean particle electrical mobility diameter of 40.7 nm. The dominant masses[5] and apparent densities of the particles determined by these measurements are also summarized in Table 3.3. The latter agrees within experimental uncertainty (< 6%) with the bulk density of ammonium sulphate.

The predicted peak positions of the response spectra match that of the measurements within experimental uncertainty. The measured response spectra, however, are lower and much wider compared to that from the predictions. As discussed in section 3.3.2, the differences between measurements and predictions can be attributed to flow recirculation in the classification region, which can substantially increase particle losses. Due to the complexity of the calculations, we did not simulate directly the turbulent flow in the classification region. To get a crude estimation of the effect of the turbulent flow, however, we used Reynolds decomposition by adding a fluctuating velocity component to the particles' mean velocity [95, 128]. Here, the mean flow velocity profile was assumed to be uniform. The turbulence strength is expressed as the root-mean square of the fluctuations v_i' for the i equi-spaced points in the particle trajectory:

[5] The term 'dominant mass' is not adequately introduced in this chapter. Please view section 2.2.3.1 for its depiction.

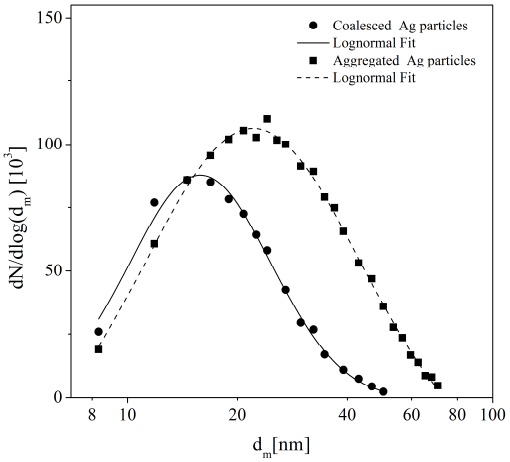

Figure 3.6. Particle size distributions of coalesced and aggregated silver particles generated with the spark discharge generator. The measurements are fitted with lognormal distributions

$$v_{rms} = \sqrt{\frac{1}{N}\sum_{i=1}^{N}\left(v_i'\right)^2}. \qquad [3.14]$$

Figure 3.5 (b) shows a measured response spectrum of the nano-PMC (operated at 9×10^3 rpm and 0.3 L/min) when 50-nm PSL spheres where passed through the classifier, in comparison with predicted spectra assuming either laminar or turbulent flow conditions. In these particular examples, the turbulence strength was considered to be (1) 2% and (2) 10% of the mean velocity $\tilde{v}$, respectively. The stronger the turbulence, the lower and wider the predicted spectrum becomes. The predicted spectrum assuming turbulent strength of 10% of the mean velocity $\tilde{v}$ agrees better with the measurements albeit not perfectly. Nevertheless, this crude calculation supports the hypothesis that turbulent flow can be the reason for the mismatch between the model described in section 3.3.1 and the measurements.

Particle generation by the moving parts within the nano-PMC would also explain the difference between measurements and predictions. Using a filter upstream and measuring the particle number concentration downstream the nano-PMC, however, we observed particles produced by the classifier but at concentrations that were negligible (~10^3 #/cm^3)

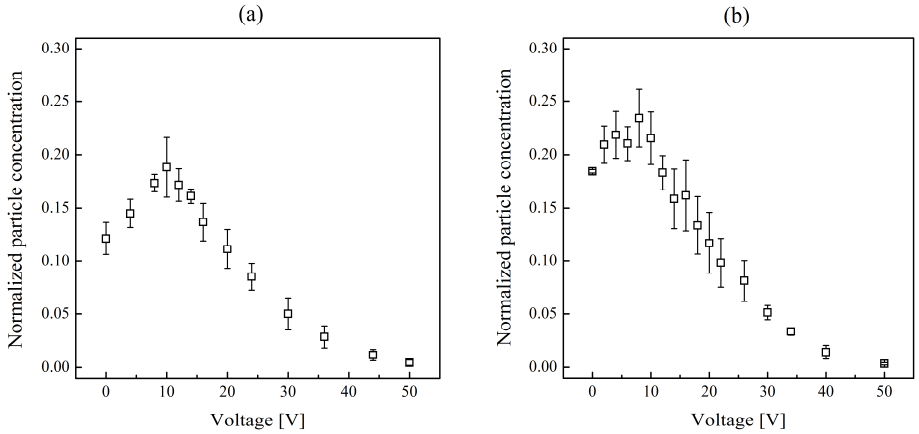

Figure 3.7. Measured response spectra of 10-nm silver spheres (a) and aggregates (b). Both spectra were measured with the nano-PMC operated at 27 × 10^3 rpm and 1.5 L/min.

compared to those of the test aerosols. Particle re-suspension from and bouncing at the walls of the classifying region, which would also explain the differences between measurements and predictions were estimated to be improbable.

3.5.2. Shape factor of sodium chloride particles

The size distribution of the NaCl particles had a mean mobility diameter of 71.4 nm and a geometric standard deviation of 1.82. The total particle number concentration was in the range of 10^7 cm^{-3}. The measured dominant particle masses as well as calculated apparent densities and dynamic shape factors are summarized in Table 3.4.

When assuming that the NaCl particles had spherical shape, the estimated apparent densities were slightly lower than the bulk material density. This difference, however, can be corrected by considering the NaCl particles having cubic shape. The dynamic shape factors (Eq. 3.11) needed to correct for this effect, are also shown in Table 3.4. These were determined after calculating the volume equivalent diameter d_{ve} of spheres using the bulk NaCl density of 2.17 g/cm^3. Interestingly, the dynamic shape factor increased from 1.04 ± 0.03 to 1.19 ± 0.06 with decreasing particle size from ca. 120 to 15 nm. This is in agreement with theoretical predictions [129] and indirect observations [130, 131] that the dynamic shape factor of cubic particles increases with decreasing particle size in the transition and free molecular regime.

TABLE 3.5:
Dominant mass, apparent density and dynamic shape factor of the coalesced silver particles measured with the tandem DMA-nano-PMC system.

Diameter d_m (nm)	Rotational speed ω (rpm)	Particle mass M_C (ag)	Apparent Density ρ_{ap}(g/cm³)	Dynamic shape factor χ
10.0 ± 0.2	27 × 10³	3.51 ± 0.59	5.60 ± 1.12	1.50 ± 0.23
20.5 ± 0.3	18 × 10³	29.04 ± 2.63	6.43 ± 0.59	1.35 ± 0.09
30.5 ± 0.4	12 × 10³	100.98 ± 5.94	6.79 ± 0.40	1.30 ± 0.05

3.5.3. Morphology of silver particles generated by spark ablation

The mean mobility equivalent diameter of the silver particles generated by spark ablation could be controlled by changing the flow rate through the generator. The smallest particles analysed (5 nm) were generated using a flow rate of 8 L/min through the spark generator. The largest particles (50 nm) were generated at a flow rate of 0.3 L/min. Figure 3.6 shows an example of particle size distributions (measured with an SMPS) of silver particles generated with the spark discharge generator using a 3-L/min quenching flow rate. The two size distributions correspond to aerosols with either coalesced particles or aggregates, i.e., when the furnace in front of the DMA was used or not. The mean mobility diameters and geometric standard deviations were 17.0 nm and 1.55 for the coalesced particles and 24.3 and 1.70 for the aggregates.

3.5.4. Spherical silver nanoparticles

Figure 3.7 (a) shows the measured response of the nano-PMC when coalesced 10-nm silver particles were passed through the classifier operated at 27×10^3 rpm. Table 3.5 shows the dominant masses of the coalesced particles having different diameters as determined with the nano-PMC downstream the DMA. The measured values of the apparent density were lower than the material density of silver (10.5 g/cm³). Following the calculations used for sodium chloride particles, the estimated shape factors of the sintered silver particles ranged from 1.32 to 1.52, indicating that the original aggregates were coalesced, but not to spherical particles, when they passed through the oven.

To further investigate the shape of the coalesced particles, fractions with a narrow range of mobilities downstream the DMA were collected by electrophoresis on silicon wafers and analysed using a scanning electron microscope (SEM; Hitachi Model SU8030). Figure

TABLE 3.6:
Dominant particle mass, apparent density and dynamic shape factor of the silver aggregates.

Diameter d_m (nm)	Rotational speed ω (rpm)	Particle mass M_C (ag)	Apparent Density ρ_{ap}(g/cm³)	Dynamic shape factor χ
5.0 ± 0.1	32 × 10³	0.42 ± 0.08	6.41 ± 1.24	1.38 ± 0.21
10.0 ± 0.2	27 × 10³	2.35 ± 0.58	4.48 ± 1.12	1.73 ± 0.23
12.0 ± 0.2	24 × 10³	3.71 ± 0.74	4.15 ± 0.82	1.83 ± 0.28
20.5 ± 0.3	24 × 10³	16.15 ± 1.49	3.58 ± 0.33	1.97 ± 0.12
25.5 ± 0.4	20-24 × 10³	20.50 ± 1.57	2.35 ± 0.35	2.54 ± 0.12
50.5 ± 0.5	6-12 × 10³	81.50 ± 3.63	1.20 ± 0.06	3.64 ± 0.11

3.8 shows an image of a sample with coalesced 30-nm silver particles. The imaged particles exhibited an ellipsoid shape. Electron dispersive X-ray (EDX) spectra on individual particles validated that they consisted of elemental silver without any sign of contamination. Additionally, as demonstrated with the magnified particle, some particles consisted of two or three compacted spheres, corroborating the results obtained with the tandem DMA-nano-PMC system.

3.5.5. Silver aggregates

Figure 3.7 (b) shows the measured response spectrum of the nano-PMC when 10-nm silver aggregates were passed through the classifier. Table 3.6 shows the dominant particle masses, apparent densities and dynamic shape factors of silver aggregates with mobilities within a narrow range, measured using the tandem DMA-nano-PMC system. For particles with a mobility diameter of 25.5 nm and 50.5 nm, response spectra were measured under different rotational frequencies, yielding dominant masses and apparent densities that agreed within experimental uncertainty with each other.

Interestingly, the smallest measured aggregates with a mean electromobility diameter of 5 nm exhibited an apparent density similar to that of the coalesced silver particles, indicating that they were either non-spherical primary silver particles or consisted of a few compacted spheres. The largest aggregates in turn showed an apparent density almost ten times lower than that of bulk silver.

The apparent densities shown in Table 3.6 decreased with increasing mobility diameter as expected. In turn, the dynamic shape factor increased with increasing particle size. A linear model fitted to the double-logarithmic representation of the data yields a mass-

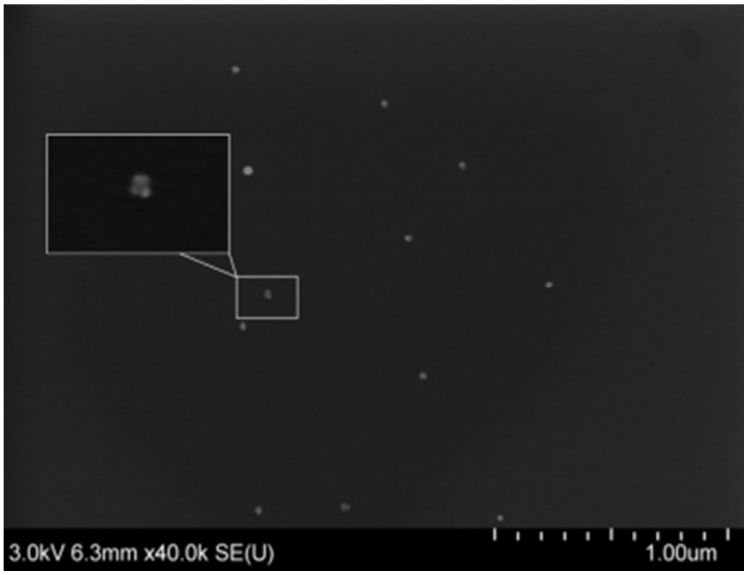

Figure 3.8. SEM images of coalesced silver particles deposited on silicon wafers. The particles were collected downstream the DMA used to select particles with d_m = 30.5 nm.

mobility scaling exponent of $D = 2.3 \pm 0.1$. The apparent density and mass-mobility scaling exponent estimated using our data agree well with recent measurements by Charvet *et al.* (2014) [132] who used a tandem DMA-APM system.

3.6. Conclusions and outlook

The nano-PMC introduced in this paper has the ability to measure particles with masses in the zg range, and it was shown experimentally that it is able to effectively resolve na noparticles having masses down to ca. 0.5 ag. Measured response spectra using spherical PSL and ammonium sulphate particles were compared with predictions by a particle-trajectory-based model. The predicted peak location of the response spectra, which is the defining parameter for determining the dominant particle mass, agreed well with the observations. Deviations of the amplitude and the width between measured and predicted response spectra can be attributed to the enhanced losses due to turbulent flow in the

classification region[6]. Despite that, for both PSL spheres and ammonium sulphate nanoparticles, the measured apparent densities were in agreement with the bulk material density, providing a proof-of-concept for the nano-PMC.

In tandem with a DMA, the nano-PMC system was further used to determine the apparent density and dynamic shape factor of dry NaCl particles. The established value of χ = 1.08 was confirmed for the larger NaCl particles used in our experiments. For smaller particles, the shape factors were substantially higher, corroborating previous theoretical and experimental studies showing that it is size dependent in the transition regime. The DMA-nano-PMC system was also employed to measure the apparent density and to estimate the mass-mobility scaling coefficient of coalesced and aggregated silver nanoparticles, produced by spark ablation. The apparent density of the coalesced particles was lower than that of bulk silver, corroborating SEM observations showing that their shape was slightly non spherical. The mass-mobility scaling exponent of the aggregated particles was $D = 2.3 \pm 0.1$, confirming previous observations.

ACKNOWLEDGEMENTS

We kindly thank Peter McMurry for providing valuable comments and suggestions, and Ulrich Gernert from ZELMI for his help in the SEM analysis. This work was supported by funding from the Deutsche Forschungsgemeinschaft (DFG INST 131/631-1).

[6] This statement refers to the modelling results described in section 3.5.1 and is too conclusive. Since the model was not able to fully match the experimental data, the results can only be interpreted as indications that turbulent flow was responsible for a mismatch of experimental data and simulated spectra.

APPENDIX 3.A: Diffusional wall losses in the nano-PMC

The rate of particles penetrating a tubular channel of length L is given by:

$$\xi = 1 - 5.5\,\phi^{2/3} + 3.77\,\phi, \quad \text{for } \phi < 0.009, \qquad [3.15]$$

$$\xi = 0.819\,e^{-11.5\,\phi} + 0.0975\,e^{-70.1\,\phi}, \quad \text{for } \phi \geq 0.009, \qquad [3.16]$$

where

$$\phi = \frac{\delta\,L}{Q} \qquad [3.17]$$

where δ is the diffusion coefficient of the particles.

Chapter 4: The Cyto-TP

Abstract

We have developed the Cyto-TP, a thermal precipitator capable of depositing airborne nanoparticles onto living cells directly from the gas. A temperature gradient is established between two parallel plates, therefore particles migrate toward the colder plate due to thermophoresis. The colder plate contains two transwells with attached cells forming a monolayer at the air–liquid interface. The front transwell is used for the cell exposure to particles transported into the device and deposited on the cells. Nanoparticles in the size range of 10–300 nm deposit homogeneously on the cell monolayer. All particles are deposited before the rear transwell hence its cells are exposed to the particle-free gas only, allowing for a differentiation between particle and gas effects. The modelling of the deposition of unit-density spherical nanoparticles in the flow channel led to the design and construction of this device. The Cyto-TP was initially tested by depositing fluorescent polystyrene-latex (PSL) nanoparticles on A549 alveolar epithelial cells, a common cell line for inhalation toxicology. The predicted deposition was verified, by the absence of particles on the rear transwell after exposure and in parallel the detection of PSL particles on the front transwell. Additionally, the experimental requirements for the Cyto-TP to function have at the most an insignificant effect on the cells as proven by assaying the living cell count of the transwells after exposure to particle-free air. Consequently, potential cell damages can unambiguously be related to particle and gas exposure.

This chapter has been published as:
D. Broßell, S. Troeller, N. Dziurowitz, Plitzko, G. Linsel, C. Asbach, N. Azong-Wara, H. Fissan, A. Schmidt-Ott (2013): *"A thermal precipitator for the deposition of airborne nanoparticles onto living cells – Rationale and development"*, Journal of Aerosol Science, Volume 63, 75-86

4.1. Introduction

Following the latest considerations for the definition of nanomaterials, they typically consist of particles with at least one geometric dimension below 100 nm, i.e. so-called nanoparticles [133]. As the variety of industrial applications of nanoparticles and hence the production volume increases, concerns rise whether nanoparticles may pose risks to exposed humans, especially at workplaces [134].

As part of a research strategy, the Federal Institute for Occupational Safety and Health (BAuA) focusses among other aspects of occupational hygiene on the identification of health effects, induced by nanoparticle aerosols after inhalation exposure [135]. Inhalation is the most direct and probable way of uptake of airborne nanoparticles [28]. Due to their small size, nanoparticles can reach deep into the lung, deposit in the tracheobronchial or alveolar section of the pulmonary tract and directly interact with the lung tissue and its cells [136].

Common methods to study hazardous effects of aerosols are in vivo studies on animals, like rats and [137, 138]. But concurrently, concerns have risen because of animal welfare and the high costs of such studies. As an alternative, in vitro studies are considered, analyzing the biological response of cell cultures after exposure to nanoparticles. The simplest and commonly used in vitro method consists of exposing submerged cells by suspending nanoparticles in cellular culture media. The cells are exposed to the particles via sedimentation [139]. But apart from the obvious fact that the exposure mode does not represent inhalation exposure, the physico-chemical properties of nanoparticles may be altered when being suspended in liquid, potentially changing the toxicity of the particles [13, 140]. For example, nanoparticles tend to agglomerate in suspensions so that they differ in size, morphology and number concentration, compared to the actual airborne nanoparticles [141]. As a result, there is a need for new and more sophisticated in vitro methods, which focus on the exposure of cells to nanoparticle aerosols [33, 142]. By recognizing the flaws of traditional techniques, in this paper, we shape a clear rationale behind developing an in vitro method, exposing living lung cells to airborne nanoparticles by mimicking the diffusive deposition on cells in the lung.

Consequently, the cells have to be in direct contact with the exposure atmosphere. Therefore, the air–liquid interface technique is selected to cultivate cells [63]. The cells grow adherent on microporous membranes at the air–liquid interface. The setup of a membrane, mounted on a supporting frame, is called transwell. The cells are fed with nutrient

solution through the membrane and are left exposed to the atmosphere on the other side of the membrane.

Several air–liquid interface methods for the cell exposure to potentially harmful substances have been introduced, ranging from devices designed for gas exposure to instruments capable of depositing granulous dust as well as water droplets containing nanopowders [65, 143]. When applied to dry nanoparticle aerosols, however, exposure with those instruments is typically limited by the low deposition rate when depending on diffusive transport. An additional force is needed to precipitate the nanoparticles toward the cells. Recently, air–liquid interface instruments using electrostatic precipitation have been developed, for the deposition of charged particles onto cells [35, 144]. However, the charge of the particles can influence the cellular action. It has been shown that the surface charge of gold nanoparticles mediates [145]. Additionally, several studies have shown that the cellular uptake of charged nanoparticles differs from their neutral counterparts because of different charge levels [146].

A mechanism, directly influencing the path of the diffusive transport of a nanoparticle in gas phase, is thermodiffusion. Also called thermophoresis, it is the forced orientation of the diffusive motion in the presence of a temperature gradient toward the cold source. Since thermophoresis and diffusion both stem from particle interactions with surrounding gas molecules undergoing Brownian motion, the resulting thermophoretic and diffusional velocities are very similar and hence thermophoresis is a suitable mechanism to mimic the diffusional deposition in the lung. It is not required to manipulate the physico-chemical properties of the aerosol, like size or charge distribution for thermophoretic precipitation. Devices capable of establishing a temperature gradient in the flow channel and depositing nanoparticles with the help of thermophoresis are called thermal precipitators. Recent developments typically consist of two parallel metal plates with a uniform temperature gradient in-between [147-149]. In a thermal precipitator, nanoparticles therefore deposit onto the colder plate. Another advantage of using thermophoresis is its size independency in the nanoparticle size range. Therefore, size fractionation does not occur in the deposition of nanoparticle aerosols.

We designed and constructed an advanced model of a parallel plate thermal precipitator, customized for the exposure of cells to nanoparticles, the so-called Cyto-TP. It contains two transwells with cells, one for the deposition of particles, whereas the second one gets exposed to the identical, but particle-free atmosphere for control purposes.

In this work, we show how the application of the rationale mentioned above led to the concept of the Cyto-TP, the implementation of the air–liquid interface method into a parallel plate thermal precipitator. The calculation of the trajectories of spherical nanoparticles in the Cyto-TP yields the optimal positions of the transwells and therefore the dimensions of the flow channel. These preliminary considerations led to the design and realization of the Cyto-TP pre-prototype. To prove the concept, the new device was utilized in a set of experiments, where the cells were exposed to fluorescent particles, chosen to resemble the particles used in the calculation of trajectories. Additionally, zero exposure experiments were conducted to test, whether the cells are affected by the experimental conditions and the device itself.

4.2. Thermal precipitator for cell exposure to nanoparticles: Cyto-TP

The basic elements of the Cyto-TP are two metal plates, placed in parallel and with a certain distance a to each other, with a uniform temperature gradient ∇T over a. The plates form a flow channel for the aerosol, transported into the device with a flow rate Q. The particles settle on the cold plate. Temperature gradient and flow rate can be adjusted. The transwells are implemented in the top plate, which is intended to be the cold plate.

The concept of the Cyto-TP is shown in Figure 4.1. The top plate contains two transwells, one in the front and the other in the rear. A temperature gradient can be established from the top to the bottom plate, by adjusting the plate temperatures. The particles move with the air flow into the flow channel. If the thermophoresis is greater than the counter-directed gravitation, the particles move perpendicular to the air flow direction toward the cold plate. The concept foresees that all particles deposit in the region of the front transwell. Consequently, the rear transwell gets exposed to the same but particle-free atmosphere and hence helps to distinguish between gas and particle induced effects. For the design of the Cyto-TP, a nanoparticle size range of $d_p = 10 - 300$ nm is considered, since thermophoresis is size independent for these particle sizes.

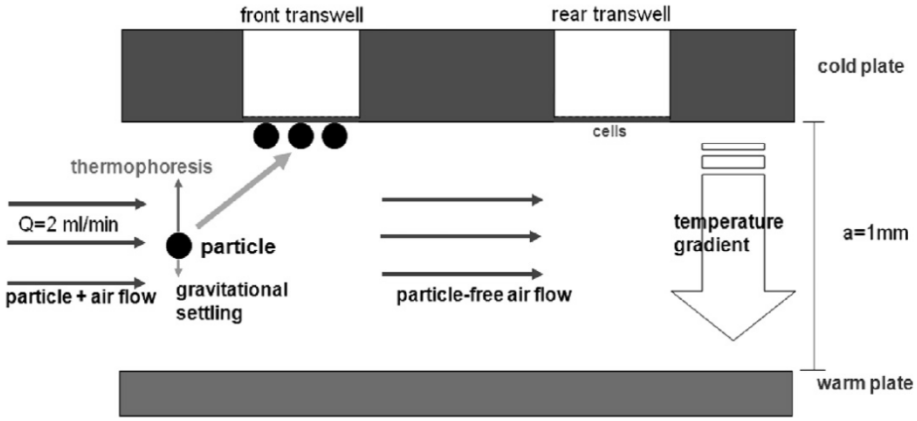

Figure 4.1: Sketch of the concept of the Cyto-TP

The basic design of the Cyto-TP is based on a personal, parallel plate thermal precipitator for nanoparticle sampling [147, 148]. This thermal precipitator consists of two parallel plates placed at a distance of a =1 mm to each other. The temperature of the plates can be adjusted to create a uniform temperature gradient from the cold to the warm plate in the range of $\nabla T = 3 - 20$ K/mm. A silicon wafer serves as the cold plate, which can be removed to be analyzed with electron microscopy, after collecting nanoparticle samples from the air with a flow rate of $Q = 2$ ml/min. Due to the largely size-independent thermophoretic particle velocity, the particles are homogenously deposited on the substrate, which significantly simplifies the data evaluation.

The exact plate distance a and flow rate Q is adapted for the Cyto-TP as well as the range of the temperature gradient ∇T. The flow channel has to be long enough to allow the deposition of all particles in the area before the rear transwell. The optimal dimensions of the flow channel as well as the exact position of the transwells were found by evaluating the deposition profiles of the particles on the cold plate of the Cyto-TP. The deposition profiles were obtained by calculating the exact settling positions of the particles on the cold plate, from the trajectories of the particles in the flow channel, considering the thermophoretic and gravitational motion as well as the convective motion with the flow.

4.2.1. Thermophoretic velocity of spherical nanoparticles

The thermophoretic force results from the inhomogeneous transfer of momentum, caused by collisions of gas molecules with the particle surface in a temperature gradient. Since the gas molecules in warmer regions have higher kinetic energy than in colder regions, the collisions on the surface facing the heat source transfer a greater momentum compared to the opposite side. Consequently, the interaction of the gas molecules with the particle results in a net motion of the particle in a temperature gradient from the warm to the cold region [150].

For the particle size range of $d_p = 10$ nm to $d_p = 300$ nm, two cases for the description of the thermophoretic motion have to be considered: particles with particle sizes $d_p < \lambda$ and particles with $d_p > \lambda$, where λ is the mean free path of gas molecules ($\lambda \approx 66$ nm for air at standard pressure) [17]. In this paper, we focus on the simple case of single unit density sphere.

For $d_p < \lambda$, the resulting thermophoretic velocity for spherical particles is:

$$v_{th} = -\frac{0.55\eta\nabla T}{\rho_g T}, \text{for } d_p < \lambda \qquad [4.1]$$

where T is the ambient temperature, ∇T the temperature gradient, η the kinematic gas viscosity and ρ_g the gas density at room temperature. The movement is in the direction of decreasing temperature. The thermophoretic velocity in Eq. 4.1 is independent of particle size d_p, since thermophoresis and the counterdirected drag force have the same size dependency.

For $d_p > \lambda$, the particle establishes an internal temperature gradient, which affects the surrounding gas temperature and hence the temperature gradient near the particle. This effect depends on the particle size and the ratio of the thermal conductivity of the surrounding gas k_g and the particlek_p. This results in the definition of the coefficient H [104]:

$$H = \left(\frac{1}{1 + 6\,\frac{\lambda}{d_p}}\right)\left(\frac{\frac{k_g}{k_p} + 4.4\,\frac{\lambda}{d_p}}{1 + 2\frac{k_g}{k_p} + 8.8\frac{\lambda}{d_p}}\right) \qquad [4.2]$$

Also, for particle sizes near the mean free path of the gas molecules, the Cunningham slip has to be taken into account, with the correction factor

$$C_c = 1 + \frac{\lambda}{d_p}\left(A + Be^{-C\frac{\lambda}{d_p}}\right) \quad [4.3]$$

with $A = 2.34,\ B = 1.05$ and $C = 0.39$ for solid particles [78]. The resulting thermophoretic velocity for particles with $d_p > \lambda$ is

$$v_{th} = \frac{3\eta C_c H \nabla T}{2\rho_g T}, \text{ for } d_p > \lambda \quad [4.4]$$

Contrary to the $d_p < \lambda$ case, the thermophoretic velocity becomes size dependent and decreases with larger particle sizes. However, in ambient air and for unit thermal conductivity spheres with a diameter $d_p = 300$ nm, the thermophoretic velocity calculated with Eq. 4.4 is only 10% smaller than the thermophoretic velocity for $d_p < \lambda$ calculated with Eq. 4.1 In this paper, we therefore assume that the size independent thermophoretic velocity defined in Eq. 4.1 is applicable for all particle sizes.

4.2.2. Effect of gravitation on nanoparticles

In the Cyto-TP, gravitation is counter-directed to thermophoresis. The gravitational velocity v_g depends on the particle size and particle density ρ_p

$$v_g = \frac{d_p^2 \rho_g g}{18\eta} \quad [4.5]$$

where g is the gravitational acceleration [17].

4.2.3. Flow profile in a rectangular flow channel

Apart from the forces affecting the velocity of the particles perpendicular to the flow, the flow velocity profile in the channel has to be known to calculate the exact trajectory of transported particles. No acceleration of the particles in the flow direction occurs, therefore the particles do have the same velocity as the flow.

The width of the flow channel of the Cyto-TP is specified to be b = 15 mm, much larger than the height a = 1 mm. Therefore, the flow velocity profile can be approximated by

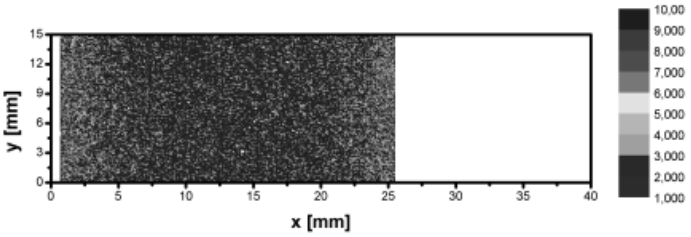

Figure 4.2: Calculated deposition density profile for ∇T=3K/mm and *Q*=2 ml/min

modelling a plane Poiseuille flow [95] the hyperbolic flow pattern between two parallel plates. For flow rates in the magnitude of 1 ml/min, the flow is laminar. Boundary effects near the inlet as well as in the corners are neglected.

In Cartesian coordinates, with the origin of ordinates at the center of the inlet, the flow velocity $v_x(z)$ depends on the position z relative to the height a of the flow channel

$$v_x(z) = \frac{6Q}{ba}\left(\left(\frac{z}{a}\right) - \left(\frac{z}{a}\right)^2\right) \qquad [4.6]$$

The flow velocity in the center is 1.5 $\tilde{v}_x$, where $\tilde{v}_x$ is the mean flow velocity. Since the flow is laminar, the flow velocity at the edges is zero. Consequently, as the particles approach the cold plate due to thermophoresis, they also slow down at the same time in the flow direction.

4.2.4. Calculation of particle trajectories and deposition density profiles in the Cyto-TP

With all velocity components determined, the particle trajectories can now be calculated. The terminal velocity $\boldsymbol{v_z}$ of the particles perpendicular to the flow velocity $\boldsymbol{v_x}$ is

$$v_z = (v_{th} + v_g)e_z \qquad [4.7]$$

where $\boldsymbol{e}$ is the unit vector (here, in the z-direction). The trajectory is then calculated for the particle entering the flow channel at height z_0 and width y_0 at the inlet. It is assumed that no forces influence the particles trajectory in the direction of y. A simple, parameterized, ballistic equation of motion is used

$$\mathrm{y}(t) = y_0 e_y \quad [4.8]$$

$$\mathrm{z}(t) = (z_0 - v_z t) e_z \quad [4.9]$$

$$\mathrm{x}(t) = \big(v_x\big(z(t)\big)t\big) e_x \quad [4.10]$$

where t is the time after entering the flow channel. For the x-component of the trajectory, first the location of the particle in the z-direction has to be known.

A custom Wolfram Mathematica script was compiled to calculate deposition density profiles of nanoparticles on the cold plate. To obtain a sophisticated profile, a large number of virtual, monodisperse and spherical particles were generated. At $t = 0$, the particles are distributed homogenously across the cross-section of the inlet, allotting y_0 and z_0 to each particle. Subsequently, the trajectories of all particles were calculated. The script counts all particles deposited in a definite number of small squares of 100 µm × 100 µm dividing the deposition area into a total of 6×10^4 squares. The deposition density therefore is the number of deposited particles in each square over the deposition area.

Figure 4.2 shows the contour plot of the deposition density in the flow channel for 100000 unit density spherical 100 nm particles. The profile is computed for the minimum temperature gradient of the Cyto-TP, $\nabla T = 3$ K/mm with flow rate $Q = 2$ ml/min.

The profile shows that all particles deposit within the first 25 mm in the flow channel. The increased particle deposition density at the beginning and the end of the profile can be explained by the hyperbolic flow profile. The second transwell is chosen to be located behind the end of the deposition area. The Cyto-TP uses Corning 3470 clear transwells. The membranes of these transwells have a diameter of 6.5 mm. Accordingly, the center of the front transwell is located at x = 6.5 mm from the inlet, so that its membrane is located in the deposition area. The center of the rear transwell is located at x = 33.5 mm from the inlet. Both transwells are centered in the y-direction, i.e. y = 7.5 mm. As a result of the simulation, a length of the flow channel of c = 40 mm was considered for the design of the Cyto-TP.

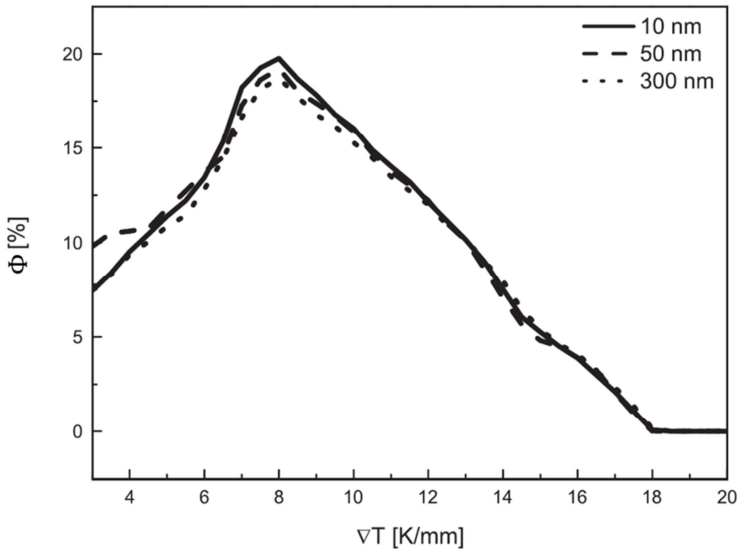

Figure 4.3. Calculated deposition efficiency ϕ for some nanoparticle diameters in the Cyto-TP size range in dependence of the temperature gradient.

4.2.5. Simulated deposition efficiency of the Cyto-TP

The Mathematica script counts all particles, deposited on the membrane of the front and rear transwells. Therefore, the script defines the membranes as circular areas with equal diameters (6.5 mm) and centers, located at the same distance (6.5 mm and 33.5 mm) from the inlet. The particle count $N_{transwell}$ in the considered area is put in relation to the total number N_{total} of particles deposited on the cold plate to yield the deposition efficiency Ω:

$$\phi = \frac{N_{transwell}}{N_{total}} \qquad [4.11]$$

Figure 4.3 shows the calculated deposition efficiency ϕ for different diameters of spherical nanoparticles on the front transwell for temperature gradients in the range of $\nabla T = 3–20$ K/mm and a flow rate of $Q = 2$ ml/min. Following the simulation results, the maximum efficiency, roughly 17–20% for the front transwell was found for 8 K/mm. The results yield an optimal temperature gradient at 8 K/mm with a flow rate of 2 ml/min, to

attain the maximum deposition efficiency in the area of the front transwell for a wide range of particle diameters d_p. Results for the rear transwell show no deposition.

The simulation also indicates that within the considered size range particle size has little influence on the deposition efficiency. This is to be expected, since thermophoresis is size independent. Small differences appear, due to gravitation, but for particles in the considered size range, it is in orders of magnitude smaller than the thermophoretic force. No particles deposit on the rear transwell for temperature gradients higher than 5 K/mm.

4.3. Air–liquid interface setup

4.3.1. Lung cell line and culture conditions

Pulmonary alveoli are anatomic structures of the lower respiratory tract, responsible for the exchange of gas between the blood and alveolar air and are potential targets of inhaled contaminants, e.g. nanoparticles. Histologically, the alveolus surface contains epithelial cells attached to the basal membrane. A layer of surfactants covers the cells. Additionally, alveolar macrophages are present to remove contaminants like dust particles.

The A549 cell line, human lung adenocarcinoma/type II alveolar epithelial cells (DSMZ, No. ACC-107), is widely used to represent the epithelial cells of the pulmonary alveolus [151]. The cells are cultured in Dulbecco's modified Eagle's medium (DMEM) supplement with 10 v/v% fetal calve serum (FCS), 5 µg/mL gentamicin in a humidified incubator at 37 °C with 5% CO_2. When a confluency of 85% is reached, the cells are subcultured.

4.3.2. Transwells

The cells are grown on Costar 3470 clear transwells (24 well, 0.6 cm membrane diameter), polystyrene frames supporting microporous membranes composed of polyethylene terephthalate (PET) with pore diameters of 0.4 µm. The usual application of transwells is adapted, because the cells need to attach and grow on the side of the membrane, counterfacing the inside of the transwell to allow the alignment of the cells with the cold plate. Figure 4.4 shows the usual setup of a transwell with cells and nutrient solution and the adaptation for the Cyto-TP.

After conditioning the transwells in nutrient solution, DMEM with fetal calf serum (FCS), in a companion plate, the transwells were taken out of the solution and turned upside

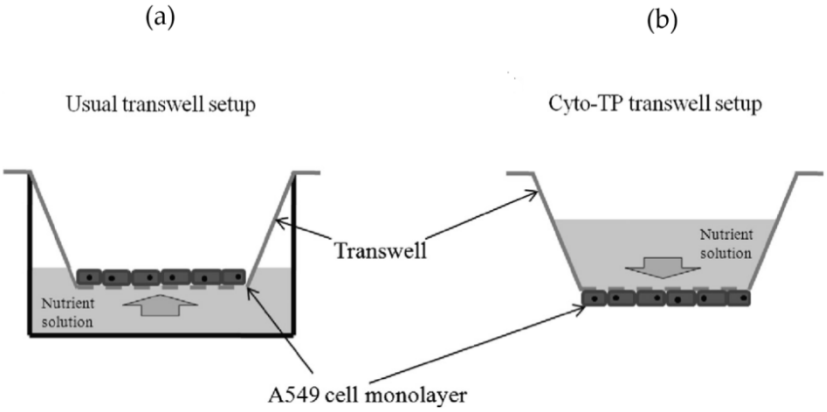

Fig. 4.4. (a) Usual setup of transwell with A549 cells inside the transwell. (b) Adapted Cyto-TP setup of transwell with nutrient solution inside the transwell and A549 cells on the counterface of the membrane.

down with the transwell membrane facing up. A drop of cell suspension (50 µl with $(2.5 \pm 0.2) \times 10^5$ cells/ml) was placed on the membrane, meaning that (9500 ± 600) cells/cm^2 were seeded. The transwell was stored in a humidified incubation chamber for 1 h for cell adhesion. Afterwards, the transwell was put back to the companion plate for 72 h, where the cells grew submerged to about 95% confluency. Then, 24 h before exposure, FCS was withdrawn from the nutrient solution and the cells were set at air–liquid interface conditions, meaning that the companion plate was put in a dry incubation chamber as well as the cells were supplied with nutrient solution only through the membrane from inside the transwell. The transwell membrane was carpeted with cells with a density of approximately 8×10^5 cells/cm^2 at the end of the growth cycle.

4.4. Prototype

The Cyto-TP pre-prototype consisted of three main assembly parts which will be described in detail: bottom plate, top plate with transwell fittings, and plate separator with inlet and outlet. The main parts and the whole device are presented in Figure 4.5 extracted from the CAD model. They are held together with screws and can easily be disassembled for cleaning.

The bottom plate is connected to a Peltier element, semi-conductive elements that create an internal temperature gradient between its two sides, if current runs through. The average temperature of the Peltier element remains at room temperature, hence one side gets cold and the other side hot. The warm side of the element is attached to a gold-coated copper plate with thermally conductive glue. A thermocouple is placed inside the warm copper block to measure its temperature. The bottom plate is connected to a Peltier element, semi-conductive elements that create an internal temperature gradient between its two sides, if current runs through. The average temperature of the Peltier element remains at room temperature, hence one side gets cold and the other side hot. The warm side of the element is attached to a gold-coated copper plate with thermally conductive glue. A thermocouple is placed inside the warm copper block to measure its temperature. The second part is the top plate, which functions as the cold plate. It consists of a gold-coated copper block with two inserts for the transwells. The temperature is controlled with two ring-shaped Peltier elements, to fit around the inserts. The copper block is attached to the cold side of the ring-shaped Peltier elements to cool down the cold plate. Two K-type thermocouples are placed into the copper block, one at the front insert and the other at the rear insert to measure the temperatures at both transwells separately.

The Peltier element sides, not facing the flow channel, are both connected to metal sheets with serrated wings for heat transfer. The sheets and the plates are thermally isolated with polyether ether ketone (PEEK) frames.

The bottom and top plates are separated and thermally insulated with another PEEK frame, the third part. As mentioned earlier, the distance between the warm and cold copper plates is 1 mm so that a rectangular flow channel is formed with two walls from the PEEK frame, an inlet at the front and an outlet at the rear. The flow channel is 40 mm long and 15 mm wide. The holes for the insertion of the transwells are milled into the copper block, 6.5 mm and 33.5 mm in distance from the inlet and in the center of the flow channel.

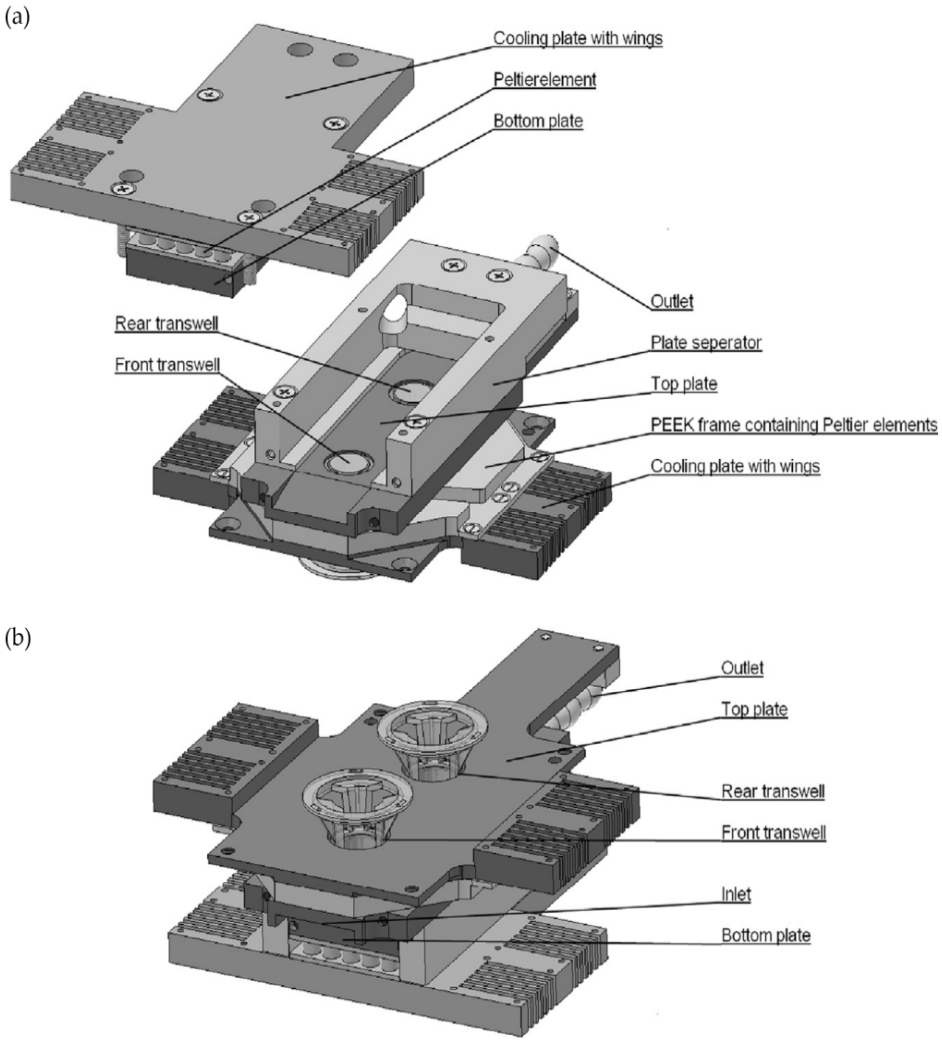

Figure 4.5. (a) Upside down view of the disassembled Cyto-TP and (b) assembled Cyto-TP.

4.5. Materials and Methods

The experimental work presented in this paper focused primarily on the proof-of-concept of the Cyto-TP. This was accomplished firstly with the qualitative verification of the predicted deposition of 100 nm unit density spheres on the front transwell and no deposition on the rear transwell. Fluorescent 100 nm polystyrene-latex particles were deposited on cells with the Cyto-TP, which can be detected via fluorescence microscopy. Secondly the effect of the Cyto-TP itself on the cells was examined by assaying the living cell count of the transwells after exposure to particle-free air.

4.5.1. Fluorescent 100 nm polystyrene-latex (PSL) particles and aerosol generation

Polystyrene-latex (PSL) spheres with an embedded fluorescent dye, Polysciences Fluoresbrite microspheres, were deposited on the cells with the Cyto-TP. The material properties, stated by the manufacturer, describe spherical particles with a diameter of $d_p = 100\,\text{nm}$, a geometric standard deviation of $\sigma_g = 1.04$ and a particle density of $\rho_g = 1.05\,\text{g/cm}^3$. The particles are stabilized in aqueous suspension by the manufacturer to avoid massive agglomeration, with a concentration of 4.55×10^{13} particles/ml. The PSL microspheres closely resembled the virtual, monodisperse, spherical particles used in the simulation.

The PSL microspheres suspension was diluted with ultrapure water, sonicated for 15 min and dispersed with an atomizer (TSI model 3079). This aerosol generator was chosen for its stable output particle number concentration. It disperses droplets with nanoparticles as seeds. The droplets evaporate in a diffusion dryer and the nanoparticles are left as aerosols. Since the suspension was stabilized, it is assumed that only one or no particle was present in each dispersed droplet. The atomizer emissions after the diffusion dryer should therefore consist mostly of single PSL sphere.

4.5.2. Experimental setup

The setup is shown in Figure 4.6. The aerosol, generated with the combination of atomizer and diffusion dryer, was led into the exposure chamber, a sealed chamber with a volume of 6 l. A baffle plate was placed directly in front of the aerosol inlet to distribute the aerosol homogenously in the chamber. The chamber had two outlets, one for the aerosol characterization instruments and the other to relieve the pressure. The chamber itself was

placed inside a laminar flowbox to allow clean handling of the Cyto-TP and samples as well as for protection from nanoparticle emissions. All ubiquitous particles and chamber emissions were removed by the filter of the flowbox. The aerosol was pumped from outside into the chamber. This setup allowed a quick exchange of transwells after exposure, by just opening the exposure chamber, removing the used transwells and exchanging them with fresh transwells, without contaminating the samples. A Thomafluid RCT-type high precision pump for low flow rates connected through the exposure chamber wall to the Cyto-TP. The Cyto-TP could be left in the chamber during the sample exchange, fully connected, and does not need to be removed in the process.

the electronic circuit, measuring and controlling the temperatures by changing the currents for the Peltier elements, connected through the chamber walls to the Cyto-TP. The measured temperatures were transferred using a datamodule to a computer with a custom LabVIEW software for this experiment. The LabVIEW software controlled the temperatures of the Cyto-TP plates, by adjusting the currents of the Peltier elements according to the measured temperature changes. The currents were generated using a multichannel current generator.

A scanning mobility particle sizer (SMPS) consisting of a Vienna-type differential mobility analyser (DMA) and a condensation particle counter (Model 5403 CPC) by GRIMM Aerosol Inc. were used to measure the particle size distribution of the aerosol in the chamber in a size range of 10 – 1000 nm. An SMPS measures particle number size distributions based on the electrical mobility diameter, which in case of spherical particles equal their geometric diameter [17].

4.5.3. Exposure of A549 cells using the Cyto-TP

The Cyto-TP was set to a temperature gradient of 8 K/mm, by adjusting the temperature of the bottom (warm) plate around 45 °C, whereas the cold plate was maintained at a temperature of 37 °C, optimal for the cells. The aerosol was led into the chamber and distributed homogenously. Both plate temperatures reached the preset values in 10 min, establishing the desired temperature gradient. Two transwells with A549 cells were gently put into the intended inserts of the Cyto-TP. The low flow rate pump for the Cyto-TP is switched on with a flow rate set at $Q = 2$ ml/min, to start the exposure of the cells to the aerosol. The exposure time was 1 h. The particle number concentration of the aerosol in the chamber as well as the temperatures of the Cyto-TP was monitored during the exposure time. After the exposure, the transwells were gently taken out of the Cyto-TP.

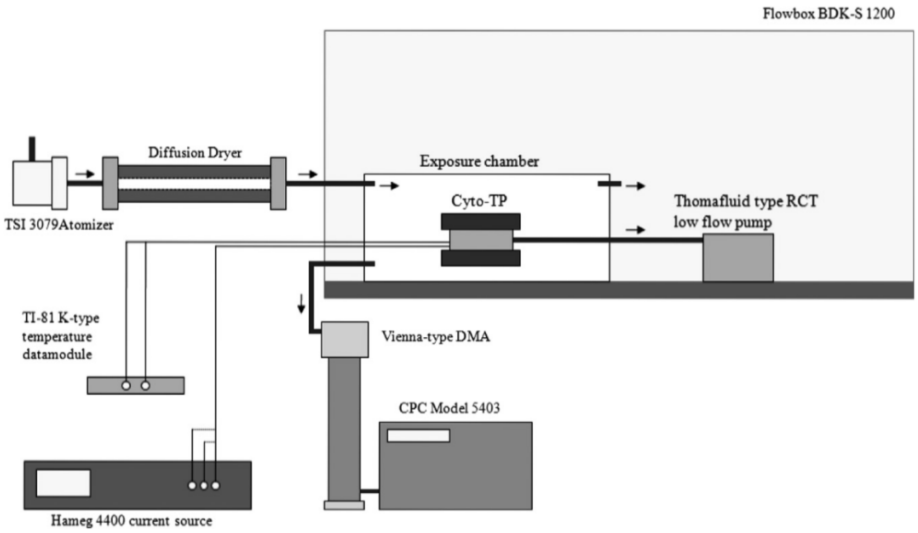

Figure 4.6. Schematic of the Cyto-TP control setup, aerosol generation and characterization.

Zero exposure experiments were conducted. Zero exposure means the exposure of cells to particle-free air, filtered inside the flow box. The particle number concentration as well as the temperature and humidity of the air is monitored over the whole exposure duration.

After the exposure, the cells were analyzed either with fluorescence microscopy for particle detection or with a living cell count assay for effects on the viability of the cells of the transwells.

4.5.4. Detection of fluorescent 100 nm PSL particles with fluorescence microscopy

After an experiment, the transwells were removed from the Cyto-TP and immediately prepared to be put under the fluorescent microscope. The PSL microspheres fluorize after excitation using a laser with 441 nm wavelength. The emissions can be detected using a 486 nm bandpass filter. A Leica DMIRB fluorescence microscope was used to detect the deposited 100 nm PSL particles for qualitative evaluation.

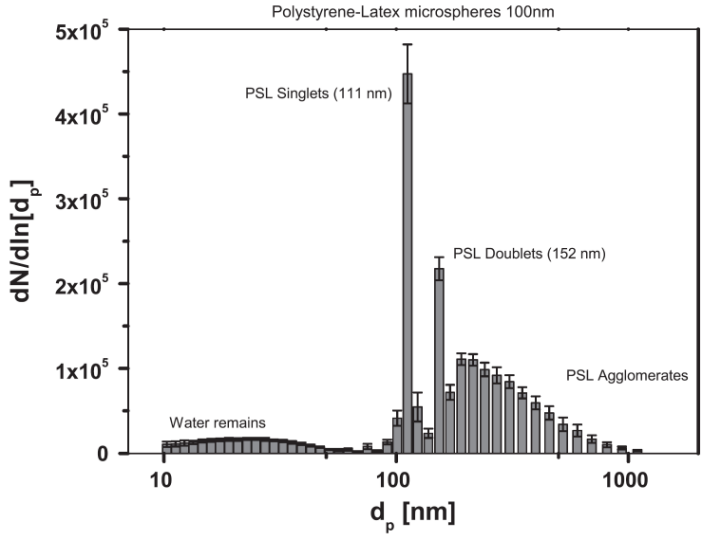

Figure 4.7. Size distribution of 100 nm PSL particles 0.1 μm, measured with the SMPS. Arithmetic mean values from 20 measurements.

4.5.5. Living cell count assay

The cell viability assay was conducted with the CASY cell counting technology. It is capable of counting resuspended single cell and distinguishing living and dead cells. The identification of living cells exploits the fact that cells with an intact membrane are insulators, contrary to ones with destroyed membranes. Cells are harvested from the transwell membrane by trypsination and resuspended in an electrolyte. The suspension is sucked through a capillary with two electrodes. Every passing cell is identified by a peak in resistance, where the magnitude of each peak depends on the cell volume. The measurement results in a resistance distribution which is translated into the cell size distribution. The integral over a defined range of size channels yields the total cell count T_{cc}. The living cell count L_{cc} is determined by the cell count down to a limit size defined for the specific cell line. The ratio of the living and total cell count is called cell viability, typically expressed in percentage.

For all exposure experiments, a third transwell is left in the incubation chamber during the exposure, at the air–liquid interface. Besides having the rear transwell for control of

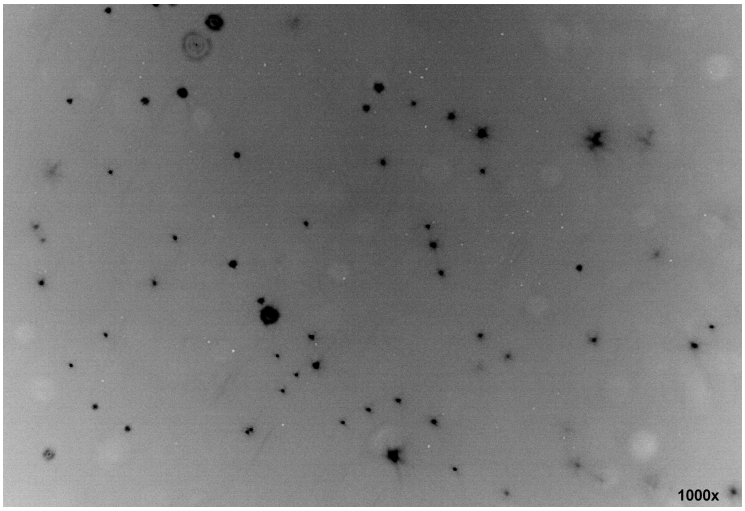

Figure 4.8. Micrograph of deposited 100 nm PSL particles with a particle number concentration of 85000±2000/cm3 on the front transwell. The image shows particles on cells directly after exposure. Some particles are out of focus since the cell surface is uneven. The cells itself are not visible.

effects of deposited nanoparticles, the transwell in the incubator functions as the control for potential additional effects which may be caused by the Cyto-TP itself, e.g. because of heat radiation.

4.6. Results and Discussion

To prove the concept of the Cyto-TP, two different aspects of the concept were tested (a) the general ability of the Cyto-TP to deposit particles onto living cells and (b) potential effects of the Cyto-TP itself on the living cell count of the transwells.

4.6.1. Aerosol generation

Stabilized PSL suspension (400µl) was diluted with ultrapure water (40 ml) and dispersed using the atomizer. Figure 4.7 shows the size distribution of the test aerosol. The relatively small error bars, representing single standard deviation, indicate the high reproducibility of the size distribution.

The aerosol mostly consisted of single PSL sphere with a size of 111 nm, at 152 nm and agglomerates consisting of several spheres. The size distribution data also showed a lognormal peak of nanoparticles formed due to crystallization of dissolved components remaining in the ultrapure water.

The measured relative humidity in the chamber was 40–50%. No humidification of the exposure atmosphere was performed, to rule out the droplet formation with the PSL particles as condensation seeds, which would render the deposition model not valid. However, it should be noted that dehydration of the cells has to be taken into account for toxicity studies and humidification of the exposure atmosphere may hence need to be considered.

Primary 100 nm PSL particles as well as doublets can be identified by their representative peaks in the size distribution. The identification of the PSL doublets in the 152 nm electromobility size channel is due to the fact that for non-spherical particles, the electromobility diameter is the equivalent diameter of a sphere with the same electromobility. Consequently, PSL agglomerates, consisting of three or more primary particles, appear to be distributed lognormally in the size distribution.

The region in the size distribution, representing the 100 nm PSL particles, was in the range of 100–1000 nm. To count only the single PSL particle as well as the occurring doublets and triplets and agglomerates, the measurement of the particle number concentration was limited to the size channels within this region. For the size distribution, presented in this section, the particle number concentration *was* $85000 \pm 2000/\mathrm{cm}^3$, measured over 1 h during the exposure.

4.6.2. Fluorescence detection of 100 nm PSL particles

Figure 4.8 displays a representative micrograph of a cell-carpeted membrane after the exposure to 100 nm PSL particles with the size distribution shown in Figure 4.7. The photo shown in this paper is color-inverted and changed in contrast, to blend out the background glow from the cells, for reasons of visibility. The 100 nm PSL particles can be detected as luminous spots on the cells and distinguished from the background glow at 1000×1000× magnification. Even the doublets and agglomerates can be differentiated as two or more connected luminous spots.

The image qualitatively shows the homogeneity of particle deposition. PSL microspheres could be detected over the whole membrane of the front transwell. No luminous spots can be found on the rear transwell.

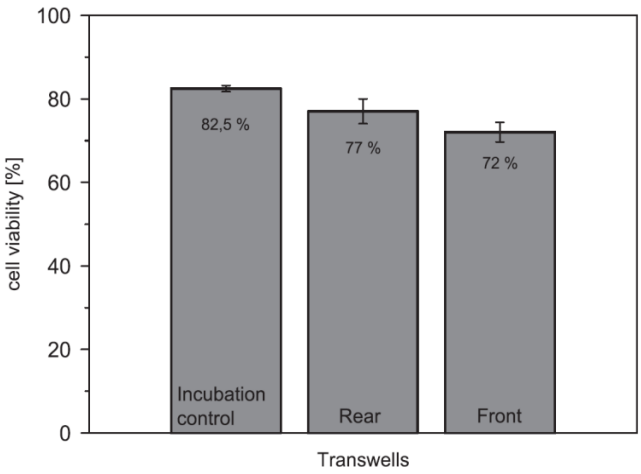

Figure 4.9. Cell viabilities of control transwells (incubator), front transwell and rear transwell from three exposures with HEPA filtered air (15% humidity) and equal Cyto-TP control parameters. The values are determined by calculating the arithmetic mean value for the results from each experiment. The experimental results itself were the arithmetic mean for the viabilities from 4 to 6 exposures conducted in each experiment. The error bars indicate the standard deviation.

The results verify that the parameters, chosen for the design and operation of the Cyto-TP following the simulation results, enable the deposition of 100 nm PSL particles on the front transwell, while the rear transwell remains particle-free.

Due to the homogeneity of the deposition density, the total number of deposited particles can be extrapolated from particle counts in a sufficient number of random areas on the membrane. By comparison with the total number of particles transported into the device, known from the online aerosol characterization, the deposition efficiency can be determined. However, due to the wet surface of the cells, the particles tend to move from their original position during the sample preparation for the fluorescence microscope, especially when putting the cover slip on the sample. This is verified by the fact that a large number of particles are found rinsed from the membrane onto the object plate. This cutback disqualifies this method for the experimental verification of the quantitative results of the deposition model.

4.6.3. Living cell count at zero exposure conditions

In a series of exposure studies with filtered air, the effect of the Cyto-TP itself on the cells was evaluated by comparing the living cell count L_{cc} of the transwells put into the device with the control transwell in the incubator. The particle number concentration was zero during the 1 h exposure time. The relative humidity was kept constant at 15%. After the exposure, the front and rear transwells are put into the incubator for 24 h. Figure 4.9 shows a comparison of the statistical mean of all measured cell viabilities.

The data is expressed as the mean standard deviation from three independent experiments. Statistical analysis was performed by one-way ANOVA (Tukey post test) using OriginPro 8.5, with the P-value as the measure of the statistical significance. The difference between the two results was significant if $P \leq 0.05$. The results yielded no significant differences of cell viabilities between incubator and rear transwell as well as rear and front transwell. However, there was a significant difference between the cell viabilities of incubator and front transwell.

It was found afterwards that the dimensions of the commercial transwells, e.g. the membrane diameter, vary with the magnitude of 10–100 µm. The shape and dimensions of the holes however were exactly adjusted for those transwells, in which dimensions were measured during the construction phase of the device. Therefore, bigger transwells deformed when being put into the intended hole. The membrane of the transwell got stretched or bulged during the insertion potentially causing some parts of the cell monolayer to detach from the membrane. These cells were then dried out, lowering the viability. Additionally, since the manufacturing tolerance of the individual building parts of the Cyto-TP was around 10 µm, a small difference in the dimensions of the holes could also explain the variance of the cell viabilities.

The experimental conditions during the exposure potentially influencing the cells like the heat radiation from the warmer plate – if at all – only have a negligible effect on cell viability. Therefore, potentially observed effects can unambiguously be traced back to the cell exposure to gas and particles.

4.7. Conclusions and outlook

The Cyto-TP, introduced in this paper, is, to the best of our knowledge, the first thermal precipitator specifically designed for cell exposure to nanoparticles. It was shown that the constructed Cyto-TP works in principle as predicted and that potential cell damages can unambiguously be traced back to particle and gas exposure. Differentiation of effects caused by the gas and particles is possible by the use of two transwells.

Realistically, nanoparticle aerosols do not consist of monodisperse spherical primary particles like the PSL microspheres dispersed in this study. The simulation, presented in this paper, has to be further developed to model the trajectories of polydisperse aerosols with a log-normal distribution and different morphologies in the transition regime. Since toxicity studies may have to be conducted with a humidified carrier gas, the influence of potential droplet formation on the deposition has to be taken into account. With a sophisticated deposition model, the dosimetric properties of the Cyto-TP can be analyzed.

In the next step, an optimized Cyto-TP will be constructed. The next version will implement design changes that eliminate the mechanical stress on the transwells when being put into the device. Different transwells will be used, easier to align with the cold plate of the Cyto-TP without stretching or bulging the membranes. The chosen transwells will also feature larger membranes which greatly increases the living cell count of the cell monolayer. Protocols analyzing more sensitive endpoints like cytokines (ELISA and flow cytometry) will become more applicable with higher cell counts. The next version of the Cyto-TP will also feature three parallel flow channels allowing six transwells being applied during one exposure, for a higher statistical relevance of the toxicity data.

The optimized Cyto-TP will be put into use in a series of experiments, exposing cells to known cytotoxic nanoparticles for positive control and to non-toxic nanoparticles for negative control.

The Cyto-TP prototype is designed for laboratory use under controlled conditions. Apart from the potential contamination of the cells in an unclean environment, ruled out in the laboratory with the use of a flow box, there are also practical requirements for the Cyto-TP to function, much easier to follow under laboratory conditions, like maintaining the temperatures of the plates or performing assays for the cytotoxicological evaluation after exposure. There are many more influencing factors to be taken into account that can have an effect on the cells and therefore bias the results. Future versions of the Cyto-TP as well

as the experimental protocol have to be optimized, to ultimately develop a screening method, applicable in tests, e.g. the workplace atmosphere for possible hazardous particles and gases in the field.

ACKNOWLEDGEMENT

This research project was funded by the Seventh Framework Program (FP7/2007–2013) of European Commission under Grant agreement no. 211464-2.

Chapter 5: Further development of the Cyto-TP

Chapter 4 introduced the first prototype of the Cyto-TP, mainly constructed to conduct a proof-of-concept study for the method, which was considered successful. In the next step, the design of the Cyto-TP was critically reviewed in regards to flaws identified in the previous study. Defects were mainly found in the uptake of transwells not being optimal. In addition, since toxicological studies usually apply standardized protocols to test for toxicity endpoints, further development focussed on the optimization of the instrument towards a better compatibility with common protocols, like Enzyme Linked Immunosorbent Assay (ELISA) and flow cytometry.

It was decided to follow two different approaches. The first approach focussed on the redesign of the Cyto-TP with the first prototype as the basis, called prototype-2. The second approach combined the basic technology behind the Cyto-TP, thermal precipitation, with a commercial air-liquid interface sampler, namely the Vitrocell® CF exposure module. This version is henceforth called prototype-3, which was applied in a nanoparticle exposure study with a barium sulphate nanomaterial to explore adverse effects with low exposure doses.

5.1. Cyto-TP prototype-2

In the conclusions of chapter 4.7, several design flaws of the first Cyto-TP prototype were identified that only surfaced after extensive testing during the proof-of-concept study. In addition, it was argued that design changes should be made with a better compatibility with commonly applied toxicity assays in mind. It was concluded that a redesign of the Cyto-TP should focus on the following aspects:

- Elimination of mechanical stress on transwells when they are put into the device.
- Use of larger transwells, namely so-called 12-well transwells yielding a larger number of cells hosted on its membranes.
- Upscaling of the instrument by comprising three flow channels for parallel exposures.

After the proof-of-concept study, further analysis of the performance of the Cyto-TP revealed one additional defect that could potentially harm cells, namely a raise of temperature in the nutrient solution due to constantly being under effect of heat radiation stemming from the warm plate of the thermal precipitator. In the first prototype, the cold plate is basically thermally isolated, therefore acting as a heat reservoir. The two Peltiérelements, added to temper the cold plate, were found to underperform when cooling down the cold plate, evident after measuring an elevated temperature of the nutrient solution after exposure compared to before. This was damaging for the cells and had to be avoided. Naturally, a temperature increase of the cold plate would also affect the stability of the temperature gradient, crucial for a well-controlled particle dosimetry.

In the next section, the design changes and added features to the concept that resulted in the construction of the prototype-2 are introduced. In accordance with the abovementioned points, the Cyto-TP was scaled up to allow three parallel exposures and larger transwells. In addition, a "life-support" system for the cells was implemented, i.e. a supplement that regulates the temperatures of the nutrient solution as well as cold plate better than the Peltiérelements of the original Cyto-TP.

5.1.1. Changes and added features to the design of the Cyto-TP

Naturally, cell physiological assays require a concentration of markers the assay is testing for that is greater than its lower detection limit. When the markers are secreted by cells in a low amount, the number of cells needs to be sufficient depending on the chosen assay. For example, the common ELISA identifies proteins on a biomolecular level [152]. Since one individual cell can only produce a limited amount of marker molecules, a high enough number of cells would be required to reach the lower detection limit of the assay. To increase the amount of cells per monolayer, it was therefore decided to use different transwells with larger membranes compared to those employed in the original Cyto-TP which where so-called 24-well transwells. Instead, 12-well transwells are used with membrane diameters of 12 mm instead of 6 mm, resulting in cell counts on each transwell about 4 times larger in comparison.

The use of 12-well transwells requires a wider duct channel. The width of the flow channel was widened to 18 mm. This increased the cross-sectional area of the flow channel. Consequently, a higher flow rate would be required to reach the same mean flow velocity of the original Cyto-TP.,

A Posseuille flow profile, given by Eq. 4.6 and used in the prediction of particle deposition on the cold plate, is not yet fully developed at the entrance of the flow channel. For laminar flows, its profile is fully developed after a distance L_e, the hydrodynamic entrance length, that can be estimated by:

$$L_e = 0.05 \frac{2ab}{a+b} Re \qquad [5.1]$$

For example, with a flow rate of $Q = 5$ ml/min, the Posseuille flow profile would be fully developed ca. 9 mm from the entrance. Hence, the location of the front transwell was put further back in the flow channel. The center of the membrane of the front transwell is located 18 mm from the entrance, i.e. the edge of the front transwell's membrane has a distance of 12 mm to the entrance. The rear transwell is also located further back, 58 mm from the entrance. A larger flow rate, $Q = 5$ ml/min, instead of 2 ml/min, was found to be optimal for particle deposition.

The Cyto-TP prototype-2 employs three parallel but separate flow channels for three parallel exposures. Similar to the prototype presented in chapter 4, all flow channels employ two transwells, one for exposure and one for control. By exposing three transwells in

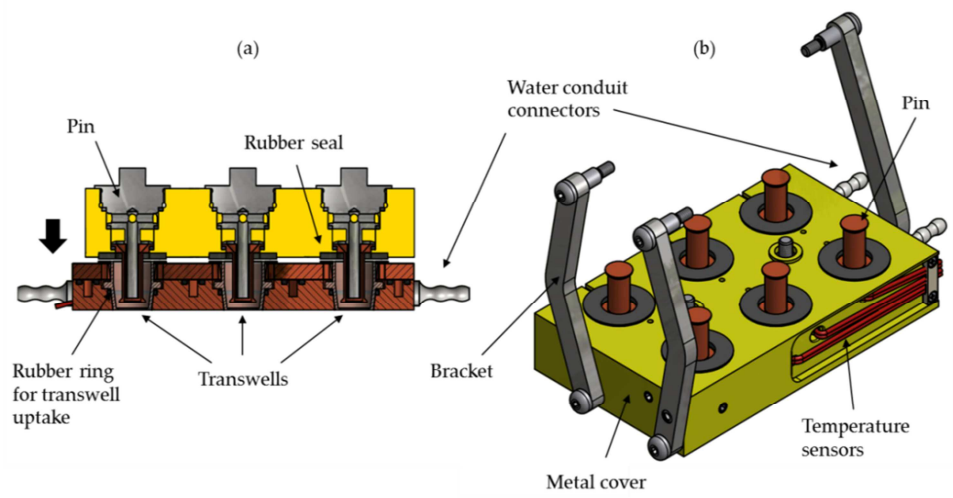

Figure 5.1: Transwell uptake and cover in the Cyto-TP prototype-2. In (a), a cross-section of the cold plate with the cover as well as pins lowered is shown whereas in (b) the whole cover is shown upside down.

parallel during one exposure, the statistical significance of the result of one exposure session can be improved.

Although not statistically significant, a shift of cell viability to lower values was observed after the transwells were put into the original Cyto-TP prototype. Mechanical stress on the membranes of the transwells would potentially cause cells to detach and subsequently become undernourished and dry. This effect was found to be caused by dimensionally unfitting holes in the cold plate serving as inserts for the transwells. They were fitted to sample-transwells. However, transwells from a different production lot differed in size and would not fit perfectly. Figure 5.1 (a) shows a cross-section of the transwell inserts for the prototype-2. Two rubber bands were placed in each hole to both retain the transwell and seal the insert airtight, allowing tolerance between the insert walls and the transwell, so that firstly the transwells wouldn't be deformed and secondly the membranes wouldn't be put under any mechanical stress.

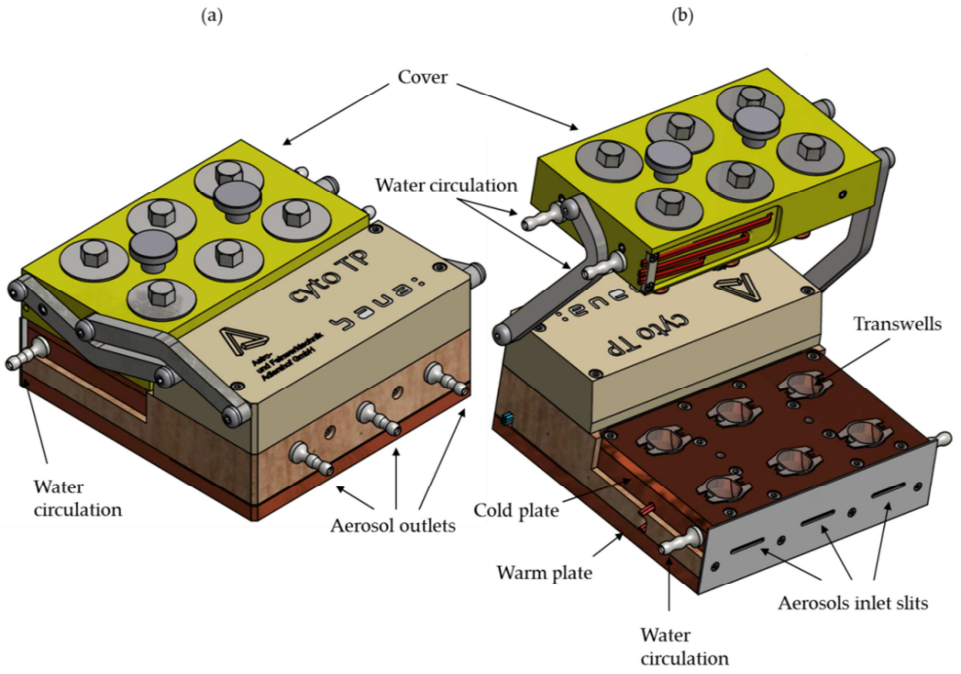

Figure 5.2: Complete CAD-model of the Cyto-TP prototype-2. (a) shows the Cyto-TP in back view in its closed state, i.e. when the cover is lowered on the cold plate. In the front view of (b), the cover is lifted, revealing the transwells.

Apart from mechanical stress to the transwells, a raise in temperature of the nutrient solution was identified to be the cause for decrease of cell viability, caused by constant radiation from the warm plate, absorbed by the cold plate.

As shown in Figure 5.1 (a), this issue was solved by lowering gold-coated metallic pins into the nutrient solution. For temperature control, it was decided to thermally couple the cold plate and the pins with a sufficient cooling system. Water conduits run through both the cold plate and the pins, where the water temperature can be controlled by a peripheral pump. The pins fit into the wells of the transwells by lowering a cover on the cold plate, as shown in Figure 5.1 (b). This design change greatly improved the temperature control of the Cyto-TP, which became stable over five hours. The complete CAD-model of the Cyto-TP prototype-2 is shown in Figure 5.2 in back view with its cover lowered (a) and in front view, with its cover lifted (b).

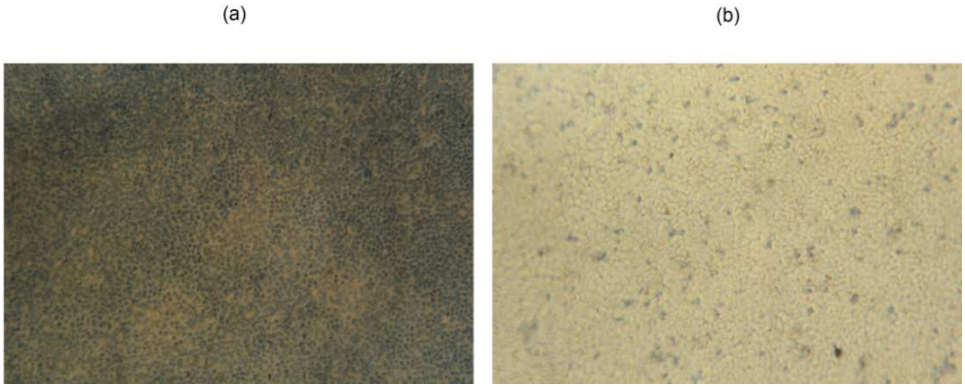

Figure 5.3. A549 cell monolayers coloured with the Trypan Blue assay after 30 minutes under zero exposure conditions in the Cyto-TP prototype-2 (a) and left in the incubator (b).

5.1.2. Performance of the prototype-2

Cell monolayers showed a significantly worse cell viability compared to the monolayers grown using the 24-well transwells in prototype-1. The reason was found using the Trypan Blue assay on the monolayers. This test uses a blue dye that can traverse through the damaged cell membranes of necrotic and apoptotic cells but not through the intact membranes of living cells. Hence dead cells are coloured blue whereas living cells are not, made visible using a microscope. Figure 5.3 shows typical microscopy images of cell monolayers hosted for 30 minutes in the prototype-2 (a) as well as left in the incubator (b) and coloured afterwards by the Trypan Blue assay. Figure 5.3 (a) is therefore an example of a cell monolayer comprising mostly dead cells whereas (b) shows a monolayer with living cells. Most cell monolayers hosted in the prototype-2 under zero exposure conditions showed monolayers of dead cells. Occasionally, cell monolayers were more intact, but not confluent, an important feature of the air-liquid interface to obtain a physiologically fit cell model. Not confluent monolayers are more sensitive to external stimulants. It is important to note that these observations were not made only for cell monolayers put into the prototype-2. Occasionally, loss of cell viability happened for control transwells that were left in the incubator as well, i.e. under conditions optimal for cell hosting. For this reason, it was concluded that the ALI cultivation protocols, described in chapter 4, are not applicable for 12-well transwells and it was found necessary to develop a modified SOP. This work is still being conducted as of the writing of this thesis.

5.1.3. Dosimetric properties of the Cyto-TP prototype-2

Similarly to the procedure described in chapter 4, particle trajectories in the Cyto-TP prototype-2 flow channels were determined to analyse the dosimetric properties in terms of deposition efficiencies. Appendix B shows the commented script that calculated deposition density profiles as well as deposition efficiencies in the areas of the front and rear cell monolayer for the prototype-2, assuming the Waldmann-model for thermophoresis (particle size independent thermophoretic force).

The flow conditions are equivalent in each of the three flow channels. Figure 5.4 (a) shows a deposition density profile for spheres deposited on the cold plate assuming a flow rate of $Q = 5$ ml/min and temperature gradient of $\nabla T = 5$ K/mm. The red circles mark the location of the transwell area. The particle density cannot be considered homogenous in the area of the highest particle density (red colour) but fairly homogenous in the area behind. The shown deposition density profile was obtained for operating conditions that yield not the maximum deposition efficiency but homogenous deposition. The deposition efficiency on the front transwell area was ca. 10% in this case.

Figure 5.4 (b) shows the deposition efficiency assuming the Waldmann-model for thermophoresis, as a function of the temperature gradient for a flow rate of $Q = 5$ ml/min. A temperature gradient of $\nabla T = 5$ K/mm yields the highest deposition efficiency. The peak deposition efficiency is slightly larger compared to the prototype-1 (see Figure 4.3).

The same technique as during the proof-of-concept study (chapter 4) was used to determine whether particles deposited. Counts of deposited particles were similar in all three flow channels, i.e. number of deposited particles on the front transwells. Qualitatively, the deposition density of the front transwells was homogenous and far greater compared to the deposition density on the rear transwells. By the time this thesis was written, deposition efficiencies have not yet been quantified.

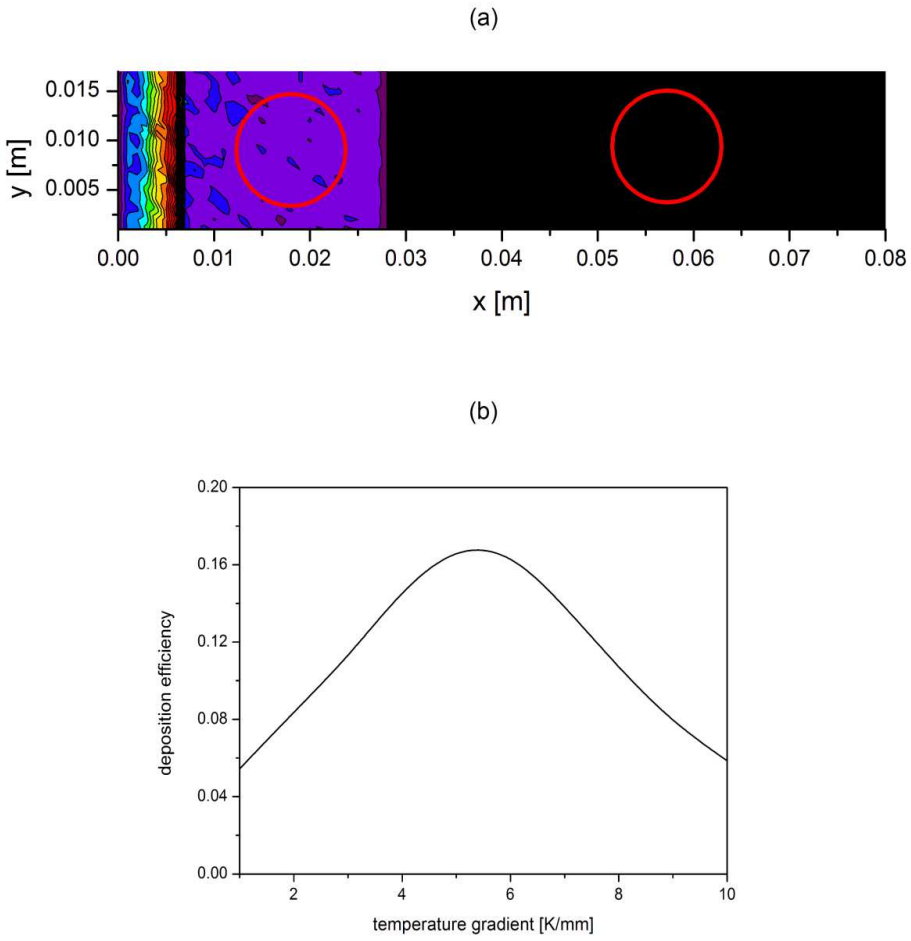

Figure 5.4. (a) Deposition density profile for particles deposited via thermal precipitation onto the cold plate of the prototype-2 assuming the Waldmann-model for thermophoresis. The flow rate was $Q = 5$ ml/min and the temperature gradient $\nabla T = 4$ K/mm. (b) Deposition efficiency on the area of the front transwell as a function of temperature gradient for a flow rate of $Q = 5$ ml/min.

In addition to that, the dependency of the deposition efficiency from both temperature gradient and flow rate was analysed to obtain the set of control parameters that would yield the best dose rate. Again, the particles were 100-nm spheres with standard density and the Waldmann-model was used for thermophoresis [99].

Figure 5.5 (a) shows a contour plot in which the colour scheme represents the deposition efficiency. The deposition efficiency is at its highest when the flow rate is kept lower than 8 ml/min. As the flow rate increases, a higher temperature gradient must be achieved to keep the deposition efficiency at its maximum.

Figure 5.5 (b) shows a different contour plot in which is colour scheme represents the standard deviation (in percentage) of the deposition density. The standard deviation for each set of control parameters was obtained by evaluating the respective deposition density profile by overlaying the deposition area with a grid of squares with 10 μm side length. The squares were then checked for deposited particles after calculating their trajectory. The yield was a statistic of particle counts for the screened area, with a mean particle count and a standard deviation. The values for the standard deviation shown in Figure 5.5 (b) were therefore measures of the deposition homogeneity. The more the colour shifts towards blue, the smaller is the standard deviation, i.e. the more homogenous is the deposition density. Homogeneity of the deposition density profile in the Cyto-TP prototype-2 was best for flow rates up to 10 ml/min and two ranges of the temperature gradient, 0-4 K/mm and $10 - 14$ K/mm.

The control parameters should be chosen to yield high particle deposition efficiency while keeping the standard deviation of the deposition density low (homogeneity high). Based on this theoretical evaluation of its dosimetric properties, the Cyto-TP prototype 2 is being used most effectively when using a flow rate of 3-5 ml/min and a temperature gradient of 12-14 K/mm[7].

[7] One must also keep in mind that the higher the flow rate the higher the dose rate is. A flow rate of 5 ml/min is therefore recommended.

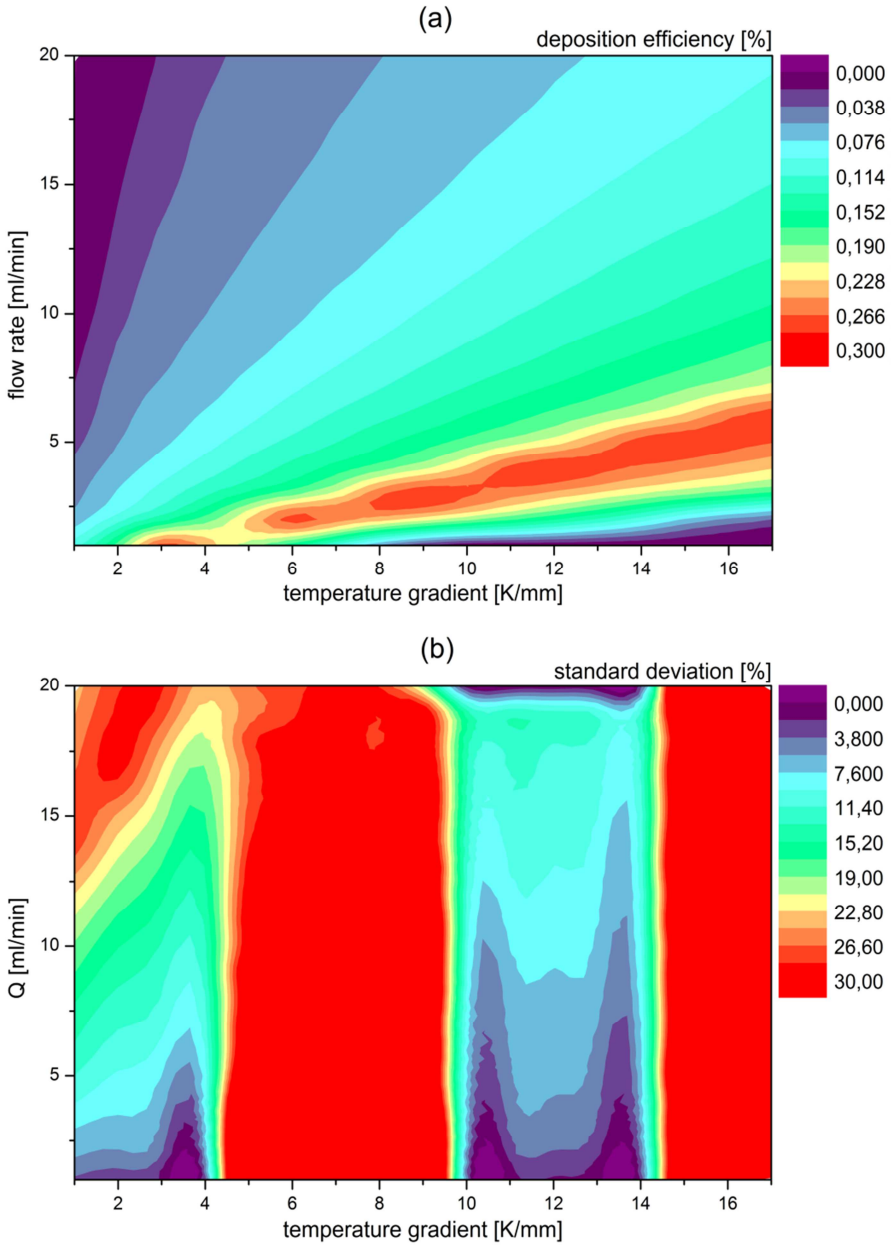

Figure 5.5. (a) Contour plot of the deposition efficiency in the prototype-2 as a function of the flow rate and temperature gradient. (b) Contour plot of standard deviation of the deposition density in the prototype-2 as a function of the flow rate and temperature gradient.

5.2. Cyto-TP prototype-3

The concept of an implementation of the Cyto-TP technology in a commercial product is rationalized by the fact that a new exposure module employing modified air-liquid interfaces also requires a modified technique for cell cultivation, as described in chapter 4. However, for an application of the device by third parties and independent reproduction of results, cell cultivation must be standardized, i.e. described in a standard operation procedure (SOP). The formulation of such SOP itself requires extensive experimental testing. By introducing the Cyto-TP technology to a commercial device employing already established standards, this mayor step could potentially be skipped.

This rationale resulted in the modification of a commercial Vitrocell® exposure system, so that cell monolayers, cultivated with a SOP developed for this system that is presented in Appendix C, could be exposed to nanoparticles via thermal precipitation.

The modified system was tested for enhanced particle deposition using fluorescent PSL particles in a similar manner as presented in chapter 4. However, this time, the deposition efficiencies were determined experimentally. In addition, to test for potential adverse effects by the experimental conditions, a nanoparticle exposure study was conducted with barium sulphate, a nanomaterial without any acute toxic effect. Hence, the dose-response relationship should be equivalent to a negative control study in which cells were exposed to particle-free synthetic air but under otherwise equivalent experimental conditions. Different doses of particles were deposited, expressed in the metrics of effective deposited number, surface area, volume and mass. For determining the the mass dose, the DMA-nano-PMC system was applied to measure the apparent density of the barium sulphate nanoparticles. A more complex set of toxicological endpoints were assessed to probe for biological response of the cells to the exposure, namely metabolic activity, cell viability, production of reactive oxygen species and secretion of interleukin-8 by the cells.

5.2.1. Vitrocell® exposure system for inhalation toxicology

Figure 5.6 shows the schematic layout of the gas exposure unit of the Vitrocell® exposure system. It comprises the exposure module with compartments for the transwells, filled with culture medium, so that the surface of the liquid is in contact with the (cell-less) bottom side of the transwell membrane. In practice, the culture medium is supplied though conduits using syringes until the medium touches the transwell membrane. A

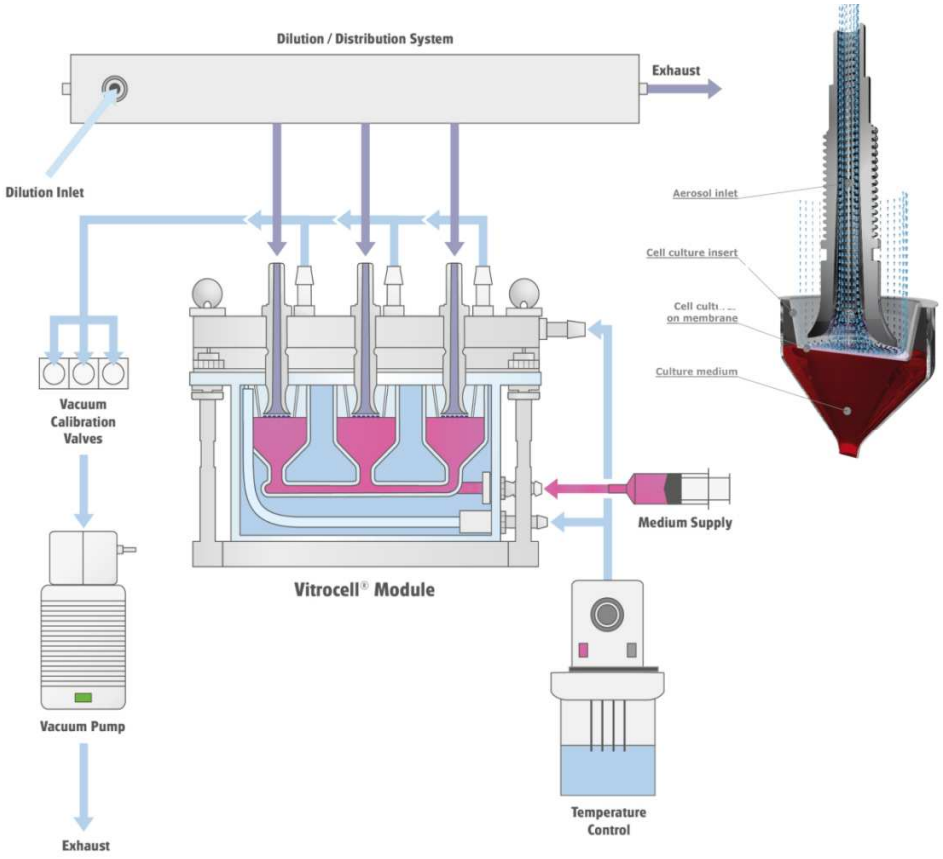

Figure 5.6. Schematic layout of the Vitrocell® exposure system. Apart from the displayed peripherals (see text for details), the system comprises a Vitrocell® CF module containing compartments for the transwells as well as pipes for gas exposure that are shown in more detail in on the right-hand side. Images are courtesy of Vitrocell Systems GmbH.

cover is placed on top to seal the compartments from the environment. One exposure system comprises three compartments for three parallel cell exposures.

Each compartment contains a metallic pipe that is lowered down to the cells by the cover. The pipe exit then usually has a distance of 1-2 mm to the cell monolayer. The pipe exit is shaped conically, similar to the bell of a trumpet. Figure 5.6 shows the design of the pipes in more detail as a schematic layout on the right hand side. The gas flow follows the

streamlines drawn into the schematic layout. It is first directed towards the cell monolayer, floods the cells and then leaves via the opening of the transwells towards the exit of the compartment for the transwell.

This exposure unit is incorporated in the exposure system. The aerosol enters the system via the dilution/distribution system which has one inlet for the aerosol, one inlet for optional dilution gas and one outlet for exhaust. The dilution/distribution system also contains three outlets for the exposure flows, i.e. the flows that are lead to each pipe in the exposure module. The aerosol flow is created by flow splitter, the "vacuum calibration valves", and a vacuum pump downstream the exposure module. The temperature of the exposure module and the nutrient solution is maintained by a temperature control unit, a heated water bath with a pump for water circulation.

This exposure module was pre-validated for exposing cells to potentially toxic gases like ozone [143], although the system has also been used to expose cells to aerosols consisting of nanoparticles, but rather unsuccessfully. In these studies, the only deposition mechanism was diffusion, providing very low deposition efficiency ($\sim 0.01 - 0.1\%$). The basic setup shown above has successfully been applied to deposit larger particles like cigarette smoke [64, 153]. Modifications to increase the depositions efficiency of nanoparticles focussed on either applying an electrical field between the inlet and the cell monolayer for an additional electrophoretic deposition or on increasing the particle size with droplet formation. Droplet formation and deposition by the cloud effect was first introduced by Lenz (2009) [65], resulting in the so-called Vitrocell® Cloud system. Electrostatic precipitation of particles on cells has initially been developed by Savi (2008) [35]. A variant of the Vitrocell® exposure module applies electrostatic precipitation by placing a metallic grid on the exit of the aerosol pipe and a metallic plate underneath the transwell. The grid and the plate act as the electrodes. The aerosol is charged before entering the exposure system and subsequently electrostatically moved towards the cell monolayer.

In this work, an alternative model was worked out that employs thermal precipitation. Taking the basic design described above, thermal precipitation was applied by placing a copper grid at the pipe's outlet. By heating up the grid, a temperature gradient is established from the cell monolayer (37 °C) to the grid. The particles that pass the grid enter the gradient, move towards the cell monolayer and deposit thermophoretically. This setup, shown in Figure 5.7, was implemented into a Vitrocell® CF exposure module for 12-well transwells (CF 12/3). Note that the idea of placing a grid on the exit of the pipe was devel-

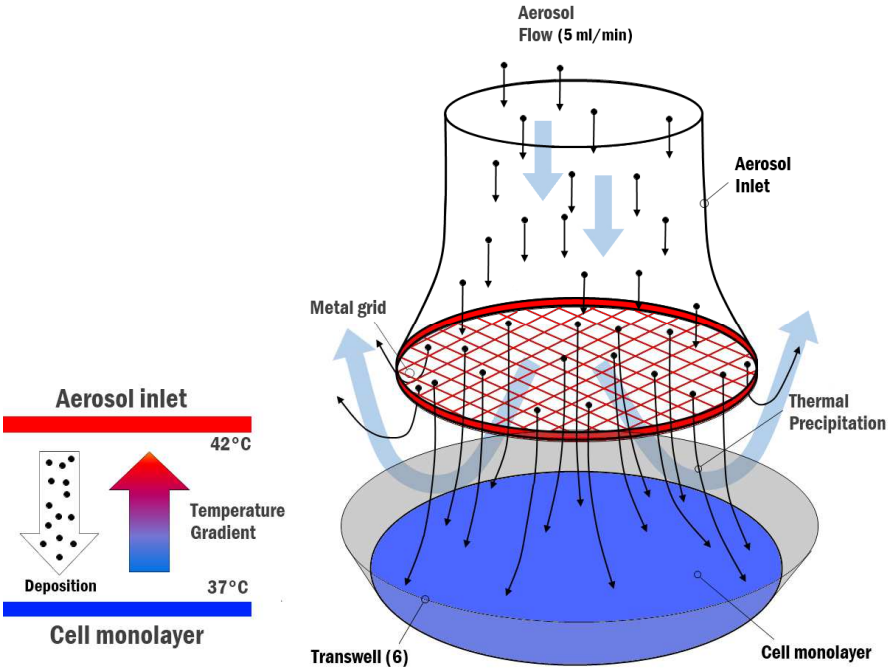

Figure 5.7: Thermophoresis driven deposition of particles in an insert of the Vitrocell® exposure module. The temperature gradient is established from the cell monolayer situated at the bottom of the transwell (37°C) to the metal grid at the exit of the metallic aerosol inlet (42°C). The blue arrows indicate the flow direction and the black arrows show an approximation of the particle trajectories.

oped independently, before the above mentioned details of the implementation of electrostatic precipitation technique were known.

The metallic cover of the module was heated up using water running through conduits, as shown in Figure 5.6. By heating up the cover to 60 °C, a constant temperature of 42 °C was reached at the grid via heat conduction, establishing a temperature gradient of 5 K/a between the cell monolayer and the grid, where a is distance between cells and grid.

A preliminary qualitative proof-of-concept study was conducted with one insert with thermophoresis-driven particle deposition and two inserts without. Under conditions similar to the ones described in chapter 4, fluorescent PSL particles were generated with

(a) (b)

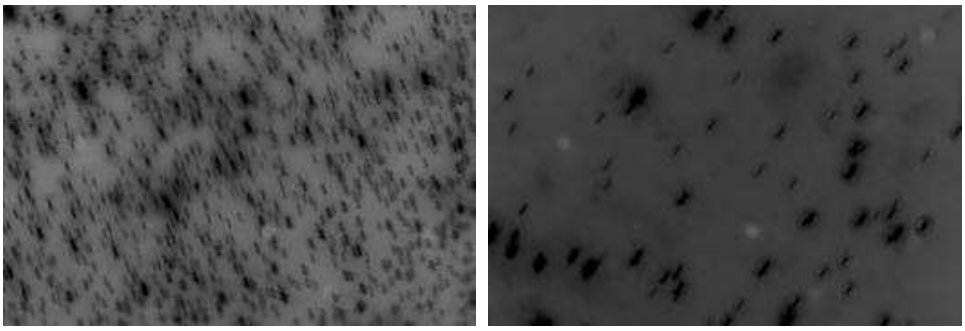

Figure 5.8. Micrographs with 1000 × magnification of 100-nm PSL particles deposited on A549 cells in the Vitrocell exposure system with (a) thermophoretic-driven deposition and (b) without thermophoretic-driven deposition

the TSI 3079 atomizer. Fluorescent 100-nm PSL particles were deposited on cells in all three inserts. Plastic tubes were used for the other two inserts to guarantee that no temperature gradient was existent in those inserts.

Analogous to Figure 4.8, Figure 5.8 shows micrographs of deposited 100-nm PSL particles on the cells, where (a) particle deposition was supported by thermophoresis with a temperature gradient of 5 K/a and (b) with only diffusion as the deposition mechanism. The photo is colour-inverted and changed in contrast, to blend out the background glow from the cells, for reasons of visibility. The images show the particles on cells immediately after exposure. The number of deposited particles was far greater on the cells in the inserts with thermophoresis-driven deposition compared to those without. In addition, the deposition density seemed to be fairly homogenous. Note that the particles are partly out of focus and appear larger because they were situated on different focal planes.

After enhanced deposition efficiency was achieved for the modified CF 12 module, two CF 6 exposure modules[8] with three compartments (CF 6/3) were provided by the manu-

[8] The CF 6 exposure module incorporates three 6-well transwells with membranes with a diameter of 24 mm.

facturer, both with grids made of stainless steel mounted to the exits of the aerosol inlets, for a more thorough investigation of the dosimetric properties.

The combination of established Vitrocell® technology with Cyto-TP technology show promising results and can be viewed as the first step towards an easy-to-use ALIS employing thermophoresis. The existence of established standard operation procedures for both generating the ALI and running the system are the mayor advantages of using this system.

5.2.2. Deposition efficiency of PSL nanoparticles in prototype-3

Different to the Cyto-TP prototype-1 and -2, particle trajectories are difficult to determine in the prototype-3. The flow profile cannot be modelled analytically so that the particle equations of motion are undetermined. For a future further development of the system, it is adequate to model the flow profile with the help of computer fluid dynamics.

A new experimental setup was used to experimentally determine de deposition efficiency of 100-nm PSL particles with the prototype-3 (Vitrocell® CF 6/3 module), which is shown in Figure 5.9 as a simplified drawing. The setup is similar to the one used in chapter 4, consisting of an aerosol generator, ALI exposure and aerosol characterization. Different to that experimental setup, the atomizer was kept within an ultrasonic bath (USB) to stabilize the PSL-water suspension. Also, the diffusion dryer was custom-built, using an Erlenmeyer flask comprising a spiral mesh-tube and silica gel. The ALI exposure system, consisting of a modified CF 6/3 module, a small chamber for pressure compensation and the so-called HD-3 distribution system, was located inside a flowbox. The HD-3 distribution system is mounted on top the CF 6/3 module and is a sophisticated flow splitter to divide the aerosol stream with a volume flow rate of 1 L/min into three equal parts. Downstream the splitter, the exposure module generates a small pressure drop to draw three aerosol flows with 5 ml/min from each of the airstreams. The HD-3 distribution system minimizes diffusive losses of nanoparticles on tube walls that can be large otherwise because of small flow rates required for exposure.

Particles were deposited on 6-well transwell membranes with 2.4 cm diameter. Confluent A549 monolayers were grown on the membranes following the protocol presented in Appendix C. As mentioned earlier, the temperature on the grids (warm side of the thermal precipitator) was controlled with hot water running through conduits in the cover of the exposure module. For the CF 6/3 module, to maintain a temperature of (42 ± 1) °C on the grids, a water-temperature of 57 °C was required. The surface of the cells had a tem-

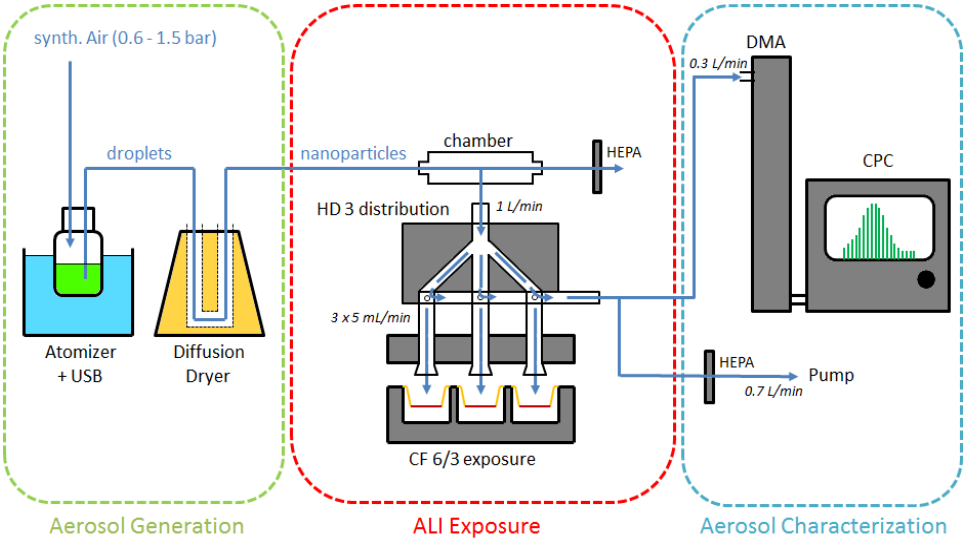

Figure 5.9. Experimental setup applied to determine the dosimetric properties of the Cyto-TP prototype-3. The individual components can be allocated to the tasks of aerosol generation, ALI exposure and aerosol characterization. For aerosol generation, a TSI 3079 atomizer was combined with a custom-made diffusion dryer. A modified CF 6/3 exposure module was used, combined with a HD-3 distribution system. Aerosol characterization was conducted with a SMPS system (TSI DMA 3081 + CPC 3776). Further details can be found in the text.

perature of 37 °C, equal to the temperature of the nutrient solution, maintained by a second water bath. After exposure, the membranes were cut with a scalpel and put on slides for the fluorescence microscope.

Two types of fluorescent PSL particles were chosen, 100-nm and 200-nm, to show that

1) The deposition efficiency of the Vitrocell-system with thermophoretis-driven deposition is greatly enhanced compared to the same system whre the termperature gradient was zero.

2) The deposition efficiency of 200 nm particles is smaller than that of 100 nm. Both particle types can be considered to underlie conditions valid for the continuum model for thermophoresis which is then size-dependent (PSL particles considerable in the free molecular regime (e.g. 50-nm) could not be detected using a fluo-

rescent microscope). However, the thermophoretic velocity of the particles with both sizes should be fairly equal.

Particles were counted in ten different, randomly chosen locations on the membrane with the help of a fluorescence microscope. Each analysed square had an area of 100 × 100 µm^2. The total amount of deposited particles was extrapolated from the area-averaged deposition density. It is important to note, that for the extrapolation of the total number of deposited particles, homogenous deposition efficiency over whole membrane was assumed. Evaluated were the deposition efficiencies of the modified exposure module with and without applying thermophoresis. This procedure was conducted nine times for each nanomaterial.

The evaluation procedure is demonstrated here exemplarily for one exposure.

Figure 5.10 shows a typical measured particle size distribution $dN/d\log(d_m)$ as a function of d_m of an aerosol containing 100-nm PSL particles measured with the SMPS (TSI DMA 3081 + CPC 3776). It was modelled with five impulse functions (yellow) that were superpositioned to yield an enveloping curve (blue) that fitted the data well. The impulse functions were lognormal distributions:

$$\frac{dN}{d\log(d_m)}(d_m) = \frac{N}{\sqrt{2\pi}\,\log(\sigma_g)}\,\mathrm{Exp}\left[-\frac{\left(\log(d_m)-\log(\tilde{d})\right)^2}{2\,log(\sigma_g)^2}\right], \qquad [5.2]$$

where N is the amplitude (i.e. number concentration), $\tilde{d}$ is the mode and σ_g is the geometric standard deviation. Peaks 2 – 5 were considered to represent different modes of the PSL particles that, once deposited, would be visible as single light dots under a fluorescence microscope[9]. Because single PSL particles were 100-nm small and the magnification only $1000x$ (see Figure 5.7) individual light dots could not be differentiated into single particles and agglomerates.

[9] The particle size distribution presented in Figure 4.7 does not show a peak that is similar to peak 2 in Figure 5.9. This additional peak consistently showed up in the measurements described here and could not be identified with certainty. However, since its shape was similar to the peak clearly representing single PSL particles and the same base suspension was used but three years later, it might be that peak 2 characterized particles that partially disintegrated over time. The manufacturer only guarantees one year shelf life.

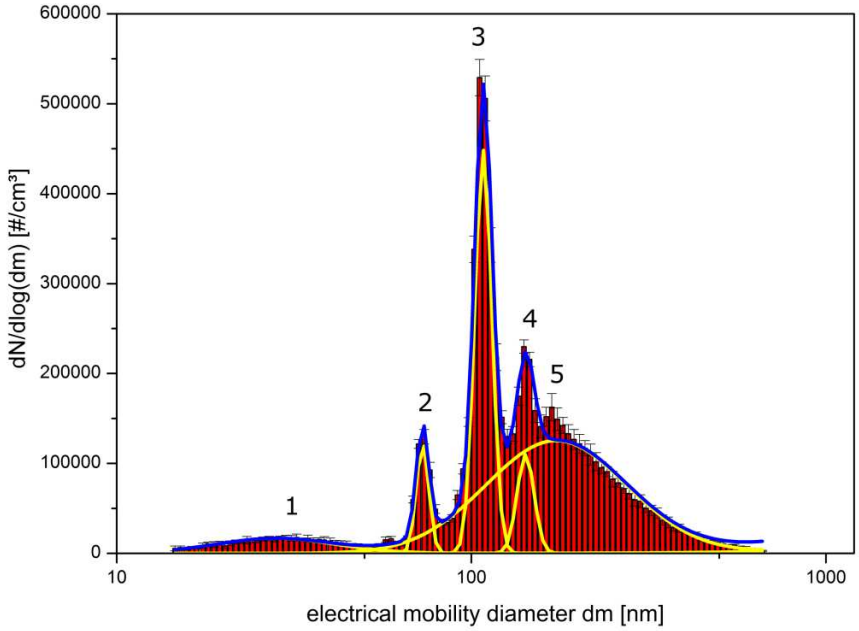

Figure 5.10. Particle size distribution of an aerosol generated over ca. 21 min with the TSI 3079 (1.5 bar) 100-nm PSL (Polysciences Fluoresbrite microspheres). The distribution (red) was multipeak-fitted with five lognormal impulse curves (yellow, Eq. 5.2) to yield the model curve (blue).

The sum of the amplitudes of peaks 2 – 5 was 99204 ± 3212 #/cm^3, i.e. the average number concentration of the particles being or comprising single PSL particles.

The exposure time was 21 minutes (seven three minutes long scans with the SMPS) at a flow rate of 5 ml/min. The administered dose was therefore $21 \times 5 \times (99204 \pm 3212) = (10.42 \pm 0.33) \times 10^6$. Counting of all light dots visualized under the fluorescence microscope yielded mean particle count of 43 ± 16 particles per 100×100 µm^2, i.e. when assuming homogenous deposition density, the effective deposited number was $(43 \pm 16) \times 10^4$/cm^2. The area of the cell monolayer was 4.52 cm^2. Hence the deposition efficiency was according to Eq. 4.11:

$$\phi = \frac{4.52\ (43 \pm 16) \times 10^4}{(10.42 \pm 0.33) \times 10^6} = 0.18 \pm 0.07 \qquad [5.3]$$

Applying Eqs. 2.59 – 2.62 yield the dose rates for number, surface area, volume and mass. The administered number dose rate was $R_N = 9{,}42 \times 10^4 \#/\text{min}$, the surface area dose rate $R_{SA} = 1.46 \times 10^{-3} \text{cm}^2/\text{min}$, the apparent volume dose rate $R_V = 3.13 \times 10^3 \mu\text{m}^3/\text{min}$ and the mass dose rate assuming a density of $1.05\ \text{g/cm}^3$ for PS was $R_M = 3.27\ \text{pg/min}$. Note that for this estimation, even though not all particles were primary particles and hence spherical, their apparent density was assumed to be equivalent to the bulk density of PSL.

In conclusion, for the 100-nm PSL particles, a deposition efficiency of $19 \pm 4\ \%$ was determined. For the 200-nm particles, a deposition efficiency of $14 \pm 3\ \%$ was determined. The deposition density in the inserts without thermophoresis-driven deposition (zero temperature gradient) was lower than 1%.

5.2.3. Toxicity study with barium sulphate nanoparticles

ALI exposure was conducted with barium sulphate ($BaSO_4$) nanoparticles. This material was used to serve as a negative control for particle toxicity as part of a larger study with several nanomaterials that was still being conducted by the time this thesis was written.

An experimental setup equivalent to Figure 5.9 was used with one change: A second modified Vitrocell® CF 6/3 exposure module was used for exposure with particle-free synthetic air for control so that potential toxic effects could be unambiguously related to particle and gas exposure. In addition, the DMA-nano-PMC system was used to probe the apparent densities of mobility-selected barium sulphate particles to enable dose metric conversion from number to mass. ***This experimental setup is also depicted on the front cover of this thesis book.***

5.2.3.1. Particle generation and characterization

The aerosol comprising barium sulphate nanoparticles was generated from an aqueous suspension with the nanomaterial labelled NM220 ($BaSO_4$), provided by the JRC[10] Nanomaterials Repository. The primary particle size of NM220 was 25 nm. The suspensions were made by suspending 50 mg of NM220 in 50 ml of Millipore water that was additionally autoclaved and filtered. Prior to aerosol generation, the suspension were put into the ultrasonic bath for 15 minutes. The output particle number concentration generated with

[10] Joint Research Centre of the European Commission

the atomizer was controlled with the pressure drop which was 0.6, 0.8, 1.0 and 1.5 bar, resulting in concentrations ranging from $10 \times 10^3 - 1.6 \times 10^6$ #/cm^3.

Figure 5.11 (a) shows a typical particle size distribution measured with the SMPS when the atomizer was operated with 1.0 bar. The particle size distribution was modelled with two super-positioned lognormal functions (Eq. 5.2) (yellow and green) so that the enveloping curve (blue) fitted the data. It exhibits two modes, one in the size range of 10-70 nm (water remains) and a dominant in the range of 20-500 nm. The mean particle size of the second peak, identified as the NM220-mode was 92 nm with a standard deviation of 1.7.

To convert the particle size distribution to a particle mass distribution, the tandem DMA-nano-PMC system was used to measure the particle mass and apparent density when the upstream DMA was operated to yield particles with an electromobility diameter of 30-90 nm. The nano-PMC was operated with a flow rate of 0.3 L/min and rotational speed of 6000-12000 rpm. Figure 5.10 (b) shows the response spectrum of the tandem DMA-nano-PMC for 50-nm NM220 particles, yielding a peak at 30 V.

Table 5.1 shows the classified particle masses (Eq. 3.3) and respective apparent densities (Eq. 3.11). The larger the classified particle mobility diameter was the larger was the apparent density, which, at first, seems unexpected in light of the discussion presented in chapter 3.4.4. However, it is reasonable to assume that the amount of water remains decreased as the chosen electromobility class increased, given the shape of the particle size distribution. Assuming that the density of the particles labelled "water remains" was smaller than the bulk density of barium sulphate (4.5 g/cm³), the average apparent density of the aerosol would increase with larger mobility size class and thereby smaller mixing rate of water remains and NM 220. Following this discussion, for the conversion of number concentration to mass concentration, an apparent density of 3.1 g/cm³ for NM220 was assumed, measured for the largest selected electromobility size class of 90 nm, in which the fraction of barium sulphate particles was highest.

5.2.3.2. Dose characterization

For each exposure, the average particle size distribution was modelled analogous to the abovementioned case. The area of the second mode yielded the particle number concentration of NM220. The dose rates were calculated according to Eq. 2.59 – 2.62, assuming a deposition efficiency of 0.19 at a flow rate of 5 ml/min. To obtain the surface area, volume and mass concentrations, the size-basis of the impulse curve representing the particle size distribution of barium sulphate was first converted to the respective metrics. The resulting

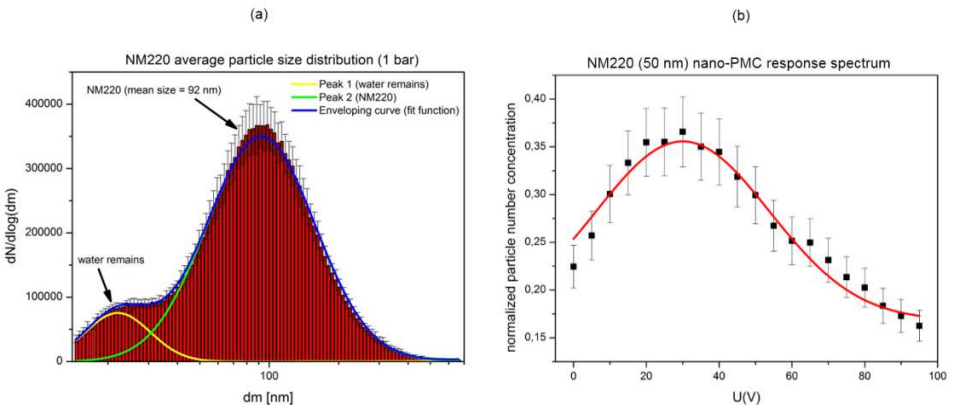

Figure 5.11 Results of particle characterization for an aerosol generated by atomization of an aqueous suspension with NM220 (barium sulphate). (a) Particle size distribution measured with the SMPS and fitting results. (b) Response spectrum of the DMA-nano-PMC system operated at 6×10^3 rpm and 0.3 L/min of 50-nm particles.

distributions were then integrated. Considering that each exposure time was 30 minutes for this study, the dose rates yielded the effective deposited doses which are summarized in Table 5.2.

From exposures with barium sulphate, no adverse effects were expected in this dose range. They showed no acute toxicity in much higher doses in various *in vitro* [154] and *in vivo* [155, 156] inhalation studies. For reference, in a study by Svensson *et al.* (2016) [157], who exposed A549 monolayers at the ALI to copper, palladium and silver nanoparticles

TABLE 5.1:
Dominant mass and apparent density of barium sulphate (NM220) particles, generated with the atomizer and measured with the tandem DMA-nano-PMC system.

Diameter d_m (nm)	Rotational speed ω (rpm)	Particle mass M_C (ag)	Apparent density ρ_{ap}(g/cm³)
30	12×10^3	37	2.62
50	6×10^3	178	2.72
70	6×10^3	534	2.97
90	6×10^3	1187	3.11

TABLE 5.2:
Particle number concentrations, particle mass concentration, effective deposited doses in terms of number, surface area, volume and mass during of ALI exposure to NM220 (barium sulphate).

Particle number concentration #/cm³	Particle mass concentration ng/cm³	Number 10^6/cm²	Surface area mm²/cm²	Volume µg³/cm²	Mass ng/cm²
11000	0,23	0,07	0,017	505	1,49
12839	0,27	0,08	0,019	589	1,74
13845	0,29	0,09	0,020	635	1,88
60940	1,31	0,40	0,074	2798	8,29
77689	1,67	0,51	0,093	3567	10,57
119260	2,57	0,79	0,141	5477	16,22
322406	6,96	2,13	0,370	14806	43,8
424075	9,16	2,81	0,490	19476	57,70
469362	10,13	3,11	0,540	21555	63,86
1298640	28,05	8,61	1,493	59641	176,71
1581040	34,15	10,48	1,817	72611	215,14

generated by spark ablation, nanomaterials known to have damaging effects on cells, the dose ranges were $0.6 - 9.7\ \mathrm{cm^2/cm^2}$ at which the respective dose-response relationships showed significant decrease of cell viability. These doses could not be obtained with the experimental setup used for this study. For the highest dose rate, at a number concentration of $1.58 \times 10^6\ \#/\mathrm{cm^3}$, the required exposure time for an effective deposited surface area dose of $1\ \mathrm{cm^2/cm^2}$ would need to be around 24 h. For an exposure time of 30 min, the required number concentration would need to be roughly at $1 \times 10^8\ \#/\mathrm{cm^3}$.

For a full validation of the system, an adequate positive control is required which was not yet conducted by the time this thesis was written.

5.2.3.3. Toxicological Endpoints

Two different assays for cell viability were conducted as well as one assay for ROS production and one for interleukin-8 secretion. The individual assays are described not in detail since commercially available kits were used, but can be comprehended with the help of the respective references

Metabolic activity was probed with the Alamar Blue, prestoblue A13261 [158]. The Alamar Blue assay makes use of a solution of resazurin, a weakly fluorescent blue dye that vital cells transform to pink resofurin that is red fluorescent. Hence non-vital cells are blue where as vital cells are red. By measuring the amount or red fluorescent light with a spectrophotometer, the cell viability (ratio of the number of vital cells to the total number of cells) cells can be determined.

Cell viability was tested with the lactate dehydrogenase (LDH) assay, CytoTox-ONE™ Homogeneous Membrane Integrity Assay [159]. The LDH assay determines the amount of lactate dehydrogenase, an enzyme that is released by damaged cells, by using an enzymatic reaction that results in the formation of formazine. The red compound can then be measured with the help of colorimetry.

ROS production is determined using the dichlorofluorescein (DCF) assay, CM-H2DCFDA [160]. In short, after passing the cell membranes, a non-fluorescent compound is oxidized by ROS present in the cells to fluorescent DCF.

Interleukin-8 secretion was tested with the Enzyme-linked Immunosorbent Assay (ELISA) IL-8 ELISA Set - Cat. No. 555244 [161], which makes use of specialized antibodies to mark certain proteins, for example interleukin-8 that cells release into the nutrient solution as a marker for inflammation.

5.2.3.4. Biological response

Figure 5.12 (a)-(d) shows the results after testing the A549 monolayers 24 h after exposure for the endpoints described above. Results are shown as dose-response data where the response is normalized to the average response of the control cells that were exposed to particle-free synthetic air in the second modified CF 6/3 exposure module under otherwise equivalent exposure conditions. The dose is shown here in the metric of effective deposited mass (ng/cm^2) using a logarithmic scale. Since for each exposure, three cell monolayers were exposed, the mean response values are given. The error bars are determined by the respective standard deviations.

The results show that exposure to barium sulphate, at these doses, would have no adverse effect to A549 cells, hosted at the air-liquid interface.

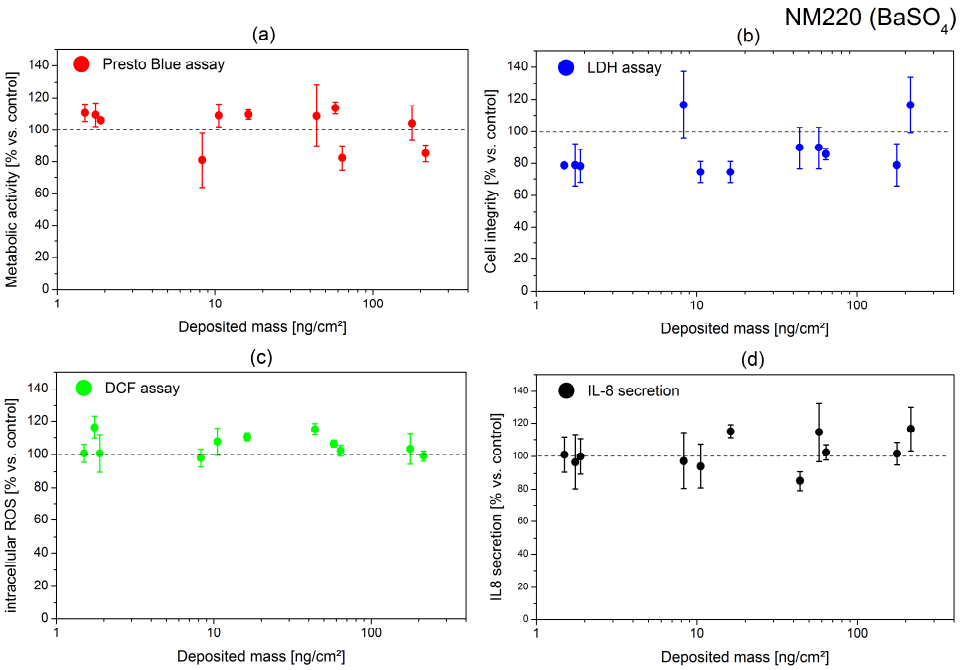

Figure 5.11. Dose-response data for NM220 nanoparticles deposited on A549 cells at the air-liquid interface. The dose is expresses as effective deposited mass and shown in a logarithmic scale. Response is expressed as the endpoint value of the exposed cells normalized to the endpoint values of the control cells. The dashed line therefore marks the response value at which exposed cells would show no difference to the control cells. Endpoints were (a) Presto Blue assay, (b) LDH assay, (c) DCF assay and (d) IL-8 secretion. The results demonstrate that exposure to barium sulphate particles had no adverse effect on the cells.

A second batch of control cells were kept in the incubator and did not show any significant difference in metabolic activity, cell viability, ROS production or IL-8 secretion when compared to the control cells exposed to particle-free synthetic air.

In conclusion, the exposure study with NM220 barium sulphate nanoparticles yielded results as expected – no adverse effects in a relatively low dose range of $(0.07 - 10.48) \times 10^6$ #/cm², $(0.017 - 1.817)$ mm²/cm², $(505 - 72611)$ µg³/cm² or $(1.49 - 215.14)$ ng/cm². The experimental conditions had no effect on the biological response of the cells, corroborating the statement that adverse effects would be unambiguously be relatable to exposure to nanoparticles. However, a study using nanomaterials that are known to be toxic at

dose ranges attainable with this experimental setup would significantly help to validate the dosimetry of the Cyto-TP prototype 3. The next experimental step should therefore focus on depositing nanomaterials like silver or zinc oxide with much larger dose rates accomplishable most probably with a different aerosol generator.

Chapter 6: Future application in safety-by-design for nanomaterials

---

The rationale in developing both the Cyto-TP and nano-PMC is strongly connected to providing the instrumentation necessary to perform testing in the context of safety-by-design. Risk assessment during the innovation phase of the nanomaterial is pre-regulatory. Similar to regulatory testing to compile a chemical safety report under REACH, pre-regulatory testing assesses both hazard and exposure but in a much more simplified way. Regulatory testing is comprehensive and detailed: To assess the hazard, the chemical usually undergoes a variety of toxicity tests using in vivo models, i.e. animals, to predict the hazard to humans or the environment. Similarly, human exposure is assessed by testing e.g. dustiness with a test on a model reflecting a scenario under which humans can be exposed. For pre-regulatory testing, it is not required to obtain results in similar detail; its results provide a general idea, where the innovation is headed towards, a safe or an unsafe nanomaterial. This idea can be the motivator for the developer to optimize the nanomaterial so that it might pose lower risk potential after the next development cycle.

A series of tests gather specific information necessary to compile a fingerprint of the hazard of a nanomaterial in development, its 'bio-identity'. The bio-identity must have a predictive value. Since the most likely route of exposure is inhalation, the capability of the nanomaterial to produce respirable dust particles under influence of an excitation for aerosol emission, 'bio-availability', must also be assessed.

In the following section, the endpoints of pre-regulatory testing are defined, the abovementioned bio-identity and bio-availability. Based on the information required to compile these fingerprints, the testing strategy is then introduced. The Cyto-TP can be part of a hazard potential test, whereas the nano-PMC can be essential for characterizing the exposure potential, the nanomaterial exhibits.

6.1. Bio-identity of a nanomaterial

In this work, a bio-identity means a list of nanomaterial properties that are identified as mediators for toxicity of the nanomaterial as particulate matter. As stated in the introduction, based on current knowledge, properties of nanoparticles that drive toxicity are equivalent to those that drive the toxicity of conventional particles (fine dust). Those properties comprise particle morphology, surface chemistry, and apparent (agglomerate) density. Three groups of toxic particles can be identified: high aspect-ratio materials (HARN), chemically toxic materials and granular biopersistent particles (GBP) [50]. A bio-identity can therefore be compiled by testing for these specific properties.

6.2. Bio-availability of a nanomaterial

Here, bio-availability describes the chance of it being situated in the breathing zone. It depends on the propensity of the base nanomaterial to produce dust, i.e. its dustiness. The probability of particle release from a bulk material depends on two factors, the state of the source material and the mode and magnitude of dust generation. For example, a powdery source material may already consist of particles that can easily be picked up by an air-stream. In turn, if the source material is solid, strong abrasive forces would be necessary for particles to form in the first place. In other words, the mode of dust generation either causes the transition of a granular material from a powder to an aerosol phase or particle release from solids. Often used to quantify dustiness are process-specific emission factors, determined by the ratio of the emitted mass to the mass of the base material. These can be differentiated into emission factors in regard to inhalable dust and dust that is not only inhalable but also respirable. These are simply called dustiness coefficients.

6.3. Strategic safety-by-design

Figure 6.1 illustrates the flow of the proposed pre-regulatory testing strategy. The initial state of the nanomaterial development process at which the pre-regulatory testing strategy is applied is at the end of a development cycle where the nanomaterial is available in similar state as the desired end product. This section gives an overview of the proposed procedure without going into details of the tests. See the respective sections further below.

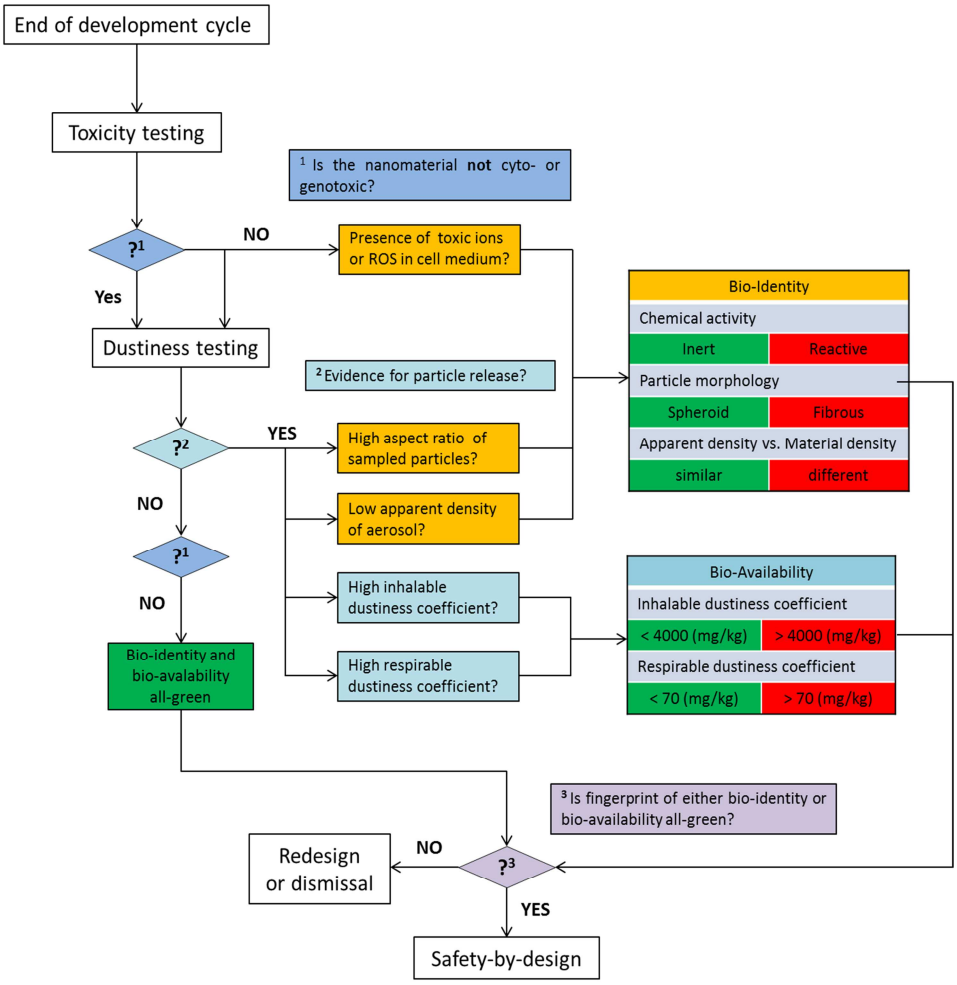

Figure 6.1. Flow scheme of the pre-regulatory testing procedure for nanomaterials in development. Details can be found in the text. Values for the dustiness coefficients are given by the DIN EN 15051 standard.

First, an *in vitro* toxicity study is conducted to test for cytotoxicity. Cytotoxicity is measured as cell viability as well as concentration of inflammatory markers in the cell media after exposure to the nanomaterial. Similarly, the effect of the nanomaterial on the genetic information is assessed, genotoxicity, by a suitable assay on the exposed cells. This study

is put in front to serve as a negative test for the need of further analysis of chemical toxicity.

If cytotoxicity is observed in the study, toxic ions, ROS or both are identified in the cell media that was extracted after exposure and chosen incubation time. Genotoxicity is also associated with certain ROS. Not specifically mentioned in the scheme is the possibility to conduct a series of high-throughput screenings that identify one or more physicochemical properties of the nanomaterial the ROS production stems from or increases its water solubility. Such screenings are not required in the context of this testing procedure, but are recommended in case the developer needs more information on the nanomaterial for their analysis.

Dustiness testing is conducted on the base nanomaterial. If the nanomaterial releases airborne nanoparticles, the emissions can be monitored and size-characterized to quantify the emitted particle mass of the two dust fractions, inhalable and respirable. Beneficial for simplicity of the dustiness test, by measuring the apparent density of the aerosol, not only one of the aerosol properties critical for the bio-identity can be determined but also the conversion factor to convert measured emitted particle number to mass. The latter is important for the calculation of the dustiness coefficients. The limit values shown in Figure 6.1 classify materials with larger values as moderately dusty, according to the DIN EN 15051 standard [162]. With the help of electron microscopy, collected aerosol samples are analysed in regard to particle morphology. High aspect-ratio materials can be identified that way.

From toxicity testing, chemical analysis and dustiness testing, both fingerprints for the nanomaterial's bio-identity and bio-availability can be compiled. For simplification, the fingerprints comprise only binary information, i.e. whether the nanomaterial exhibits a certain hazardous feature or not.

Safety-by-design was successful if this testing procedure yielded beneficial results (all categories are green) for either its bio-availability or bio-identity. It is reasoned that only one beneficial result is required with the fact that the predicted harmfulness of a nanomaterial scales with both. Presumed that a nanomaterial shows toxicity in testing, it has only a low chance of being harmful to the lungs when it cannot be inhaled. In turn, a nanomaterial releasing high amounts of inhalable particles has a low chance of being harmful to human health if the nanoparticles can be regarded as non-toxic. Note that, technically, all lung contaminants cause some kind of biological response. In case of non-toxic

particles, however, the biological response would not be the result an acute toxic effect. It is therefore desirable to obtain both a bio-identity and bio-availability that are beneficial for the nanomaterials safety.

6.4. In vitro toxicity testing employing the Cyto-TP

Selecting a specific method to test for a toxicity potential of a nanomaterial requires an analysis of the conditions it has to fulfil to be applicable in the context of the pre-regulatory testing strategy.

For the application of toxicity tests, careful considerations have to be made about the relevance of results for predicting health effects. Since toxicity tests try to depict the 'real world', a test with low predictive significance is simply irrelevant, because results allow no reliable implications and predictions. This is particularly true for *in vitro* toxicity tests that usually try to emulate a specific situation that can happen locally in an organism. As an example, the Cyto-TP deposits airborne nanoparticles on living alveolar epithelial cells and therefore tries to mimic contamination of the alveolar region to inhaled dust nanoparticles. However, all components of *in vitro* tests are models. The relevance of results strongly depends on the accuracy of these models. Otherwise, no predictive conclusions can be drawn after applying such a test.

It has therefore come into practice to assess toxicity tests with similar criteria as clinical diagnostic tests [163]. Toxicity tests are usually designed to allow reliable estimates of their positive and negative predictive values. A positive/negative predictive value is defined by the proportion of the true-positive/true-negative results to the entirety of positive/negative results. The positive predictive value (PPV) and negative predictive value (NPV) of a toxicity test are therefore measures of its reliability. A prerequisite of this assumption is that the distribution of positive and negative results from the toxicity test is equivalent to the distribution of positives and negatives for the health effect. In other words, the prevalence of the toxic effect in the artificial study must be equal to the prevalence of the health effect in the real world. Unfortunately, this is usually not the case, especially for an *in vitro* test trying to predict the toxicity of a chemical *in vivo* [59]. For example, an *in vitro* assay yielding positives for genotoxicity of a chemical cannot reliably predict its carcinogenicity or even mutagenicity in animals. In this case, prevalence of genotoxicity in the cells cultures is higher than prevalence of cancer in the test animals. In addition to that, for toxic effects stemming from chemicals, even the positive predictive

value of *in vivo* animal studies towards human health effects is debatable [164]. It is therefore often impossible to determine the PPV of a toxicity test. This is particularly true for health effects of nanomaterials, aggravated by the fact that toxicity data obtained *in vivo* is sparse. However, toxicity tests are considered to be highly predictive towards negatives, because the influence of prevalence on the reliability of negative results is far lower [163]. Taking the example of genotoxicity, an organism most likely won't develop cancer from exposure to a chemical when the genotoxicity assay on the chemical showed negative results, e.g. in the Comet-assay [165]. For a toxicity test to be considerable in the chemical-regulatory context, a high NPV is extremely important. It would be fatal when a chemical proves to be harmful to humans after it was rendered as 'safe' by regulatory testing.

Similarly, the toxicity test that is considered for this pre-regulatory testing must deliver results with a high NPV, since negatives are used to justify no further analysis of chemical toxicity. Factors that can falsify negative results must be identified and eliminated. For an *in vitro* toxicity test on nanoparticles, several falsifying factors can be identified, described in the next paragraphs.

The most relevant way of uptake of nanomaterials is inhalation of particle emitted by the nanomaterial. Most nanoparticles are in the size fraction that has the highest deposition efficiency in the lower respiratory tract, the alveolus. The toxicity test should therefore focus on evaluating effects on the alveolus after inhalation exposure. The alveolar epithelium consists of a basal membrane made of type-1 epithelial cells that hosts type-2 epithelial cells. The type-2 cells form a surface-active lipoprotein complex, called pulmonary surfactant, a protective layer between the cells and the alveolar air-sacs. Occasional alveolar macrophages are also situated in this region. The basal membrane is connected via the interstitium to blood capillaries. Simply put, the alveolar epithelium forms an interface between the vascular tissue and the air. Chosen cell lines for the *in vitro* model must represent the cell types that are local to the tissue. It is obvious that a liver cell line is not suitable to test for effects on the lung. Not trivial is the fact that cell lines can differ from each other even if they represent the same cell types. Cell lines can be finite or continuous, meaning that their proliferation is either limited or unlimited in number. For practical reasons, the latter, so-called immortalized cell lines, are often used even if they are technically cancer cells. The A549 cell line is often chosen to represent type-2 alveolar epithelial cells. For example, this cell line was used in the proof-of-concept study of the Cyto-TP prototype (chapter 4). However, doubts have been surfaced whether A549 are a good model for type-2 cells [166, 167]. False negative results in toxicity tests can stem from inhibited sensitivity of such cells towards the toxin. Similarly, cells can be hosted in differ-

ent environments. Examples are cells that are grown in a flask under submerged conditions or the cellular configuration at the air-liquid interface.

There is insufficient information whether the environment affects cellular functions, apart from a publication by Lenz *et al.* (2013) [168] who investigated differences in the response of A549 cells to exposure to ZnO nanoparticles under submerged conditions and at the air-liquid interface. Their cautious conclusion was that ALI-exposure would generate less false negatives and has therefore a higher NPV.

The exposure mode of a toxicity study can be relevant for the response of the cells. Deposition of inhaled dust particles in the respiratory tract happens either via inertial impaction or diffusion. For large particles, the former is the dominant deposition mechanism in the tracheobronchial region. In the alveolar region, the region with the highest deposition efficiency for nanoparticles, diffusion is the underlying deposition mechanism. However, traditionally, nanoparticles in suspension are administered to nutrient solution of the cells. Teeguarden (2007) [13] showed that particles can exhibit chemistry and morphology different to airborne particles. Their toxicity also might be different. A diffusive deposition of airborne nanoparticle would therefore better mimic the exposure mode in the alveolar region.

This toxicity test shall probe cyto- and genotoxicity. A cytotoxic effect is the impairment of essential cell functions that can ultimately lead to cell death. Cell viability of a culture, the ratio of surviving (living) cell count to the total cell count, is a measure of cytotoxicity. However, a damaged cell doesn't necessarily die. It can regenerate with the help of repair mechanisms that are part of the cellular functions. Hence, a cytotoxic effect might not be visible in a cell viability assay. This would be a false negative result. Alternatively, pathways leading to cytotoxicity can be assessed by determining the presence of certain messenger proteins (cytokines) released by cells to mediate an immune response. Methods like the ELISA are capable of detecting cytokine concentrations and can help to significantly lower the rate of false negative results in a cytotoxicity assay. Genotoxicity is usually assessed with assays like the Comet-Assay, which are proven to yield results with high negative predictive value [165].

Controls cells are valuable to assure that no secondary mechanism can influence the outcome of the toxicity test. Two types of controls are proposed. Firstly, cells are left in the incubator to identify and quantify effects originating from the cultivation technique. Secondly, control cells are exposed to the same conditions as the test cells, just without the

presence of nanoparticles. Effects on the cells due to circumstantial conditions that stem from e.g. the carrier gas can be identified. A negative toxicity for the exposed cells with coincidental negative results for the control cells can be carefully considered as true negative.

The Cyto-TP can be regarded as an exposure module for *in vitro* inhalation toxicity studies which can help to increase the predictive value of the results. Based on the abovementioned considerations, the following design for a toxicity test to be applied in preregulatory testing procedure can be formulated that employs the Cyto-TP:

1) The nanomaterial is administered as airborne nanoparticles in the Cyto-TP via thermophoresis. Dose as well as toxicity of the nanomaterial is therefore not affected by the delivering technique.

2) Cells are hosted in the Cyto-TP at the air-liquid interface to allow for nanoparticle deposition from the gas-phase as well as provide the currently best known *in vitro* model for the alveoli. ALI-cultivation increases the negative predictive value of the results. For the cell model, the A549 monoculture is used, but a better cell model might exist.

3) Toxicity endpoints are cell viability, cytokine secretion and genotoxicity assessed employing the CASY-assay (see chapter 4) and ELISA as well as the Comet-assay, respectively. The application of the ELISA can be viewed as a control for a negative in the CASY-assay, increasing the negative predictive value of cytotoxicity results. The Comet-assay yields results with a favourable negative predictive value.

4) Two kinds of control cell cultures are employed in the test to rule out influences of cell cultivation (incubator control) and exposure mode (exposure control). In the first and second prototype of the Cyto-TP, the exposure control is directly situated in the flow channel where nanoparticles don't deposit.

6.5. Detection of ROS and toxic ions in the nutrient solution

ROS are a number of highly reactive molecules that oxidize proteins and lipids that are essential for cellular functions. Most common are the superoxide anion (O_{2-}), hydrogen peroxide (H_2O_2), the hydroxyl radical ($HO^{\cdot}$) and singlet oxygen ($^1O_2$). They can naturally appear in cells during electron transports, but catalytically active nanoparticles can generate ROS at levels so that the natural defences of cells are overwhelmed. This can result in inflammatory response and cytotoxicity.

The most common assays to detect ROS-levels in *in vitro* systems are based on colorimetric, fluorescent or luminescent dyes. Others are based around electron spin resonance (ESR) measurements. It has been shown that ROS-assays yield an unexpected wide range of results when being applied after nanoparticle exposure of *in vitro* systems. For example, the common 2′7-dichlorodihydrofluorescein (DCFH) assay [169, 170], used in many toxicity studies involving nanomaterials, would produce artefacts due to interaction of nanoparticles with the unstable dye. As a consequence, the specificity of the assay is significantly lowered. An optimized protocol for the DCFH-assay, so that it would deliver more reliable results, was developed by Zhao and Riediker (2014) [171], which they proposed to be the basis for a new standard. However, it is also difficult to find a suitable positive control for this test, as Roesslein *et al.* (2013) [172] demonstrated, so that the observed ROS-levels could be put into relation. Still, the optimized DCFH-assay currently seems to be the best choice to test for increased levels of ROS after nanoparticle exposure.

It has been demonstrated that the water solubility of nanoparticles depend on the particle size [173]. Solubility values, known for the bulk material, can therefore not simply be applied for nanomaterials and should therefore be obtained experimentally. Levels of ions, released into cellular media by nanoparticles, can be measured with a variety of methods. The most accurate method is Inductively Coupled Plasma Optical Emission Spectrometry (ICP-OES), which uses argon plasma to stimulate optical emission of elements. The signal intensity of the ion in question allows for the estimation of the ion-level in the sample. An alternative is Inductively Coupled Plasma Mass Spectrometry (ICP-MS).

6.6. Dustiness testing employing the nano-PMC

The task of a dustiness test is to describe the chance of humans being exposed to dust particles released from the nanomaterial. It consists of dust generation and monitoring of

emissions. If particle emissions are evident, they need to be characterized so that the dustiness test yields important information for the compilation of both bio-availability and bio-identity. Size-characterization of released nanoparticles yields important information for the bio-availability of the nanomaterial. By aerosol sampling with subsequent analysis with electron microscopy, the morphology of the emitted nanoparticles can be determined. Finally, by employing the nano-PMC in particle characterization, the apparent density of the released aerosol can be estimated, which is valuable information for both the bio-identity and conversion of monitored particle number concentration into mass concentration.

Recent studies showed that the dustiness of nanomaterials depends strongly on the method of dust generation [174, 175]. That is why, for regulatory testing, dustiness is usually assessed in regard to an identified exposure scenario. Accordingly, an appropriate mode for dust generation must be chosen. One common example of such a scenario is the transfer a freshly produced powder of a nanomaterial from the production line to a storage container via decantation. The dustiness test would employ a dust generator that mimics this process.

Common dustiness tests have been optimized to be used with powdery nanomaterials. The rotating drum test continuously reallocates a powder and picks up released nanoparticles with an air flow [174, 176, 177]. The continuous drop method transports powder to a drop pipe in which settling nanoparticles can be picked up by a side stream [178]. Both the rotating drum and continuous drop method are part of the EN 15051 standard for dustiness tests assessing the generation of fine dusts. As the rotating drum and continuous drop method both mimic particle generation during reallocation of powder, the vibrating bed aerosol generator is regarded as a simulation of dust generation by vibrations. In the vibrating bed aerosol generator, a fluidized bed is formed by a small air flow through the powder. Since it is relatively hard to generate a fluidized bed for nanomaterials, the powder bulk density is artificially lowered by vibrational excitation, which supports fluidization [179-181]. The vortex shaker also uses vibrations to create dust, not from a fluidized bed state but from the powder state, thereby employing a much higher flow rate [182, 183]. Dust generations from solids embedding nanomaterials comprise abrasion [184] and sanding [185, 186] amongst others.

It would be too demanding for a pre-regulatory testing procedure to compose exposure scenarios first and choose appropriate dust generators second, although the developer of the nanomaterial usually has specific future applications of the product in mind and

might be capable of identifying exposure scenarios for both workers and consumers on this basis. The developer should know whether the nanomaterial would be produced, handled and stored as a bulk powder or as a composite material. It is therefore proposed to conduct only one dustiness test that is chosen based on the state of the base material. The dustiness test must be standardized to allow ranking of results. The currently available standard for bulk powders suggests using either the rotating drum or continuous drop method. To the author's knowledge, there are no European standards available that define one or more tests for particle release from solid structures. However, a standard operation procedure for the testing for abrasive nanoparticle release from solids has been developed in the German project NanoGEM and has been suggested to be implemented into the ISO-TC229 standard.

Nanoparticle release is usually measured as the emitted particle concentration as a function of time. The condensation particle counter (CPC) is a suitable instrument to monitor the particle number concentration over the course of the dustiness test. However, current devices measure in the size range of 10-1000 nm. To obtain the concentration of the whole inhalable fraction (< 30μm), a combination of the CPC and another optical particle counter which counts larger particles must be applied.

To quantify the respiratory size fraction of the released aerosol, the use of a particle classifier measuring the aerodynamic particle size is suggested. Aerodynamic size classification can either be accomplished by inertial impaction or by time-of-flight spectroscopy. The current cut-off-diameter for respirable particle is 4 μm. Another method would be the employment of an SMPS system for the measurement of the particle electrical mobility number distribution with the nano-PMC acting as a mass filter. As described earlier, the determined apparent density and dynamic shape factor can then be used to convert the electrical mobility number distribution into an aerodynamic diameter number distribution (Eq. 1.1).

The total amount of released particles for each size fraction, inhalable and respirable, can be converted into released mass. These values, in ratio with the applied mass of the base nanomaterial for dust generation, yield size-range specific dustiness coefficients. To obtain information on particle mass, the nano-PMC is employed. In conjunction with a mobility-filter like the DMA, the apparent density of the aerosol can also be determined. Using Eq. 1.2, the particle number size distribution, obtained during size classification, can then be converted into a particle mass distribution.

An aerosol sampler like the electrostatic precipitator can be employed to collect emitted particles. With the help of electron microscopy, the released particles can be analysed for their morphology. Fibrous nanomaterials can therefore be assessed in regard to their potential to release high aspect-ratio particles.

Summary

Nanomaterials are designed on the molecular level, yielding properties and functions that are optimal for their desired application. Often, the nanomaterial even features properties that have not been observed for the bulk material. However, these features coincidentally fan public fears that nanomaterials can lead to new dangers for humans and the environment. Fuel is added to the fire by concerns about the current rapid growth of the number of innovations in nanotechnology, which challenges regulators to find suitable testing procedures to assess nanomaterials for their risk towards humans and the environment. Testing procedures that were established for bulk materials are often not applicable for nanomaterials because, for once, the characterization of nanomaterials usually requires specialized instrumentation not yet available.

Good examples are exposure limit values like Occupational Exposure Levels (OELs) that are given as mass concentrations of particles in air. The results of exposure assessments are usually evaluated in comparison with these values. Their definition requires either the ability to measure the mass concentration or knowledge about the mass of single particles when the number concentration is known. For ubiquitous fine dust particles, the mass concentration can be measured with gravimetrical methods. However, nanoparticles (ultra-fine dust) are so light that the accumulated mass cannot be measured even by the most sensitive scales. The other option of converting number to mass concentrations is more promising, since current instrumentation can measure the mobility equivalent size distribution of aerosols as well as the apparent densities of particles with certain mobility diameters. When both properties are available, the particle mass distribution and subsequently the mass concentration can be calculated. Measuring the mobility equivalent size distribution of an aerosol of nanoparticles is an already established procedure, accomplished by employing systems of particle classifiers and counters, like the Scanning Mobility Particle Sizer (SMPS). Information about mass and apparent density of nanoparticles, in turn, is difficult to obtain with currently available instrumentation. Commercial Particle Mass Classifiers (PMC) can hypothetically measure particle masses down to the equivalence of the mass of a sphere with standard density and a diameter of ~10 nm, but only with high uncertainty in the obtained value. In practice, these PMCs are mainly applied to classify fine dusts like urban aerosols. The first goal of this thesis was therefore to develop an optimized PMC, capable of classifying very small nanoparticles. Such a PMC might be readily employed to convert number

concentrations to mass concentrations of nanoparticles to meet the standards of particle exposure assessment.

PMCs basically balance out an electrostatic force acting on charged particles by a counteracting centrifugal force that depends on particle mass. Whether a particle penetrates a PMC is therefore decided by its mass-to-charge ratio. However, the window of "right" mass-to-charge ratios becomes wider the smaller the forces acting on the particle become. Unlike the electrostatic force, the centrifugal force cannot be easily adjusted to higher strength since it is limited by the rotational speed of the cylindrical capacitor, the core element of a PMC. Development of the new PMC thereby focussed on a drastic increase of the number of rotations per second it can reach. Another goal was to miniaturize the basic design of a commercial PMC to obtain a more compact instrument that is easy to employ in the field for e.g. workplace exposure assessment.

The result of this development process is the nano-PMC, introduced in chapter 3, a particle mass classifier that can measure particle masses down to the zeptogram-range, lowering the mass lower classification limit by almost two orders of magnitude. It can reach numbers of rotations that are almost three times as large compared to its competitors. Also, it is much smaller and lighter.

In a series of validation tests using spherical particles with known mass and size (and therefore density), the response of the nano-PMC was characterized and comprehended with the help of a particle trajectory-based numerical model. Response spectra for 50-nm polystyrene-latex (PSL) spheres and spherical ammonium sulphate particles of various mobility diameters were adequately predicted. In addition, by using the nano-PMC downstream a Differential Mobility Analyser (DMA), the apparent density of mobility classified particles could be measured. The apparent densities of both of the PSL and ammonium sulphate spheres could be determined which are equivalent to the known respective material densities. In addition, cubic sodium chloride particles and silver-agglomerates were classified. Due to the nano-PMC's capability to determine the mass of very small particles, the size-dependency of the dynamic shape factors, predicted to occur in the free molecular regime, could be confirmed by direct measurements of the apparent density of sodium chloride particles. The mass of silver aggregates, generated by diffusion-limited cluster-cluster aggregation after spark generation of silver nanoparticles, could be determined for mobility diameters as small as 5 nm. The relationship of particle mass and mobility for such aggregates, characterized by the mass-mobility scaling exponent, could be comprehended. These tests primarily proved that the nano-PMC works as desired but also demonstrated the vari-

ous potential applications of the instrument in particle characterization in both the field and the laboratory. The nano-PMC can therefore be seen as the missing link between established instrumentation for nanoparticle exposure assessment and the concurrent requirement to derive mass concentrations, comparable with exposure limit values.

For the determination of risk associated with nanomaterials, determination of their toxicity is of similar importance as exposure assessment. Basically every new nanomaterial introduced to the market and produced in higher amounts must undergo toxicity testing by *in vivo* studies, as stated by European chemical regulation laws. However, simply due to the high rate of new nanotechnology innovations, and also due to ethical reasons, the current practice of *in vivo* toxicity testing is under debate. Alternatives are *in vitro* models that try to predict health effects based on toxic effects observed in cell cultures. However, for inhalation toxicity, the basic requirement for such a prediction, namely that results for nanoparticles obtained with the *in vitro* test correlate with effects observed *in vivo*, are not met by the current generation of methods. Reasons can be found in the design of most *in vitro* tests. Firstly, the chosen mode of suspension exposure, i.e. sedimentation of nanoparticles suspended in the culture media on cells, can influence the chemistry of the particles so that the test yields false results. Secondly, suspension exposure requires cultivation and exposure to cells submerged in culture media. Such conditions are not found in the human lung. The other mayor goal of this thesis was therefore to develop an *in vitro* test more representative towards inhalation exposure.

The result was the Cyto-TP, introduced in chapter 4, an *in vitro* exposure system capable of depositing nanoparticles as aerosols onto living cells. Its basic design comprises monolayers of cells hosted at the air-liquid interface (ALI) inside a thermal precipitator. ALIs are configurations at which the cells are grown adherent on semipermeable membranes and left exposed to gas. The nutrient solution is provided through the holes of the membrane. This setup mimics the anatomy of the lung alveolus. By implementing ALI, particles can be deposited via thermophoresis, a mechanism providing gentle particle deposition as well as well-defined dosimetry.

First a prototype was constructed to conduct a proof-of-concept study which comprised two parts, evidence of enhanced particle deposition efficiency and the absence of any adverse effects of the exposure device itself on the cells, so that toxic effects can unambiguously be related to nanoparticle exposure. To mimic the pulmonary alveolus, monolayers of epithelial type-2 cancer cells (A549) were cultivated on transwell membranes at the air-liquid interface which were inserted into the Cyto-TP. Enhanced deposition was qualitatively proven

by exposing the cells to fluorescent polystyrene-latex (PSL) particles and subsequent detection by fluorescence microscopy. In a series of zero-exposures (particle-free and conditioned synthetic air), it was confirmed that the viability of the cells was not significantly lowered by being situated in the Cyto-TP. However, cell viabilities of applied cells were still lower compared to the cell viability of cells left in the incubator for control. Reasons were identified and related to the handling of the device. Variances in transwell dimensions were evident so that deformation of their membranes could be observed after being inserted into the Cyto-TP. In addition, maintaining the temperatures of both plates of the thermal precipitator proved to be difficult. A significant effect on the temperature of the culture medium by the warm plate was observed, which was that the hosting conditions of the Cyto-TP for the cells were not optimal. It was decided to construct a second, optimized, prototype, based on the results of the proof-of-concept study.

The second prototype of the Cyto-TP, introduced in chapter 5, showed better temperature control by employing maintenance by tempered water circulation. Part of the temperature control was pins that could be lowered into the nutrient solution so that heat absorbed from the warm plate could be conducted. The result was the maintenance of stable temperatures in all critical parts of the Cyto-TP. The new design also comprised three parallel aerosol flow channels to allow for three parallel exposures during one session. That way, the statistical significance of the results measured after exposure could be strengthened. Similarly, by using larger transwell membranes, the statistical significance of certain toxicity-assays requiring higher cell numbers could be increased. Particle deposition proved to be similar as in the Cyto-TP prototype-1. However, adoption of the cell cultivation protocol, introduced in chapter 4 and applied or the original Cyto-TP, proved to be difficult.

In addition to the construction of a second prototype for the Cyto-TP, a first design was created that combines the Cyto-TP technology with an established commercial air-liquid interface exposure system. The so-called Vitrocell® CF exposure module, initially applied for toxic gas exposure, was modified in a rather simple way to allow deposition via thermal precipitation. The concept is also introduced in chapter 5. First results show nanoparticle deposition efficiencies, increased by up to three orders of magnitude compared to the original version. This version of the Cyto-TP was used to explore adverse effects on A549 cells of deposited barium sulphate nanoparticles which were known to have no acute toxic effects on cells. To express the dose in several relevant metrics, namely number, mass, volume and surface area, the nano-PMC was applied to measure the apparent density of the aerosol. As expected, the cells that were exposed to barium sulphate nanoparticles showed no biological response that was different to control cells, corroborating the statement that firstly barium

sulphate is not acute toxic and secondly that the exposure conditions would have no negative effects on cells.

The practical work shown in this thesis was the design, construction and validation of prototypes of two devices that at first glance don't have anything in common apart from being designed to work with aerosols. However, both serve the purpose in closing instrumental gaps for risk assessment of particulate nanomaterials. This becomes visible in chapter 6, in which the rationale and concept of a pre-regulatory testing strategy is presented. 'Pre-regulatory' means that the testing procedure should be applied after certain steps in the development process of the nanomaterial, before it is introduced into the market. The advantages of employing such an innovation-accompanying routine are manifold, above all the promotion of sustainable nanotechnology by safety-by-design. This procedure answers the requirements stated by the European precautionary approach to risk management that basically prompts innovators to also desire safety for humans and the environment for their product, apart from its functionality.

The approach to pre-regulatory testing employs both the nano-PMC and the Cyto-TP. The Cyto-TP is used as an *in vitro* toxicity test conducted at the beginning of the testing routine. Its results define the path that leads to the determination of the so-called bio-identity of the nanomaterials, a fingerprint of particle properties that evidently mediate inhalation toxic effects. Part of the the routine is a dustiness test that employs the nano-PMC to obtain information about the apparent density of the particulate form of the nanomaterials which is part of its bio-identity. In addition, the nano-PMC can be used to measure the mass concentration of the aerosol emitted during the dustiness test to derive the dustiness coefficients of the inhalable and respirable dust fractions. These numbers define the bio-availability of the nanomaterial with regard to inhalation, i.e. the possibility of the nanomaterial being transported as dust into the breathing zone of humans.

Unknown risks fan fears of the general public that nanotechnology is accompanied by unidentified dangers to humans and the environment. These fears could ultimately lead to a loss in confidence in what would otherwise be a promising source of innovations beneficial for human society. The instruments that are introduced in this thesis were developed for closing instrumental gaps in order to provide a solid basis for risk assessment associated with nanoparticulate materials.

Samenvatting

Nanomaterialen worden ontworpen op een moleculair niveau waardoor eigenschappen en functies gecreëerd worden die optimaal zijn voor de gewenste toepassing. Vaak beschikken de nanomaterialen zelfs over eigenschappen die niet gemeten werden in het bulkmateriaal. Deze eigenschappen voeden echter de angst van het publiek dat nanomaterialen nieuwe gevaren kunnen opleveren voor mens en milieu. Deze angst wordt gevoed door zorgen over de snelle groei van innovaties in de nanotechnologie. Inspecteurs worden uitgedaagd om methodes te ontwikkelen waarmee risico's voor mens en milieu gemeten kunnen worden. De testmethodes voor bulkmateriaal zijn vaak ongeschikt voor het inspecteren van nanomaterialen omdat voor het classificeren van nanomaterialen gespecialiseerde instrumenten vereist zijn. Deze instrumenten zijn momenteel niet verkrijgbaar.

Blootstellingswaarden zoals 'Occupational Exposure Levels (OELs)', grenswaardes van beroepsmatige blootstelling aan massaconcentraties van deeltjes in de lucht, zijn hiervan een duidelijk voorbeeld. De resultaten van blootstellingsmetingen worden in principe geëvalueerd op basis van deze waarden. Voor een correcte waardebepaling moet het mogelijk zijn om de massaconcentratie te meten of dient kennis ter beschikking te zijn over de deeltjesconcentratie. De massaconcentratie van de overal aanwezige fijnstofdeeltjes kan gemeten worden met gewichtsanalyses. Nanodeeltjes (zeer fijnstof) zijn echter zo licht dat de geaccumuleerde massa niet gemeten kan worden, zelfs niet met zeer gevoelige meetapparatuur. Maar het converteren van deeltjesconcentraties naar massaconcentraties is een veelbelovende optie omdat de huidige instrumenten de mobiliteit kunnen meten op basis van de verdeling van de aërosolen en de schijnbare dichtheid van deeltjes binnen bepaalde mobiliteitsdiameters. Als beide eigenschappen beschikbaar zijn kunnen de deeltjesmassadistributie en de massaconcentratie gemeten worden. Het meten van de mobiliteit op basis van de verdeling van deeltjes van een aërosol van nanodeeltjes is een gestandaardiseerde methode waarbij gebruik gemaakt wordt van deeltjesclassificatie en deeltjestelsystemen, zoals de 'Scanning Mobility Particle Sizer (SMPS)'. Informatie over massa- en schijnbare dichtheid van deeltjes is dan weer moeilijk te verkrijgen met momenteel beschikbare instrumenten. Commerciële 'Particle Mass Classifiers (PMC)' kunnen in theorie deeltjesmassa's meten tot op het niveau van de massa van een bol met een standaard dichtheid en een diameter van of ~10 nm. Maar de gemeten waarde is alsnog zeer onzeker. In de praktijk worden deze PMC's vooral gebruikt om fijnstof zoals aërosolen in steden te meten. De belangrijkste doelstelling van dit proefschrift was dan ook het ontwikkelen van een geoptimaliseerde PMC waarmee

zeer klein nanodeeltjes gemeten kunnen worden. Een dergelijke PMC kan heel eenvoudig gebruikt worden om deeltjesconcentraties te converteren naar massaconcentraties van nanodeeltjes. Op deze manier kan voldaan worden aan de standaardprocedures met betrekking tot blootstelling aan deeltjes.

In principe compenseren PMC's de werking van elektrostatische kracht op geladen deeltjes door het neutraliseren van de centrifugale kracht die afhankelijk is van de deeltjesmassa. Of een deeltje de PMC binnenkomt is dus afhankelijk van de lading/massa-verhouding. Maar het spectrum van 'juiste' massa/lading-verhoudingen wordt een stuk breder als de op de deeltjes inwerkende krachten kleiner zijn. In tegenstelling tot elektrostatisch kracht kan centrifugale kracht niet eenvoudig aangepast worden aan een hogere weerstand. Centrifugale kracht wordt beperkt door de rotatiesnelheid van de cilindervormige condensator, het kernelement van een PMC. Bij de ontwikkeling van een nieuwe PMC lag de focus dan ook heel sterk op het drastisch verhogen van de te realiseren rotaties per seconde. Een andere doelstelling was om het basisontwerp van een commerciële PMC te miniaturiseren om zo een compacter instrument te verkrijgen dat heel gemakkelijk te gebruiken is voor een beoordeling van de blootstelling in het veld c.q. op de werkplek.

Het resultaat van dit ontwikkelingsproces is de nano-PMC, besproken in hoofdstuk 3, een deeltjesmassaclassificatie-instrument dat deeltjesmassa kan meten tot het niveau van een zeptogram. Hierbij wordt de lagemassaclassificatie met twee ordes van grootte verkleind. Er kunnen rotatiesnelheden gerealiseerd worden die wel drie keer groter zijn dan de snelheden die gemeten werden door andere instrumenten. En het apparaat is ook aanzienlijk kleiner en lichter.

In een reeks van valideringstests waarbij gebruik gemaakt werd van bolvormige deeltjes waarvan de grootte en massa (en dus ook de dichtheid) bekend was, werd de responsie van de nano-PMC gekarakteriseerd en geanalyseerd met behulp een numeriek model waarbij uitgegaan wordt van het door de deeltjes afgelegde traject. Responsiespectra van 50-nm polystyreenlatex-(PSL)-bollen en bolvormige ammoniumzwaveldeeltjes met verschillenden mobiliteitsdiameters werden nauwkeurig voorspeld. Als naast de nano-PMC met de stroom mee een Differential Mobility Analyser (DMA) gebruikt wordt kon de schijnbare mobiliteitsdichtheid van bepaalde deeltjes gemeten worden. Van zowel het polystreenlatex en de ammoniumzwavelbolletjes kon de schijnbare dichtheid bepaald worden die overeenkomt met de bekende materiaaldichtheid van deze stoffen. Bovendien werden kubische natriumchloridedeeltjes en zilveragglomeraties geclassificeerd. Omdat nano-PMC's de massa van zeer kleine deeltjes kan bepalen, kan de grootteafhankelijkheid van dynamische vormfacto-

ren, die zullen plaatsvinden in het moleculair stelsel, bevestigd worden via een directe meting van de schijnbare dichtheid van de natriumchloridedeeltjes. De massa van zilveraggregaten gegenereerd door diffusiebeperkte cluster-cluster-aggregatie na vonkopwekking van zilvernanodeeltjes kon bepaald worden voor mobiliteitsdiameters tot 5 nm. De relatie van deeltjesmassa en mobiliteit van dergelijke aggregaten, gekenmerkt door de massa-mobiliteit-schaalexponenten, kon gemeten worden. Dergelijke tests toonden in principe aan dat de nano-PMC werkt zoals gewenst en toonden eveneens diverse mogelijkheden aan van de nano-PMC om deeltjes te karakteriseren, zowel in het veld als in het laboratorium. De nano-PMC kan dan ook beschouwd worden als de 'missing link' tussen standaardapparatuur voor het meten van blootstelling aan nanodeeltjes en de concrete eis om massaconcentraties te kunnen afleiden die vergelijkbaar zijn met de blootstellingsgrenswaarden.

Voor het vaststellen van risico's van nanomaterialen is het bepalen van hun toxiciteit net zo belangrijk als een blootstellingsmeting. Volgens de Europese regelgeving m.b.t. tot chemische stoffen moet van elk nanomateriaal dat op de markt gebracht wordt de toxiciteit via een in-vitro-test vastgesteld te worden. Omdat recentelijk heel veel nanotechnologische innovaties op de markt gebracht worden, maar ook om ethische redenen, staat de huidige praktijk van in-vitro-toxiciteitstests ter discussie. Alternatieven hiervoor zijn in-vitro-modellen die de gezondheidsrisico's proberen te bepalen op basis van de toxische effecten die in celstructuren vastgesteld werden. Met de huidige testmethodes kunnen de basisvereisten voor een dergelijke voorspelling, nl. dat de in-vitro verkregen resultaten voor nanodeeltjes overeenkomen met de in vivo vastgestelde effecten, niet gerealiseerd worden. Het ontwerp van de meeste in-vitro-tests is hiervoor de belangrijkste reden. Enerzijds kan de gekozen ophangingsblootstelling, d.w.z. de sedimentatie van nanodeeltjes in het kweekmedium op cellen, de chemische samenstelling van de deeltjes beïnvloeden en zo tot foute resultaten leiden. Anderzijds vereist ophanging het kweken van en blootstellen aan de in het kweekmedium ondergedompelde cellen. Deze condities worden niet vastgesteld in menselijk longen. Een andere belangrijke doelstelling was dan ook het ontwikkelen van een in-vitro-test die representatiever was m.b.t. inhalatieblootstelling.

Dit leidde tot de Cyto-TP, besproken in hoofdstuk 4, een in-vitro-blootstellingssysteem dat nanodeeltjes als aërosolen kan plaatsen op levende cellen. Het basisontwerp bestaat uit monolaag van cellen geënt in de air-liquid interface (ALI) binnenin de thermische precipitator. ALI's zijn configuraties waarop cellen gekweekt worden, die zich hechten aan halfdoorlatende membranen en blootgesteld worden aan gas. De voedingsoplossing wordt via de openingen in de membranen ingebracht. Op deze manier wordt de anatomie van de longblaasjes geïmiteerd. Door het implementeren van ALI worden cellen direct blootgesteld aan

gas waardoor zwevende stofdeeltjes via thermoforese kunnen bezinken. Een mechanisme met een zachte deeltjesbezinking en een perfect gedefinieerde dosismeting.

Eerst werd een prototype gemaakt om een proof-of-concept-test uit te voeren. Deze test bestond uit twee delen: onderzoek naar een hoger efficiëntie van de deeltjesafzetting en onderzoeken of de cellen op geen enkele manier negatief beïnvloed worden door de blootstelling aan het apparaat zelf. Alleen dan kan er met zekerheid vastgesteld worden dat de toxische effecten uitsluitend te wijten zijn aan de blootstelling aan nanodeeltjes. Voor het nabootsen van longblaasjes werden monolagen van epiteel-type-2-kankercellen (A549) gekweekt op Transwell-membranen op de air-liquid-interface die in de Cyto-TP geplaatst wordt. Verhoogde bezinking wordt kwalitatief vastgesteld door het blootstellen van de cellen aan fluorescerende polystyreenlatex-(PSL)-deeltjes, gevolgd door vaststelling met de fluorescentiemicroscoop. In een aantal nulblootstellingen (geconditioneerde, deeltjesvrije synthetische lucht) werd bevestigd dat de levensvatbaarheid van de cellen niet significant lager was door de blootstelling in de Cyto-TP. De levensvatbaarheid van de gebruikte stellen was echter nog steeds lager in vergelijking met de levensvatbaarheid van de cellen die ter controle achterbleven in de incubator. Deze afwijkingen hielden verband met de manier waarop het apparaat gebruikt werd. Variaties in de Transwellafmetingen waren duidelijk, waardoor na het inbrengen in de Cyto-TP-vervormingen vastgesteld konden worden. Daarnaast bleek het moeilijk om beide platen van de thermische precipitator op de juiste temperatuur te houden. De warmteplaat had een significant invloed op het kweekmedium, nl. dat de condities van de Cyto-TP niet ideaal waren voor de cellen. Daarom werd besloten om een nieuw, verbeterd prototype te maken, waarbij rekening gehouden werd met de resultaten van het proof-of-concept-onderzoek.

Bij het tweede prototype van de Cyto-TP, besproken in hoofdstuk 5, kon de temperatuur door gebruikmaking van watercirculatie beter gecontroleerd worden. Belangrijk onderdeel van deze temperatuurcontrole waren pinnetjes die in de voedingsoplossing zakten waardoor de hitte van de warmteplaat kon geabsorbeerd worden. Dit leidde tot stabiele temperaturen in alle kritische onderdelen van de Cyto-TP. Het nieuwe ontwerp omvatte ook drie parallelle aërosolstroompijpen waardoor in één sessie drie blootstellingen tegelijk mogelijk werden. Hierdoor werd de statistische betrouwbaarheid van de gemeten resultaten na blootstelling verhoogd. En door het gebruiken van grotere transwell-membranen werd de statistische betrouwbaarheid van de toxische test waarbij een hoger aantal cellen nodig was eveneens verhoogd. De afzetting van de deeltjes bleek identiek aan de afzetting in Cyto-TP-prototype-1. Het aanpassen van het celkweekprotocol, besproken in hoofdstuk 4 en toegepast bij de originele Cyto-TP, bleek echter moeilijk.

Tegelijkertijd met de constructie van een tweede Cyto-TP werd een tweede ontwerp gemaakt waarbij de Cyto-TP-technologie gecombineerd werd met een beproefd commercieel air-liquid-interface-blootstellingssysteem. De zogenaamde Vitrocell®- exposure module, oorspronkelijk toegepast voor blootstelling van giftige gassen werd op een vrij eenvoudige manier aangepast waardoor bezinking via thermische afscheiding mogelijk wordt. Dit concept wordt eveneens besproken in hoofdstuk 5. De eerste resultaten laten afzettingen van nanodeeltjes zien met een orde van grootte van drie keer de bezinking van de originele versie. Deze versie van de Cyto-TP werd gebruikt om de negatieve effecten van A549 cellen van bezonken zwavelnanodeeltjes te meten omdat deze geen directe giftige effecten op cellen hebben. Om de dosis te vermelden in de desbetreffende, relevante meetwaarden, nl. aantal, massa, volume en oppervlaktes, werd de nano-PMC gebruikt om de waarschijnlijke dichtheid van de aërosol te meten. Zoals verwacht, hadden de cellen die blootgesteld werden aan bariumsulfaatnanodeeltjes geen andere biologische reactie dan de controlecellen. Hiermee wordt ten eerste bevestigd dat bariumsulfaat niet acuut toxisch is en ten tweede dat de blootstellingscondities geen negatief effect hebben op de cellen.

Het praktische werk dat beschreven wordt in dit proefschrift omvatte het ontwerp, de constructie en het testen van prototypes van twee apparaten die op het eerste zicht, behalve dat ze ontworpen zijn om te werken met aërosolen, weinig gemeenschappelijks hebben. Beide apparaten kunnen echter het probleem van onvoldoende beschikbare apparatuur voor de risicobeoordeling van fijnstofnanodeeltjes enigszins oplossen. Dit wordt duidelijk gemaakt in hoofdstuk 6. In hoofdstuk 6 worden het basisprincipe en het concept van 'pre-regulatory'-testprocedures besproken. 'Pre-regulatory' betekent in deze context dat na bepaalde stappen in de ontwikkeling van nanomaterialen testprocedures gevolgd moeten worden voordat het nanomateriaal op de markt gebracht wordt. De voordelen van de toepassing van een dergelijke vernieuwende procedure zijn velerlei, waarbij het verbeteren van het imago van duurzame nanotechnologie via 'safety-by-design' een belangrijk voordeel is. Deze procedure voldoet aan de eisen zoals vermeld in Europese voorzorgsbenadering risicobeheersing. Deze voorzorgsbenadering verplicht ontwikkelaars van nieuwe producten ertoe om nieuwe producten te ontwikkelen die niet alleen veilig zijn in het gebruik, maar ook geen gevaar opleveren voor mens en milieu.

De genoemde voorzorgsbenadering geldt zowel voor de nano-PMC alsook voor de Cyto-TP. De Cyto-TP wordt gebruikt als een in-vitro-toxiciteitstest aan het begin van de testprocedure. De resultaten van deze test creëren een pad dat leidt tot het bepalen van de zogenaamde 'bio-identiteit' van nanomaterialen, een vingerafdruk van de eigenschappen die toxische effecten duidelijk weergeeft. Deel van de procedure is een stofbelastingtest waarbij

gebruik gemaakt wordt van de nano-PMC om informatie te verkrijgen over de waarschijnlijke dichtheid van het gedeelte van de nanomateriaal dat niet tot de bio-identiteit behoort. Daarnaast kan de nano-PMC gebruikt worden om de massaconcentratie van de tijdens de fijnstoftest vrijgekomen aërosolen te meten, om zo het fijnstofcoëefficiënt van de inhaleer- en inadembare stofhoeveelheden te meten. Deze aantallen bepalen de biobeschikbaarheid van nanomateriaal met betrekking tot inhalatie, d.w.z. de kans dat het nanomateriaal als stof in de luchtwegen van mensen kan komen.

Onbekende risico's voeden de angst bij het grote publiek dat nanotechnologie gepaard gaat met ongekende gevaren voor mens en milieu. Deze angst kan uiteindelijk leiden vertrouwensverlies in de ontwikkeling van producten en materialen die zeer positieve effecten kunnen hebben voor de maatschappij. De in dit proefschrift besproken instrumenten werden ontwikkeld om de beperkingen van oudere instrumenten op te heffen en tevens een stevige basis te creëren voor het beoordelen van risico's die zouden kunnen ontstaan door het gebruik van nanomaterialen.

Appendix A: Response spectrum of the nano-PMC

This script for Mathematica 10.0 calculates the response spectrum of the experimental setup that first classifies a mass-mobility-distributed aerosol on the basis of mobility using a DMA and subsequently on the basis of mass using the nano-PMC. The input is a particle number concentration where the particles are distributed in mobility. The systems response (output) is the particle number concentration at the outlet of the nano-PMC. The spectrum of responses is the outlet particle number concentration as a function of nano-PMC operating conditions (here, only the voltage U is variable).

All comments are black whereas all script-related text is blue (dark cyan for running variables).

The script starts with loading different function-packages to solve differential equations numerically.

```
Needs["DifferentialEquations`NDSolveProblems`"];
Needs["DifferentialEquations`NDSolveUtilities`"];
Needs["FunctionApproximations`"];
```

Definition of functions describing Stolzenburg-McMurry equations governing the DMA (see chapter 2.2.2), where ϵ is defined via the error function, Zp is the centroid electrical mobility, σ is the standard deviation, G is the DMA-geometry factor, Iγ described the laminar velocity profile in in the DMA flow channel. diff represents the diffusion coefficient and Z the mobility. Cc is the Cunningham-Slip correction factor. r1, r2 and L define the DMA dimenions, radius inner cylinder, radius outer cylinder and length respectively. Qs and Qa are the DMA shealth flow and sample flow rates respectively, β their quotient. UDMA defines the potential difference between inner and outer cylinder of the DMA. density is the apparent density and d the diameter of the particles.

```
ϵ[x_] := x Erf[x] + Exp[-x^2] / Sqrt[π]

Zp[V0_,Qs_,r1_,r2_,L_,Z_] := Z/((2Qs)/(4π)) Log[r2/r1]/(L V0)
```

```
σ[G_,diff_,L_,Qs_] := Sqrt[ Abs[G]*(4π*L*diff)/(2Qs) ]

G[β_,γ_]:=(4(1+β)^2)/(1-γ) (Iγ[γ]+(1/(2(1+β)κ^2))^2)

Iγ[X_]:=((1/4)(1-X^2)(1-X)^2+(5/18)(1-X^3)(1-X)Log[X]+
(1/12)(1-X^4)Log[X]^2)/((1-X)(-(1/2)(1+X)Log[X]-(1-X))^2)

diff[d_]:=((1.38*10^-23)300)/(3π(1.81*10^-5)d)
(1+(2*66*10^-9)/d*(1.142+0.558*Exp[-0.999*d/(2*66/*10^(-9))]))

Z[d_]:=(1*1.602*10^-19 Cc[d])/(3π(1.81*10^-5)d)
Cc[d_]:=(1+(2*66*10^-9)/d*(1.142+0.558*Exp[(-0.999*d)/(2*66*10^-9)]))

r1=0.00935; r2=0.0196; L=0.114; κ=L*r2/(r2^2-r1^2); γ=(r1/r2)^2;

Qs=3000/60/1000000; Qa=1500/60/1000000; β=Qa/Qs; UDMA=544; density=1050; d=50*10^
-9;
```

The particle number is characterized by the mobility number distribution dZlognormal that is assumed to be lognormal. N is the total particle number, σg the geometric standard deviation. The centroid mobility Zp functions as the mean electrical mobility.

```
dZlognormal[N_,Zp_,σg_,Z_] := N/(Sqrt[2π]*Log[σg])*Exp[-((Log[Z]-
Log[Zp])^2/(2Log[σg]^2))]
```

The classified mobility distribution is obtained by convolving dZlognormal with the DMA-transfer function. The script produces a list ResultingdZ of electrical mobilities based on the convolution. The length of the list is given by the total number of electrical mobilities in the resulting classified mobility number distribution.

```
ConvolveDMA[NN_,P_,σ_] := Transpose[{ Table[x,{x,0.1,5,0.1}],
Table[NIntegrate[dZlognormal[NN,1,σ,x]*
(P/(Sqrt[2]β)(ϵ[((x-τ)-(1+β))/(Sqrt[2]P)]+ϵ[((x-τ)-(1-β))/(Sqrt[2]P)]-2ϵ[((x-τ)-
1)/(Sqrt[2]P)])),
{τ,-∞,∞}],{x,0.1,5,0.1}]}
];

ResultingdZ = Re[ ConvolveDMA[10,σ[G[β,γ],diff[d],L,Qs],1.7] ];
```

The list ResultingdZ (normalized by the centroid electrical mobility) is converted into a list of electrical mobilities, electrical mobility diameters DM and particle masses M.

```
xZ[V0_] := Table[
ResultingdZ[[i,1]]*(2Qs)/(4π)Log[r2/r1]/(L*V0),{i,1,Length[ResultingdZ]}
]

xD[V0_] := Table[
FindRoot[(1*1.602*10^-19Cc[a])/(3π(1.81*10^5))==
xZ[V0][[i]]*a,{a,d}][[1,2]],{i,1,Length[ResultingdZ]}
]

xM[V0_,ρ_] := xD[V0]^3(π/6)*ρ

DM[V0_] := Transpose[
{xD[V0], Table[ResultingdZ[[i,2]],{i,1,Length[ResultingdZ]}]}
];

M[V0_,ρ_] := Reverse[ Transpose[
{xM[V0,ρ],Table[ResultingdZ[[i,2]],{i,1,Length[ResultingdZ]}]}]
];
```

The next part numerically calculates the particle trajectory s in the nano-PMC from the particle equations of motion. a, b, c are constants that are calculated by the operating conditions of the nano-PMC. m is a list of particle masses, Vmean is the mean flow velocity calculated by the volume flow rate over the cross-sectional area of the nano-PMC flow channel. δ is the deviation from the original particle path due to diffusion. s is the component of the particle trajectory perpedicular to the rotational axis and is nummerically solved with iteration steps defined by prec. The differential equation is coupled to the equation of motion xx of the particle that gives the component parallel to the rotational axis, given by Vx, the Poiseuille flow profile.

```
a[w_,d_,ρ_] := 2/3 d^3 π3 ρ w^2

b[U_,q_] := (U q)/Log[0.019/0.015]

m[d_,ρ_] := (π ρ d^3)/6

c[d_] := 3π (1.81 10^-5)d Cc[d];

Vmean[Q_] := ((Q/60/1000000)/(π(0.019^2-0.015^2)));
```

```
δ[d_,t_] := Sqrt[2 diff[d] t];

s[Q_,U_,q_,w_,d_,ρ_,H_] := NDSolve[
{c[d](y'[t])==(a[w,d,ρ]y[t]-b[U,q]/y[t]),y[0]==H},y,{t,0.,10},MaxSteps->prec
];

Vx[Q_,H_] := (3/2)*Vmean[Q](1.-4(H/0.004)^2)

xx[Q_,H_,t_] := Vx[Q,H] t
```

Using these equation, the particle trajectories are calculated by the loop Partikel. The user defines the operating conditions of the nano-PMC and known particle properties that are U (nano-PMC voltage), q (particle charge), Q (nano-PMC flow rate), rpm (nano-PMC frequency), ρ (particle density) and ϵ which is the running variable of the loop, indexing the particle of the list w that is created subsequently from the particle mass distribution M.

```
Partikel[U_,q_,Q_,rpm_,ρ_,ϵ_]:=
Do[
 Δ={};
 Δ=Table[RandomReal[NormalDistribution[0,1]],{i,0,10 ,step}];
        H=RandomReal[{0.0161,0.0179}];
        Producey={};
        ProduceVy={};

         Do[
             Ap-
pendTo[Producey,(y[i]+δ[w[[ϵ,k]],step]*Δ[[1+i*(1/step)]])/.s[Q,U,q,rpm,w[[ϵ,k]],ρ,H][[1]]],
             {i,0,10,step}
];

        ProduceVx={};
        Do[
            AppendTo[ProduceVx,Vx[Q,Select[Producey,0.015<#<0.019&]
-0.017][[i]]],{i,1,Length[Select[Producey,0.015<#<0.019&]]}
            ];

            Producex  = Table[(Select[ProduceVx,#>0&][[i]])*
step,{i,1,Length[Select[ProduceVx,#>0&]]}];
            Producexx=Table[Sum[Producex[[i]]+δ[w[[ε,k]],step]*Δ[[i]],{i,1,N}],
{N,1,Length[Producex]}];
         AppendTo[Partikelkurven,Transpose[{Producexx,
```

```
Take[Producey,Length[Producexx]]}]],
 { k,1,Length[w[[ϵ]]]}
  ]
```

The nano-PMC transfer function is calculated on the basis of voltage. For the calculations, several lists and variables must be declared. The lists are empty before they are filled with elements by the loop above. Nano-PMC operating conditions are defined here, as well as precision parameters of the trajectory determination and resolution of the transfer functions of the nano-PMC to be calculated. flowrate and RPM are the volume flow rate and number of rotation of the nano-PMC. step is the time step size of for the numerical determination of s, lowend, topend and stepvoltage are the first voltage, last voltage and voltage step size of the transfer function. Diffusion reduces the transfer rates.

```
Partikelkurven = {};
Partikelvelocity = {};
Partikelvelocity2 = {};
Transferraten = {};
Partikelkurven2 = {};
Partikelkurven3 = {};
Producey = {};
ProduceVy = {};
ProduceVx = {};
Producex = {};
Producexx = {};
CollectedTR = {};
ToF = {};
ToF2 = {};
k = 1;
step = 0.01;
prec = 1000;
flowrate = 300;
RPM = 9000;
lowend = 10;
topend = 400;
stepvoltage = 10;
TFstepsize = 1;
particlenumber = 30;
effectiveLength = 0.1;
μ[d_,Q_] := (π diff[d] (0.1) (0.019+0.015))/(Q (0.019-0.015));
P1[d_,Q_] := 1-2.96μ[d,Q]^(2/3)+0.4  μ[d,Q]
P2[d_,Q_] := 0.91 Exp[-7.54 μ[d,Q]]+0.0531 Exp[-85.7 μ[d,Q]]
loss[d_,Q_] := Evalu-
ate[{μ[d,(Q/60/1000000)],P1[d,(Q/60/1000000)],P2[d,(Q/60/1000000)]}]
```

The next part is the actual calculation, where the do-loop is running with the voltage and the subloop calculates the transfer function for each voltage.

```
Do[
    Partikelkurven={};
Partikelvelocity={};
Partikelvelocity2={};
Transferraten={};
Partikelkurven2={};
Partikelkurven3={};
Producey={};
ProduceVy={};
ProduceVx={};
Producex={};
Producexx={};
ToF={};
    ToF2={};
diameters={};


w = Table[
Table[Sqrt[6(1.602*10^(-19)*j/
(4π^2(RPM/60)^2*Log[0.019/0.015])]/density/π,3],{i,1,particlenumber,1}],{j,U-
(0.8*U),U+(4*U),U/(20*TFstepsize)}
];

Do[
 Partikel[U,1*1.692 10^-19,flowrate,RPM/60,density,ϵ];
 AppendTo[Partikelkurven2,Partikelkurven];
 Partikelvelocity = {};
 Partikelkurven = {},
 {ϵ,1,Length[w],1}
 ];


diameters = Table[First[w[[k]]],{k,1,Length[w]}];


Do[
Partikelkurven3 = Table[
Part[Partikelkurven2[[k,j]],Count[Table[First[ Part[Partikelkurven2[[k,j]], i]] < effectiveLength,
{i, 1,Length[Partikelkurven2[[k,j]]]}],True]],
```

```
{j,1,Length[Partikelkurven2[[k]]]}
];
Transferrate = Count[Table[0.016 < Last[Partikelkurven3[[i]]] < 0.018,
{i, 1, Length[Partikelkurven3]}],
True]/Length[Partikelkurven2[[k]]]//N;

AppendTo[Transferraten,Transferrate*loss[d,flowrate][[2]]];
 Partikelkurven3={},
 {k,1,Length[Partikelkurven2]}
 ];

AppendTo[CollectedTR,Transpose[{diameters^3
(π/6)*density,Transferraten}]];

{U,lowend,topend,stepvoltage}
 ]
```

This loop generates list CollectedTR in which all transfer functions are collected. Export of the data to a ASCII file.

```
Table[Export["C:\\Users\\Dirk\\Desktop\\paperPMC\\Datensaetze\\
TF_"<>ToString[i]<>"_"<>ToString[Date[][[1]]]<>"_"<>
ToString[Date[][[2]]]<>"_"<>
ToString[Date[][[3]]]<>"-particle_"<>
ToString[d/10^-9]<>"nm_"<>"_"<>
ToString[density]<>"kgpcm3"<>"-settings_"<>
ToString[flowrate]<>"lpm_"<>
ToString[RPM]<> "rpm.dat",CollectedTR[[i]]],
{i,1,topend/stepvoltage}
] ;
```

The next part first declares empty lists for the fit of the transfer functions as well as mass distribution for the subsequent convolution for the prediction of the nano-PMC response. The data is imported back, so that this part can be repeated without calculating the transfer functions again.

```
FITTF = {};
FITMASS = {};
TFimp = {};
TFimport = {};
fit1 = {};
ConvertedU = {};
```

```
fit2 = {};
MASS = M[UDMA,density];
Do[
TFimp = Import["C:\\Users\\Dirk\\Desktop\\paperPMC\\Datensaetze\\TF_"<>
ToString[j]<>"_"<>ToString[Date[][[1]]]<>"_"<>ToString[Date[][[2]]]<>"_"<>
ToString[Date[][[3]]]<>"-particle_"<>
ToString[d/10^-9]<>"nm_"<>"_"<>ToString[density]<>"kgpcm3"<>"-settings_"<>
ToString[flowrate]<>"lpm_"<>ToString[RPM]<>"rpm.dat"];

 AppendTo[TFimport,TFimp],
 {j,1,topend/stepvoltage}
];
```

The next loop converts the mass distribution into a voltage distribution based on Eq. 2.37 and fits a lognormal distribution to the data. A convolution becomes much more simple when both functions are well-defined, therefore the transfer functions data is also fitted with a lognormal distribution.

```
Do[

CONVERTVOLTAGE=Transpose[{
Table[TFimport[[j,i,1]]/(1.602*10^-19/
(4π2(RPM/60)^2*0.017^2*Log[0.019/0.015])),
{i,1,Length[TFimport[[j]]]}],
Table[TFimport[[j,i,2]],{i,1,Length[TFimport[[j]]]}]
}];

AppendTo[ConvertedU,CONVERTVOLTAGE];

CONVERTVOLTAGE2 = Transpose[{
Table[MASS[[i,1]]/(1.602*10^-19/(4π2
(RPM/60)^2*0.017^2*Log[0.019/0.015])),{i,1,Length[MASS]}],
Table[MASS[[i,2]],{i,1,Length[MASS]}]
}];

TFMODEL = A*Exp[-((-p+Log[x])^2/(2o^2))]/(Sqrt[2 π] x o);

MASSMODEL = A*Exp[-((-p+Log[x])^2/(2o^2))]/(Sqrt[2 π] x o);

 fit1 = FindFit[
CONVERTVOLTAGE,TFMODEL,{A,o,p},x, Gradient->"FiniteDifference",
Method->NMinimize
```

```
];

 fit2=FindFit[
CONVERTVOLTAGE2,MASSMODEL,{A,o,p},x,Gradient->"FiniteDifference"
];

 AppendTo[FITTF,fit1];
 AppendTo[FITMASS,fit2];

 fit1={};
 fit2={},
 {j,1,Length[TFimport]}
]

TFFIT[x_]:=TFMODEL/.FITTF;
MASSFIT[x_]:=MASSMODEL/.First[FITMASS];
```

The response is calcutated from the convolution of both fit-functions (voltage number distribution with voltage based transfer function). The response spectrum comprises the results of the convolution of the voltage number distribution with each transfer functions.

```
Convolution[x_]:=Integrate[MASSFIT[x-τ]*TFFIT[x][[i]],{τ,0,1}];

Response={};

Do[
 R = Re[NIntegrate[Convolution[x],{x,0,∞}]]/Re[Integrate[MASSFIT[x],{x,0,∞}]];
     AppendTo[Response, Re[R]],
     {i,1,Length[TFimport]}
 ]


RS=Transpose[{
Table[i,{i,lowend, stepvoltage*Length[Response], stepvoltage}],Response}
];
```

Export of the response spectrum data into an ASCII file.

```
Export["C:\\Users\\Dirk\\Desktop\\paperPMC\\Datensaetze\\"<>
ToString[Date[][[1]]]<>"_"<>ToString[Date[][[2]]]<>"_"<>ToString[Date[][[3]]]<>"-
particle_"<>ToString[d/10 ^-9]<>"nm_"<>ToString[g]<>"_"<>
ToString[density]<>"kgpcm3-nano-PMC_"<>
```

```
ToString[flowrate]<>"lpm_"<>ToString[RPM]<>"rpm-DMA_"<>ToString[Qa/Qs//N]<>"_"<>
ToString[UDMA]<>"V.dat",RS]
```

Appendix B: Cyto-TP dosimetry

This script for Mathematica 10.0 calculates the deposition density profile of monodisperse spherical particles on the cold plate in the flow channel of the Cyto-TP prototype-2 based on the Waldmass-model.

All comments are black whereas all script-related text is blue (dark cyan for running variables).

A tuple of particles is generated representing a monodisperse aerosol of, in this case, 50-nm spheres.

```
δ=Table[50 10^-9,{i,1,1000}];
```

The velocity components stemming from thermophoresis, Vth and gravity, Vg, are defined. Vth is result of the product of the thermophoretic mobility Psi and the termparture gradient τ.

```
Vg[d_]:=(d^2*9.81)/(18 1.81*10^-5);

Vth[Psi_,τ_]:=Psi *τ;

V[d_,Psi_,τ_]:=-Vg[d]+Vth[Psi,τ];
```

The function S defines the numerical calculation of the particle trajectories bases on their equations of motion. A Poisseuille flow profile is assumed in x-direction.

```
 S[Q_,d_,Psi_,τ_,y0_]:=
NDSolve[{x'[t]==((3/2)Q)/(0.018*0.001)
(14((y[t]0.0005)/0.001)^2),y'[t]==V[d,Psi,τ],y[0]==y0,x[0]==0},
{x[t],y[t]},{t,0,10}]
```

The function EOM calculates the particle trajectories by applying S with a random starting conditions y0, which is the entering height of the particle at the entrance of the flow channel.

```
EOM[Q_,Psi_,τ_]:=
 Do[
          trajectory=S[Q,δ[[i]],Psi,τ,RandomReal[{0.0001,0.0009}]];
```

```
        AppendTo[trajectories,trajectory],
        {i,1,Length[δ]}]
```

The function deposition plane calculates the drop position of each particle at position "dropposition", which is a x-value. The procedure is repeated along certain steps over the width of the flow channel, where the stepsize is defined by the variable "resolution", effectively allocating a drop position {x,z} to each particle.

```
dropplane={};

depositionplane[Q_,Psi_,τ_,resolution_]:=
Do[
        trajectories={};
        EOM[Q,Psi,τ];
        droppositions={};
        Do[
            tdrop=FindRoot[D[x[t]/.trajectories[[i]],t]&&t>0,{t,1}];
            dropposition=x[t]/.trajectories[[i]]/.tdrop;
            AppendTo[droppositions,dropposition],
        {i,1,Length[trajectories]}];
    AppendTo[dropplane,Table[{droppositions[[k]][[1]],j},{k,1,Length[droppositions]}]],
    {j,0.001,0.017,resolution}]
```

The function depositionprofil counts particles deposited in individual squares to obtain a deposition density profile. The resolution of the profile is defined by the variable "resolution".

```
 depositionprofil[resolution_]:=
Do[
count=Transpose[{Table[dropplane[[j,1,2]],{i,0,0.08,resolution}],Table[i,{i,0,0.08,resolution}],
Table[Length[Select[Table[dropplane[[j,k,1]],
{k,1,Length[dropplane[[1]]]}],i<#<i+resolution&]],{i,0,0.08,resolution}]}];
        AppendTo[countsplane,count],
    {j,1,Length[dropplane]}]
```

The function circlecount counts all particles deposited in the area representing the front transwell. An iterative approach is implemented where initially all particles within a square with side-lengths equal to the circles diameter are counted which would be an overestimation. The side-lengths are decreased stepwise until the egdes of the square touches the circle. A particle count in that square is an underestimation. The particle count of all squares is compared to the total number of particles to obtain the deposition efficiencies for all squares.

```
efficiencies={};

individualcounts={};

circlecount[resolution_]:=
    Do[
        individualcounts={};
        Do[
            subcounts=
Total[Cases[Flatten[Table[Cases[countsplane[[i]],{i*resolution,j,_}],
{j,Round[0.012+k,resolution],Round[0.024-k,resolution],resolution}]],_Integer]];
            AppendTo[individualcounts,subcounts],
        {i,k/resolution,Length[countsplane]-k/resolution}];
        efficiency=(Total[individualcounts]/(Length[δ]*Length[countsplane]))//N;
        AppendTo[efficiencies,efficiency],
    {k,0,Round[0.012-0.012/Sqrt[2],resolution],resolution}]
```

Now all the calculations are conducted. The Waldmann-model is assumed to define the thermophoretic mobility ($0.55 \times (\eta/\rho_g/T)$) for the calculation of the drop positions for all particles. In this case the profile is calculated for a flow rate of 5 ml/min and a temperature gradient of 4000 K/m. Then the deposition density profile is generated, shown in the "heat-map" beneath. The white circle represents the area where the front transwell is located. Then the function circlecount is applied to calculate the deposition efficiencies.

```
resolution=0.001;

depositionplane[5/1000000/60,0.55 (1.81 10^-5)/(1.2 300),4000,resolution]

countsplane={};

depositionprofil[resolution]
Show[ListContourPlot[Flatten[countsplane,1],ColorFunction->"Warm",PlotLegends-
>Automatic],Graphics[{White, Thick,Circle[{0.009,0.018},0.006]}]]
```

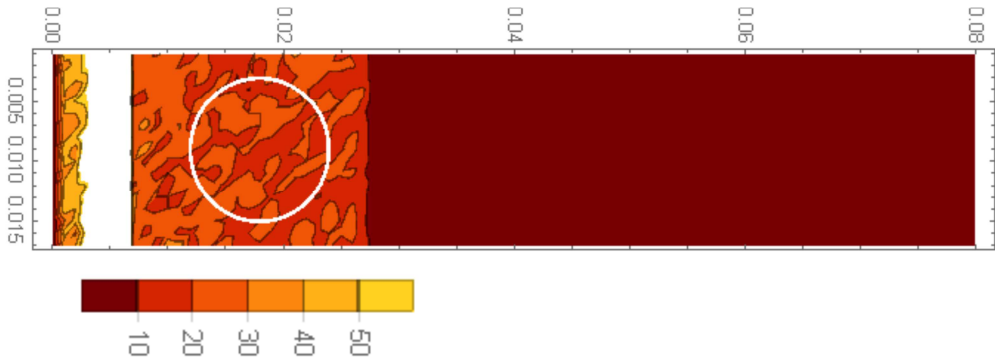

The function circlecount is applied. The mean of all obtained square efficiencies is an estimate of the deposition efficiency in the area of the front transwell (In the example shown above, the deposition efficieny is 0.142 (14.2%).

circlecount[resolution]

Mean[efficiencies]
0.142365

Appendix C: Culture conditions

Material:

- Cells: A549
- Transwells: 6Well; PET, 0,4µm pore size, (Costar 4,67cm², ref:3450)
- FBS (Biochrom S0115)
- Gentamycin (Invitrogen, #15750-037)
- PBS (biochrom L1825)
- HBSS(biochrom L2035)
- Trypsin (biochrom L2163)
- RPMI without phenolred (biochrom F1275)
- L-Glutamin (biochrom K0282)
- RPMI 1640 m. 25mM HEPES (biochrom L2163)
- VLE RPI 1640 (biochrom F1415)

Media:

RPMI vor cell passage:
500 ml RPMI (biochrom F1415)
55,5 ml FCS (Biochrom S0115)
55 µl Gentamycin (Invitrogen, #15750-037)

RPMI + HEPES (for exposure):
500 ml RPMI mit 25mM (biochrom L2163)
55.5 ml FCS (Biochrom S0115)
55 µl Gentamycin (Invitrogen, #15750-037)

RPMI without phenol red (for ROS-Assay):
500 ml RPMI mit 25mM (biochrom F1275)
55.5 ml FCS (Biochrom S0115)
55 µl Gentamycin (Invitrogen, #15750-037)
5,6 ml L-Glutamin (biochrom K0282)

Experimental design:

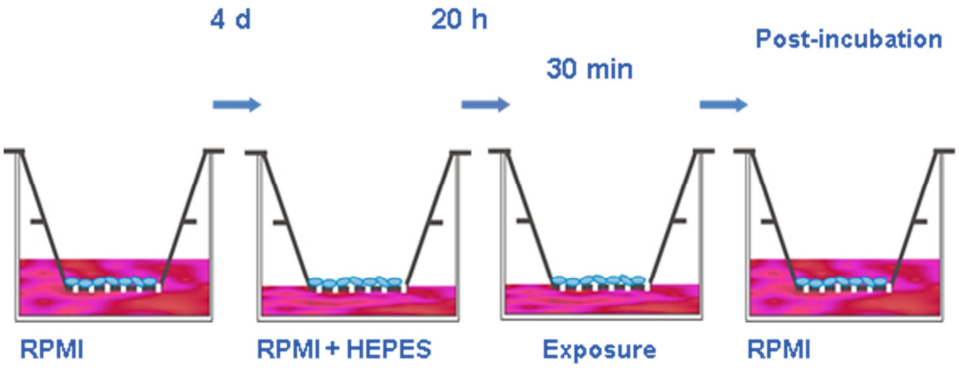

Protocol for culture of cells on transwells for ALI exposure

Exposure of A549 monoculture

Thursday afternoon (~14:00 o'clock): 80 000 A549 cells/ml (1ml by transwell) are seeded on apical side of each transwell (costar 4,67 cm^2) (density=17130 cells/cm^2)

Monday morning (~11:00 o'clock): cells are at confluency and medium is changed. On basal side medium is removed and 2x washed with 500 ml PBS on apical side to pass the culture in ALI.

Tuesday morning (~9:30 o'clock): cells are exposed in vitrocell system after 20h adaptation to ALI (30 min) and then transwells are put in new plate with fresh medium in basal side.

Wednesday: approximatively 24 hours post exposure, biological activity is assessed

List of Symbols and Abbreviations

List of abbreviations

ALI	Air-Liquid Interface
APM	Aerosol Particle Mass Analyzer
BAuA	Federal Institute for Occupational Safety and Health (Bundesanstalt für Arbeitsschutz und Arbeitsmedizin)
BSI	British Standards Institute
BUND	Bund für Umwelt und Naturschutz Deutschland
CAD	Computer-Aided Design
CNT	Carbon Nanotube
CPC	Condensation Particle Counter
CPMA	Centrifugal Particle Mass Analyzer
DCHF	Dichlorodihydrofluorescein-assay
DEMC / DMA	Differential Electrical Mobility Classifier / Differential Mobility Analyzer
DMEM	Dulbecco's Modified Eagle's medium
DNEL	Derived No-Effect Exposure Limit
EDX	Electron dispersive X-ray
ELISA	Enzyme Linked Immunosorbent Assay
EPA	Environmental Protection Agency
EU	European Union
FCS	Fetal Calve Serum
GBP	Granular Biopersistent Particle
HARN	High Aspect-Ratio Material
ICP-OES	Inductively Coupled Plasma Optical Emission Spectrometry
ICP-MS	Inductively Coupled Plasma Mass Spectrometry
IRCP	International Commission of Radiological Protection
MMAD	Mass Median Aerodynamic Diameter
MMVF	Man Made Vitreous Fibre
MPPD	Multiple Path Particle Deposition
MWCNT	Multi-Walled Carbon Nanotube
NO(A)ELs	No Observed (Adverse) Effect Level
NPV	Negative Predictive Value
OEL	Occupational Exposure Limit
PEEK	Polyether Ether Ketone

PM	Particulate matter
PMC	Particle Mass Classifier
PPV	Positive Predictive Value
PSL	Polystyrene-Latex
REACH	Registration, Evaluation, Authorisation and Restriction of Chemicals
ROS	Reactive Oxygen Species
SEM	Scanning Electron Microscopy
SMPS	Scanning Mobility Particle Sizer
SWCNT	Single-Walled Carbon Nanotube
TP	Thermal Precipitator
WHO	World Health Organization

List of symbols

Greek symbols

$\beta(t)$	Time dependent particle clearance rate in the lung
β_d	Fraction of gas molecules reflected diffusively from particle surface
γ_m	Frictional slip coefficient
γ_S	Thermal slip coefficient
γ_t	Temperature jump slip coefficient
Γ	Chapman-Enskog perturbation
δ	Dummy variable for function convolution
ϵ	Volume element
η	Dynamic viscosity
κ_G	Gas thermal conductivity
κ_P	Particle thermal conductivity
λ	Gas mean free path
λ_c	PMC classification performance parameter
ξ	Diffusive particle penetration rate
ρ	Density
ρ_0	Standard density 1 g/cm^3
ρ_{ap}	Apparent density
ρ_g	Gas density
ρ_p	Particle (material) density
σ	Standard deviation
σ_g	Geometric standard deviation
ς	Diffusive deviation in particle trajectory

φ	Thermophoretic parameter
ϕ	Deposition efficiency
ϕ_A	Deposition efficiency in the alveolar region
χ	Dynamic shape factor
ψ	Thermophoretic mobility
$\Omega(s)$	Transfer function of parameter s
$\Omega_{DMA}(Z)$	DMA transfer function for electrical mobility
$\Omega_{PMC}(M)$	PMC transfer function for particle mass
$\Omega_{nano-PMC}(M)$	Nano-PMC transfer function for particle mass
ω	Rotational speed

Other symbols

A	(Surface) area
$A_\emptyset$	Cross-sectional area
a	Thermal precipitator plate distance
B	(Mechanical) mobility
b	Thermal precipitator flow channel width
$C(\epsilon)$	Particle number concentration in volume ϵ
C_C	Cunningham-Slip factor
C_M	Particle mass concentration in the breathing zone
C_V	Particle volume concentration in the breathing zone
D	Mass-mobility scaling exponent
$\mathcal{D}$	Diffusion coefficient
d	Geometric diameter of a sphere
d_A	Surface equivalent diameter
d_{ae}	Aerodynamic diameter
d_m	Mobility (equivalent) diameter
d_{ve}	Volume equivalent diameter
$\mathrm{erf}(x)$	Error function
F_{Cb}	Electrostatic force (Coulomb force)
F_{Cn}	Centrifugal force
F_D	Drag force
F_G	Gravitational force
F_{th}	Thermophoretic force
$f_0(u)$	Maxwell-Boltzmann distribution of molecular velocity u in gas
G	DMA-geometry factor
g	Gravitational acceleration

$\mathcal{G}$	Random variable from Gaussian distribution
I_γ	Laminar flow profile in DMA flow channel
K	Thermophoretic coefficient
L_{CC}	Living cell count
L_{DMA}	DMA cylinder length
$\mathcal{L}$	Operator for Laplace-transformation
M	(Particle) mass
M_C	Centroid mass (Mass channel of a PMC)
m	Mass of gas molecules
N	Number of particles
n	Number
$n_{in}(d)$	Input particle size (number) distribution
$n_{in}(M)$	Input particle mass (number) distribution
$n_{in}(Z)$	Unclassified particle mobility (number) distribution
$n_{out}(d)$	Output particle size (number) distribution
$n_{out}(M)$	Input particle mass (number) distribution
$n_{out}(Z)$	Classified particle mobility (number) distribution
$n(d_m)$	Particle mobility diameter number distribution
$n(M)$	Particle mass number distribution
$R(\lambda_c)$	Nano-PMC resolution parameter
R_1	Outer radius of inner DMA cylinder
R_2	Inner radius of outer DMA cylinder
R_{N}	Number dose rate
R_{SA}	Surface area dose rate
R_{V}	Volume dose rate
R_{M}	Mass dose rate
r	Radius
$r(t)$	Time-dependent, radial component of trajectory
r_1	Outer radius of inner nano-PMC cylinder
r_2	Inner radius of outer nano-PMC cylinder
r_c	Radial center of nano-PMC flow channel
Re	Reynolds-number
q	Charge
Q	Volumetric flow rate
$Q_{a,in}$	DMA unclassified sample flow rate
$Q_{a,out}$	DMA classified sample flow rate
Q_{br}	Volumetric breathing rate

$Q_{sh,in}$	DMA sheath flow rate
$Q_{sh,out}$	DMA excess flow rate
P	Statistical variance
$S_{3/2}^{(r)}(x)$	Sonine-polynome
T	Temperature
t	Time
U	Potential difference (voltage)
U_C	Centroid potential difference of nano-PMC response spectrum
V	Volume
V_{ap}	Apparent volume
V_{AV}	Volume of an alveolar macrophage
V_{CV}	Accumulated particle volume in alveolar region
u	Velocity of gas molecules
v	Velocity
$\tilde{v}$	Mean velocity
v_G	Gravitational settling velocity
v_{rms}	Root-mean spare of fluctuation velocity
v_{th}	Thermophoretic velocity
v_x	Cartesian x-component of velocity
v_y	Cartesian y-component of velocity
v_z	Cartesian z-component of velocity
$x(t)$	Time-dependent input signal
$x(t)$	Time-dependent, Cartesian x-component of trajectory
$y(t)$	Time-dependent output signal
$y(t)$	Time-dependent, Cartesian y-component of trajectory
Z	Electrical mobility
Z_P	Centroid electrical mobility
$z(t)$	Time-dependent, Cartesian z-component of trajectory

Fundamental constants

e	Electrical charge ($e \approx 1.602 \times 10^{-19}$ C)
k_B	Boltzmann constant ($k_B \approx 1.380 \times 10^{-23}$ JK^{-1})

Bibliography

[1] BMBF, *Nano.De-Report 2013: Status Quo Der Nanotechnologie in Deutschland*. 2013: Bonn.

[2] BUND. *Datenbank Für Nano-Produkte*. 2015; Available from: http://www.bund.net/themen_und_projekte/nanotechnologie/nanoproduktdatenbank/.

[3] Maynard, A.D., Aitken, R.J., Butz, T., Colvin, V., Donaldson, K., Oberdorster, G., Philbert, M.A., Ryan, J., Seaton, A., Stone, V., Tinkle, S.S., Tran, L., Walker, N.J., and Warheit, D.B. (2006), *Safe Handling of Nanotechnology*. Nature. **444**(7117): p. 267-269.

[4] WHO, *Hazard Prevention and Control in the Work Environment: Airborne Dust*. 1999, Occupational and Environmental Health Department of Protection of the Human Environment, World Health organization: Geneva.

[5] Simko, M., Nosske, D., and Kreyling, W.G. (2014), *Metrics, Dose, and Dose Concept: The Need for a Proper Dose Concept in the Risk Assessment of Nanoparticles.* Int J Environ Res Public Health. **11**(4): p. 4026-48.

[6] Delmaar, C.J., Peijnenburg, W.J., Oomen, A.G., Chen, J., de Jong, W.H., Sips, A.J., Wang, Z., and Park, M.V. (2015), *A Practical Approach to Determine Dose Metrics for Nanomaterials.* Environ Toxicol Chem. **34**(5): p. 1015-22.

[7] Schmid, O. and Stoeger, T. (2016), *Surface Area Is the Biologically Most Effective Dose Metric for Acute Nanoparticle Toxicity in the Lung.* Journal of Aerosol Science. **99**: p. 133-143.

[8] Pauluhn, J. (2011), *Poorly Soluble Particulates: Searching for a Unifying Denominator of Nanoparticles and Fine Particles for Dnel Estimation.* Toxicology. **279**(1-3): p. 176-88.

[9] Rodriguez, S., Alastuey, A., and Querol, X. (2012), *A Review of Methods for Long Term in Situ Characterization of Aerosol Dust.* Aeolian Research. **6**: p. 55-74.

[10] Vashist, S.K. and Vashist, P. (2011), *Recent Advances in Quartz Crystal Microbalance-Based Sensors.* Journal of Sensors.

[11] Ames, B.N., McCann, J., and Yamasaki, E. (1975), *Methods for Detecting Carcinogens and Mutagens with the Salmonella/Mammalian-Microsome Mutagenicity Test.* Mutat Res. **31**(6): p. 347-64.

[12] Rothen-Rutishauser, B., Blank, F., Muhlfeld, C., and Gehr, P. (2008), *In Vitro Models of the Human Epithelial Airway Barrier to Study the Toxic Potential of Particulate Matter.* Expert Opinion on Drug Metabolism & Toxicology. **4**(8): p. 1075-1089.

[13] Teeguarden, J.G., Hinderliter, P.M., Orr, G., Thrall, B.D., and Pounds, J.G. (2007), *Particokinetics in Vitro: Dosimetry Considerations for in Vitro Nanoparticle Toxicity Assessments.* Toxicol Sci. **95**(2): p. 300-12.

[14] Maiorano, G., Sabella, S., Sorce, B., Brunetti, V., Malvindi, M.A., Cingolani, R., and Pompa, P.P. (2010), *Effects of Cell Culture Media on the Dynamic Formation of Protein-Nanoparticle Complexes and Influence on the Cellular Response.* ACS Nano. **4**(12): p. 7481-91.

[15] Baron, P.A. and Willeke, K. (2005), *Aerosol Measurement, Principles, Techniques and Applications*. 2nd Edition ed.: Wiley-Interscience.

[16] Agarwal, J.K. and Sem, G.J. (1980), *Continuous Flow, Single Particle Counting Condensation Nucleus Counter.* Journal of Aerosol Science. **11**: p. 347-57.

[17] Hinds, W. (1999), *Aerosol Technology*. Wiley.

[18] ICRP (1994), *Human Respiratory Tract Model for Radiological Protection. A Report of a Task Group of the International Commission on Radiological Protection.* Ann ICRP. **24**(1-3): p. 1-482.

[19] EPA (2013), *National Ambient Air Quality Standards for Particulate Matter.* Federal Register. **79**(10): p. 3086-3287.

[20] BAuA, *Trgs 402 Ermitteln Und Beurteilen Der Gefährdungen Bei Tätigkeiten Mit Gefahrstoffen: Inhalative Exposition*. 2010.

[21] Ehara, K., Hagwood, C., and Coakley, K.J. (1996), *Novel Method to Classify Aerosol Particles According to Their Mass-to-Charge Ratio - Aerosol Particle Mass Analyser.* Journal of Aerosol Science. **27**(2): p. 217-234.

[22] Tajima, N., Fukushima, N., Ehara, K., and Sakurai, H. (2011), *Mass Range and Optimized Operation of the Aerosol Particle Mass Analyzer.* Aerosol Science and Technology. **45**(2): p. 196-214.

[23] Olfert, J.S. and Collings, N. (2005), *New Method for Particle Mass Classification - the Couette Centrifugal Particle Mass Analyzer.* Journal of Aerosol Science. **36**(11): p. 1338-1352.

[24] McMurry, P.H., Wang, X., Park, K., and Ehara, K. (2002), *The Relationship between Mass and Mobility for Atmospheric Particles: A New Technique for Measuring Particle Density.* Aerosol Science and Technology. **36**(2): p. 227-238.

[25] Slowik, J.G., Stainken, K., Davidovits, P., Williams, L.R., Jayne, J.T., Kolb, C.E., Worsnop, D.R., Rudich, Y., DeCarlo, P.F., and Jimenez, J.L. (2004), *Particle Morphology and Density Characterization by Combined Mobility and Aerodynamic Diameter Measurements. Part 2: Application to Combustion-Generated Soot Aerosols as a Function of Fuel Equivalence Ratio.* Aerosol Science and Technology. **38**(12): p. 1206-1222.

[26] Borm, P.J., Robbins, D., Haubold, S., Kuhlbusch, T., Fissan, H., Donaldson, K., Schins, R., Stone, V., Kreyling, W., Lademann, J., Krutmann, J., Warheit, D., and Oberdorster, E. (2006), *The Potential Risks of Nanomaterials: A Review Carried out for Ecetoc.* Part Fibre Toxicol. **3**: p. 11.

[27] Savolainen, K., Alenius, H., Norppa, H., Pylkkanen, L., Tuomi, T., and Kasper, G. (2010), *Risk Assessment of Engineered Nanomaterials and Nanotechnologies--a Review.* Toxicology. **269**(2-3): p. 92-104.

[28] Bakand, S., Hayes, A., and Dechsakulthorn, F. (2012), *Nanoparticles: A Review of Particle Toxicology Following Inhalation Exposure.* Inhal Toxicol. **24**(2): p. 125-35.

[29] Gebel, T., Marchan, R., and Hengstler, J.G. (2013), *The Nanotoxicology Revolution.* Arch Toxicol. **87**(12): p. 2057-62.

[30] Oberdorster, G., Maynard, A., Donaldson, K., Castranova, V., Fitzpatrick, J., Ausman, K., Carter, J., Karn, B., Kreyling, W., Lai, D., Olin, S., Monteiro-Riviere, N., Warheit, D., Yang, H., and Group, I.R.F.R.S.I.N.T.S.W. (2005), *Principles for Characterizing the Potential Human Health Effects from Exposure to Nanomaterials: Elements of a Screening Strategy.* Part Fibre Toxicol. **2**: p. 8.

[31] Nel, A., Xia, T., Meng, H., Wang, X., Lin, S., Ji, Z., and Zhang, H. (2013), *Nanomaterial Toxicity Testing in the 21st Century: Use of a Predictive Toxicological Approach and High-Throughput Screening.* Acc Chem Res. **46**(3): p. 607-21.

[32] Stone, V., Johnston, H.J., Balharry, D., Gernand, J.M., and Gulumian, M. (2016), *Approaches to Develop Alternative Testing Strategies to Inform Human Health Risk Assessment of Nanomaterials.* Risk Anal.

[33] Paur, H.R., Cassee, F.R., Teeguarden, J., Fissan, H., Diabate, S., Aufderheide, M., Kreyling, W.G., Hanninen, O., Kasper, G., Riediker, M., Rothen-Rutishauser, B., and Schmid, O. (2011), *In-Vitro Cell Exposure Studies for the Assessment of Nanoparticle Toxicity in the Lung-a Dialog between Aerosol Science and Biology.* Journal of Aerosol Science. **42**(10): p. 668-692.

[34] Wittmaack, K. (2011), *Excessive Delivery of Nanostructured Matter to Submersed Cells Caused by Rapid Gravitational Settling.* Acs Nano. **5**(5): p. 3766-3778.

[35] Savi, M., Kalberer, M., Lang, D., Ryser, M., Fierz, M., Gaschen, A., Ricka, J., and Geiser, M. (2008), *A Novel Exposure System for the Efficient and Controlled Deposition of Aerosol Particles onto Cell Cultures.* Environmental Science & Technology. **42**(15): p. 5667-5674.

[36] Donaldson, K. and Seaton, A. (2012), *A Short History of the Toxicology of Inhaled Particles.* Part Fibre Toxicol. **9**: p. 13.

[37] Matthew S.P. Boyles, L.C.S., Paul Schlinkert, Martin Himly and Albert Duschl (2014), *The Significance and Insignificance of Carbon Nanotube-Induced Inflammation.* Fibres. **2**(1): p. 45-71.

[38] Donaldson, K., Murphy, F.A., Duffin, R., and Poland, C.A. (2010), *Asbestos, Carbon Nanotubes and the Pleural Mesothelium: A Review of the Hypothesis Regarding the Role of Long Fibre Retention in the Parietal Pleura, Inflammation and Mesothelioma.* Part Fibre Toxicol. **7**: p. 5.

[39] Cooke, W.E. (1924), *Fibrosis of the Lungs Due to the Inhalation of Asbestos Dust.* Br Med J. **2**(3317): p. 147-140 2.

[40] Borow, M., Conston, A., Livornese, L., and Schalet, N. (1973), *Mesothelioma Following Exposure to Asbestos: A Review of 72 Cases.* Chest. **64**(5): p. 641-6.

[41] Greenberg, M.I., Waksman, J., and Curtis, J. (2007), *Silicosis: A Review.* Dis Mon. **53**(8): p. 394-416.

[42] Castranova, V. (2004), *Signaling Pathways Controlling the Production of Inflammatory Mediators in Response to Crystalline Silica Exposure: Role of Reactive Oxygen/Nitrogen Species.* Free Radic Biol Med. **37**(7): p. 916-25.

[43] BAuA, *Sicherheit Und Gesundheit Bei Der Arbeit 2013*. 2013, Bundesministerium für Arbeit und Soziales (BMAS).

[44] Kim, I.Y., Joachim, E., Choi, H., and Kim, K. (2015), *Toxicity of Silica Nanoparticles Depends on Size, Dose, and Cell Type.* Nanomedicine.

[45] Warheit, D.B., Reed, K.L., and DeLorme, M.P. (2013), *Embracing a Weight-of-Evidence Approach for Establishing Noaels for Nanoparticle Inhalation Toxicity Studies.* Toxicol Pathol. **41**(2): p. 387-94.

[46] Oberdorster, G., Oberdorster, E., and Oberdorster, J. (2005), *Nanotoxicology: An Emerging Discipline Evolving from Studies of Ultrafine Particles.* Environ Health Perspect. **113**(7): p. 823-39.

[47] Poland, C.A., Duffin, R., Kinloch, I., Maynard, A., Wallace, W.A., Seaton, A., Stone, V., Brown, S., Macnee, W., and Donaldson, K. (2008), *Carbon Nanotubes Introduced into the Abdominal Cavity of Mice Show Asbestos-Like Pathogenicity in a Pilot Study.* Nat Nanotechnol. **3**(7): p. 423-8.

[48] Sargent, L.M., Hubbs, A.F., Young, S.H., Kashon, M.L., Dinu, C.Z., Salisbury, J.L., Benkovic, S.A., Lowry, D.T., Murray, A.R., Kisin, E.R., Siegrist, K.J., Battelli, L., Mastovich, J., Sturgeon, J.L., Bunker, K.L., Shvedova, A.A., and Reynolds, S.H. (2012), *Single-Walled Carbon Nanotube-Induced Mitotic Disruption.* Mutat Res. **745**(1-2): p. 28-37.

[49] Ault, J.G., Cole, R.W., Jensen, C.G., Jensen, L.C.W., Bachert, L.A., and Rieder, C.L. (1995), *Behavior of Crocidolite Asbestos During Mitosis in Living Vertebrate Lung Epithelial-Cells.* Cancer Research. **55**(4): p. 792-798.

[50] Gebel, T., Foth, H., Damm, G., Freyberger, A., Kramer, P.J., Lilienblum, W., Rohl, C., Schupp, T., Weiss, C., Wollin, K.M., and Hengstler, J.G. (2014), *Manufactured Nanomaterials: Categorization and Approaches to Hazard Assessment.* Arch Toxicol.

[51] Arts, J.H.E., Hadi, M., Irfan, M.A., Keene, A.M., Kreiling, R., Lyon, D., Maier, M., Michel, K., Petry, T., Sauer, U.G., Warheit, D., Wiench, K., Wohlleben, W., and Landsiedel, R. (2015), *A Decision-Making Framework for the Grouping and Testing of Nanomaterials (Df4nanogrouping).* Regulatory Toxicology and Pharmacology. **71**(2): p. S1-S27.

[52] Donaldson, K. and Poland, C.A. (2013), *Nanotoxicity: Challenging the Myth of Nano-Specific Toxicity.* Curr Opin Biotechnol. **24**(4): p. 724-34.

[53] Krug, H.F. (2014), *Nanosafety Research-Are We on the Right Track?* Angewandte Chemie-International Edition. **53**(46): p. 12304-12319.

[54] Braakhuis, H.M., Oomen, A.G., and Cassee, F.R. (2016), *Grouping Nanomaterials to Predict Their Potential to Induce Pulmonary Inflammation.* Toxicology and Applied Pharmacology. **299**: p. 3-7.

[55] Hartung, T. (2010), *Food for Thought ... On Alternative Methods for Nanoparticle Safety Testing.* ALTEX. **27**(2): p. 87-95.

[56] Doke, S.K. and Dhawale, S.C. (2015), *Alternatives to Animal Testing: A Review.* Saudi Pharmaceutical Journal. **23**(3): p. 223-229.

[57] Liou, S.H., Tsai, C.S., Pelclova, D., Schubauer-Berigan, M.K., and Schulte, P.A. (2015), *Assessing the First Wave of Epidemiological Studies of Nanomaterial Workers.* J Nanopart Res. **17**: p. 413.

[58] Olson, H., Betton, G., Robinson, D., Thomas, K., Monro, A., Kolaja, G., Lilly, P., Sanders, J., Sipes, G., Bracken, W., Dorato, M., Van Deun, K., Smith, P., Berger, B., and Heller, A. (2000), *Concordance of the Toxicity of Pharmaceuticals in Humans and in Animals.* Regul Toxicol Pharmacol. **32**(1): p. 56-67.

[59] Landsiedel, R., Sauer, U.G., Ma-Hock, L., Schnekenburger, J., and Wiemann, M. (2014), *Pulmonary Toxicity of Nanomaterials: A Critical Comparison of Published in Vitro Assays and in Vivo Inhalation or Instillation Studies.* Nanomedicine (Lond). **9**(16): p. 2557-85.

[60] Hong, T.K., Tripathy, N., Son, H.J., Ha, K.T., Jeong, H.S., and Hahn, Y.B. (2013), *A Comprehensive in Vitro and in Vivo Study of Zno Nanoparticles Toxicity.* Journal of Materials Chemistry B. **1**(23): p. 2985-2992.

[61] Kim, Y.H., Boykin, E., Stevens, T., Lavrich, K., and Gilmour, M.I. (2014), *Comparative Lung Toxicity of Engineered Nanomaterials Utilizing in Vitro, Ex Vivo and in Vivo Approaches.* J Nanobiotechnology. **12**(1): p. 47.

[62] Mirowsky, J.E., Jin, L., Thurston, G., Lighthall, D., Tyner, T., Horton, L., Galdanes, K., Chillrud, S., Ross, J., Pinkerton, K.E., Chen, L.C., Lippmann, M., and Gordon, T. (2015), *In Vitro and in Vivo Toxicity of Urban and Rural Particulate Matter from California.* Atmospheric Environment. **103**: p. 256-262.

[63] C. Voisson, C.A., E. Jakubczak, T. Tonnel (1977), *Cell Culture in the Gas Phase.* Bulletin European de Physiologie Respiratoire. **13**: p. 69–82.

[64] Rach, J., Budde, J., Mohle, N., and Aufderheide, M. (2014), *Direct Exposure at the Air-Liquid Interface: Evaluation of an in Vitro Approach for Simulating Inhalation of Airborne Substances.* Journal of Applied Toxicology. **34**(5): p. 506-515.

[65] Lenz, A.G., Karg, E., Lentner, B., Dittrich, V., Brandenberger, C., Rothen-Rutishauser, B., Schulz, H., Ferron, G.A., and Schmid, O. (2009), *A Dose-Controlled System for Air-Liquid Interface Cell Exposure and Application to Zinc Oxide Nanoparticles.* Particle and Fibre Toxicology. **6**.

[66] Anjilvel, S. and Asgharian, B. (1995), *A Multiple-Path Model of Particle Deposition in the Rat Lung.* Fundam Appl Toxicol. **28**(1): p. 41-50.

[67] Baan, R.A. and Grosse, Y. (2004), *Man-Made Mineral (Vitreous) Fibres: Evaluations of Cancer Hazards by the Iarc Monographs Programme.* Mutation Research-Fundamental and Molecular Mechanisms of Mutagenesis. **553**(1-2): p. 43-58.

[68] BAuA, *Trgs 521: Abbruch-, Sanierungs- Und Instandhaltungsarbeiten Mit Alter Mineralwolle*, B.f.A.u. Arbeitsmedizin, Editor. 2008: Dortmund.

[69] Bellmann, B., Muhle, H., Kamstrup, O., and Draeger, U.F. (1994), *Investigation on the Durability of Man-Made Vitreous Fibers in Rat Lungs.* Environ Health Perspect. **102 Suppl 5**: p. 185-9.

[70] Packroff, R., *Biosoluble Fibres: A Win-Win Strategy of Regulation and Product Innovation for Quality of Work in Small and Medium Enterprises (Sme)*, in *European Week for Safety and Health at Work 2003*. 2003: Bilbao, Spain.

[71] Johnston, H.J., Hutchison, G.R., Christensen, F.M., Peters, S., Hankin, S., Aschberger, K., and Stone, V. (2010), *A Critical Review of the Biological Mechanisms Underlying the in Vivo and in Vitro Toxicity of Carbon Nanotubes: The Contribution of Physico-Chemical Characteristics.* Nanotoxicology. **4**(2): p. 207-46.

[72] Liu, Y., Zhao, Y., Sun, B., and Chen, C. (2013), *Understanding the Toxicity of Carbon Nanotubes.* Acc Chem Res. **46**(3): p. 702-13.

[73] Ma-Hock, L., Strauss, V., Treumann, S., Kuttler, K., Wohlleben, W., Hofmann, T., Groters, S., Wiench, K., van Ravenzwaay, B., and Landsiedel, R. (2013), *Comparative Inhalation Toxicity of Multi-Wall Carbon Nanotubes, Graphene, Graphite Nanoplatelets and Low Surface Carbon Black.* Part Fibre Toxicol. **10**: p. 23.

[74] Ma-Hock, L., Treumann, S., Strauss, V., Brill, S., Luizi, F., Mertler, M., Wiench, K., Gamer, A.O., van Ravenzwaay, B., and Landsiedel, R. (2009), *Inhalation Toxicity of Multiwall Carbon Nanotubes in Rats Exposed for 3 Months.* Toxicol Sci. **112**(2): p. 468-81.

[75] Savolainen, K., Backman, U.,, Brouwer, D., Fadeel, B., Fernandes, T., Kuhlbusch, T., Landsiedel, R.,, and Lynch, I. and Pylkkänen, L., *Nanosafety in Europe 2015-2025: Towards Safe and Sustainable Nanomaterials and Nanotechnology Innovations*, F.I.o.O. Health, Editor. 2013: Helsinki.

[76] Brossell, D., Valenti, M., Bezantakos, S., Schmidt-Ott, A., and Biskos, G. (2015), *The Nano-Particle Mass Classifier (Nano-Pmc): Development, Characterization, and Application for Determining the Mass, Apparent Density, and Shape of Particles with Masses Down to the Zeptogram Range.* Aerosol Science and Technology. **49**(7): p. 495-507.

[77] Brossell, D., Troller, S., Dziurowitz, N., Plitzko, S., Linsel, G., Asbach, C., Azong-Wara, N., Fissan, H., and Schmidt-Ott, A. (2013), *A Thermal Precipitator for the Deposition of Airborne Nanoparticles onto Living Cells-Rationale and Development.* Journal of Aerosol Science. **63**: p. 75-86.

[78] Allen, M.D. and Raabe, O.G. (1985), *Slip Correction Measurements of Spherical Solid Aerosol-Particles in an Improved Millikan Apparatus.* Aerosol Science and Technology. **4**(3): p. 269-286.

[79] BSI, *British Standard Bs 2955 Glossary of Terms Relating to Particle Technology*. 1991: London.

[80] Ku, B.K. and Maynard, A.D. (2005), *Comparing Aerosol Surface-Area Measurements of Monodisperse Ultrafine Silver Agglomerates by Mobility Analysis, Transmission Electron Microscopy and Diffusion Charging*. Journal of Aerosol Science. **36**(9): p. 1108-1124.

[81] Li, M., Mulholland, G.W., and Zachariah, M.R. (2014), *Understanding the Mobility of Nonspherical Particles in the Free Molecular Regime.* Phys Rev E Stat Nonlin Soft Matter Phys. **89**(2): p. 022112.

[82] Morrow, P.E. (1988), *Possible Mechanisms to Explain Dust Overloading of the Lungs.* Fundamental and Applied Toxicology. **10**(3): p. 369-384.

[83] Morimoto, Y., Oyabu, T., Horie, M., Kambara, T., Izumi, H., Kuroda, E., Creutzenberg, O., Bellmann, B., Pohlmann, G., Schuchardt, S., Hansen, T., and Ernst, H. (2013), *Pulmonary Toxicity of Printer Toner Following Inhalation and Intratracheal Instillation.* Inhal Toxicol. **25**(12): p. 679-90.

[84] Jarabek, A.M., Asgharian, B., and Miller, F.J. (2005), *Dosimetric Adjustments for Interspecies Extrapolation of Inhaled Poorly Soluble Particles (Psp).* Inhalation Toxicology. **17**(7-8): p. 317-334.

[85] van Leeuwen, C.J. and Vermeire, T.G. (2007), *Risk Assessment of Chemicals: An Introduction*. Springer.

[86] Pauluhn, J. (2014), *Derivation of Occupational Exposure Levels (Oels) of Low-Toxicity Isometric Biopersistent Particles: How Can the Kinetic Lung Overload Paradigm Be Used for Improved Inhalation Toxicity Study Design and Oel-Derivation?* Particle and Fibre Toxicology. **11**.

[87] Borm, P., Cassee, F.R., and Oberdorster, G. (2015), *Lung Particle Overload: Old School - New Insights?* Part Fibre Toxicol. **12**: p. 10.

[88] Stolzenburg, M.R. and McMurry, P.H. (2008), *Equations Governing Single and Tandem Dma Configurations and a New Lognormal Approximation to the Transfer Function.* Aerosol Science and Technology. **42**(6): p. 421-432.

[89] Mamakos, A., Ntziachristos, L., and Sarnaras, Z. (2007), *Diffusion Broadening of Dma Transfer Functions. Numerical Validation of Stolzenburg Model.* Journal of Aerosol Science. **38**(7): p. 747-763.

[90] Girod, B., Rabenstein, R., and Stenger, A. (2001), *Signals and Systems, 2nd Ed.*: Wiley.

[91] Winklmayr, W., Reischl, G.P., Lindner, A.O., and Berner, A. (1991), *A New Electromobility Spectrometer for the Measurement of Aerosol Size Distributions in the Size Range from 1 to 1000 Nm.* Journal of Aerosol Science. **22**(3): p. 289-296.

[92] Reischl, G.P., Makela, J.M., and Necid, J. (1997), *Performance of Vienna Type Differential Mobility Analyzer at 1.2-20 Nanometer.* Aerosol Science and Technology. **27**(6): p. 651-672.

[93] Stratmann, F., Kauffeldt, T., Hummes, D., and Fissan, H. (1997), *Differential Electrical Mobility Analysis: A Theoretical Study.* Aerosol Science and Technology. **26**(4): p. 368-383.

[94] He, M.L. and Dhaniyala, S. (2013), *A Multiple Charging Correction Algorithm for Scanning Electrical Mobility Spectrometer Data.* Journal of Aerosol Science. **61**: p. 13-26.

[95] Panton, R. (2005), *Incompressible Flow*. Wiley.

[96] Hagwood, C., Sivathanu, Y., and Mulholland, G. (1999), *The Dma Transfer Function with Brownian Motion a Trajectory/Monte-Carlo Approach.* Aerosol Science and Technology. **30**(1): p. 40-61.

[97] Zheng, F. (2002), *Thermophoresis of Spherical and Non-Spherical Particles: A Review of Theories and Experiments.* Advances in Colloid and Interface Science. **97**(1-3): p. 255-278.

[98] Chapman, S. and Cowling, T., G. (1990), *The Mathematical Theory of Non-Uniform Gases: An Account of the Kinetic Theory of Viscosity, Thermal Conduction, and Diffusion in Gases*. Cambridge University Press.

[99] Waldmann, L. (1959), *Über Die Kraft Eines Inhomogenen Gases Auf Kleine Suspendierte Kugeln.* Z. Naturforsch. **14a**: p. 589-599.

[100] Gallis, M.A., Rader, D.J., and Torczynski, J.R. (2004), *A Generalized Approximation for the Thermophoretic Force on a Free-Molecular Particle.* Aerosol Science and Technology. **38**(7): p. 692-706.

[101] Young, J.B. (2011), *Thermophoresis of a Spherical Particle: Reassessment, Clarification, and New Analysis.* Aerosol Science and Technology. **45**(8): p. 927-948.

[102] Gallis, M.A., Torczynski, J.R., and Rader, D.J. (2004), *Molecular Gas Dynamics Observations of Chapman-Enskog Behavior and Departures Therefrom in Nonequilibrium Gases.* Physical Review E. **69**(4).

[103] Keh, H.J. and Ou, C.L. (2004), *Thermophoresis of Aerosol Spheroids.* Aerosol Science and Technology. **38**(7): p. 675-684.

[104] Brock, J. (1962), *On the Theory of Thermal Forces Acting on Aerosol Particles.* Journal of Colloid Science. **17**: p. 768–780.

[105] Talbot, L., Cheng, R.K., Schefer, R.W., and Willis, D.R. (1980), *Thermophoresis of Particles in a Heated Boundary-Layer.* Journal of Fluid Mechanics. **101**(Dec): p. 737-758.

[106] Mackowski, D.W. (2006), *Monte Carlo Simulation of Hydrodynamic Drag and Thermophoresis of Fractal Aggregates of Spheres in the Free-Molecule Flow Regime.* Journal of Aerosol Science. **37**(3): p. 242-259.

[107] McMurry, P.H. (2000), *A Review of Atmospheric Aerosol Measurements.* Atmospheric Environment. **34**(12-14): p. 1959-1999.

[108] Biskos, G., Vons, V., Yurteri, C.U., and Schmidt-Ott, A. (2008), *Generation and Sizing of Particles for Aerosol-Based Nanotechnology.* Kona Powder and Particle Journal. **26**: p. 13-35.

[109] Schmid, S., Kurek, M., Adolphsen, J.Q., and Boisen, A. (2013), *Real-Time Single Airborne Nanoparticle Detection with Nanomechanical Resonant Filter-Fiber.* Sci Rep. **3**: p. 1288.

[110] Olfert, J.S., Reavell, K.S.J., Rushton, M.G., and Collings, N. (2006), *The Experimental Transfer Function of the Couette Centrifugal Particle Mass Analyzer.* Journal of Aerosol Science. **37**(12): p. 1840-1852.

[111] Tajima, N., Sakurai, H., Fukushima, N., and Ehara, K. (2013), *Design Considerations and Performance Evaluation of a Compact Aerosol Particle Mass Analyzer.* Aerosol Science and Technology. **47**(10): p. 1152-1162.

[112] Park, K., Kittelson, D.B., Zachariah, M.R., and McMurry, P.H. (2004), *Measurement of Inherent Material Density of Nanoparticle Agglomerates.* Journal of Nanoparticle Research. **6**(2-3): p. 267-272.

[113] Geller, M., Biswas, S., and Sioutas, C. (2006), *Determination of Particle Effective Density in Urban Environments with a Differential Mobility Analyzer and Aerosol Particle Mass Analyzer.* Aerosol Science and Technology. **40**(9): p. 709-723.

[114] Reddy, J.N. (2005), *An Introduction to the Finite Element Method*. McGraw-Hill.

[115] Hagwood, C., Coakley, K., Negiz, A., and Ehara, K. (1995), *Stochastic Modeling of a New Spectrometer.* Aerosol Science and Technology. **23**(4): p. 611-627.

[116] Lall, A.A., Ma, X.F., Guha, S., Mulholland, G.W., and Zachariah, M.R. (2009), *Online Nanoparticle Mass Measurement by Combined Aerosol Particle Mass Analyzer and Differential Mobility Analyzer: Comparison of Theory and Measurements.* Aerosol Science and Technology. **43**(11): p. 1075-1083.

[117] Lin, G.Y., Liao, B.X., Tzeng, N.J., Chen, C.W., Uang, S.N., Chen, S.C., Pui, D.Y.H., and Tsai, C.J. (2014), *The Effect of Nanoparticle Convection-Diffusion Loss on the Transfer Function of an Aerosol Particle Mass Analyzer.* Aerosol Science and Technology. **48**(6): p. 583-592.

[118] Tian, L. and Ahmadi, G. (2007), *Particle Deposition in Turbulent Duct Flows - Comparisons of Different Model Predictions.* Journal of Aerosol Science. **38**(4): p. 377-397.

[119] Schwyn, S., Garwin, E., and Schmidtott, A. (1988), *Aerosol Generation by Spark Discharge.* Journal of Aerosol Science. **19**(5): p. 639-642.

[120] Pfeiffer, T.V., Feng, J., and Schmidt-Ott, A. (2014), *New Developments in Spark Production of Nanoparticles.* Advanced Powder Technology. **25**(1): p. 56-70.

[121] DeCarlo, P.F., Slowik, J.G., Worsnop, D.R., Davidovits, P., and Jimenez, J.L. (2004), *Particle Morphology and Density Characterization by Combined Mobility and Aerodynamic Diameter Measurements. Part 1: Theory.* Aerosol Science and Technology. **38**(12): p. 1185-1205.

[122] Virtanen, A., Ristimaki, J., and Keskinen, J. (2004), *Method for Measuring Effective Density and Fractal Dimension of Aerosol Agglomerates.* Aerosol Science and Technology. **38**(5): p. 437-446.

[123] Schmid, O., Karg, E., Hagen, D.E., Whitefield, P.D., and Ferron, G.A. (2007), *On the Effective Density of Non-Spherical Particles as Derived from Combined Measurements of Aerodynamic and Mobility Equivalent Size.* Journal of Aerosol Science. **38**(4): p. 431-443.

[124] Kasper, G. (1982), *Dynamics and Measurement of Smokes .1. Size Characterization of Non-Spherical Particles.* Aerosol Science and Technology. **1**(2): p. 187-199.

[125] Schmidt-Ott, A. (1988), *In Situ Measurement of the Fractal Dimensionality of Ultrafine Aerosol Particles.* Applied Physical Letters **52**(12): p. 954–956.

[126] Schmidtott, A., Baltensperger, U., Gaggeler, H.W., and Jost, D.T. (1990), *Scaling Behavior of Physical Parameters Describing Agglomerates.* Journal of Aerosol Science. **21**(6): p. 711-717.

[127] Sorensen, C.M. (2011), *The Mobility of Fractal Aggregates: A Review.* Aerosol Science and Technology. **45**(7): p. 765-779.

[128] Schlichting, H., Gersten, K. (1999), *Boundary-Layer Theory*. Spinger.

[129] Dahneke, B.E. (1973), *Slip Correction Factors for Nonspherical Bodies. Iii, the Form of the General Law.* Journal of Aerosol Science. **4**: p. 163–170.

[130] Biskos, G., Russell, L.M., Buseck, P.R., and Martin, S.T. (2006), *Nanosize Effect on the Hygroscopic Growth Factor of Aerosol Particles.* Geophysical Research Letters. **33**(7).

[131] Wang, Z., King, S.M., Freney, E., Rosenoern, T., Smith, M.L., Chen, Q., Kuwata, M., Lewis, E.R., Poschl, U., Wang, W., Buseck, P.R., and Martin, S.T. (2010), *The Dynamic Shape Factor of Sodium Chloride Nanoparticles as Regulated by Drying Rate.* Aerosol Science and Technology. **44**(11): p. 939-953.

[132] Charvet, A., Bau, S., Coy, N.E.P., Bemer, D., and Thomas, D. (2014), *Characterizing the Effective Density and Primary Particle Diameter of Airborne Nanoparticles Produced by Spark Discharge Using Mobility and Mass Measurements (Tandem Dma/Apm).* Journal of Nanoparticle Research. **16**(5).

[133] Lövestam, G., Rauscher, H., Roebben, G., Sokull-Kluettgen, B., Gibson, N., Putaud, J., & Stamm, H. (2010), *Considerations on a Definition of Nanomaterial for Regulatory Purposes.* JRC Reference Letters.

[134] Kuhlbusch, T.A., Asbach, C., Fissan, H., Gohler, D., and Stintz, M. (2011), *Nanoparticle Exposure at Nanotechnology Workplaces: A Review.* Part Fibre Toxicol. **8**: p. 22.

[135] P. Orthen, M.R., R. Zimmer (2007), *Nanotechnology: Health and Environmental Risks of Nanomaterials.* BAuA, BfR, UBA.

[136] Geiser, M. and Kreyling, W.G. (2010), *Deposition and Biokinetics of Inhaled Nanoparticles.* Part Fibre Toxicol. **7**: p. 2.

[137] Ma-Hock, L., Burkhardt, S., Strauss, V., Gamer, A.O., Wiench, K., van Ravenzwaay, B., and Landsiedel, R. (2009), *Development of a Short-Term Inhalation Test in the Rat Using Nano-Titanium Dioxide as a Model Substance.* Inhal Toxicol. **21**(2): p. 102-18.

[138] Landsiedel, R., Kapp, M.D., Schulz, M., Wiench, K., and Oesch, F. (2009), *Genotoxicity Investigations on Nanomaterials: Methods, Preparation and Characterization of Test Material, Potential Artifacts and Limitations-Many Questions, Some Answers.* Mutation Research-Reviews in Mutation Research. **681**(2-3): p. 241-258.

[139] Maier, K.L., Alessandrini, F., Beck-Speier, I., Hofer, T.P.J., Diabate, S., Bitterle, E., Stoger, T., Jakob, T., Behrendt, H., Horsch, M., Beckers, J., Ziesenis, A., Hultner, L., and Frankenberger, M. (2008), *Health Effects of Ambient Particulate Matter - Biological Mechanisms and Inflammatory Responses to in Vitro and in Vivo Particle Exposures.* Inhalation Toxicology. **20**(3): p. 319-337.

[140] T. Meissner, A.P., V. Richter (2009), *Suspension Characterization as Important Key for Toxicological Investigations.* Journal of Physics: Conference Series. **170**: p. 012012.

[141] Hotze, E.M., Phenrat, T., and Lowry, G.V. (2010), *Nanoparticle Aggregation: Challenges to Understanding Transport and Reactivity in the Environment.* Journal of Environmental Quality. **39**(6): p. 1909-1924.

[142] Maynard, A.D., Warheit, D.B., and Philbert, M.A. (2011), *The New Toxicology of Sophisticated Materials: Nanotoxicology and Beyond.* Toxicol Sci. **120 Suppl 1**: p. S109-29.

[143] Aufderheide, M. (2005), *Direct Exposure Methods for Testing Native Atmospheres.* Experimental and Toxicologic Pathology. **57**: p. 213-226.

[144] M. Silanpaa, M.G., H. Phuleria, C. Sioutas (2008), *A High Collection Efficiency Electrostatic Precipitator for in Vitro Cell Exposure to Concentrated Ambient Particulate Matter (Pm).* Journal of Aerosol Science. **39**: p. 335–347.

[145] Schaeublin, N.M., Braydich-Stolle, L.K., Schrand, A.M., Miller, J.M., Hutchison, J., Schlager, J.J., and Hussain, S.M. (2011), *Surface Charge of Gold Nanoparticles Mediates Mechanism of Toxicity.* Nanoscale. **3**(2): p. 410-420.

[146] Schrade, A., Mailander, V., Ritz, S., Landfester, K., and Ziener, U. (2012), *Surface Roughness and Charge Influence the Uptake of Nanoparticles: Fluorescently Labeled Pickering-Type Versus Surfactant-Stabilized Nanoparticles.* Macromolecular Bioscience. **12**(11): p. 1459-1471.

[147] Azong-Wara, N., Asbach, C., Stahlmecke, B., Fissan, H., Kaminski, H., Plitzko, S., and Kuhlbusch, T.A.J. (2009), *Optimisation of a Thermophoretic Personal Sampler for Nanoparticle Exposure Studies.* Journal of Nanoparticle Research. **11**(7): p. 1611-1624.

[148] Azong-Wara, N., Asbach, C., Stahlmecke, B., Fissan, H., Kaminski, H., Plitzko, S., Bathen, D., and Kuhlbusch, T.A.J. (2013), *Design and Experimental Evaluation of a New Nanoparticle Thermophoretic Personal Sampler.* Journal of Nanoparticle Research. **15**(4).

[149] Thayer, D., Koehler, K.A., Marchese, A., and Volckens, J. (2011), *A Personal, Thermophoretic Sampler for Airborne Nanoparticles.* Aerosol Science and Technology. **45**(6): p. 744-750.

[150] L. Waldmann, K.S. (1966), *Thermophoresis and Diffusiophoresis of Aerosols*. London: Academic Press.

[151] Lieber, M., Smith, B., Szakal, A., Nelson-Rees, W., and Todaro, G. (1976), *A Continuous Tumor-Cell Line from a Human Lung Carcinoma with Properties of Type Ii Alveolar Epithelial Cells.* Int J Cancer. **17**(1): p. 62-70.

[152] Lequin, R.M. (2005), *Enzyme Immunoassay (Eia)/Enzyme-Linked Immunosorbent Assay (Elisa).* Clinical Chemistry. **51**(12): p. 2415-2418.

[153] Nara, H., Fukano, Y., Nishino, T., and Aufderheide, M. (2013), *Detection of the Cytotoxicity of Water-Insoluble Fraction of Cigarette Smoke by Direct Exposure to Cultured Cells at an Air-Liquid Interface.* Experimental and Toxicologic Pathology. **65**(5): p. 683-688.

[154] Landsiedel, R., Ma-Hock, L., Kroll, A., Hahn, D., Schnekenburger, J., Wiench, K., and Wohlleben, W. (2010), *Testing Metal-Oxide Nanomaterials for Human Safety.* Adv Mater. **22**(24): p. 2601-27.

[155] Buesen, R., Landsiedel, R., Sauer, U.G., Wohlleben, W., Groeters, S., Strauss, V., Kamp, H., and van Ravenzwaay, B. (2014), *Effects of Sio2, Zro2, and Baso4 Nanomaterials with or without Surface Functionalization Upon 28-Day Oral Exposure to Rats.* Archives of Toxicology. **88**(10): p. 1881-1906.

[156] Keller, J., *Biokinetics and Inhalation Toxicity of Cerium Dioxide and Barium Sulfate Nanoparticles after 1, 4, 13 and 52 Weeks of Exposure*. 2015, Justus-Liebig-Universität, Gießen.

[157] Svensson, C.R., Ameer, S.S., Ludvigsson, L., Ali, N., Alhamdow, A., Messing, M.E., Pagels, J., Gudmundsson, A., Bohgard, M., Sanfins, E., Karedal, M., Broberg, K., and Rissler, J. (2016), *Validation of an Air-Liquid Interface Toxicological Set-up Using Cu, Pd, and Ag Well-Characterized Nanostructured Aggregates and Spheres.* J Nanopart Res. **18**: p. 86.

[158] invitrogen, *Prestoblue™ Cell Viability Reagent Protocol*. 2010.

[159] Promega, *Cytotox-One™ Homogeneous Membrane Integrity Assay - Instructions for Use of Products G7890, G7891 and G7892*. 2009.

[160] invitrogen, *Reactive Oxygen Species (Ros) Detection Reagents*. 2006.

[161] BD, *Technical Data Sheet Human Il-8 Elisa Set - Cat. No. 555244*. 2015.

[162] DIN, *Workplace Exposure - Measurement of the Dustiness of Bulk Materials - Part 3: Continuous Drop Method; German Version En 15051-3:2013*. 2014.

[163] Hoffmann, S. and Hartung, T. (2005), *Diagnosis: Toxic! - Trying to Apply Approaches of Clinical Diagnostics and Prevalence in Toxicology Considerations.* Toxicological Sciences. **85**(1): p. 422-428.

[164] Bracken, M.B. (2009), *Why Animal Studies Are Often Poor Predictors of Human Reactions to Exposure.* Journal of the Royal Society of Medicine. **102**(3): p. 120-122.

[165] Fairbairn, D.W., Olive, P.L., and Oneill, K.L. (1995), *The Comet Assay - a Comprehensive Review.* Mutation Research-Reviews in Genetic Toxicology. **339**(1): p. 37-59.

[166] Foster, K.A., Oster, C.G., Mayer, M.M., Avery, M.L., and Audus, K.L. (1998), *Characterization of the A549 Cell Line as a Type Ii Pulmonary Epithelial Cell Model for Drug Metabolism.* Experimental Cell Research. **243**(2): p. 359-366.

[167] Swain, R.J., Kemp, S.J., Goldstraw, P., Tetley, T.D., and Steyens, M.M. (2010), *Assessment of Cell Line Models of Primary Human Cells by Raman Spectral Phenotyping.* Biophysical Journal. **98**(8): p. 1703-1711.

[168] Lenz, A.G., Karg, E., Brendel, E., Hinze-Heyn, H., Maier, K.L., Eickelberg, O., Stoeger, T., and Schmid, O. (2013), *Inflammatory and Oxidative Stress Responses of an Alveolar Epithelial Cell Line to Airborne Zinc Oxide Nanoparticles at the Air-Liquid Interface: A Comparison with Conventional, Submerged Cell-Culture Conditions.* Biomed Research International.

[169] He, W., Liu, Y., Wamer, W.G., and Yin, J.J. (2014), *Electron Spin Resonance Spectroscopy for the Study of Nanomaterial-Mediated Generation of Reactive Oxygen Species.* J Food Drug Anal. **22**(1): p. 49-63.

[170] Kohno, M. (2010), *Applications of Electron Spin Resonance Spectrometry for Reactive Oxygen Species and Reactive Nitrogen Species Research.* J Clin Biochem Nutr. **47**(1): p. 1-11.

[171] Zhao, J.Y. and Riediker, M. (2014), *Detecting the Oxidative Reactivity of Nanoparticles: A New Protocol for Reducing Artifacts.* Journal of Nanoparticle Research. **16**(7).

[172] Roesslein, M., Hirsch, C., Kaiser, J.P., Krug, H.F., and Wick, P. (2013), *Comparability of in Vitro Tests for Bioactive Nanoparticles: A Common Assay to Detect Reactive Oxygen Species as an Example.* International Journal of Molecular Sciences. **14**(12): p. 24320-24337.

[173] Fan, C.F., Chen, J., Chen, Y., Ji, J.F., and Teng, H.H. (2006), *Relationship between Solubility and Solubility Product: The Roles of Crystal Sizes and Crystallographic Directions.* Geochimica Et Cosmochimica Acta. **70**(15): p. 3820-3829.

[174] Schneider, T. and Jensen, K.A. (2008), *Combined Single-Drop and Rotating Drum Dustiness Test of Fine to Nanosize Powders Using a Small Drum.* Ann Occup Hyg. **52**(1): p. 23-34.

[175] Tsai, C.J., Lin, G.Y., Liu, C.N., He, C.E., and Chen, C.W. (2012), *Characteristic of Nanoparticles Generated from Different Nano-Powders by Using Different Dispersion Methods.* Journal of Nanoparticle Research. **14**(4).

[176] Breum, N.O. (1999), *The Rotating Drum Dustiness Tester: Variability in Dustiness in Relation to Sample Mass, Testing Time, and Surface Adhesion.* The Annals of Occupational Hygiene. **43**(8): p. 557-566.

[177] BOHS (1985), *Dustiness Estimation Tests for Dry Materials*, in *British Occupational Hygiene Society Technical Guide No. 4.*, Science Reviews Ltd,
: Northwood.

[178] Pensis, I., Mareels, J., Dahmann, D., and Mark, D. (2010), *Comparative Evaluation of the Dustiness of Industrial Minerals According to European Standard En 15051, 2006.* Ann Occup Hyg. **54**(2): p. 204-16.

[179] Prenni, A.J., Siefert, R.L., Onasch, T.B., Tolbert, M.A., and DeMott, P.J. (2000), *Design and Characterization of a Fluidized Bed Aerosol Generator: A Source for Dry, Submicrometer Aerosol.* Aerosol Science and Technology. **32**(5): p. 465-481.

[180] Plitzko, S., Gierke, E., Dziurowitz, N., and Brossell, D. (2010), *Generation of Cnt/Cnf Dusts by a Shaker Aerosol Generator in Combination with a Thermal Precipitator as the Collection System for Characterization of the Fibre Morphology.* Gefahrstoffe Reinhaltung Der Luft. **70**(1-2): p. 31-35.

[181] van Ommen, J.R., Valverde, J.M., and Pfeffer, R. (2012), *Fluidization of Nanopowders: A Review.* Journal of Nanoparticle Research. **14**(3).

[182] Morgeneyer, M., Le Bihan, O., Ustache, A., and Aguerre-Chariol, O. (2013), *Experimental Study of the Aerosolization of Fine Alumina Particles from Bulk by a Vortex Shaker.* Powder Technology. **246**: p. 583-589.

[183] Le Bihan, O.L.C., Ustache, A., Bernard, D., Aguerre-Chariol, O., and Morgeneyer, M. (2014), *Experimental Study of the Aerosolization from a Carbon Nanotube Bulk by a Vortex Shaker.* Journal of Nanomaterials.

[184] Vorbau, M., Hillemann, L., and Stintz, M. (2009), *Method for the Characterization of the Abrasion Induced Nanoparticle Release into Air from Surface Coatings.* Journal of Aerosol Science. **40**(3): p. 209-217.

[185] Gohler, D., Stintz, M., Hillemann, L., and Vorbau, M. (2010), *Characterization of Nanoparticle Release from Surface Coatings by the Simulation of a Sanding Process.* Ann Occup Hyg. **54**(6): p. 615-24.

[186] Koponen, I.K., Jensen, K.A., and Schneider, T. (2011), *Comparison of Dust Released from Sanding Conventional and Nanoparticle-Doped Wall and Wood Coatings.* J Expo Sci Environ Epidemiol. **21**(4): p. 408-18.

List of publications

D. Broßell, M. Valenti, S. Bezantakos, A. Schmidt-Ott and G. Biskos (2015): *„The nanoparticle mass classifier (nano-PMC): Development, characterisation and application for determining the mass, apparent density and shape of particles with masses down to the zeptogram range*", Aerosol Science and Technology, Volume 49, Issue 7, 2015.

D. Broßell, S. Tröller, N. Dziurowitz, Plitzko, G. Linsel, C. Asbach, N. Azong-Wara, H. Fissan, A. Schmidt-Ott (2013): *"A thermal precipitator for the deposition of airborne nanoparticles onto living cells – Rationale and development"*, Journal of Aerosol Science, Volume 63, 75-86

Curriculum Vitae

Dirk Broßell
Born September 11th 1981 in Papenburg, Germany

2001	Abitur at Staatliches Gymnasium Papenburg
2002-2009	Diplom in Physics at the Free University of Berlin. Topic of graduate research: Charge transport over molecular break junctions.
since 2009	Scientist in the unit „Particulate hazardous substances, innovative materials“ at the Federal Institute for Occupational Safety and Health, Berlin, Germany
Since 2011	Guest scientist and PhD-student at the Faculty of Applied Science of Delft University of Technology. Topic of research: Instrument Development for Nanomaterial Risk Assessment. Promoter: Prof. Dr. A. Schmidt-Ott.